Dissertation

submitted to the
Combined Faculties for the Natural Sciences and for Mathematics
of the
Ruperto-Carola University of Heidelberg, Germany
for the degree of

Doctor of Natural Sciences

put forward by
Mgr. Dalibor Nedbal
born in Prague

Oral examination: 17$^{\text{th}}$ December 2008

A Study of

Very High Energy Gamma-Ray Emission from Extragalactic Objects with **H.E.S.S.**

Referees: Prof. Dr. Werner Hofmann
Prof. Dr. Stefan Wagner

Abstract

Very-high-energy (VHE) γ-ray astronomy has opened a unique window into the Universe of the highest energies, allowing one to efficiently investigate the question of the origin of high-energy cosmic rays. The H.E.S.S. array of four imaging atmospheric Čerenkov (IACT) telescopes is utilised in this work to search for VHE γ-rays from selected candidate extragalactic objects that are expected to contain significant populations of cosmic rays: galaxy clusters Abell 496, Abell 85, Coma cluster, Abell 754, Centaurus cluster and Hydra A, starburst galaxies NGC 253 and M 83, from an ultraluminous infrared galaxy Arp 220 and from an active galactic nucleus (AGN), RGB J0152+017. The instrument is described, giving an overview of the IACT technique, the data acquisition, data-quality determination, calibration, performance, and the actual analysis that was used to obtain the results.

In the starburst galaxy NGC 253, a hint of a VHE signal is found at a $\sim 3\sigma$ significance level. No significant VHE signal is found from the remaining non-AGN objects, and upper limits are presented. The upper limits of Abell 85 and Abell 496 are used to constrain the non-thermal to thermal energy ratio, which is $\sim$8% for Abell 85 and is thus challenging theoretical estimates. The AGN, RGB J0152+017, is in this work discovered in VHE γ rays and its first-time broad-band spectral energy distribution is presented. While no new type of a VHE emitter is established, the presented theoretical expectations are very promising for the planned CTA observatory.

Kurzfassung

Hochenergetische Gamma-Astronomie hat in der letzten Jahre ein einzigartiges Fenster in das Universum der höchsten Energien eröffnet. Das H.E.S.S. Experiment, bestehend aus vier abbildenden atmosphärischen Čerenkov Teleskopen, wurde in dieser Arbeit verwendet, um nach der Gammastrahlung von ausgewählten extragalaktischen Objekten zu suchen. Die untersuchten Objekte sind die Galaxienhaufen Abell 496, Abell 85, Coma cluster, Abell 754, Centaurus cluster und Hydra A, die "starburst" Galaxien NGC 253 und M 83, die im Infrarot ultraleuchtkräftige Galaxie Arp 220 und der aktive galaktische Kern (AGN), RGB J0152+017. Anhand des H.E.S.S. Experiments wird die Technik, die Datenaufnahme, die Datenqualitätüberprüfung, die Kalibrierung und die Sensitivität beschrieben. Weiterhin wird die Datenanalyse, mit der die Ergebnisse gewonnen wurden, dargestellt.

Im Falle der Galaxie NGC 253 wurde ein mögliches Signal mit der Signifikanz $\sim 3\sigma$ gefunden. Es wurde kein signifikantes Signal von den anderen nicht-AGN Objekten gemessen und es wurden Flußobergrenzen hergeleitet. Die Flußobergrenze von Abell 85 wird benutzt um Obergrenze für das Verhältniss der Energie der nicht-thermischen und der thermischen Komponente des Galaxienhaufens zu berechnen ($\sim$8%). Weiterhin wird die Entdeckung des AGNs, RGB J0152+017, präsentiert, und die spektrale Energieverteilung über mehrere Wellenlängenbereiche für dieses Objekt erstmals gezeigt. Abschließend wird das Potential des zukünftigen CTA Observatorium diskutiert.

Contents

List of Figures

List of Tables

Chapter 1

Introduction

The field of *astroparticle physics*, the study of non-thermal phenomena of the highest energies in the Universe, has experienced major advances in the last few decades. The field itself will soon celebrate 100 years since V. Hess in 1912 first claimed a discovery of ionizing rays coming from the cosmos. Over this time period, a number of crucial discoveries concerning cosmic rays were achieved. In the first half of the 20th century, cosmic rays became the main playground for particle physicists. Particles such as the muon, positron and pion were discovered in interactions of cosmic rays. In the second half of the century, during the dawn of man-made particle accelerators, the interest of astroparticle physicists was turned to the question of the origin of cosmic rays.

The problem of the origin, propagation and composition of cosmic rays has been targeted by numerous astroparticle experiments. The composition and spectrum of primary cosmic rays at energies below $\sim 10^{13}$ eV has been studied by balloon and space-based experiments. The higher energies, however, remain explicitly an area of interest of Earth-bound experiments, which detect mostly secondary particles produced by interaction of CR in the atmosphere. Experiments were built capable of detecting extensive air showers (EAS) initiated by high-energy cosmic-ray particles interacting in the atmosphere. In this way, experiments such as *AGASA* (Chiba et al. 1992), Yakutsk (Ivanov et al. 2003), HiRes (Corbató et al. 1992; Abbasi et al. 2005), the Haverah Park array (Tennent 1967), KASCADE (Grande) (Antoni et al. 2003) and recently the Pierre Auger Observatory(Abraham et al. 2004) managed to measure the spectrum (see Fig. 1.1) of ultra-high-energy cosmic rays (UHECRs) in energy ranges far beyond possibilities of the Earth-bound particle accelerators. Using these instruments, even particles with energies up to $\sim 3 \times 10^{20}$ eV have been detected by independent experimental groups (Bird et al. 1995; Hayashida et al. 1994).

Despite all the experimental advances and discoveries, the question of the origin of the cosmic rays remains yet to be answered. There is at the moment no experimentally confirmed mechanism capable of accelerating particles to energies beyond 200 TeV. Recently, a correlation of UHECR direction with nearby (< 100 Mpc) active galactic nuclei (AGNs) was claimed (Abraham et al. 2007), which could indicate that UHECRs are produced in AGNs or in locations with a similar spatial distribution. The location of the acceleration is however far from being unveiled and the result itself is still a question of controversy (Moskalenko et al. 2008). The problem of identifying and understanding the astrophysical sources of such cosmic rays presents a challenge for both experimental and theoretical

physicists.

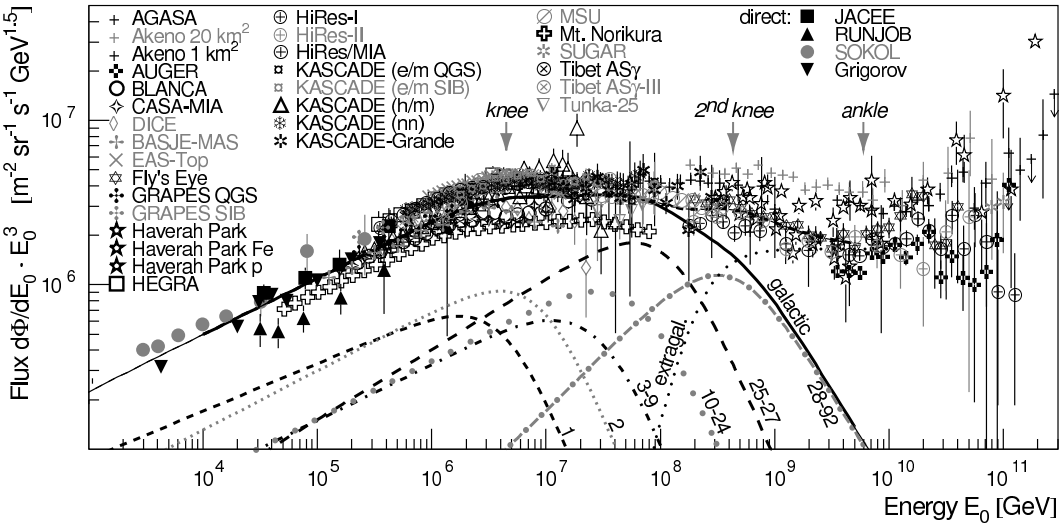

Figure 1.1: *All-particle cosmic-ray differential energy spectrum multiplied by E^3. The figure is a compilation of results from multiple experiments, adapted from Hörandel (2008). The lines represent spectra for elements of a given Z and their sum modeled by Hörandel (2003). In this* poly-gonato *model, the knee (a spectral break at energy $\sim 3 \times 10^{15}$ eV) is a result of a sum of energy spectra of all elements, each exhibiting a Z-dependent cut-off due to the acceleration and propagation.*

Experimental detection of the cosmic sites of particle acceleration via non-thermal mechanisms is complicated by numerous obstacles. Using *charged particles* for identifying distant extragalactic sources of all but the highest energy cosmic-rays is not possible, mainly because the intergalactic magnetic field (IGMF) deflects the CR particles. The distance scale accessible for probing the spatial distribution of the charged particles is thus constrained by their gyroradius[1]:

$$R_{\rm G} = 1.08 \times \left(\frac{E}{\rm PeV}\right)\left(\frac{Z\,B}{1\ \mu{\rm G}}\right)^{-1}\ {\rm pc} \tag{1.1}$$

Assuming the IGMF in the Local group of galaxies to be $\sim 10^{-9}$ G[2], the accessible distance for energies $E = 100$ PeV is limited to only $R_{\rm G} < 0.1$ Mpc. Given the size of $\sim$1 Mpc of the Local group and the fact that particles of higher energies cannot be confined in such small regions, any directional studies in these energies are impossible. Only particles beyond $\sim 5 \times 10^{19}$ eV can be used for finding extragalactic astrophysical CR sources. Particles of these energies have been detected, but the incidence rate is extremely low ($\sim$1 particle/km^2/century), which makes astronomy in this energy range very difficult and costly. Additionally, the charged cosmic rays are absorbed in interactions with the 2.7K cosmic microwave background (CMB), which makes the Universe opaque for UHECRs of the highest energies — this is known as the Greisen-Zatsepin-Kuzmin (GZK) limit (Greisen 1966; Zatsepin & Kuz'min 1966).

[1] A uniform magnetic field is assumed.

[2] This is a typically quoted number, but is rather uncertain

Instead of detecting the primary cosmic rays, it is possible to search for neutral secondaries created in various interactions of cosmic rays with the ambient medium. The best approach in studying the sites of particle acceleration thus seems to be using *very-high-energy (VHE) γ rays* as tracers of cosmic rays, which is the field of *VHE γ-ray astronomy* — the main subject of this work. VHE γ rays are not deflected by the IGMFs and their mean path length in the intergalactic medium extends beyond the GZK distance of UHECRs.

VHE γ-ray astronomy has undergone a major breakthrough in the recent years. In particular, imaging atmospheric Čerenkov telescope (IACT) arrays have proven themselves to be a very successful tool for probing the non-thermal processes in the Universe. Among other successes, IACTs detected VHE γ rays from various classes of *Galactic* objects. In Aharonian et al. (2004b, 2006c) it was for the first time proven that cosmic rays of energies at least 100 TeV are present in shells of supernova remnants[3]. Other unexpected Galactic sites where cosmic rays are accelerated to energies ∼100 TeV were also found, including: pulsar wind nebulae, stellar binary systems and interacting winds from Wolf-Rayet stars. See Fig. 1.2 for a map of all sources detected up-to-date (as of August 2008).

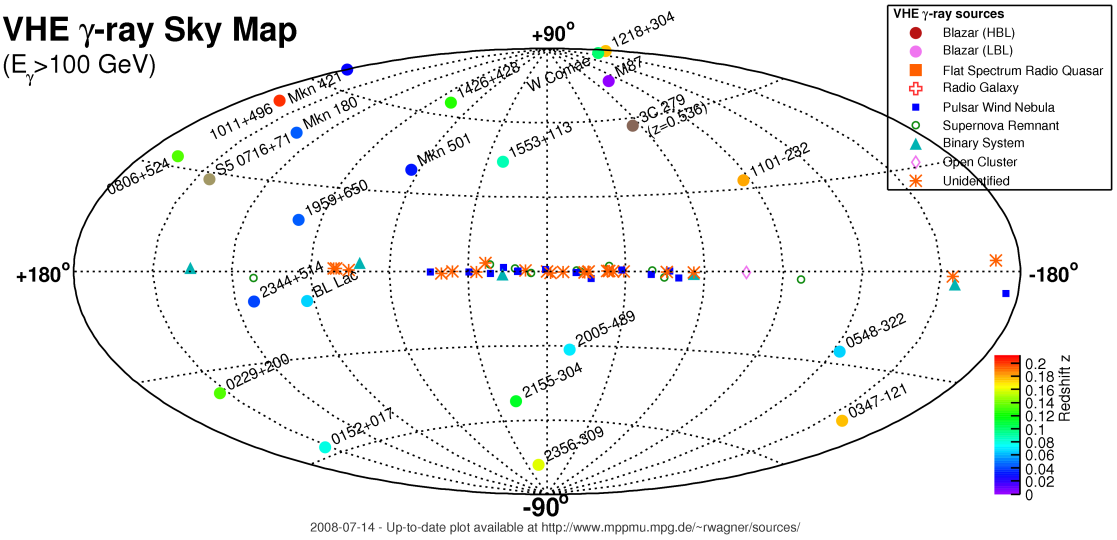

Figure 1.2: *Map of objects detected in VHE energy range in galactic coordinates. The only extragalactic objects detected up to now in this energy band are AGNs, the vast majority belonging to the class of high-frequency-peaked BL Lacs (HBLs). The redshift of extragalactic objects is color coded in order to indicate the distance. Labels of galactic sources are omitted for the sake of readability. Also note that the colors of galactic sources correspond to the type of a source (Compilation made by Wagner (2008)).*

The most plausible general mechanism for accelerating cosmic rays in the Galactic sources is the first order *Fermi shock acceleration* (see section 2.1.1). It can be shown that in environments of e.g. shells of supernova remnants it is possible to accelerate particles to energies ∼100 TeV. The hypothesis is consistent with the locally observed cosmic-ray spectrum[4] and the assumed energy content in the cosmic rays in the Milky Way.

However, currently it seems that the Galactic sources only account for the lower part

[3]Note that the maximum energy achievable in shells of SNR is not expected to exceed 10^{15} eV and can thus only explain CRs below the knee in the CR spectrum.

[4]The predicted spectrum has to be corrected for diffusion losses

of the spectrum in Fig. 1.1, below the potential second knee[5] (energies $\sim 10^{17}$ eV). There is no evidence and no firm theoretical prediction that the particles above the second knee are produced in the Milky Way. These particles cannot be confined in the $\sim \mu$G Galactic magnetic field and their existence in the Milky Way is thus improbable. The most conventional mechanisms explaining the CR acceleration in this energy range thus involves *extragalactic sources*. Several types of extragalactic objects were proposed to be capable of reaching energies > 100 TeV. The most promising candidates are:

- Jets of *active galactic nuclei (AGN)* (see e.g. Dermer (2007) for a review)
- γ-ray bursts (GRBs) (e.g. Dermer (2007))
- Galaxy clusters (Kang et al. 1996)
- Starburst galaxies (Anchordoqui et al. 1999; Torres & Anchordoqui 2004)

The mechanisms of particle acceleration in these objects are discussed in chapter 2. Other candidates for cosmic particle accelerators, not necessarily reaching UHE energies, are Ultraluminous IR galaxies (ULIRGs)[6]. From this list, so far only AGNs were detected in energies above 100 GeV (see Fig. 1.2). Apart from GRBs, all of these objects are investigated in this thesis to search for a VHE γ-ray signal. A special focus is placed on galaxy clusters, because of a great deal of evidence of non-thermal processes in them and because of acknowledged existence of various qualitatively different processes that are capable of producing observable VHE fluxes (see the chapter 3 for more details).

Thesis aim and structure

The main goal of this thesis is a search for a VHE γ-ray signal from several types of extragalactic objects. Discovery of such kind and a further study in the TeV energy range of these objects would increase our very limited (as it is discussed above) knowledge about the processes at the origin of the observed cosmic rays. The plausible candidates for such a study are in this work identified and results of their observations are presented and discussed.

The thesis is divided into eight chapters, including this introduction. In chapter 2, the theoretical mechanisms of accelerating particles in extragalactic objects are summarized. CR acceleration and energy losses mechanisms are discussed and general relations are derived that are later used for estimating non-thermal energy content in the studied objects and for estimating VHE γ-ray flux from these objects.

Several classes of extragalactic objects are in chapter 3 identified to be viable candidates for a VHE emission that could be detected by the H.E.S.S. instrument; these consist of galaxy clusters, starburst galaxies, ultraluminous infrared galaxies (ULIRG) and AGNs. Using relations derived in the previous chapter 2, the cosmic-ray content of these objects and the VHE γ-ray fluxes from them are estimated. Specific targets are selected that are most suitable for observations with H.E.S.S..

[5] The existence of the second knee seems to be now established, given that four major experiments have shown an evidence for this spectral feature (Bergman & Belz 2007). The exact location of the spectral break and its composition is yet to be unveiled.

[6] This is not intended to be a complete list. Other hypotheses exist for other types of objects.

An emphasis is placed on galaxy clusters as it was mentioned before. These form the largest gravitationally bound structures in the Universe and are important from a cosmological point of view. In chapter 3, it is shown that hadronic cosmic rays up to 10^{15} eV are confined within them for a time exceeding the age of the Universe. It is shown that the total accumulated energy in hadronic cosmic rays could be $\sim 10^{62}$ erg in case of the clusters Abell 496 and Abell 85. The secondary VHE γ rays produced in inelastic interactions of these CR particles could thus convey an information about the cluster evolution, and their discovery could establish a new link between astroparticle physics and cosmology. In the following part, starburst galaxies and ULIRGs are discussed that are both characterized by significantly increased star-formation rates in the central regions. A specific class are AGNs that already are established VHE γ emitters. The theory of active galactic nuclei represents such a broad field that a complete summary of non-thermal processes would go beyond the scope of this work, and hence is discussed in less detail.

Chapter 4 describes the H.E.S.S. experiment and the analysis technique used in H.E.S.S, which is the instrument used to obtain the results in this thesis. The IACT technique, employed by H.E.S.S., is reviewed, and the basic data-flow in the experiment is discussed. This involves calibration, data-quality monitoring and the complete analysis chain.

Chapter 5 discusses the performance of the H.E.S.S. experiment. A special emphasis is placed on the sensitivity estimate because it is crucial for estimating detectability of generally weak (in the VHE energy range) non-AGN extragalactic objects. In particular, the effect of effective areas and of an angular resolution on the telescope sensitivity is described. Several systematic issues concerning the analysis are also addressed.

Chapter 6 summarizes H.E.S.S. observations of the extragalactic objects that were selected in the previous chapter 3. Analysis results for galaxy clusters Abell 496, Abell 85, Coma cluster, Abell 754, Centaurus cluster and Hydra A are presented. No significant signal is found, but the results of Abell 496 and Abell 85 are used to put an upper limit on the non-thermal energy content in the clusters, which is already challenging theoretical estimates. For starburst galaxies, a hint of a signal at a $\sim 3\sigma$ level is found from NGC 253, but further observations are needed to conclude on the nature of this excess. No signal is found from the starburst galaxy M 83 and from a ULIRG Arp 220. Finally, a discovery of a new BL Lac AGN, RGB J0152+017, is presented and a spectral energy distribution (SED) is derived for the first time for this object. RGB J0152+017 thus also represents an example of a positive result, obtained by the analysis presented in chapter 4 and 5

Chapter 7 shortly addresses the prospects for detecting the extragalactic objects described in this thesis using the extensive array of IACTs CTA which is in preparation at the current time.

In chapter 8, the work is summarized and conclusions from the presented results are drawn.

Chapter 2

Extragalactic cosmic rays

In this chapter, the general mechanisms concerning cosmic-ray (CR) acceleration and VHE γ-ray production are discussed. The physics introduced in this chapter is later used in chapter 3 to estimate a γ-ray flux from concrete extragalactic objects.

The purpose of the first section (2.1) is to discuss the general CR acceleration. The widely acknowledged acceleration by first order Fermi mechanism is described. Subsequently, in order to consider the limitations of such acceleration in various environments, the cosmic-ray losses due to cooling are reviewed in the next section (2.2). Afterwards, a very general constraint on the candidate objects is discussed in section 2.3 constraining their sizes and magnetic fields. Finally, the processes of VHE γ-ray production are described in section 2.4. Hadronic as well as leptonic mechanisms are discussed. The general problem of a limited photon horizon of TeV γ rays is considered in section 2.4.2 in order to put constraints on the distance of studied objects.

2.1 Acceleration of cosmic rays

2.1.1 Fermi mechanism

Presently the most widely accepted mechanism of particle acceleration to energies above 1 TeV is based on Fermi acceleration in shocks.

Second order Fermi acceleration

The basic mechanism was first proposed by Fermi (1949). In this picture, charged particles are accelerated in interstellar space by colliding against magnetized clouds. The particle is reflected by moving magnetic irregularities, which behave with respect to the considered particles as infinitely massive[1] magnetic "mirrors" or clouds. The particles diffuse in the cloud, moving now by their original velocity and additionally, by a motion of the cloud, relative to the original direction of a particle. After escaping the cloud, the particle gains energy in case of a head-on collision and loses energy in case a of tail-on collision. On average, the particles gain energy because head-on collisions are statistically more

[1] By "infinitely massive" is meant that the change of momentum of the magnetized cloud after a collision with a CR particle is negligible

probable. It is possible to show (see Longair (1994) for a review) that the energy gain per collision is:

$$\left\langle \frac{\Delta E}{E} \right\rangle = \frac{8}{3}\beta^2, \tag{2.1}$$

where β is the velocity of the magnetic "mirror". The energy gain is thus merely second order in β and the acceleration is not efficient enough to account for observed CR fluxes.

First order Fermi acceleration

A more efficient mechanism employing strong shocks[2] was proposed by several independent theoretical groups (Krymskii 1977; Axford et al. 1977; Bell 1978; Blandford & Ostriker 1978). A strong shock provides an environment where the head-on collisions of the CR particles with magnetic turbulences surrounding the shocks are dominant. The tail-on collisions, decreasing the efficiency of the second order Fermi acceleration, are thus effectively eliminated (see Fig. 2.1 for an illustration of this effect). In the following, this fact is explained using simple qualitative arguments.

Strong shocks are phenomena, common in e.g. SNR shells, pulsar wind nebulae and large scale cluster formation sites, i.e. sites currently known to produce non-thermal particles. In case of supernovae, the shock is formed formed at the interface between the material swept up by the SN ejecta and the ambient medium. The swept up material gains velocity V of the SN ejecta (typically $\sim 10^4$ km s^{-1}). The ambient medium consists mainly of atomic hydrogen, for which the shock speed v_s can be expressed as $v_\mathrm{s} = 4/3V$ (Longair 1994). The shock front is thus moving at a speed of $V/3 = v_\mathrm{s}/4$ away from the material accumulated behind it. The swept up material in the region behind the shock (downstream region) moves at a speed $3v_\mathrm{s}/4v_\mathrm{s}$ towards the material in front of the shock (upstream region).

In Fig. 2.1, it is shown that a particle passing the shock experiences a on average head-on collisions in both directions, which is the main qualitative fact that makes this process more efficient than the second order Fermi acceleration.

It is possible to show (see e.g. Longair (1994)) that the mean gain of energy of a particle crossing the shock and returning back is:

$$\left\langle \frac{\Delta E}{E} \right\rangle = \frac{4}{3}\beta, \tag{2.2}$$

where β is a speed of the shock. From this equation, it follows that a particle with energy E_0 will have energy $E = a\,E_0$ after the cycle, where $a = 1+4/3\beta$. Let P be the probability that a particle remains in the accelerating region after a cycle. Then, after k cycles, there will be $N = N_0 P^k$ particles with energies $E = a^k E_0$. From this it follows that:

$$N = \left(\frac{E}{E_0}\right)^{\ln P/\ln a}, \tag{2.3}$$

It is therefore an intrinsic characteristic of the Fermi acceleration that the differential

[2]Strong shock is characterized by a speed much larger than the sound speed in a given medium, i.e. $v_\mathrm{shock} \gg c_\mathrm{s} = \sqrt{\left(\frac{\partial P}{\partial \rho}\right)_\mathrm{s}}$, where c_s is the speed of sound, P is pressure, ρ is density and the derivative is performed at a constant entropy s.

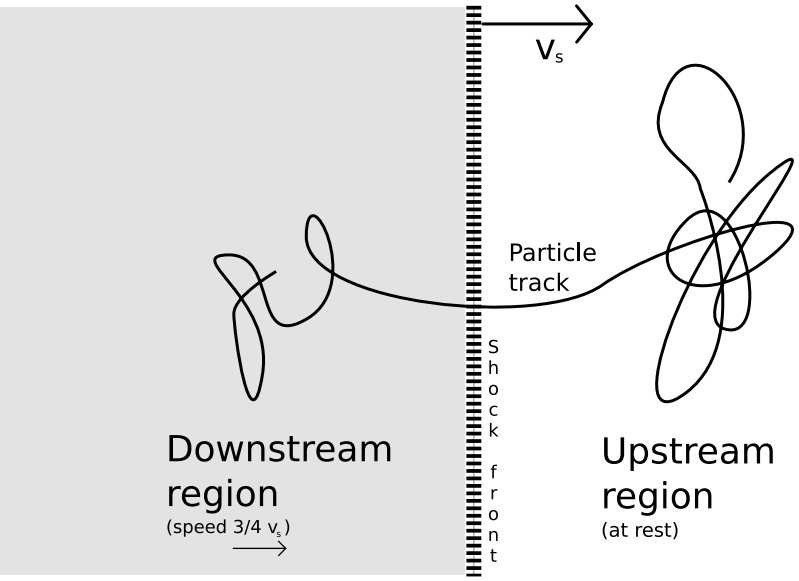

Figure 2.1: *Schematic illustration of the first order Fermi acceleration in strong shocks. The figure is drawn at rest frame of the upstream ambient material, in which the shock front moves at a speed v_s and material in the downstream region moves at a speed $3/4v_s$ in the same direction. A particle that crosses the shock into the upstream region collides with magnetic "mirrors" moving at a relative speed $3/4v_s$ and gains energy in this head-on collision. When traversing back into the downstream region, the particle again encounters the shocked gas in a head-on direction.*

energy spectrum of the accelerated CR particles is a power-law of a form:

$$\frac{\mathrm{d}N}{\mathrm{d}E} \propto E^{-\Gamma}, \tag{2.4}$$

which is also the form of the observed spectrum (see Fig. 1.1).

The maximum energy that can be obtained by the Fermi acceleration in non-relativistic shocks (as found for instance in SNRs or large scale structure formation shocks) can be estimated (Lagage & Cesarsky 1983) as:

$$E_{\mathrm{max}} = 5 \times 10^6 \; Z \left(\frac{B}{10^{-5} \; \mathrm{G}} \right) \; \mathrm{GeV} \tag{2.5}$$

For a quantitative illustration — in the example of a galaxy cluster ($B \sim 5$ μG — see section 3.1), the maximum energy of a proton can be approximately $E_{\mathrm{max}} \approx 2.5 \times 10^{15}$ eV.

2.2 Cooling of relativistic particles

A limiting factor for accelerating particles to high or very-high energies is their convective escape (discussed separately by the objects in chapter 3) and energy losses (cooling) due to various processes. In order to accelerate particles efficiently, the energy gains (discussed in the previous section) need to happen on timescales smaller than the cooling and escape times. Cosmic-ray particles are cooled by several mechanisms, depending on the energy

range, type of a particle and the ambient medium. Only an overview is given here, for a more detailed description see e.g. Longair (1994). In principle the mechanisms can be divided into:

- *Interaction with matter* - proton cooling due to a *pp* interaction and bremsstrahlung
- *Interaction with magnetic fields* - synchrotron radiation
- *Interaction with photon fields* - inverse Compton process (for ultra-high energies, photomeson production also becomes important, as well as $e^{\pm}$ pair production in proton interactions with photons.)

2.2.1 Proton cooling time

The main process causing protons to lose energy when passing through matter is a p-p interaction. A by-product of this interaction are VHE γ-rays that make this process particularly interesting for TeV γ-ray production discussed in section 2.4.1. The proton energy losses through this interaction can be expressed as:

$$\left\langle \frac{\mathrm{dE}}{\mathrm{dt}} \right\rangle = n_{\mathrm{H}}\ \sigma_{\mathrm{pp}}\ c\ f\ E, \tag{2.6}$$

where n_{H} is the gas density of the medium, σ_{pp} is the total inelastic cross section for the *pp* interaction, c is the relative speed (to a good approximation for HE particles, the speed of light) and $f = \Delta E/E \approx 0.5$ is the inelasticity (fraction of proton energy lost per interaction). σ_{pp} can be in the energy range GeV - TeV approximated as (Kelner et al. 2006):

$$\sigma_{\mathrm{pp}} \approx (34.3 + 1.88L + 0.25L^2)\left[1 - \left(\frac{E_{\mathrm{T}}}{E_{\mathrm{p}}}\right)^4\right]^2 \ \mathrm{mb}, \tag{2.7}$$

where $L = \ln(E_{\mathrm{p}}/1\ \mathrm{TeV})$ and $E_{\mathrm{T}} = m_{\mathrm{p}} + 2m_{\pi} + m_{\pi}^2/2m_{\mathrm{p}} = 1.22$ GeV is the threshold energy of π^0 production. The threshold of the inelastic pp interaction is $E_{\mathrm{th}} = 2m_{\pi}c^2(1 + m_{\pi}/4m_{\mathrm{p}}) \simeq 0.3$ GeV. Proton cooling thus sets in only for energies beyond 1 GeV. Note that for proton energies $E_{\mathrm{p}} \gtrsim 3E_{\mathrm{T}}$, the energy dependence is very weak and for the purposes of estimating the cooling time, the total cross-section can be approximated as $\sigma_{\mathrm{pp}} \approx 40$ mb. Assuming that on average a proton loses half of its energy per interaction (i.e. $f = 0.5$) and for $\sigma_{\mathrm{pp}} = 40$ mb the cooling time is:

$$\tau_{\mathrm{pp}} = \frac{E}{\langle \mathrm{dE/dt} \rangle} \approx 5.3 \times 10^7 \left(\frac{n_{\mathrm{H}}}{1\ \mathrm{cm}^{-3}}\right)^{-1}\ \mathrm{yr} \tag{2.8}$$

Obviously, the pp cooling becomes important in environments with high material density. In a low density environment, such as in galaxy clusters ($n_{\mathrm{H}} \sim 10^{-3}$), the cooling time (in this case $\sim 5\times 10^{10}$ yr) may exceed the age of the Universe.

As stated above, τ_{pp} is to a good approximation independent of proton energy. Proton cooling thus does not change the primary spectrum. This is an important and positive fact, which means that a possible γ-ray spectrum produced by primary protons does not suffer a substantial spectral steepening (softening) because of this process and is therefore easier to detect at higher energies.

2.2.2 Synchrotron cooling

A charged particle gyrating in a magnetic field loses energy by a synchrotron radiation. The energy losses per particle with an electric charge q can be calculated using electrodynamics as:

$$\left(\frac{\mathrm{d}E}{\mathrm{d}t}\right)_{\mathrm{synchr}} = -\frac{q^2\ |a|^2}{6\pi\epsilon_0 c^3}, \tag{2.9}$$

where $|a|$ is the absolute value of the acceleration of the gyrating particle. In a uniform magnetic field B, an electron loses energy at rate:

$$\left(\frac{\mathrm{d}E}{\mathrm{d}t}\right)_{\mathrm{synchr}} = -\frac{4}{3}\sigma_{\mathrm{T}} c\ U_{\mathrm{mag}} \beta^2\gamma^2, \tag{2.10}$$

where $\sigma_{\mathrm{T}} = e^4/(6\pi\epsilon_0^2 c^4 \mathrm{m_e})$ is the Thomson cross-section and $U_{\mathrm{mag}} = B^2/(2\mu_0)$ is the energy density of the magnetic field. Note that the general equation for non-electron losses would instead of σ_{T}, include a term $\frac{8\pi}{3}\left(\frac{q^2}{m_0\, c^2}\right)^2$ and the energy losses are then proportional to:

$$\left(\frac{\mathrm{d}E}{\mathrm{d}t}\right)_{\mathrm{synchr}} \propto \frac{1}{m_0^2}\beta^2\gamma^2, \tag{2.11}$$

where m_0 is the rest mass of the particle. For relativistic energies, β can be approximated as $\beta \sim 1$ and the losses at a given particle energy E thus depend on $(\mathrm{d}E/\mathrm{d}t)_{\mathrm{synchr}} \propto m_0^{-4}$. The mass dependence is therefore very strong. For a comparison, the synchrotron energy losses of a proton of energy E are suppressed by a factor $(m_{\mathrm{p}}/m_{\mathrm{e}})^4 \approx 10^{13}$ as opposed to losses of an electron of the same energy. In astrophysical environments, the synchrotron radiation thus becomes relevant for protons only at UHE energies.

The cooling time of an electron in a magnetic field B is given by:

$$\tau_{\mathrm{synchr}} = \frac{E}{\langle \mathrm{d}E/\mathrm{d}t\rangle} \approx 4\times 10^{10}\left(\frac{B}{100\mu\mathrm{G}}\right)^{-2}\left(\frac{E}{1\ \mathrm{TeV}}\right)^{-1}\ \mathrm{s} \tag{2.12}$$

The synchrotron cooling is therefore significant for high B-fields and high particle energies E. For a relatively high intergalactic magnetic field of galaxy clusters ($B \approx 5\,\mu$G — see further in section 3.1.2), the cooling time for 10 TeV electrons is $\tau_{\mathrm{synchr}} \approx 5\times 10^4$ yr, which is extremely short compared to the timescales over which hadronic cosmic rays accumulate in the clusters. From this it directly follows that contrary to hadronic cosmic rays, the leptonic ones would have to be accelerated much more effectively in order to balance the radiative energy losses.

Note that the cooling is faster at higher energies, where the spectrum gets consequently steeper with increasing time.

2.2.3 Inverse Compton cooling

High-energy electrons and positrons lose energy via inverse Compton scattering on low-energy background photons. Typically the background photons consist of EBL, cosmic microwave background (CMB) or synchrotron radiation of the $\mathrm{e}^{\pm}$ themselves. The process is discussed in more detail in section 2.4.2 as a mechanism of γ-ray production. Here, only

the timescale is discussed, which is relevant for estimating CR energy losses.

Assuming small photon energies (where the Thomson cross-section is valid), the mean energy loss rate of an electron is:

$$\left(\frac{\mathrm{d}E}{\mathrm{d}t}\right)_{\mathrm{IC}} = -\frac{4}{3}\sigma_{\mathrm{T}} c\, U_{\mathrm{rad}} \beta^2 \gamma^2, \tag{2.13}$$

where U_{rad} is the energy density of the background electromagnetic field. The cooling time of an electron is thus:

$$\tau_{\mathrm{IC}} \approx 3 \times 10^5 \left(\frac{U_{\mathrm{rad}}}{1\ \mathrm{eV/cm^3}}\right)^{-1} \left(\frac{E}{1\ \mathrm{TeV}}\right)^{-1}\ \mathrm{yr} \tag{2.14}$$

For a typical example of a CMB radiation, the radiation energy density is $U_{\mathrm{rad}} \sim 0.26$ eV cm^{-3} and the cooling time for a 10 TeV electron is then $\tau_{\mathrm{IC}} \approx 1.2 \times 10^5$ yr. The case is therefore qualitatively similar to the synchrotron losses (see discussion above).

Additionally, from eq. (2.14) and (2.12), it can be seen that the relative efficiency of IC to synchrotron losses of electrons depends only on the ratio $U_{\mathrm{rad}}/U_{\mathrm{mag}}$.

2.2.4 Bremsstrahlung cooling

During bremsstrahlung, charged particles lose energy radiatively through interactions with the electromagnetic fields of atoms in matter. The principle mechanism is the same as in the case of synchrotron radiation and the energy loss is also expressed by the formula (2.9). The acceleration a in this case depends on a matter density n, and the mean energy loss rate is then:

$$\left(\frac{\mathrm{d}E}{\mathrm{d}t}\right)_{\mathrm{brems}} = -\frac{m_{\mathrm{p}}\, c\, n}{X_0} E, \tag{2.15}$$

where X_0 is a radiation length. The cooling time is then in case of Hydrogen:

$$\tau_{\mathrm{brems}} \approx 10^{15} \left(\frac{n_{\mathrm{H}}}{1\ \mathrm{cm^{-3}}}\right)^{-1} s \tag{2.16}$$

2.3 Hillas condition

A very general limitation on the candidate objects for CR acceleration is imposed when considering the confinement of CRs. Independently of the acceleration mechanism, there is a constraint on a magnetic field B and the size L of a cosmic accelerator required to accelerate charged particles to energies exceeding a given energy E. The magnetic field B has to be high enough in order to be able to confine the particles within the given object size L for a time long enough for the CR to gain energy E. The condition introduced by Hillas (1984)[3] is:

$$\left(\frac{B}{\mu\mathrm{G}}\right)\left(\frac{L}{\mathrm{pc}}\right) > \left(\frac{E}{10^{15}\ \mathrm{eV}}\right)\frac{1}{Z\ \beta}, \tag{2.17}$$

[3]It should be noted that this condition was developed for UHECR, but can also be applied to energies $\sim 10^{15}$ eV, relevant for TeV γ-ray production.

where Z is a particle charge and β is a speed of the scattering waves of the accelerating site. Note that this is a *necessary, though not a sufficient condition* for the CR-accelerating site. The Hillas condition constraints are illustrated in Fig. 2.2.

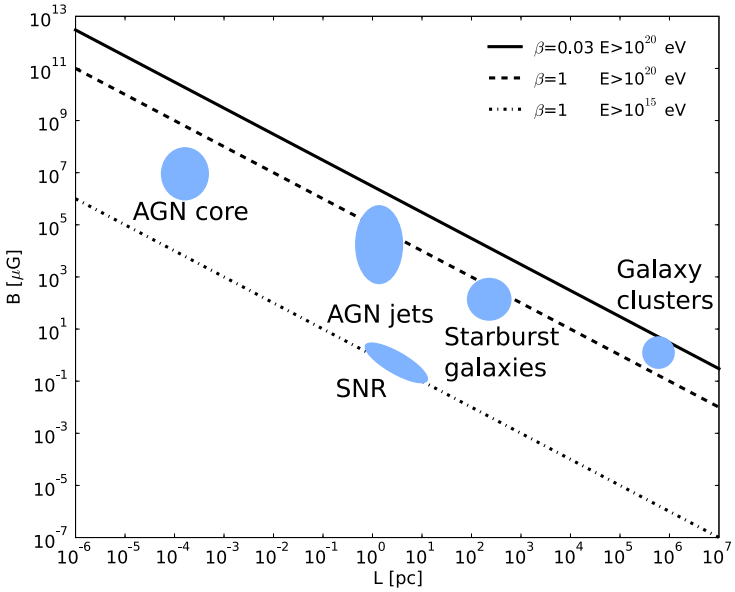

Figure 2.2: *Hillas plot for selected extragalactic and Galactic objects. The dashed line corresponds to shock speeds of $\beta = 1$ and particle acceleration to 10^{20}. It should be noted that this represents a very extreme case where the shock speeds would be close to the speed of light. A more realistic case of $\beta = 0.03$ is plotted using the solid line, corresponding to shock speeds of ~ 10000 km s^{-1}. The dash-dotted line corresponds to energies 10^{15} eV and $\beta = 1$.*

In Fig. 2.2, we see that possible extragalactic sites accelerating CRs to energies beyond 10^{15} energies are e.g. galaxy clusters, starburst regions of galaxies and AGNs. All of these are discussed further in this chapter.

2.4 Production of VHE γ rays

VHE γ rays beyond 10 GeV can be produced via several distinct mechanisms. These can be generally divided into *hadronic* and *leptonic* mechanisms depending on the primary particles. In order to produce a VHE γ photon of energy E_γ, charged cosmic ray particles of one of these types of energies exceeding E_γ are a necessary condition. This is also a reason why γ rays represent tracers of the existence of energetic charged cosmic-ray particles.

2.4.1 Hadronic mechanisms

In these mechanisms, γ rays are produced as secondaries in interactions of hadrons, typically protons.

Table 2.1: *The γ-ray emissivity for different spectral indices $\Gamma_{\rm CR}$ of the primary protons.*

$\Gamma_{\rm CR}$	$q_\gamma(\geq 1\,\mathrm{TeV})$ $\left[\frac{\mathrm{cm}^3}{\mathrm{s\,erg\,(H-atom)}}\right]$
2.1	1.02×10^{-17}
2.2	4.9×10^{-18}
2.3	2.1×10^{-18}
2.4	8.1×10^{-19}
2.5	3.0×10^{-19}
2.6	1.0×10^{-19}
2.7	3.7×10^{-20}

Proton-proton interactions

The dominant hadronic process are inelastic p-p interactions followed by subsequent decay of secondary π^0 in into two γ rays (see e.g. Kelner et al. 2006; Aharonian & Atoyan 1996):

$$\begin{aligned} \mathrm{p} + \mathrm{p} &\rightarrow \pi^{\pm,0} + X \\ \pi^0 &\rightarrow \gamma + \gamma \end{aligned}$$

The three types of pions are produced with comparable probabilities.

The γ-ray flux produced via this mechanism has been studied in numerous publications (see e.g. Kelner et al. 2006; Kamae et al. 2006; Drury et al. 1994). For our purposes, the simple approach of Drury et al. (1994) is adopted. The expected production rate Q_γ of γ rays above 1 TeV per unit volume can be evaluated as:

$$Q_\gamma = \mathcal{E}_\gamma n = q_\gamma n E_{\rm CR}, \tag{2.18}$$

where $E_{\rm CR}$ is the cosmic ray energy density, q_γ is a γ emissivity normalized to the CR energy density, i.e. $q_\gamma = \mathcal{E}/E_{\rm CR}$, and n refers to the number matter density of the target material. The coefficients q_γ depend on the proton-proton cross-section, branching ratio of the π^0 channel and on the spectral index $\Gamma_{\rm CR}$ of the primary protons. They are evaluated in e.g. Drury et al. (1994) and tabulated in Table 2.1 for several different spectra of the primary protons. Note the strong dependence of the emissivity on $\Gamma_{\rm CR}$.

It is interesting to notice that the p-p interaction also produces $\pi^\pm$ that decay, among other byproducts, into cosmic-ray neutrinos. A link is thus established through this process between VHE γ-ray astronomy and neutrino astronomy. In this sense, the results of IACT observations have been used to predict neutrino fluxes from sources detected in TeV γ rays (see e.g. Kappes et al. 2007).

Interaction of hadrons with radiation fields

Other processes involve interaction of hadrons with photons or electromagnetic fields. The cross-sections are generally lower than in the cases above, which makes these processes relevant only in sites with very high energy density of the EM fields and for UHE cosmic

rays. The processes include:

- *Photomeson production:* $\mathrm{p} + \gamma \rightarrow \mathrm{p} + \pi^0$ with a subsequent π^0 decay[4]. Note that this is the process responsible for the GZK-cutoff (Greisen 1966; Zatsepin & Kuz'min 1966).

- *Proton synchrotron radiation:* In compact sites accelerating protons to energies $\sim 10^{20}$ eV (AGNs), the synchrotron radiation can be an efficient mechanism of producing VHE γ rays of TeV energies (see e.g. Levinson 2000).

- *Inverse Compton (IC) scattering:* $\mathrm{p} + \gamma \rightarrow \mathrm{p} + \gamma'$ — This process is discussed in a more detail in the following section. In case of protons, the rate of this process is suppressed by a factor $\sim 10^{13}$ as opposed to the IC scattering of electrons.

- e^+e^- *pair production:* $\mathrm{p} + \gamma \rightarrow \mathrm{p} + \mathrm{e}^+\mathrm{e}^-$

2.4.2 Leptonic production

The most efficient process in this case is *inverse Compton scattering*[5], which was already shortly mentioned in 2.2.3 as a mechanism of cooling of primary electrons. High-energy electrons can scatter off a low-energy background photon field, transferring their momentum to the photons[6]. The target photon field is typically cosmic microwave background, IR background light, starlight or synchrotron emission from the primary electrons.

The cross-section can be evaluated in QED, and is given by the Klein-Nishina formula, which can be well approximated by an expression (see e.g. Aharonian & Atoyan 1981; Coppi & Blandford 1990):

$$\sigma_{\mathrm{KN}} = \frac{3\sigma_{\mathrm{T}}}{8\kappa_0}\left[\left(1 - \frac{2}{\kappa_0} - \frac{2}{\kappa_0^2}\right)\ln(1+2\kappa_0) + \frac{1}{2} + \frac{4}{\kappa_0} - \frac{1}{2(1+2\kappa_0)^2}\right], \tag{2.19}$$

where $\kappa_0 = \hbar\omega_0\epsilon_{\mathrm{e}}/(m_{\mathrm{e}}\,c^2)^2$ is the product of the energies of the interacting electron ϵ_{e} and the photon $\hbar\omega_0$. In the non-relativistic limit, where $\kappa_0 \ll 1$, the cross-section reduces to the energy independent Thomson cross-section $\sigma\sigma_{\mathrm{T}}$ (see Fig. 2.3). In the ultra-relativistic limit, the cross-section decreases with $\propto \kappa_0^{-1}\ln(2\kappa_0)$.

It can be shown (see e.g. Longair 1992) that the maximum photon energy achievable by the IC scattering is:

$$E_\gamma^{\mathrm{max}} \approx 4\gamma^2\hbar\omega_0 = 4\left(\frac{E_{\mathrm{e}}}{m_{\mathrm{e}}c^2}\right)^2 E_\gamma^0 \simeq 1.6 \times \left(\frac{E_{\mathrm{e}}}{1\,\mathrm{GeV}}\right)^2 E_\gamma^0 \tag{2.20}$$

[4] At higher energies, multiple pions are produced in one interaction.

[5] Other processes such as bremsstrahlung and synchrotron radiation are also possible, but only reach lower energies.

[6] The process is in its nature identical to the Compton scattering. The difference is only kinematical. High-energy electrons lose energy, rather than gain as in the case of Compton scattering. The process is therefore called "inverse".

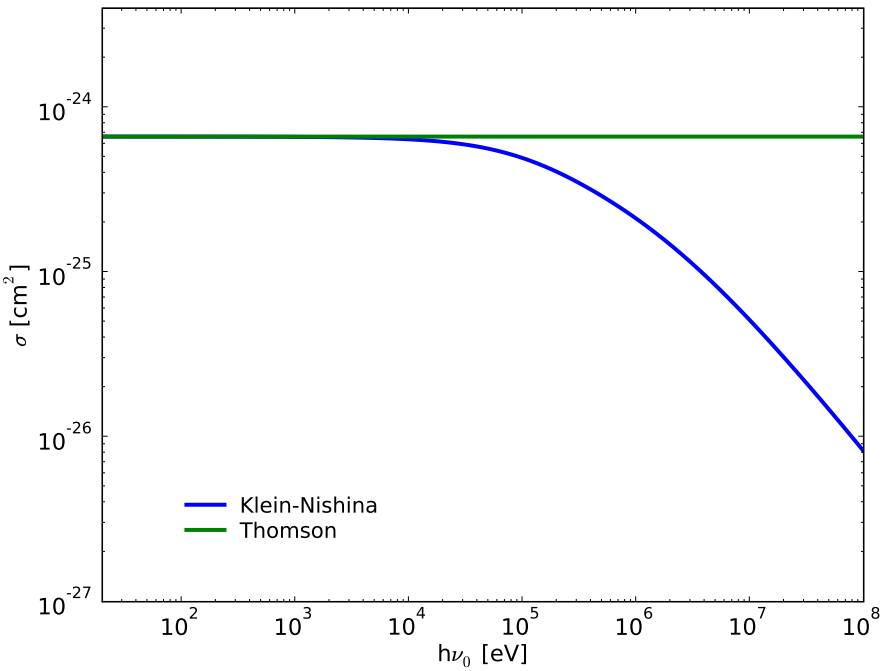

Figure 2.3: *The Klein-Nishina cross section compared to the Thomson cross section. Plotted is the dependence of the cross section on the energy of the photon $h\nu_0$ for the electron at rest. The Klein-Nishina cross section drops steeply in the energy range beyond the mass of an electron. In an analogous way, the cross section drops when $\epsilon_e\, h\nu_0/(m_e\, c^2)^2 \gg 1$ in case that the electron is not at rest. The IC scattering is thus considerably more efficient in case of $\epsilon_e\, h\nu_0/(m_e\, c^2)^2 \ll 1$. This is typically referred to as Thomson regime.*

2.4.3 Photon horizon

The mean path-length of γ rays of TeV energies is limited due to their absorption in a pair-production process $\gamma_{\rm VHE} + \gamma_{\rm IR} \rightarrow e^- + e^+$ (see e.g. Stecker et al. (1992) for a review). VHE γ rays interact with the IR extragalactic background light (EBL), making the Universe opaque beyond an energy-dependent *photon horizon*. EBL consists of direct light emitted by stars and galaxies and of re-emitted light by interstellar and intergalactic dust over the history of Universe. For more details about EBL see Hauser & Dwek (2001). Note that the absorption process was previously successfully employed to impose an upper limit on the absolute value of EBL in the Universe (see e.g. Aharonian et al. (2006d)). The absorption is governed by a cross-section σ, which can be exactly calculated using QED calculus (Heitler 1960) as:

$$\sigma(E, \epsilon_{\rm IR}) = 1.25 \times 10^{-25}(1-\beta^2)\left[2\beta(\beta^2-2) + (3-\beta^4)\ln\left(\frac{1+\beta}{1-\beta}\right)\right] {\rm cm}^2, \qquad (2.21)$$

where $\beta = \sqrt{1-(mc^2)^2/(E\epsilon_{\rm IR})}$. The cross-section is shown in Fig. 2.4.3 for three distinct incident energies E of a VHE photon. Given the VHE photon energy E, the cross section peaks at $\epsilon_{\rm IR} \sim 0.5\left(\frac{E}{1{\rm TeV}}\right)^{-1}$ eV. From this it follows that the target photons for an interaction with a γ ray above 1 TeV must have energies in the approximate range ≈ 0.1–1 eV and are thus indeed in the IR band. This can also be seen in the left panel of Fig.

2.4.3 where the process cross-section is plotted for three incident γ-ray energies, typical for VHE γ-ray astronomy.

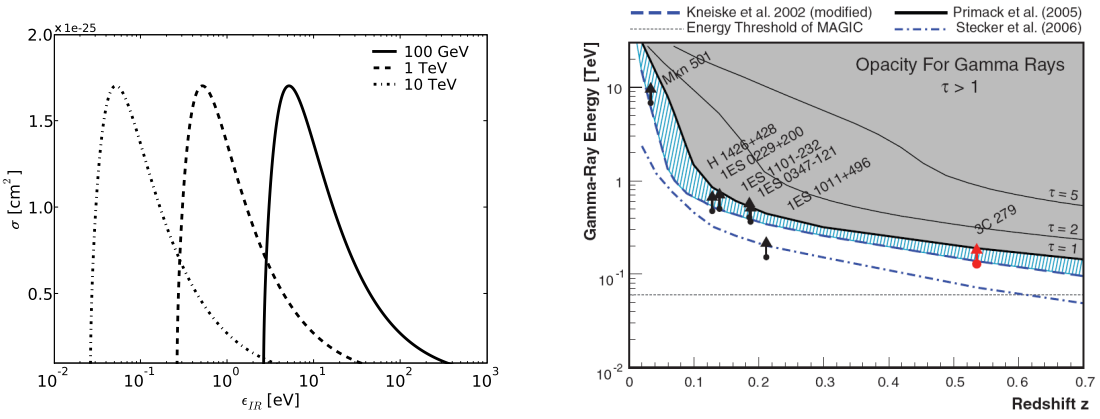

Figure 2.4: Left: *Heitler's cross section for the pair-production process for three various incident photon energies. The figure illustrates that the background photons relevant for the absorption of VHE γ rays are in the IR energy range and consist thus predominantly of cosmic infrared background (see text).* **Right:** *Photon horizon corresponding to the pair-production absorption process, depicted by a dependency of $\tau = 1$ line on the redshift and on the threshold energy. Several possible models of the EBL are plotted (figure from Albert et al. 2008).*

The right panel of Fig. 2.4.3 shows the photon horizon of VHE photons, beyond which the Universe is opaque. The solid line in the plot represents distance at which the VHE flux of photons of energy E drops by a factor of $1/e$. It is thus obvious that for energies ~ 0.2 TeV, it is impossible to detect a signal from further than a distance corresponding to a redshift $z \sim 0.3$. All further considerations are thus limited only to distances $z < 0.1$.

We have now introduced the most important relations relevant for the acceleration of cosmic rays and a consequent γ-ray production. In the following section, these methods are employed in order to estimate a detectability of galaxy clusters, starburst galaxies, ultraluminous IR galaxies and AGNs in VHE γ rays.

Chapter 3

Candidate objects for extragalactic VHE γ emission

The main goal of this chapter is to identify possible extragalactic objects, in which the cosmic-ray acceleration to VHE and UHE energies could be studied using γ-rays in TeV energy band. The objects thus have to be capable of producing γ-ray fluxes detectable by the current generation of IACT telescopes. A detection of a new type of an extragalactic VHE emitter would first of all allow one to study cosmic-ray acceleration in a different environment, which might be capable of producing UHECR, whose origin has not yet been unveiled (see chapter 1). Secondly, it would be a very optimistic signal for the planned CTA project. If it would be accomplished to detect one such source with H.E.S.S., CTA could, with its by an order of magnitude higher sensitivity, possibly detect a number of them, with the possibility to investigate the morphology of the extended ones.

Using relations derived in chapter 2, individual objects — galaxy clusters, starburst galaxies, ULIRGs and AGNs — are studied with respect to their production of non-thermal particles and VHE γ-ray flux estimates. A special emphasis is placed on galaxy clusters. AGNs are deliberately not studied in a large detail, given the broadness of the AGN physics and given they are already established as TeV sources.

3.1 Galaxy clusters

Galaxy clusters are the largest gravitationally bound objects in the Universe. Typically, they contain hundreds of galaxies and spread over 1 – 3 Mpc. The total mass is in the range of $\sim 10^{14} - 10^{15}$ $M_\odot$, out of which approximately 80% is contained in form of dark matter. The rest is contained in the hot intracluster plasma ($\lesssim$20%) and in the hadronic matter of the constituent galaxies (less than few percent).

Clusters of galaxies are believed to be able to accelerate and confine a significant amount of cosmic-ray particles. These may come from several distinct sources such as large-scale structure formation shocks, supernova explosions and AGNs. The purpose of this section is to estimate a potential VHE γ-ray flux from these objects. In order to achieve this, we first summarize the X-ray characteristics, which are used for estimating the thermal hot gas content in a cluster. Evidence for an existence of non-thermal particles is further discussed, together with the expected mechanisms for their production. The total

energy content in cosmic rays is then estimated and used in order to calculate the γ-ray flux. These predictions are later compared to the results of H.E.S.S.. observations in chapter 6.

3.1.1 X-ray characteristics

Observations of the galaxy clusters in X-ray energies convey essential information about the intracluster environment that is crucial for estimating the non-thermal particle content and is therefore summarized here.

In the 1960s, X-ray emission was detected from the nearest galaxy clusters (Virgo, Coma and Perseus clusters (Byram et al. 1966; Fritz et al. 1971; Meekins et al. 1971)). It was thus suggested (Cavaliere et al. 1971) and later confirmed by the *Uhuru* satellite (Gursky et al. 1972) that galaxy clusters are in general X-ray emitters. Given their distance, they were found to be the largest extragalactic sources on the sky. The X-ray luminosities range from 10^{43} to 10^{45} erg/s.

The X-ray emission was soon interpreted as a thermal bremsstrahlung from a hot intracluster medium (ICM) filling the cluster volume (Felten et al. 1966). The hypothesis of thermal bremsstrahlung was supported by a great deal of experimental evidence. The most important of those was a discovery of a 7-keV line in the spectrum (Mitchell et al. 1976) due to highly ionized iron. This consequently meant existence of a hot ionized plasma, consistent with the thermal bremsstrahlung hypothesis. Other experimental evidence has included: the stability of the X-ray signal over a long time and non-existence of low-energy photoabsorption, both of which are typical for a diffuse source, as opposed to a contribution from multiple compact sources. The total X-ray emissivity via thermal bremsstrahlung in a hot plasma of temperature $T_{\rm g} > 3 \times 10^7$ K can be expressed as (Sarazin 1988):

$$\epsilon_{\rm tb} \approx 3.0 \times 10^{-27} \sqrt{T_{\rm g}}\, n_{\rm g}^2 \ {\rm ergs\,cm^{-3}s^{-1}}, \tag{3.1}$$

where the emissivity $\epsilon_{\rm TB}$ is defined as the emitted energy per unit time and volume. Solar abundances were assumed and a fully ionized plasma. An important fact implied by eq. (3.1) is that the emissivity (and also luminosity) is proportional to $M_{\rm g}^2$ and $\sqrt{T_{\rm g}}$.

Intracluster gas

As shown above, galaxy clusters are filled with a hot plasma, radiating X-rays. The required temperature necessary for thermal bremsstrahlung in X-ray regime is $\sim 10^8$ K. However high this value seems to be, it has to be noted that no ongoing gas heating is necessary. The reason is that the radiative cooling of the thermal gas is negligible in all regions of the cluster apart from the center (see equation 3.2). There are several mechanisms contributing to the actual heating:

- *Heating by gravitational in-fall* — The gas can gain thermal energy by falling into the gravitational well of the galaxy cluster. While retaining a constant total energy, its potential energy is transformed into kinetic energy. Further, by colliding with the ICM, the particle gets thermalized.
- *Heating by ejection from galaxies* — Supernova ejecta are capable of heating up the interstellar material, which can be further ejected into the intracluster space.

- *Heating by galaxy motion* — Galaxies moving with respect to the ICM through the hot gas can heat up the gas by friction (Ruderman & Spiegel 1971).

- *Heating by non-thermal electrons* — Radio sources in galaxy clusters are believed to contain a significant population of high-energy electrons. These are able to heat up the intracluster gas while moving through it (Sofia 1973).

Quantitative estimates show that the first mechanism of the in-fall and compression of a gas is the most efficient mechanism for heating to temperatures $\sim 10^8$ K (Renzini 2004; Sarazin 1986). Other mechanisms seem to have a subordinate influence on the heating.

Cooling flows

The ICM gas in the center of some galaxy clusters (e.g. Perseus cluster, Centaurus cluster and Abell 85) is subjected to an intensive cooling by thermal bremsstrahlung. This process is very slow in most other clusters as can be illustrated by estimating the cooling time through thermal bremsstrahlung (Sarazin 1986):

$$t_{\mathrm{TB}} = 8.5 \times 10^{10} \left(\frac{n_{\mathrm{p}}}{10^{-3}\,\mathrm{cm}^3} \right)^{-1} \left(\frac{T_{\mathrm{g}}}{10^8\,\mathrm{K}} \right) \mathrm{yr} \tag{3.2}$$

For a typical value of a gas number density $n_{\mathrm{p}} \sim 10^{-3}$, the cooling time, $t_{\mathrm{TB}} \sim 10^{11}$ years, exceeds the age of the Universe t_{U} and the radiative losses can thus be neglected. The densities in the centers of some clusters can however be much higher ($n \sim 10^{-2}$), so that $t_{\mathrm{TB}} < t_{\mathrm{U}}$. The gas in the central region is then radiatively cooled down. In order to reestablish a hydrostatic equilibrium, the surrounding hot gas starts to flow into this cooler region, further increasing the central density and simultaneously the cooling rate. A flow of matter onto the central volume is thus initiated, referred to as a *cooling flow* (Fabian 1994) and results in a very steep rise of ICM density in the central parts of galaxy clusters. The central part is commonly called *cooling core*.

This model of a cooling core is however contradicted by X-ray spectroscopic observations that do not confirm the rapid decrease of temperature in the cluster cores (Peterson & Fabian 2006). The cooled material has to be therefore heated by some additional mechanism and the cooling flow problem is still under debate.

Gas density profiles

The knowledge of the distribution of the ICM density is critical for estimating the VHE γ-ray flux by the π^0 decay. γ-ray emissivity in this channel depends on the target number density n (see section 2.4.1), and the gas density profile $n(R)$ has to be assumed in order to estimate flux from the whole cluster. Theoretically it was shown by King (1962) that the density profile of a self-gravitating isothermal sphere can be described as $n(r) = n_0 \left[1 + (r/r_{\mathrm{c}})^2\right]^{3/2}$, where r_{c} is the core radius and n_0 the central density. This profile is known as *King profile*. Experimentally, the ICM density can be well determined by X-ray observations. Given an observed X-ray surface brightness profile, it is possible to derive analytically the density of a gas radiating X-rays by thermal bremsstrahlung (see 3.1.1). A

more precise parametrization is given by the β *model* (Cavaliere & Fusco-Femiano 1976):

$$n(r) = n_0 \left[1 + \left(\frac{r}{r_\mathrm{c}}\right)^2\right]^{3/2\beta}, \tag{3.3}$$

where β describes the radial falloff of the density.

There are several constraints connected with the equation 3.3. The X-ray emission from galaxy clusters is not always radially symmetric, especially in case of merging clusters. Nevertheless, it is found by Mohr et al. (1999) that the β model describes well enough the azimuthally averaged density profiles in most of the asymmetric clusters.

In some cases where clusters harbour a *cooling flow* (see 3.1.1), a double-β model is more suitable:

$$n(r) = \sum_{\mathrm{i}=1}^{2} n_{0\mathrm{i}} \left[1 + \left(\frac{r}{r_{\mathrm{ci}}}\right)^2\right]^{3/2\beta_\mathrm{i}} \tag{3.4}$$

In these cases the first part of the sum describes the very steeply falling profile of the cooling flow and is only significant in the central 10% of the volume.

ICM density profiles of galaxy clusters addressed by this work are summarized in Table 3.1.1 and plotted in Fig. 3.1. Additionally the profile of the Perseus cluster is shown, which was studied in a similar work by Perkins et al. (2006).

Table 3.1: *Parameters of X-ray profiles of several galaxy clusters*

Cluster	n_1 $[h_{70}^{1/2}\ \mathrm{cm}^{-3}]$	r_{c_1} $[h_{70}^{-1}\ \mathrm{kpc}]$	β_1	n_2 $[h_{70}^{1/2}\ \mathrm{cm}^{-3}]$	r_{c_2} $[h_{70}^{-1}\ \mathrm{kpc}]$	β_2	References
Abell 85	3.08×10^{-2}	45	0.662	3.87×10^{-3}	226	0.662	(a), (b)
Perseus	4.6×10^{-2}	57	1.2	4.79×10^{-3}	200	0.58	(c), (d)
Centaurus	8.05×10^{-2}	8.6	0.569	3.65×10^{-3}	99	0.569	(a), (d)
Abell 496[1]	2.6×10^{-2}	36	0.53				(k)
Abell 496[2]	3.0×10^{-3}	254	0.82				(k)
Abell 496	4.9×10^{-3}	178	0.7				(j)
Coma	3.4×10^{-3}	294	0.75				(i), (d)

[1]This model corresponds to a β-model including the central region.
[2]This model corresponds to a β-model excluding the central region.
References:
(a) Mohr et al. (1999), (b) Oegerle & Hill (2001), (c) Churazov et al. (2003), (d) Struble & Rood (1999), (e) Lahav et al. (1989), (f) McHardy et al. (1981), (g) Matsushita et al. (2002), (h) Ebeling et al. (1998), (i) Briel et al. (1992), (j) Markevitch et al. (1999), (k) Durret et al. (2000)

3.1.2 Magnetic field

In order to estimate the confinement of leptonic cosmic rays in the galaxy clusters, the knowledge of the intergalactic magnetic field is necessary. It is also crucial for interpreting the potential hard X-ray excess, as shown in the section 3.1.3.

Magnetic fields in galaxy clusters can be estimated using the Faraday rotation measure

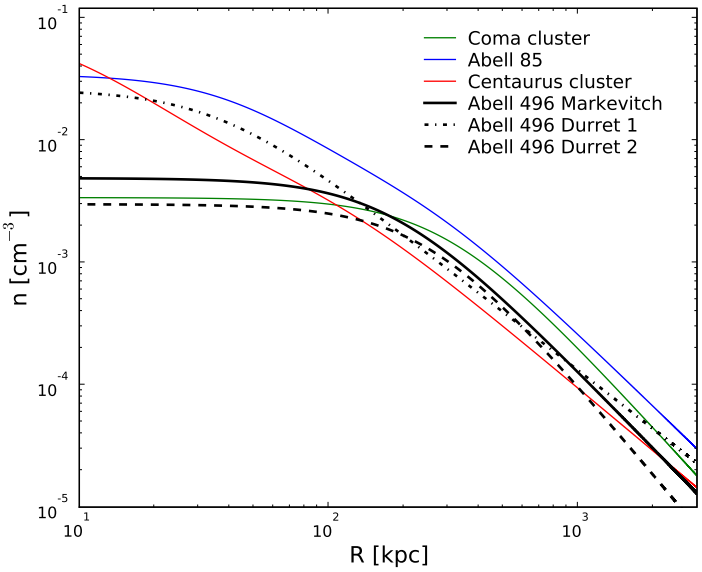

Figure 3.1: *Density profiles of selected clusters. The Centaurus cluster is clearly the most centrally peaked and Abell 85 is the most massive cluster, which is reflected in the high gas density. For Abell 496, there are three different profiles shown; Durret 1 including cooling core (Durret et al. 2000), Durret 2 excluding cooling core (Durret et al. 2000) and Markevitch from Markevitch et al. (1999). One can see the difference between cooling-core clusters Centaurus, Abell 496 (Markevitch parametrization) and Abell 85, and the non-cooling-core clusters Coma and the Durret parametrization of Abell 496.*

(RM) of linearly polarized radiation, produced by a background source. The rotation measure is typically defined as $RM = \frac{\Delta\chi}{\Delta\lambda^2}$. The magnetic field traversed by a polarized wave can be then deduced using the equation for RM (Clarke et al. 2001):

$$RM = 8.12 \times 10^5 \ \frac{\mathrm{rad}}{\mathrm{m}^2} \int_0^{z_s} (1+z)^{-2} \left(\frac{n_\mathrm{e}}{\mathrm{cm}^{-3}}\right) \left(\frac{B_\parallel}{\mathrm{G}}\right) \mathrm{dl(z)}, \tag{3.5}$$

where χ is the position angle of a linearly polarized radiation at wavelength λ and n_e is the electron density of the traversed thermal plasma, which can be determined by complementary X-ray measurements. This method was used by Clarke et al. (2001) to estimate the magnetic fields in the central 0.5 Mpc of standard non-merging clusters. The result was a relatively high value $B \sim 5\ h_{75}^{1/2}\ \mu G$ compared to the interstellar magnetic field in the Milky Way of $\sim \mu$G and to the Local group intergalactic magnetic field of $\sim$ nG. In the densest ICM of cooling cores, the magnetic fields can reach values $B \sim 40\,\mu$G (Kronberg 2001).

3.1.3 Cosmic rays in galaxy clusters

Evidence for non-thermal particles

Results from several experiments have proven the existence of significant population of non-thermal particles in galaxy clusters. Not all of the evidence is unequivocal, but the

conclusions are generally undisputed. The main observations include:

- **Radio halos and relics** — A radio halo is an extended diffuse radio source located at the center of a galaxy cluster; their typical size is ~ 1 Mpc. A prototype example is found in Coma cluster (Giovannini et al. 1993). Relics are located mostly at the outskirts of clusters and are believed to be connected to large-scale shocks, produced e.g. during galaxy mergers. A typical example is Abell 3376 (Bagchi et al. 2006), one of the few clusters with double opposite relics. The nature of the radio emission in both cases is believed to be the synchrotron radiation of high-energy electrons in the intracluster magnetic field. The detection of 1.4 GHz synchrotron radiation (see e.g. VLA results Bagchi et al. 2006)) requires existence of high-energy electrons of energies ~ 10 GeV (assuming $B = 1\,\mu$G). The electrons can be either directly accelerated, or produced as secondary particles in inelastic interactions of CR protons. It should be noted that only several clusters, especially the ones with merger activity, are sources of the radio emission.

- **Extreme UV (EUV) excess emission** — EUV (0.07 — 0.4 keV) excess above the emission produced by the thermal X-ray gas. It is assumed to be produced by inverse-Compton scattering of electrons off the CMB (Bowyer et al. 2004). There were competing theories claiming the EUV excess to be from thermal radiation of a cooler gas of $\sim$2 keV (Lieu et al. 1996), but the former explanation seems to be more feasible.

- **Non-thermal hard X-ray radiation** — Several claims exist that the hard X-ray tail of emission of several clusters is significantly inconsistent with a thermal spectrum (Fusco-Femiano et al. 1999; Rephaeli et al. 1999; Fusco-Femiano et al. 2007). The results are however a subject of a debate and the problem has not been resolved yet (Rossetti & Molendi 2007).

  Theoretically, it is impossible to explain the potential non-thermal X-ray emission in high magnetic fields ~ 5 μG as an IC emission of the same electron population that is responsible for the radio emission (see e.g. Atoyan & Völk 2000). A more sophisticated model would thus be necessary to reconcile all the observations[1].

  In a recent work by Ajello et al. (2008), the non-thermal X-ray excess was investigated using the *Swift-BAT* experiment. No non-thermal X-ray emission was found (with the exception of Perseus cluster) and upper limits were derived that are in contradiction with the previous publications. See Fig. 3.2 where the stacked spectra of several clusters are fitted by a thermal bremsstrahlung spectrum. The only exception is the Perseus cluster, where the non-thermal emission is assumed to originate from an AGN NGC 1275.

Despite the disputed nature of the EUV and hard X-ray emission, the non-thermal nature of the radio relics and halos is now firmly established. It can be thus concluded that galaxy clusters indeed are the largest observed sources of non-thermal radiation and the largest sites accelerating cosmic rays.

[1] Note that there is a possible uncertainty in the estimation of IGMF using Faraday rotation measurements. The RM only measures the B-field along the line-of-sight, which could be different from the local magnetic field in the acceleration sites.

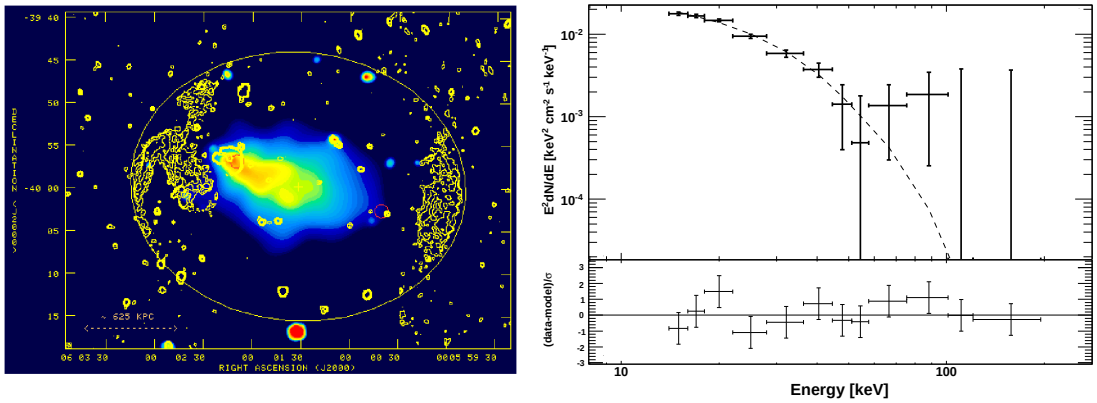

Figure 3.2: Left: *A composite map of radio (yellow contours from VLA 1.4 GHz)and X-ray thermal bremsstrahlung emissions (background image from ROSAT PSPC) from the galaxy cluster Abell 3376. The radio relics at the outskirts of the galaxy are tracers of a population of non-thermal particles. Adopted from Bagchi et al. (2006)* **Right:** *A stacked hard X-ray spectrum of Abell 3266, Abell 754, Abell 3571, Abell 2029, Abell 2142, Triangulum A, Ophiuchus and Abell 2319 measured by the* Swift-BAT *instrument. The spectrum can be well fitted by a thermal bremsstrahlung model (dashed line) and there is no hint of a non-thermal emission (see residuals in the bottom part). Adapted from Ajello et al. (2008)*

Having shown the existence of cosmic-ray particles in galaxy clusters, in the following we try to address the problem of their acceleration and estimate a possible γ-ray flux from them.

Acceleration of cosmic rays in galaxy clusters

The mechanisms for producing cosmic rays in galaxy clusters can be divided into *external processes* and *internal processes*.

In external processes, the particle acceleration is driven by the assembly of the cluster. An efficient production of high energy particles is expected in particular at the strong accretion shocks at the outskirts of clusters. The shocks are formed in these regions where a cold in-falling material plunges into the already existing hot intra-cluster medium. Consequently, these large-scale shock waves may populate the clusters with a non-thermal component of particles (see e.g. Colafrancesco & Blasi 1998; Loeb & Waxman 2000; Ryu et al. 2003; Miniati 2003). The external processes are stronger in more massive clusters and these are thus favored when searching for objects with a large cosmic-ray energy content.

In contrast to the aforementioned external processes, in the internal mechanisms, the cosmic rays are accelerated by cluster galaxies and injected into the whole cluster volume afterwards. Internal sources of cosmic rays in clusters can be supernova-driven galactic winds (Völk et al. 1996) or AGNs (e.g. Ensslin et al. (1997); Aharonian (2002); Hinton et al. (2007)).

Both mechanisms are discussed in a more detailed and also quantitative way in the next paragraph, where the non-thermal energy content of several clusters is estimated.

Cosmic-ray confinement

Owing to the relatively high magnetic field $\sim 1\mu$G (see section 3.1.2) and the vast volume of galaxy clusters, hadronic cosmic rays can be confined in them for a time exceeding the Hubble time. The escape time due to a diffusion can be estimated as $\tau_{\rm esc} \sim R^2/\kappa(E,B)$, where R is the size of a cluster and κ depends on the particle energy E and spectrum of fluctuations of the magnetic field B. Assuming a Kolmogorov spectrum, $\tau_{\rm esc}$ is calculated to be (Völk et al. 1996):

$$\tau_{\rm esc} \approx 4.9 \times 10^{11} \left(\frac{R}{1.5\,{\rm Mpc}}\right)^2 \beta^{-4/3}\gamma^{-1/3} \left(\frac{ZB}{\mu{\rm G}}\right)^{1/3} \ {\rm yr} \tag{3.6}$$

Assuming the mean cluster magnetic field is $B \sim 5\mu$G, eq. (3.6) implies escape times $\gtrsim 10^{10}$ years for particles below 10^{15} eV. The energy dependence of the escape time is demonstrated in Fig. 3.1.3. Several conclusions can be drawn from this important fact:

- Galaxy clusters act as *storehouses* of hadronic cosmic rays below 10^{15} eV and accumulate them over their entire lifetime.
- The spectrum of cosmic ray protons in this energy range in galaxy clusters is not affected by energy-dependent losses (as in the case of e.g. Milky Way, where the spectral index changes from $\Gamma = 2.1$ to $\Gamma = 2.7$ due to the diffusion losses).
- As shown in Fig. 3.1.3, electrons cool much faster than protons. Their acceleration can thus occur only at sites where the acceleration is very efficient. Such conditions could be provided e.g. by large scale shocks in the galaxy clusters.

Estimates of the non-thermal component

In the following, the total energy in non-thermal particles in galaxy clusters is estimated[2]. A precise estimate requires advanced simulations of all the processes involved and is beyond the scope of this work. These simulations were performed e.g. by Pfrommer et al. (2008). The estimate presented here is, contrary to these simulations, based on simplified physical arguments that provide a better physical insight. It is assumed that this energy is dominated by a hadronic component, given the large confinement time of particles up to $\sim 10^{15}$ eV and the expected cut-off in the electron spectrum because of energy-dependent losses. Therefore, for all the following calculations only the hadronic channel is taken into account. The estimates are quantified for Abell 496 and Abell 85, two candidate clusters selected for observations with the H.E.S.S. experiment.

As shown above, CRs are in principle produced in clusters of galaxies by two distinct mechanisms: externally via accretion shocks and hierarchical merger events, or via internal mechanisms such as supernova driven galactic winds and AGN outbursts. The energy in CRs produced by external processes will in general be proportional to the thermal energy of the ICM if it is assumed that the thermal plasma was shock-heated during the assembly of the cluster and that the CRs were accelerated in the same large scale shocks. The energetics of CRs resulting from supernova related processes will depend on the kinetic

[2]This estimate was performed as a common work, together with Wilfried Domainko

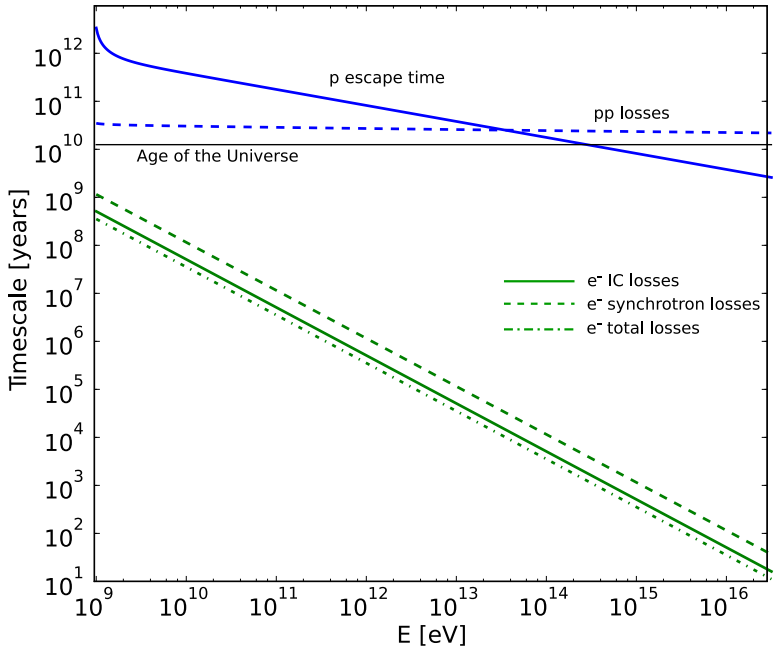

Figure 3.3: *Confinement of cosmic-ray particles in galaxy clusters is shown and compared to the age of the Universe (black line). Timescales of high-energy proton losses are depicted by green lines. Solid line shows the escape due to the diffusion on a Kolmogorov-type magnetic field fluctuations according to equation (3.6). The magnetic field is assumed to be $B = 5\,\mu G$ and the size of a cluster is taken to be $R = 1.5$ Mpc. The dashed green line shows losses in inelastic p-p collisions according to eq. (2.8). Number gas density is assumed to be $n = 1 \times 10^{-3}$ cm^{-3}. Blue solid line shows timescale of IC electron losses (formula (2.14)). It can be seen that the synchrotron losses (green dashed line calculated using eq. (2.12)) are comparable with the IC losses. The green dash-dotted line refers to the total electron losses, defined as $1/\tau_{\rm total} = 1/\tau_{\rm IC} + 1/\tau_{\rm synchr}$. Note that protons are confined within the cluster volume for age greater than the age of the Universe for energies $< 10^{15}$ eV and accumulate in the whole cluster. Electrons, on the other hand, cool very fast and their effective acceleration is only possible at certain sites, such as large-scale shocks or at the cooling cores (Gitti et al. 2002).*

energy released by the supernova activity during the entire Hubble time, and thus on the total number of supernovae exploding in the cluster volume (Völk et al. 1996). Finally the contribution from AGNs will be constrained by the kinetic power of the outbursts and the timescale of activity:

$$E_{\rm nonth} = \epsilon_{\rm ext} E^{\rm ext}_{\rm kin} + \epsilon_{\rm int} E^{\rm SN}_{\rm kin} + P_{\rm AGN} t_{\rm active} \tag{3.7}$$

In this equation, $E_{\rm nonth}$ is the total energy in CRs, $\epsilon_{\rm ext}$ is the efficiency of the accretion shock in accelerating CR particles, $E^{\rm ext}_{\rm kin}$ is the kinetic energy of the accretion process which assembled the present day cluster, $\epsilon_{\rm int}$ is the efficiency of supernovae and galactic winds in accelerating particles, $E^{\rm SN}_{\rm kin}$ is the combined kinetic energy provided by all supernovae exploding in the cluster volume, $P_{\rm AGN}$ is the mean power of AGN activity and $t_{\rm active}$ is the combined duration of all AGN outbursts. The contributions to $E_{\rm nonth}$ for the three

described mechanisms are now briefly estimated for case of Abell 496 and Abell 85, both candidates for TeV emission, studied later in chapter 6.

Accretion shocks

In galaxy clusters the kinetic energy of the accretion process $E_{\rm kin}^{\rm ext}$ is the dominant mechanism that heats the ICM (as shown in section 3.1.1). Intrinsic processes, such as supernovae, provide only a minor contribution to the thermal energy of the ICM. Hence the total thermal energy $E_{\rm th}$ of the cluster is a good measure of the kinetic energy of the in-fall of the cluster building blocks.

The thermal energy $E_{\rm th}$ of the ICM can be determined by knowing the temperature and the density profile of the ICM. Here for Abell 496, a uniform temperature of 4.7 keV throughout the cluster volume and a β density profile for the ICM is adopted (quantities from Markevitch et al. 1999). A value of 4.3×10^{62} erg for the thermal energy is computed. For Abell 85, a temperature of 7 keV and the density profile of Pfrommer & Enßlin (2004) is used. With these input values the thermal energy of the ICM in Abell 85 is found to be 2.4×10^{63} erg.

The efficiency of the conversion of $E_{\rm kin}$ into CR energy $\epsilon_{\rm ext}$ is difficult to estimate, but it is believed to be close to 0.1 (e.g. Dorfi 1991) for strong shocks. Note that authors using nonlinear simulations claim that it could be as large as 0.5 (Kang et al. 2002). For the purpose of this work a compromise value of 0.3 is adopted. However, if the accreted material is already hot, the sound velocity in such a medium is large. Hence typical Mach numbers of shocks in such media are small and these weak shocks are less efficient in accelerating particles (e.g. Dorfi & Voelk 1996). This fact could reduce the value of $\epsilon_{\rm ext}$ in case of accretion of hot gas during sub-cluster mergers significantly. Keshet et al. (2004) have argued that only a fraction of 8 - 17% of the baryonic material of a galaxy cluster is accreted in strong shocks. This accretion is also the contribution to $E_{\rm th}$ that is accompanied by effective CR acceleration because the rest of the material is assembled in weak shocks with inefficient non-thermal particle production. Here it is assumed that 10% of the ICM is accreted in strong shocks with $\epsilon_{\rm ext} = 0.3$. Consequently, in this scenario the energy in the non-thermal component will be 3% of the thermal energy for both clusters.

Supernova activity

To constrain the energetics of internal processes in the cluster, it is necessary to estimate the total number of supernovae that occurred in the cluster volume over its entire history. This can be achieved by estimating the total iron mass in the cluster.

The link between the total iron mass and the number of supernovae is, however, complicated by the different metal enrichment from supernovae Ia and core collapse supernovae. They both produce a similar kinetic energy but differ considerably in the amount of iron produced: supernovae Ia produce on average 0.7 $M_\odot$ of iron whereas the iron yield of core collapse supernovae is 0.07 $M_\odot$ (see Renzini (2004) for a review). The ejecta of supernovae Ia can be, however, distinguished from the ejecta of core collapse supernovae by the ratio of iron to oxygen (Renzini et al. 1993). By knowing the relative contribution of supernovae Ia and core collapse supernovae, respectively, and using the mean iron mass produced by each class of events, it is possible to evaluate the total number of supernovae that have

distributed the observed iron.

For the case of Abell 496, De Grandi et al. (2004) found a total iron mass of 2.1×10^{10} $M_\odot$ and for the case of Abell 85 they found 5.0×10^{10} $M_\odot$. From the Fe/O ratio found in these clusters it is evident that supernovae Ia contribute significantly to the chemical enrichment of the central cooling region (Tamura et al. 2004) but are unimportant for the total iron mass in the entire cluster (De Grandi et al. 2004). Hence it is assumed that the observed iron mass of 2.1×10^{10} $M_\odot$ (Abell 496) and 5.0×10^{10} $M_\odot$ (Abell 85) was entirely produced by core collapse supernovae, and therefore an iron production mass of 0.07 $M_\odot$ per supernovae (Renzini et al. 1993) is adopted. As a result of these considerations, it is found that 3×10^{11} supernovae (Abell 496) and 7.1×10^{11} supernovae (Abell 85) are necessary to enrich the ICM to the observed level with iron. By adopting the canonical energy per supernova to be 10^{51} erg, a total energy of internal processes of 3×10^{62} erg (Abell 496) and 7.1×10^{62} erg (Abell 85) is given. This energy is injected into the ICM in form of kinetic energy, thermal energy and CRs, and furthermore, depending on the environment of the supernova explosions, parts of it will also go to radiation losses (Dorfi 1991; Thornton et al. 1998). When assuming that 10% of the initial kinetic energy of the supernovae is converted into CRs ($\epsilon_{\rm int} = 0.1$) either in the supernova shocks themselves or in the termination shocks of supernova-driven galactic winds, it is found that supernova activity produces a component of high energy particles with about 7% (Abell 496) and 3% (Abell 85) of the thermal energy of the ICM. Note that $\epsilon_{\rm int}$ can be smaller than 0.1 if a large number of supernovae explode directly in the hot ICM (Domainko et al. 2004; Zaritsky et al. 2004) because in this case SN shocks are less efficient in accelerating CRs (Dorfi & Voelk 1996).

AGN activity

AGNs are generally considered to be an important source of CRs in galaxy clusters (e.g. Ensslin et al. 1997; Aharonian 2002; Hinton et al. 2007). In cooling core clusters, the AGN activity is usually dominated by a powerful central AGN. In the case of Abell 496 no AGN - ICM interaction is observed (Dunn & Fabian 2006), but this could be simply due to a low activity period of the central galaxy at present. It has to be noted that in several galaxy clusters, buoyantly rising bubbles filled with radio emitting relativistic electrons are found as remnants of past AGN outbursts (e.g. McNamara et al. 2001; Fabian et al. 2002), which is also not seen in the cluster Abell 496 (Dunn et al. 2005). The situation is different for the cluster Abell 85. In this cluster, bubbles filled with non-thermal electrons injected by a past AGN outburst can be seen in the ICM. These bubbles are about 10^7 years old and the energy that is necessary to inflate these bubbles is $\sim 10^{58}$ ergs (Dunn et al. 2005).

In general, AGNs can act in repetitive outbursts with up to 100 cycles over the lifetime of the galaxy cluster. In each cycle the AGN is active for ∼10% of the time (McNamara et al. 2001). One may estimate the contribution of a potential AGN activity in the past to the non-thermal particle component in this cluster. If it is assumed that a powerful AGN injects 10^{45} erg/s of hadronic CRs in the ICM and is active for 10% of the cluster lifetime (which is essentially the Hubble time) then this mechanism will distribute about 3×10^{61} ergs of CRs. Hence in an optimistic scenario, AGNs have the ability to provide non-thermal particles with an energy of 7% (Abell 496) and 1% (Abell 85) of the thermal energy of the ICM to the galaxy cluster.

In summary, it is found that all the three processes (accretion shocks, supernova activity and AGN outbursts) may contribute a comparable share to $E_{\rm nonth}$ and it is further found that in total about 17% (Abell 496) and 7% (Abell 85) of the thermal energy of the cluster Abell 496 can be in the form of CRs, corresponding to $\sim 7\times10^{61}$ erg for Abell 496 and $\sim 1.7\times10^{62}$ erg for Abell 85. Additionally it is shown that the contribution to $E_{\rm nonth}$ by internal processes is more important for less massive, cooler clusters.

Table 3.2: *Fractional non-thermal energy content in galaxy clusters Abell 496 and Abell 85 produced by the three discussed mechanisms. Tabulated values correspond to non-thermal to thermal energy ratio.*

Mechanism	Abell 496	Abell 85
Accretion shocks	3%	3%
Supernova activity	7%	3%
AGN activity	7%	1%
Total	**17%**	**7%**

3.1.4 Constraining the non-thermal energy content in galaxy clusters

In addition, it is possible to learn something about the non-thermal mechanisms from TeV observations in both cases — in case of a detection of a signal *and* in case of merely setting upper limits. A detection could provide information about the total amount of cosmic-ray energy of a cluster and also spectral information. The less optimistic scenario of an upper limit allows one still to derive upper limits on the total cosmic-ray energy content.

3.1.5 Estimating γ-ray flux from a galaxy cluster

Here we try to estimate γ-ray flux in the TeV energy band from galaxy clusters using the cosmic ray energy densities derived in the previous section. As already discussed before, due to the confinement of hadronic cosmic rays, π^0-decay is considered as a more promising γ-ray production channel, in particular when searching for a signal from the core of the cluster. Only the *hadronic channel* through π^0 decay is therefore considered, which makes the final estimate a lower limit. This is supported by the simulations of Pfrommer et al. (2008), who concludes that the dominant contribution to HE γ-ray flux at energies > 100 MeV is the π^0-decay channel (see Fig. 3.4).

To calculate the VHE flux, the formalism developed in the section 2.4.1 about hadronic production of γ rays is employed. The equation (2.18) is used for estimating the γ integral emissivity Q_γ above 1 TeV per a unit volume. The production rate per a unit volume Q_γ from equation (2.18) needs to be integrated[3] over the cluster volume and normalized to the cluster distance D to obtain the integral γ-ray flux above 1 TeV $F_{>1\rm TeV}$:

$$F(>1\rm TeV) = \frac{q_\gamma}{4\pi\, D^2} \int_0^R n_{\rm gas}(r)\, \epsilon_{\rm CR}(r)\, r^2\, {\rm d}r, \tag{3.8}$$

[3]Note that simply averaging over the cluster volume is not possible because the distribution of cosmic ray energy density is generally different from the ICM distribution.

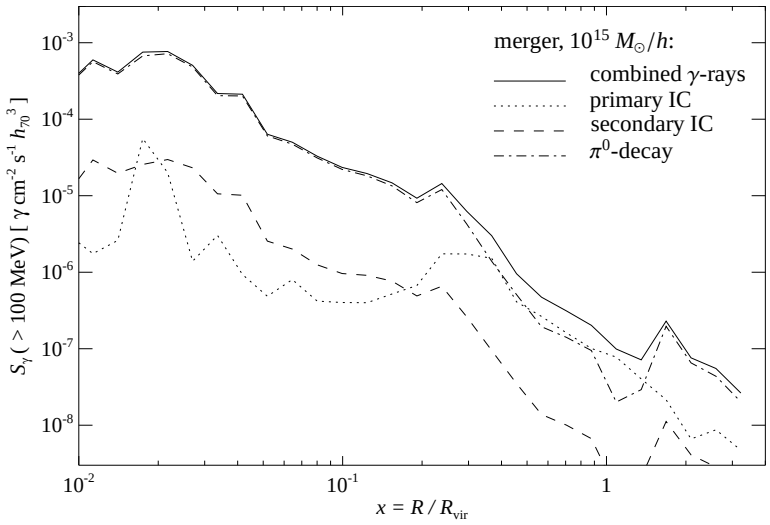

Figure 3.4: *Azimuthally averaged profile of a HE γ-ray brightness of a post-merger non-cooling core galaxy cluster, simulated by Pfrommer et al. (2008). The individual processes contributing to the total emission are depicted. The π^0-decay emission is dominating over a large range of radii. IC emission of primary electrons gets significant first at the outskirts and boundaries, where the structure-formation shocks are stronger.*

where R is the radial extent of the cosmic-ray content in the cluster and D is the distance of the cluster. Radial symmetry is assumed, which is a good approximation of a general cluster. The main assumptions necessary for estimating the non-thermal energy E_{CR} are the *cosmic-ray spectrum*, the spatial *distribution of the cosmic-ray energy density* $\epsilon_{\mathrm{CR}}(r)$ and the *radial extent* of hadronic cosmic-ray extension R.

The cosmic-ray extension R is typically approximated by the radius of the observed X-ray signal. For the spectrum, a hard power-law spectrum is assumed, with a spectral index of $\Gamma_{\mathrm{CR}} = 2.1$. This value is justified by the fact, that protons of relevant energies are confined in the clusters and the primary spectrum expected from Fermi acceleration will thus remain unchanged (Völk et al. 1996). Since this is however only an approximation, we quote also results assuming $\Gamma_{\mathrm{CR}} = 2.3$.

The cosmic-ray energy density profiles $\epsilon_{\mathrm{CR}}(r)$ in galaxy clusters are not known. The CR production rate via p-p channel generally follows the gas-density profile. This is indirectly illustrated in Fig. 3.5 produced in a complete simulation of a post-merger cluster by Pfrommer et al. (2008). The left panel of the figure shows a correlation between HE γ-ray emission from a π^0 decay, and the surface brightness in X-rays. The right panel shows the correlation in case of IC emission of primary electrons. One can see that the correlation is very good in the case of π^0 decay, which suggests that the HE emission (and also the primary protons) traces the density of the hot gas. The VHE production is then most efficient in the central core regions. The core region alone is, however, not calorimetrical as the CRs are not confined. Therefore, a flatter profile is more likely, unless there is some mechanism capable of supplying the central region with a quasi-steady source of CRs. An example is an AGN accelerating CRs in its outbursts (Hinton et al. 2007). The exact CR energy profile can thus be different for individual clusters and is quite uncertain. For this reason we assume three possible scenarios:

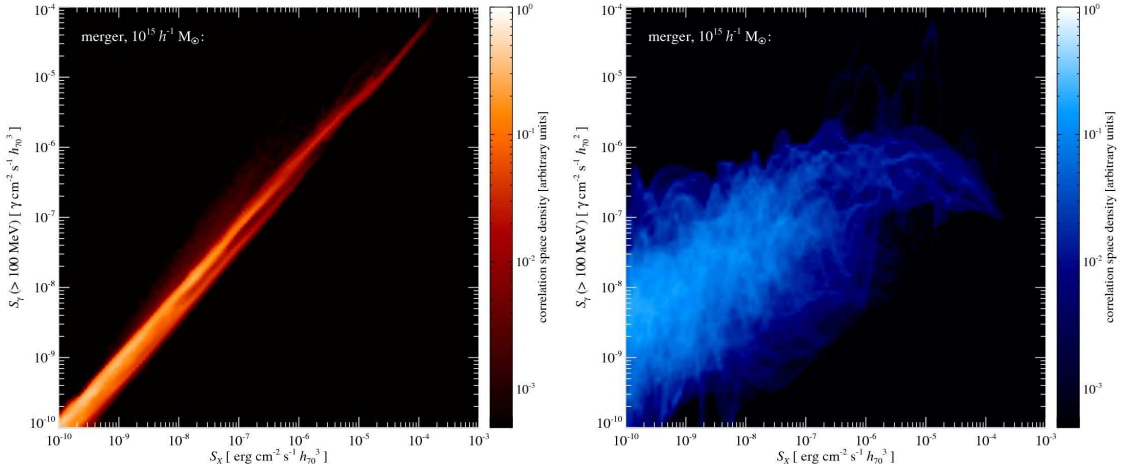

(a) π^0-decay & secondary IC emission ($E_\gamma > 100\ MeV$)

(b) Primary IC emission ($E_\gamma > 100\ MeV$)

Figure 3.5: *Correlation of HE γ-ray and X-ray (thermal bremsstrahlung) surface brightness for a post-merger galaxy cluster without a cooling core, with a mass $10^{15}\ h^{-1}\,M_\odot$.* **Left:** *The case of γ rays produced by a π^0-decay and by IC emission of the secondary electrons from pp inelastic collisions.* **Right:** *The case where γ rays are produced by IC emission of primary CR electrons. The correlation is significantly worse in the latter case and the structures in the figure correspond to the individual structure-formation shocks, where the electrons are accelerated. Figures are from Pfrommer et al. (2008).*

1. **Gas-density profile** — $\epsilon_{\rm CR}(r) \propto n_{\rm gas}(r)$ — the CR energy density profile follows the same profile as the gas-density profile (see section 3.1.1 for a review of density profiles of galaxy clusters). This assumption is rather optimistic in case of cooling-core clusters. The first reason is that due to Parker instabilities, it is impossible to maintain such high density of cosmic rays in such small volume (Parker 1966). Second reason is that the escape time of CR particles from the core (∼100 kpc) is considerably lower ($\sim 10^8$ yr) than the age of the Universe and they are not any longer confined in this region. The scenario thus yields the least conservative estimate. The result for this approach can be then compared with the work of Perkins et al. (2006), which assumes the same profile.

2. **Gas-density profile without a cooling core** - similarly as in the first case, $\epsilon_{\rm CR}$ follows the gas density profile, with the exception of the cooling flow in the center of clusters harbouring this phenomenon. This appears to be more realistic due to the reasons given in 1).

3. **Flat profile** — $\epsilon_{\rm CR}(r) \propto$ const. — the CR energy density is homogeneously distributed in the cluster within radius R. This approach yields the most conservative upper limit on $\epsilon_{\rm CR}$ because of the smallest overlap of $n_{\rm gas}(r)$ and $\epsilon_{\rm CR}(r)$ in the integral (3.8).

To summarize, the profile 1 is rather disfavored and the real CR energy profile is most likely to be between the cases 2 and 3. The results for all three scenarios are given.

Using the cosmic-ray energy density estimated in the previous section 3.1.3, the resulting estimates of γ-ray fluxes are calculated for these CR energy density profiles and tabulated in Tab. 3.1.5 for the example of Abell 85 and Abell 496. The table shows that even the hadronic mechanism alone is capable of producing a γ-ray flux detectable by ground-based IACT telescope arrays of the current generation as H.E.S.S., MAGIC or VERITAS.

Table 3.3: *Estimates of an integral γ-ray flux above 1 TeV from Abell 85 and Abell 496 produced by π^0 decay. Primary proton spectrum is assumed to be a power-law with spectral index $\Gamma = 2.1$ (left column) and $\Gamma = 2.3$ (right column). Estimates for different assumed energy density profiles as discussed in the main text are given. The region considered is in all cases 1 Mpc radius around the center.*

Abell 85		
Energy density profile	$F_\gamma^{2.1}(> 1\,\mathrm{TeV})$ $[\mathrm{cm}^{-2}\,\mathrm{s}^{-1}]$	$F_\gamma^{2.3}(> 1\,\mathrm{TeV})$ $[\mathrm{cm}^{-2}\,\mathrm{s}^{-1}]$
Constant profile	1.5×10^{-13}	3.1×10^{-14}
β profile	2.8×10^{-13}	5.8×10^{-14}
CC profile	3.7×10^{-13}	7.7×10^{-14}
Abell 496		
Constant profile	1.1×10^{-13}	2.3×10^{-14}
β profile	2.4×10^{-13}	5.0×10^{-14}
CC profile	3.0×10^{-13}	6.3×10^{-14}

So far, no galaxy cluster has been experimentally established as a γ-ray emitter (Perkins et al. 2006). A discovery of galaxy clusters in γ-rays would not only mean another type of a γ emitter. It would allow study of acceleration and propagation of cosmic rays in the galaxy clusters over the age of the Universe.

3.1.6 Target selection

The target clusters were selected in terms of optimal detectability, position and distance for an observation with H.E.S.S. Promising targets of this kind should be located on the southern hemisphere and at a redshift not much larger than $z \sim 0.05$, since more distant objects suffer substantial absorption from EBL (see section 2.4.3).

Given the rather weak expected signal from galaxy clusters (as opposed to Galactic sources), a long exposure is necessary. In order to obtain a very long exposure of one specific object, it should be located in a Right Ascension (RA) band where only very few promising other targets are in competition with the observation.

X-ray flux criterium

As a first target, a compact galaxy cluster, *Abell 496*, was selected. The sensitivity of imaging atmospheric Čerenkov telescopes decreases approximately with the square root of

the solid angle of the gamma-ray emission region, and therefore linearly with the source extension (see also section 5.1). For this reason, the detectability of a source is proportional to its gamma-ray luminosity F_γ divided by its size R_γ. If it is assumed that the X-ray size and the X-ray brightness of a cluster together are a measure of its gamma-ray flux, then F_X/R_X can be used as a figure of merit. These selection criteria were applied to the galaxy clusters of the REFLEX survey (Böhringer et al. 2004), which covers two thirds of the southern sky and contains 447 X-ray bright clusters. Based on this selection procedure, Abell 496 was found to be the prime candidate for H.E.S.S. observations. It has to be noted that this selection procedure prefers galaxy clusters that host a so called *cooling core* at their center. In a cooling core cluster, the central gas density is large enough that the radiative cooling time due to thermal X-ray emission is shorter than the Hubble time (see Peterson & Fabian 2006, for a review). This large density of target material is favorable for hadronic production of gamma rays; however, since only a small fraction of the total gas mass is contained in the cooling core, this will increase the total gamma-ray luminosity by only a modest amount.

Accretion luminosity criterium

As a second target, a massive cluster, *Abell 85*, was observed with a quite deep exposure. This object lies in the RA band between 0 and 1 hours, which is the range where observations of the Galactic plane are not possible from a southern location. Therefore a long exposure time could be obtained with H.E.S.S. without competition from galactic objects. For selecting this target, a different procedure was adopted than for Abell 496. Clusters were evaluated due to their accretion power, which scales with $M^{5/3}$ (M is the total mass of the cluster, see Gabici & Blasi 2003, 2004). Then the estimated accretion power was converted into an "accretion luminosity" by dividing it by the inverse square of the target distance. Finally the source extension was also taken into account. Since, as described above, the sensitivity of imaging atmospheric Čerenkov telescopes decreases approximately linearly with the source extension, the "accretion luminosity" was further scaled with the inverse of the cluster radius. The aforementioned criteria were applied to the X-ray selected galaxy cluster catalog of Reiprich & Böhringer (2002). Following this selection procedure the cluster Abell 85 was found to be the prime target in the RA band of 0 to 1 hrs.

Additional targets

In this work, the focus is placed on the two objects mentioned above. Other targets are also studied, though not in such detail. *Coma cluster* and *Abell 754* were also selected for observations with H.E.S.S. based on the accretion luminosity discussed above. In addition, *Centaurus cluster* was observed owing to its very high metallicity, and *Hydra A* due to its pronounced AGN outburst activity, which is predicted to be a source of VHE γ rays by Hinton et al. (2007).

3.2 Starburst galaxies

Starburst (SB) galaxies are galaxies undergoing a phase of an extreme star formation. Typically only a central subkiloparsec region is responsible for most of the activity. This region is then referred to as a *starburst region*. SB galaxies are characterized by a strong IR flux[4] caused by re-emission of radiation by a dense gas, a strong HII emission-line spectrum, and by a radio emission from supernovae. The age of the starburst phase of a galaxy evolution is believed to be $10^7 - 10^8$ years (Rieke et al. 1980).

Starburst activities are believed to be triggered by a merger activity or close encounters of galaxies. These processes distort the gas dynamics and create regions of very dense gas where SB activity can be triggered. It is also possible that starburst galaxies form an early stage of an AGN (see e.g. Levenson et al. 2001; Weaver et al. 2002; González Delgado et al. 2008).

The two archetypal examples of such objects are M 82 in the northern hemisphere and NGC 253 in the southern hemisphere (Rieke et al. 1980), the latter of which is studied by this work.

3.2.1 High supernova rate

Starburst regions are characterized by a highly increased supernova rate compared with e.g. the Local Group Galaxies. Supernovae are thus believed to be the primary sites of cosmic-ray acceleration in starburst galaxies. The knowledge of the SN rate $\nu_{\rm SN}$ is therefore crucial for estimating all non-thermal processes. In order to estimate $\nu_{\rm SN}$ in a central starburst region, IR observations are used. Van Buren & Greenhouse (1994) show[5] that the supernova rate $\nu_{\rm SN}$ is directly proportional to the FIR luminosity.

In NGC 253, a typical example of a starburst galaxy, the FIR luminosity obtained by Rice et al. (1988) is $L_{\rm FIR} = 3 \times 10^{10} L_\odot$, approximately a factor of $\sim$3 more than in the whole Milky Way (Cox & Mezger 1989). The emission in the SB galaxy comes, however, predominantly from the innermost region where the average $L_{\rm FIR}$ is higher by a factor of $\sim$20 than in the central 450 pc of the Milky Way (Cox & Mezger 1989). According to Van Buren & Greenhouse (1994), the total SN rate is estimated at $\nu_{\rm SN} \approx 0.08$ yr^{-1}. The total star formation rate (SFR) is estimated to be 5 $M_\odot$ yr^{-1}, with 70% coming from the nuclear starburst (Melo et al. 2002). For a comparison, the SN rate is an order of magnitude larger than of e.g. M31, the largest of the Local Group of Galaxies.

Galactic wind

Starburst galaxies typically harbour galactic-scale "superwinds" (Lehnert & Heckman 1996). The winds are produced when the kinetic energy of the SNR ejecta and from stellar winds of massive stars are thermalized. The collective effect of these processes creates a cavity of a hot gas of $T \sim 10^8$ K expanding into the surrounding low-pressure medium. As a result, an on-going galactic-scale wind perpendicular to the galactic disk is produced, effectively

[4] The SB region can be two orders of magnitudes brighter in IR than a center of a common spiral-type galaxy.

[5] The calculation is based on a modeling of radio emission from supernova blast waves expanding into the ejecta of their precursor stars. For details see Van Buren & Greenhouse (1994).

transporting mass from the central SB region (Chevalier & Clegg 1985; Heckman et al. 1990). In this way, the galactic winds are also believed to be responsible for e.g. metal enrichment and heating of intracluster medium in galaxy clusters. Additionally, a strong shock can be formed at the interface between the wind and the cool interstellar medium, which can efficiently accelerate CR particles.

The knowledge of the wind speed is crucial for estimating CR losses, since the wind is responsible for convective outflow of material; the wind speed is typically $100-1000\ \mathrm{km\,s^{-1}}$. In case of NGC 253, Zirakashvili & Völk (2006) provides a dedicated estimate. They derive an analytical model for the outflow from the disk, which is then used to fit radio observations (Mohan et al. 2005). The resulting velocity is $V_{\mathrm{wind}} = 900^{+1100}_{-400}$ km s^{-1}.

3.2.2 Cosmic rays in starburst galaxies

Two general mechanisms can produce cosmic rays in starburst galaxies — acceleration in individual supernova remnants (SNRs) and acceleration at the termination shock of the galactic wind (see above).

In the first mechanism, cosmic rays are accelerated in individual SNRs. These objects contain strong shock waves, where first order Fermi acceleration can occur (see section 2.1.1). Starburst regions generally contain a lot of dense material in form of dust, which is responsible for a *high supernova rate* and consequently for a conversion of large amounts of energy into cosmic rays.

A complete prediction of a cosmic-ray energy content in starbursts requires numerical simulations and goes beyond the scope of this work (see e.g. Domingo-Santamaría & Torres 2005). We will therefore restrain ourselves only to general energetics considerations concerning hadronic cosmic rays (similarly to the approach of Völk et al. 1996). In order to quantify the result, the starburst galaxy NGC 253 is used.

Assuming that in each SN explosion a total energy E_{SNR} is released and with efficiency η_{CR} converted into cosmic-ray protons via shock acceleration, the total energy output in cosmic-ray protons in the starburst region can be estimated as:

$$W_{\mathrm{CR}} = \nu_{\mathrm{SN}}\, E_{\mathrm{SNR}}\, \eta_{\mathrm{CR}}, \tag{3.9}$$

where ν_{SN} is the frequency of supernova explosions. The largest uncertainty is in the unknown efficiency η_{CR}. Here, we adopt the traditionally assumed value of $\eta_{\mathrm{CR}} = 0.1\ \mathrm{yr^{-1}}$. The total energy available in a single supernova explosion E_{SNR} is assumed to be $\sim 10^{51}$ erg, and for the frequency a rather conservative value of $\nu_{\mathrm{SN}} \approx 0.1$ is used (Rieke et al. 1988). The energy output in CR protons is then $W_{\mathrm{CR}} \sim 3.2 \times 10^{41}$ erg/s.

The second mechanism of CR acceleration occurs on the termination shock of the galactic winds. CRs accelerated by the supernovae to energies $\sim 10^{15}$ eV are carried by the starburst wind and re-accelerated in the galactic-scale shock. Maximum energies achieved in this way may reach $E_{\mathrm{max}} \approx 3.4 \times 10^{20}$ eV for an iron nucleus as it was modeled by Anchordoqui et al. (1999). In the γ-ray flux estimation, we restrain ourselves for simplicity only to the first mechanism.

3.2.3 Estimate of a γ-ray flux

Given a value for the CR energy output, it is possible to estimate the VHE γ-ray flux produced via the π^0-decay channel. Assuming that the total proton energy is lost due to inelastic p-p collisions, approximately one third of the energy is deposited in γ rays produced in π^0 decay. The final two thirds correspond to the production of $\pi^{\pm}$. The luminosity in γ-rays of the given source can then be estimated as 1/3 of the total output $W_{\rm CR}$ in protons. The total γ-ray energy flux can then be estimated as:

$$F_\gamma = \frac{1}{3}\frac{1}{4\pi D^2} W_{\rm CR} \tag{3.10}$$

In this case $F_\gamma \approx 8.2 \times 10^{-11}$ TeV/(cm^2 s).

The integral γ-ray flux $I_\gamma(> E_0)$ above a given energy E_0 is estimated from the energy flux F using the assumption that the primary protons exhibit a power law spectrum with spectral index of $\Gamma = 2.0$. This yields:

$$I_\gamma(> E_0) = \frac{1}{1.6\ \ln(1\ \mathrm{PeV}/1\ \mathrm{GeV})} \left(\frac{F_\gamma}{\mathrm{erg}}\right) \left(\frac{E_0}{1\ \mathrm{TeV}}\right)^{-1.0}, \tag{3.11}$$

where the proton spectrum between 1 GeV (the approximate energy threshold for the p-p interaction) and 1 PeV (the approximate maximum energy that can be obtained by a shock acceleration in SNR — see eq. (2.5)). Note that the supernova rate $\nu_{\rm SN}$ is determined by measuring the IR luminosity and $\nu_{\rm SN}$ scales therefore with the square of the distance. The result of equation (3.11) is thus effectively independent of the distance[6] and only depends on the infrared observations.

We find that for this calorimetrical model, where all of the energy of the protons is lost in inelastic p-p collisions, the estimated integral γ-ray flux above 1 TeV $F_\gamma(> 1\ \mathrm{TeV}) \approx 2.3 \times 10^{-12}\ \mathrm{cm}^{-2}\,\mathrm{s}^{-1}$.

In the previous discussion, all cosmic-ray particle losses have been neglected, however we can try to address these in order to estimate the scale of their effect. Note that all estimates are made for the case of NGC 253 assuming the distance $D = 2.6$ Mpc. Alternative estimates of the distance to this object exist, but these are discussed in the section 6.2.1. The main losses of the primary CR protons are convective losses due to the high-velocity motion in the starburst wind, and diffusive losses.

The timescale of convective losses of CR protons can be then estimated as $t_{\rm conv} = H/V_{\rm wind}$, where H is the linear size of the starburst region and $V_{\rm wind}$ the velocity of the wind. In case of NGC 253, assuming $H = 100$ pc (Weaver et al. 2002) and $V_{\rm wind} = 900$ km/s (Zirakashvili & Völk 2006) this time is $t_{\rm conv} = 1.1 \times 10^5$ yr.

The diffusion time is according to e.g. Aharonian et al. (2005a)

$$t_{\rm diff} = H^2/\kappa = 1.4 \times 10^5 \left(\frac{\mathrm{E}}{1\mathrm{TeV}}\right)^{-1.1}\ \mathrm{yr} \tag{3.12}$$

[6] The same distance has to be used in (3.11) as the one used in the SN rate estimates — in this case $D = 2.6$ Mpc (see Engelbracht et al. 1998).

The timescale of the convective and diffusive losses for a proton energy E =1 TeV is thus:

$$\tau_{\rm loss} = \frac{1}{1/\tau_{\rm conv} + 1/\tau_{\rm diff}} \approx 6.1 \times 10^4 \text{ yr} \tag{3.13}$$

The loss time due to inelastic collisions amounts to $t_{\rm loss} = 8.6 \times 10^4$ yr according to the eq. for p-p interaction timescale (2.8). It is thus obvious that the timescale of γ-production through the p-p interactions is comparable to that of the proton losses and the calorimetrical estimate is overestimating the flux[7]. Thus the result of equation (3.11) should be regarded as a calorimetric upper limit estimate.

A complete theoretical modeling of all the processes goes beyond the scope this work; however the considered full simulation for NGC 253 was carried out by e.g. Domingo-Santamaría & Torres (2005), who estimated the integral γ-ray flux above 1 TeV to $F(> 1\,\text{TeV}) \approx 2{\times}10^{-13}\,\text{cm}^{-2}\,\text{s}^{-1}$. An alternative estimate for the same target was also performed by Aharonian et al. (2005a) who estimates the integral flux to $F(> 1\text{ TeV}) \approx 9.8 \times 10^{-13}\text{ cm}^{-2}\,\text{s}^{-1}$. These flux levels are detectable by the current IACTs and motivate observations of NGC 253.

3.2.4 Target selection

The two obvious candidates are NGC 253 and M 82, both archetypal examples of the nearest starburst galaxies (both at ∼3 Mpc). M 82 is at declination 69° 0' and thus unreachable for an instrument in the southern hemisphere. The most optimal target for H.E.S.S. observations is therefore NGC 253. Additionally, also a starburst galaxy M 83 is here analyzed.

[7] It should be noted that higher convective losses imply also more efficient CR acceleration at the wind termination shock

3.3 Ultraluminous infrared galaxies

Ultraluminous infrared galaxies (ULIRGs[8] or ULIGs) are galaxies whose SED is dominated by infrared emission that exceeds $L_{\rm IR} > 10^{12}\ L_{\odot}$ [9] (for a review on (U)LIRGs see Sanders & Mirabel 1996). This emission indicates an existence of large amounts of dust in the galaxies. According to e.g. Scoville et al. (1991), the central 0.5 kpc of these objects can contain more than $10^{10}\ M_{\odot}$ of gas. Such dense regions are believed to be formed by galactic mergers and a consequent in-fall of material into the galactic centers. An extensive starburst activity is therefore expected in the centers of these objects with a very pronounced star formation and supernovae rate. ULIRGs are thus expected to be sources of significant cosmic-ray fluxes (Torres & Anchordoqui 2004; Smialkowski et al. 2002)

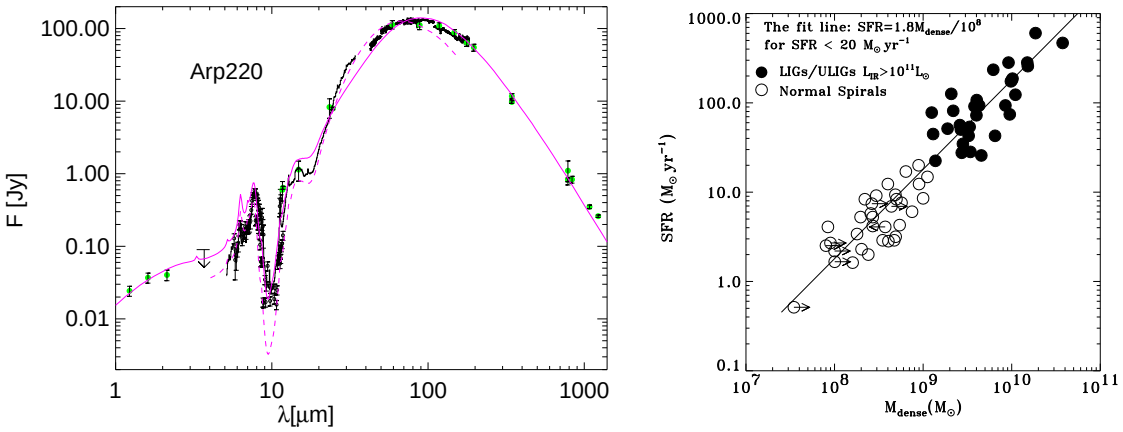

Figure 3.6: Left: *SED of Arp 220, a prototype example of a nearby ULIRG. The SED is clearly dominated by the FIR emission. Data are fitted by an emission model of Siebenmorgen & Krügel (2007). Figure from Siebenmorgen & Krügel (2007) and references therein.* **Right:** *A plot showing a star formation rate (SFR) as a function of mass of a dense molecular gas. Solid circles denote LIRGs and ULIRGs. The SFR of ULIRGs is thus by a factor of 100—1000 higher than of normal galaxies. Figure from Gao & Solomon (2004).*

3.3.1 VHE γ-ray production

With respect to the cosmic-ray production and VHE γ emission, the ULIRGs are qualitatively similar to the starburst galaxies discussed in section 3.2. In both cases the high gas density is an indicator for a high star formation rate (SFR) and supernova rate. ULIRGs are however less common and there is no ULIRG at a distance comparable to the close starburst galaxies as M 82 or NGC 253. The closest example is Arp 220 at ~ 73 Mpc. Despite this disadvantage, the distance is compensated by the SFR being $100 - 1000$ times higher (Gao & Solomon 2004) than the SFR in e.g. in the Milky Way (estimated at $\sim 1\ M_{\odot}$ yr.$^{-1}$ according to Mac Low 2002) — see also the right panel of Fig. 3.6.

[8] Note that ULIRGs are a quantitatively more extreme objects than luminous infrared galaxies (LIRGs or LIGs) with $L_{\rm IR} > 10^{11}\ L_{\odot}$.

[9] These luminosities can be compared to the IR luminosity of the starburst galaxy NGC 253 $L_{\rm IR} = 10^{10.8}\ L_{\odot}$

The cosmic-ray production and VHE γ-ray emission of the ULIRGs was studied by Torres et al. (2004); Torres (2004). The specific example of Arp 220 was analyzed by Torres (2004); Torres & Domingo-Santamaría (2005) where it was shown that Arp 220 can be a possible source of detectable γ rays at TeV energies produced by the π^0-decay. See Fig. 3.7 for a prediction of the integral flux. It can be seen that the sensitivity of current IACTs is barely touching the predicted flux. It has to be noted, however, that there are several uncertainties that are difficult to enumerate and could drive the prediction up or down. An example is the power-law photon index of primary protons, which is in the work of Torres (2004) assumed to be $\Gamma = 2.2$.

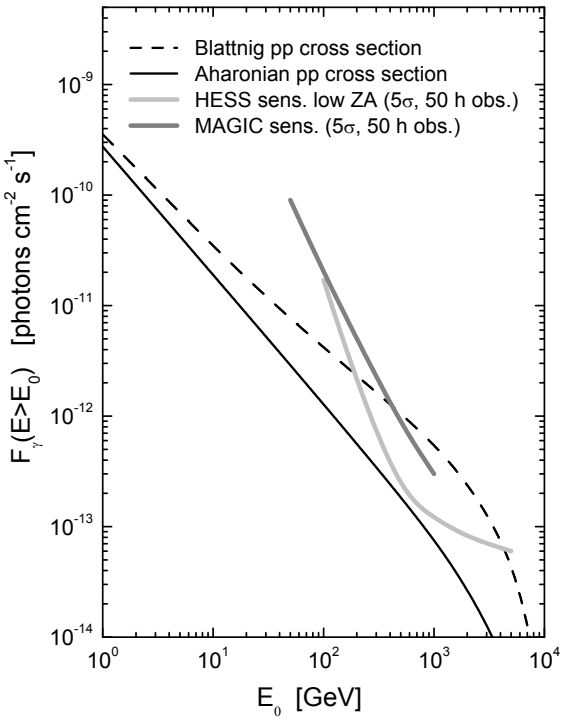

Figure 3.7: *The predicted VHE γ-ray integral flux from π^0-decay in Arp 220 according to Torres & Domingo-Santamaría (2005). Two parametrizations of the p-p interaction are shown, whereas the parametrization of Aharonian (solid line) should be used for energies above 100 GeV. Absorption effects due to $\gamma\gamma$ interaction are already taken into account.*

The main candidate for a detectable VHE γ-ray emission is clearly Arp 220. It is the closest ULIRG at z=0.018 and typically referred to as an archetypal ULIRG with $L_{\rm IR} \sim 10^{12}\ L_{\odot}$.

3.4 Active galactic nuclei

The term of an *active galactic nucleus* (AGN) refers to the central region of an active galaxy. These represent a specific class of about 3% of all observed galaxies, characterized in particular by very strong non-thermal activity, compact luminous centers (AGNs) and jets. The AGNs are believed to harbour a supermassive black hole ($\sim 10^6 - 10^{10}\ M_\odot$), surrounded by an accretion disk formed by hot ($\sim 10^5$ K) in-falling material. The material in the disk is heated up and emits a black-body radiation peaking mainly in ultraviolet wavelengths, which is also a typical characteristic for these objects. In addition, AGNs are characterized by *jets* — collimated outflows of hot plasma expelled in a direction perpendicular to the accretion disk at relativistic velocities (see Fig. 3.8 for a schematic illustration of an AGN). The formation of jets is not yet very well understood, but they are believed to be sites of particle acceleration, possibly to ultra-high energies.

Several subgroups of AGNs have been phenomenologically identified, based on their observational characteristics. Urry & Padovani (1995) argued that the distinct categories represent only one intrinsically identical type of object that is viewed under different viewing angles from Earth. The properties of the AGN classes can be then explained using simple arguments related to the geometry and structure of the regions around the supermassive black hole in the centre of the AGN (see Fig. 3.8).

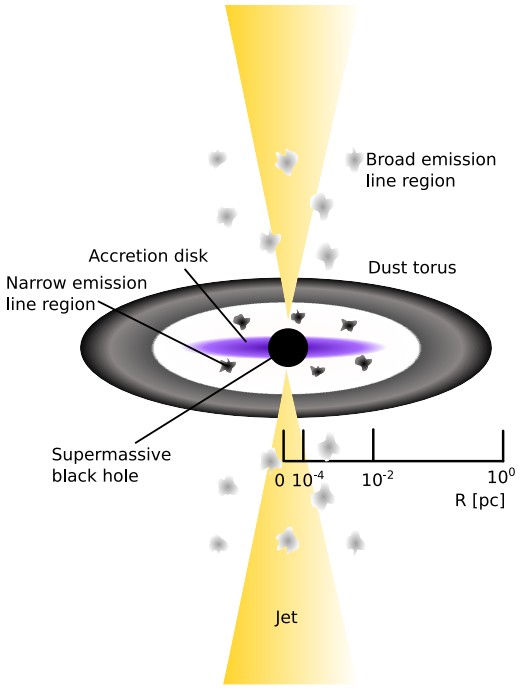

Figure 3.8: *A schematic illustration of an AGN according to Urry & Padovani (1995). According to this work, different types of AGNs correspond to intrinsically one type of object, viewed at various observation angles. The black hole is in the model surrounded by a luminous accretion disk, which can be obscured by a dusty torus further out. The regions of broad and narrow-line emissions are shown.*

Contrary to the previous objects, AGNs have already been established as TeV-emitting

objects. After the detection of the Crab Nebula, AGNs were the second type of object to be detected in the VHE energy band (Punch et al. 1992) and the very first extragalactic one. With the exception of a radio galaxy M 87 (Aharonian et al. 2006e) and a quasar 3C 279 (Albert et al. 2008), all of them belong into the category of BL Lacertae (or BL Lac).

3.4.1 BL Lac objects

BL Lac objects form a subgroup of AGNs, named after their prototype, BL Lacertae (also detected in TeV by Albert et al. 2007b). They are characterized by a rapid and large-amplitude variability of flux and the spectrum is dominated by a continuum non-thermal features, devoid of spectral lines. Their spectra energy distribution (SED) shows a typical double-peaked structure (see Fig. 3.9). Depending on the position of the peaks, BL Lacs are separated into high-frequency-peaked (HBL) and low-frequency-peaked (LBL) BL Lacs (see section B in the appendix for details about this classification).

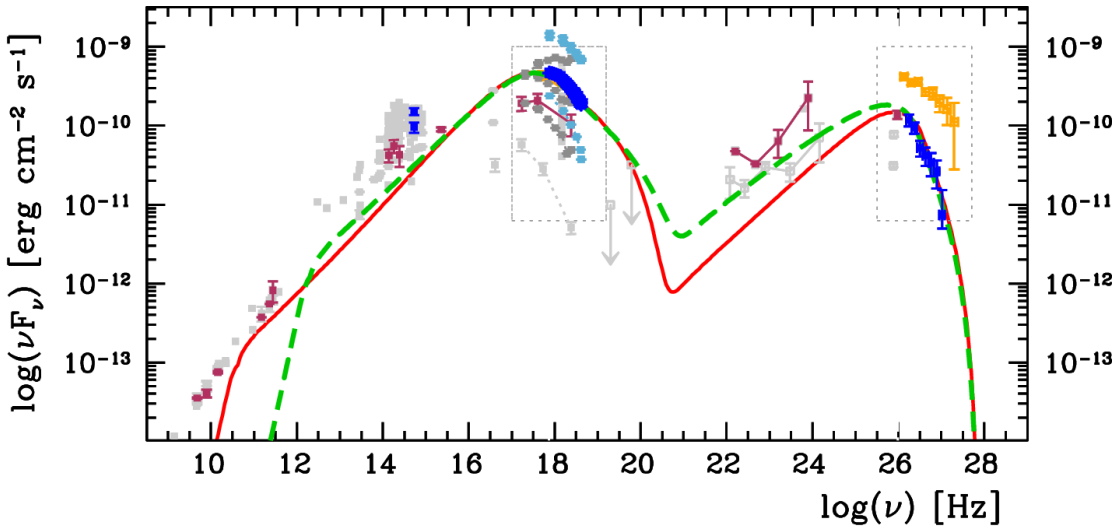

Figure 3.9: *Spectral Energy Distribution (SED) for a low-flux state of a TeV BL Lac Mrk 421. The double-peaked structure of the SED is well demonstrated by this multiwavelength compilation. The solid red line represents a fit by a simple one-zone SSC model. Plot from Fossati et al. (2008). For references, see Fossati et al. (2008)*

Within the framework of a unified model of AGNs (Urry & Padovani 1995), BL Lac objects are believed to be AGNs with the jets pointing in the direction of Earth. The relativistic motion of material in the jet, together with the small viewing angle can explain the rapid variability and the strong non-thermal emission produced by relativistic particles in the jet. Additionally, the flux observed when looking into the relativistic jet is further enhanced by a Doppler boosting.

3.4.2 VHE γ-ray production in BL Lac objects

The physics of relativistic outflows in BL Lac objects is rather complicated and not very well understood. It is generally accepted that the VHE emission from BL Lacs comes

primarily from the jets, but the nature of the primary cosmic rays, their acceleration mechanism and production of VHE γ rays remain under debate. All of the proposed models can be principally divided into leptonic and hadronic models.

Leptonic scenario

The leptonic models assume a significant population of relativistic electrons in the jet. The non-thermal emission from the radio energy band to X-ray energies in BL Lacs is then explained as synchrotron radiation from these electrons (e.g. Blandford & Konigl (1979)). The second peak of the SED in γ-ray energies (see Fig. 3.9) can be explained by IC scattering of the electrons on low energy seed photons. These may be of various origin:

- Synchrotron radiation of the same population of electrons. This model is commonly referred to as the *synchrotron self-Compton* (SSC) model (Marscher & Gear 1985).
- The UV thermal emission of the accreting material in the accretion disk. These photons either directly undergo the IC scattering (Dermer et al. 1992) or they are first re-emitted at the broad emission line region (Sikora et al. 1994).
- The jet synchrotron radiation of the electrons reflected at the broad emission line region (Ghisellini & Madau 1996).

Despite its simplicity, the leptonic SSC model is most often used as a reference. It can account for the observed variability and for the X-ray/γ-ray correlations, it explains in a simple manner the double-peaked structure of the SED of TeV blazars and is successful in fitting the X-ray and γ-ray observations of most TeV blazars.

The leptonic scenario is currently the more preferred one and we therefore focus on this one when selecting candidate objects for observing AGNs in TeV energies.

Hadronic scenario

The hadronic models assume a population of primary protons of energies $\sim 10^{20}$ eV. The observed γ-ray emission is modeled by interactions of protons with the ambient matter, photon fields, magnetic fields or both magnetic and photon fields. See e.g. Aharonian (2004) for a review on this subject.

Target selection

The basic criterium applied in search of γ ray emitting objects is a high X-ray and radio flux. This is justified in the work Costamante & Ghisellini (2002). In the SSC model (see section 3.4.2), it is assumed that the seed photons for the IC process are produced by the synchrotron radiation of the high energetic electrons, which are later targets for the IC process. Therefore there is no need for external seed photons. The synchrotron photons span from the infrared to the ultraviolet energy range; however the process is most efficient for seed photons in the IR to optical range where the IC scattering occurs in the Thompson regime (see section 2.4.2). At higher energies, the full Klein-Nishina cross section has to be taken into account which drops off with increasing energy (see Fig. 2.3). The radio

synchrotron emission is thus a good measure of the density of the seed photons. The X-ray intensity is then measure of the electron density.

This criterium was used in Costamante & Ghisellini (2002) to identify candidate BL-Lacs for a TeV emission. In Fig. 3.10 the objects within the box delimiting AGNs with high X-ray and radio flux are the most viable candidates to be observed in VHE energies according to this criterium. From this, RGB J0152+017 was selected for observations by the H.E.S.S. experiment. It is denoted by a red circle in Fig. 3.10. The results of H.E.S.S. observations are described in section 6.4.1.

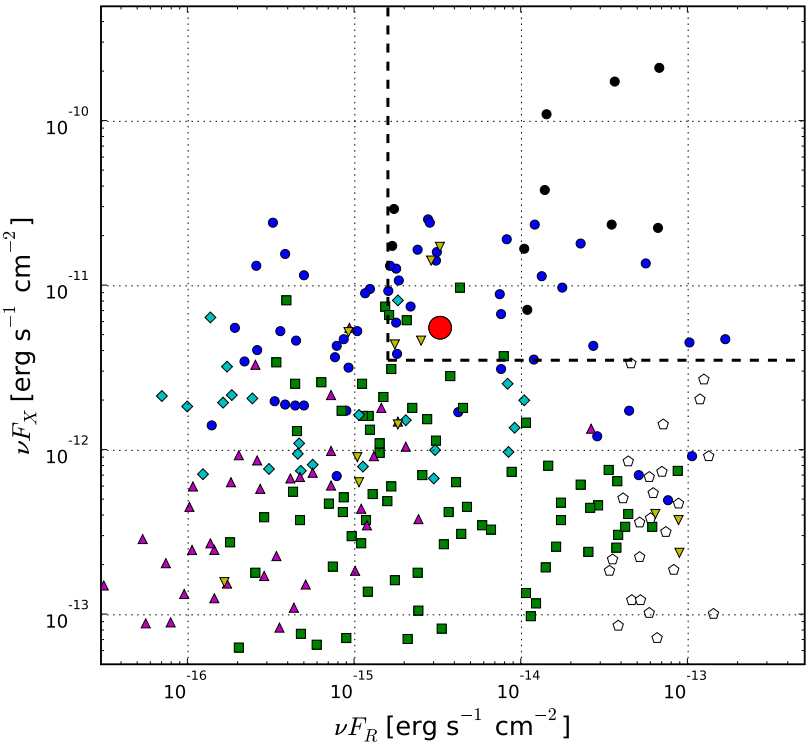

Figure 3.10: *X-ray and radio fluxes of a sample of AGNs. Red circle denotes approximate position of RGB J0152+017 based on results of Laurent-Muehleisen et al. (1999), black points denote AGNs detected in TeV band until 2002. Dash-line box shows the region of candidate TeV AGNs according to Costamante & Ghisellini (2002) (based on a figure from Costamante & Ghisellini 2002).*

Chapter 4

Experimental technique

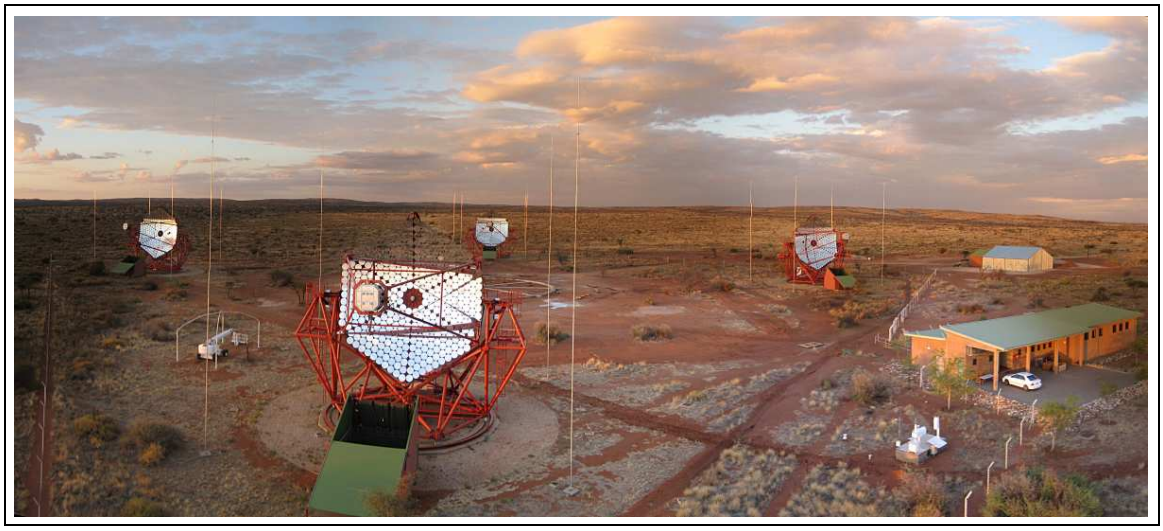

Figure 4.1: *The telescope array of four H.E.S.S. IACT telescopes. On the right side is located control room for operating the array. The telescopes are positioned at the corners of a square, in the centre of which the H.E.S.S. II telescope is going to stand.*

The High Energy Stereoscopic System (H.E.S.S.) is used in this work to study extragalactic γ-ray sources. H.E.S.S. is an array of four imaging atmospheric Čerenkov telescopes (IACTs), located in the Khomas highlands in Namibia at 1800 m above the sea level (see Fig. 4.1).

In this chapter, the experimental technique of IACT arrays is introduced in Sec. 4.1. The H.E.S.S. experiment is then described in Sec. 4.2. Afterwards, the general data-flow in H.E.S.S. is discussed in Sec. 4.3, calibration procedure in Sec. 4.4 and data-quality monitoring in Sec. 4.5. Finally, the general analysis procedure is described in Sec. 4.6. The IACT technique, as well as the H.E.S.S. experiments have already been detailed in a number of publications (see e.g. Porter & Weekes 1977; Weekes et al. 1989; Hinton 2008). This chapter presents thus only a rather basic overview of these subjects, necessary for further reading of the chapter 5 about the instrument performance and sensitivity and chapter 6 including the results.

4.1 Imaging Atmospheric Čerenkov Telescopes technique

The basic idea of the method is utilization of the Earth atmosphere as a calorimeter and a particle detector. Primary γ rays of very high energies ($\sim$TeV) interact in the atmosphere and create an electromagnetic cascade of secondary particles, which have velocities typically larger than the speed of light in air, and therefore emit Čerenkov light (Čerenkov 1937).

The light is collimated around the major axis of the cascade and the Čerenkov photons thus irradiate only a small "light pool" on the Earth's surface. The illuminated area has typically a radius $\sim$130 m for a vertical event. This corresponds to a typical height of the peak of the shower of $\sim$10 km and to an opening angle of $\sim 1^\circ$. Within this radius — referred to as the Čerenkov shoulder — the photon density is almost constant and rapidly falls off beyond the shoulder. The number of photons peaks in the energy region corresponding to blue light, and is rather dim. For a 1 TeV energy primary γ-ray, the number of photons arriving at the Earth's surface at a 2000 m altitude is $\approx$100 m^{-2}.

The Čerenkov light is observed by means of Earth-bound optical telescopes that are capable of imaging the electromagnetic shower. The light is collected by a primary mirror and projected onto the camera plane placed in the focus of the primary mirror. Given the low photon statistics, the camera uses photomultiplier tubes (PMTs) in order to detect the Čerenkov photons.

Images of the shower events in the camera plane are, after calibration, analyzed to retrieve information about the energy and direction of the primary γ ray. Energy reconstruction in case of H.E.S.S. is described in more detail in Sec. 4.6.5, and the direction reconstruction in Sec. 5.3.1. In addition, analysis of the geometry of the shower images can be used to reject the dominant background of hadronic cosmic rays. Their incidence rate dominates the γ-ray rate by a factor of 10^3 even for the strongest steady γ-ray sources (e.g. Crab Nebula). In the work of Hillas (1985, 1996), it was recognized that an analysis of simple image parameters can lead to an efficient hadronic-background separation, which was demonstrated by the detection of the Crab Nebula by the Whipple telescope (Weekes et al. 1989). The separation is based on the difference between an image of a (hadronic) cosmic-ray induced shower and a γ-ray induced shower (see also Fig. 4.2:

- *γ-ray shower* – The shower is formed only by an electromagnetic cascade of $e^\pm$ and photons (see left image in Fig. 4.2). The image in the camera plane is thus symmetrical and resembles an elongated ellipse (left image in Fig. 4.3).
- *Hadronic shower* – Typically multiple pions are produced in the first few interactions, which create individual subshowers and thus contribute to the irregularity (center and right image in Fig. 4.2). Compared with a γ ray of the same energy, a hadronic cosmic ray thus produces a shower that is much more irregular (due to the subshowers), wider (due to the larger transverse momentum), and dimmer (due to energy carried away by secondary neutrinos and muons). In addition, hadronic showers contain secondary muons, which have a distinct circular signature[1] in the camera plane. For an illustration see the simulated image in the right panel of Fig. 4.2.

[1] Note that the secondary muons are useful for calibration since they produce ring-shaped images, which have approximately constant light/arclength.

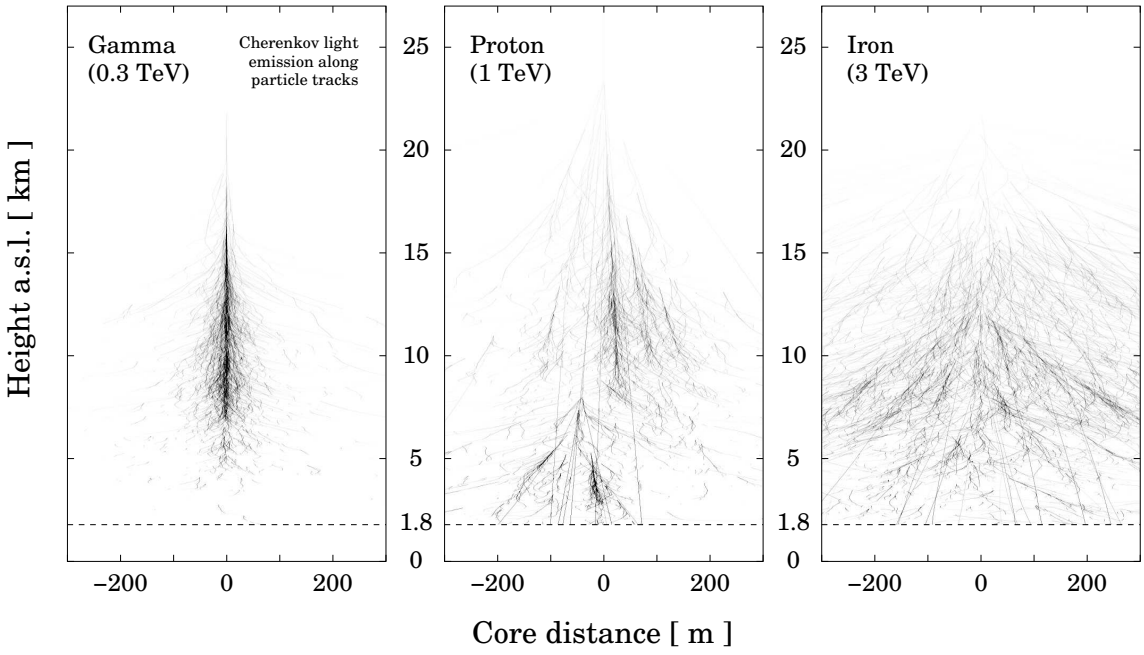

Figure 4.2: *Simulated particle cascades induced by primary γ ray (left figure), proton (centre) and iron nucleus (right figure). Shown is Čerenkov light emission along tracks of the particles. One can see that the γ-ray showers are significantly more symmetric, whereas hadronic cosmic-ray showers contain numerous subshowers (figure from Bernlöhr 2008c).*

4.2 The H.E.S.S. instrument

The H.E.S.S. experiment consists of four such IACT telescopes (see Fig. 4.1) and was described in detail in a number of works: A general description of the H.E.S.S. system can be found in Hinton (2004); The stereoscopic hardware trigger is detailed in Funk et al. (2004); The tracking of the telescopes is discussed in Bolz (2004), with further information are in Berge (2006). The instrument is thus not described in detail here and the most important instrument parameters are summarized in Tab. 4.1. Further on, we describe in a more detail the calibration procedure, data-quality checks and the analysis data-flow.

4.3 Data flow

The data flow in the experiment is depicted in figure 4.4. It can be split into the *general flow of the data* and the *analysis dataflow*. The former includes data acquisition, calibration of the data and the quality monitoring after each step, while the latter focuses on γ-ray event reconstruction. Data acquisition is described in e.g. Funk (2005b).

4.4 Calibration

Calibration is the process of conversion from raw digital counts in individual PMTs to light intensity in photoelectrons (p.e.) corrected for non-uniformity. Here, an overview of the main steps is presented. The calibration of the data in H.E.S.S. is described in further

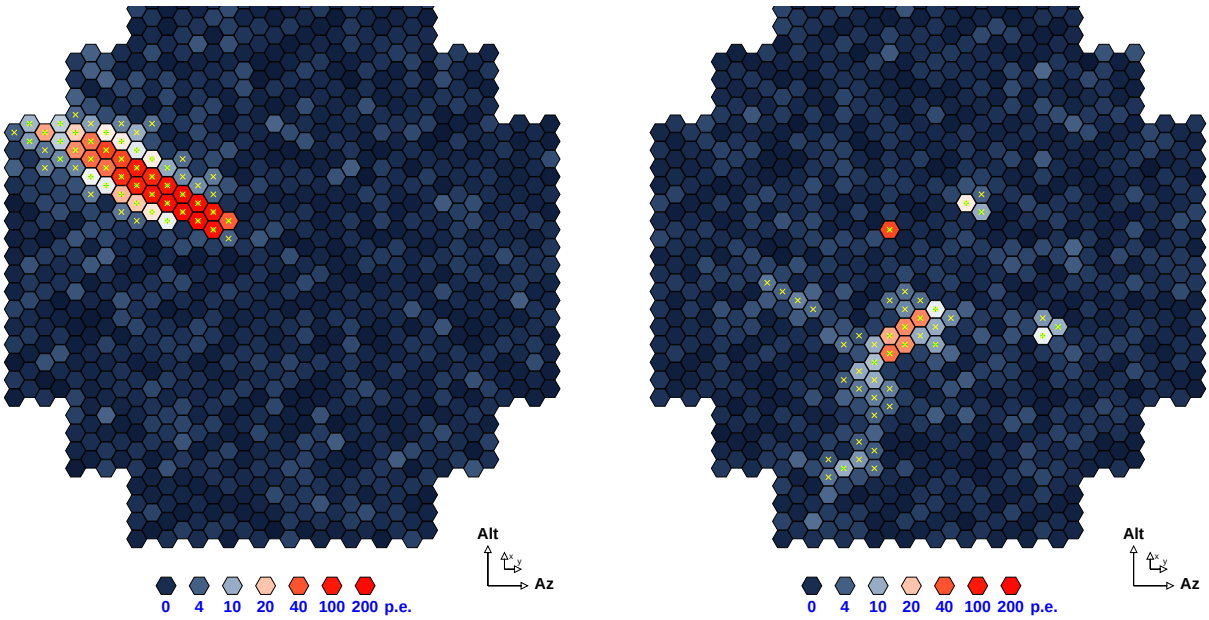

(a) Primary γ-ray, $E = 3.14$ TeV, impact 144 m from the telescope

(b) Primary proton, $E = 4.554$ TeV, impact 152 m from the telescope

Figure 4.3: *Comparison of simulated images of a γ-ray induced (left) and proton-induced (right) cascade in the atmosphere as seen by the H.E.S.S. camera. The value in each pixel corresponds to a charge measured on one PMT tube of the camera. The primary particles have a comparable energy. One can see the well-defined, symmetric image of the γ-induced EM cascade (left figure) as opposed to the scattered image of the hadronic shower induced by a proton (right figure). The hadronic shower is also noticeably dimmer, even though the energies are similar. One can also recognize a muon ring in the proton-induced image, a typical feature of a hadronic cascade.*

detail by Aharonian et al. (2004a).

During observations, the analogue signal in PMTs is integrated over a time gate of $\tau = 16$ ns and converted into digital ADC (Analogue to Digital Converter) counts ADC_i in pixel i. The raw data stored by the Data AcQuisition system (DAQ) are stored in the form of ADC counts per pixel at a given time. The following steps should assure a correct transformation of ADC counts in each pixel into the corrected signal amplitudes A in photoelectrons (p.e.):

- **Estimation of pedestals $ADC_{\mathrm{ped,i}}$:** The pedestal is defined as the mean ADC value ADC_ped in the absence of a signal and is produced by a combination of electronic voltage offsets and night-sky background (NSB) light. It is thus determined by the value of high voltage on the PMTs. The pedestal values are determined during observations from data, from which the shower images are subtracted. The pedestal value is recalculated on a regular basis, always after a fixed number of events. Additionally, dedicated *electronic pedestal* runs are used to obtained only the electronic pedestal, not containing the NSB. The fluctuations of the ADC values are Gaussian with the width depending mainly on the temperature and the NSB level.

- **Estimating conversion factor G_i between signal and ADC counts:** This

Table 4.1: *Basic parameters of the H.E.S.S. experiment*

General	
No. of telescopes	4
Location	Namibia, 23°16′18″ S, 16°30′00″ E
Altitude	1800 m asl.
Optical system (see Bernlöhr et al. 2003)	
Design of the mirror dish	Davies-Cotton[b]
Mirror dish area	107 m^2
Mirror dish radius	13 m
Mirror facet design	spherical, circular, R =60cm
Mirror facet weight	≈20 kg[c]
No. of mirror facets	380
Cameras	
Total field-of-view	5°
No. PMTs	960/Camera[a]
PMT angular size	0.16°
High gain range	0–200 p.e.
Low gain range	15–1600 p.e.
Tracking system	
Dish mount	Alt-Az
Turning range in AZM	≥385°
Elevation range	-35°–+175°
Slewing speed AZM	∼100°/min.
ALT	∼100°/min.
Pointing accuracy (van Eldik et al. 2007)	up to 6″
Maximum wind speed during operation	50 km/h
Maximum wind speed	160 km/h
Weights	
Weight of a the telescope dish structure	23.4 t
Weight of the mirrors and mirror supports	7.6 t
Weight of the camera support	3.25 t
Weight of the elevation drive rail	0.8 t
Weight of the counterweight	0.8 t

[a]PMTs are organized in 60 drawers with 16 PMTs each
[b]In the Davies-Cotton layout (Davies 1957), all mirror facets have the same focal length f and are mounted on a sphere of a radius f.
[c]Weight including the mirror support

factor, called *gain* is defined as:

$$G \equiv \left(\frac{ADC_{\text{counts}}}{\text{photoelectrons}} \right) \tag{4.1}$$

It is determined for each pixel i and is measured regularly, approximately every second observation night. The measurement is performed under a very dim illumination of the cameras, corresponding to ∼1 photoelectron per pixel per time window τ. The ADC distribution then shows two distinct peaks - one corresponding to the electronic pedestal (with no light in the integration gate, see above) and second, corresponding to one p.e. hitting the PMT within the integration time. By fitting the second peak we obtain a value $ADC_{1\text{pe}}$ (Fig. 4.5). The gain is then determined from the distance of the two peaks measured in digital counts. A third peak might also be recognized,

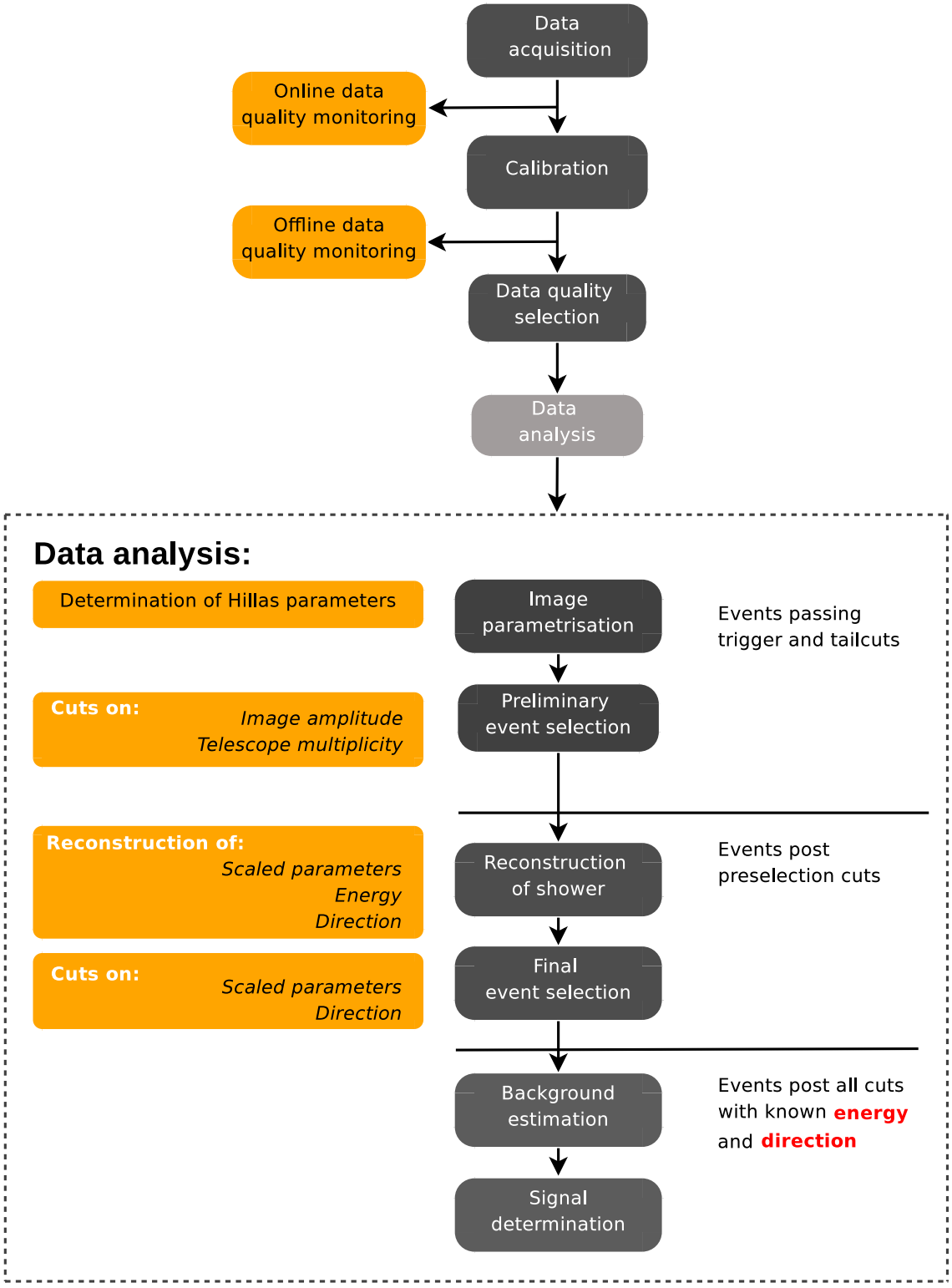

Figure 4.4: *Schematic view of the H.E.S.S.* dataflow. *The top part depicts the general data flow. The lower inset shows the data flow in the standard analysis chain, described in the text.*

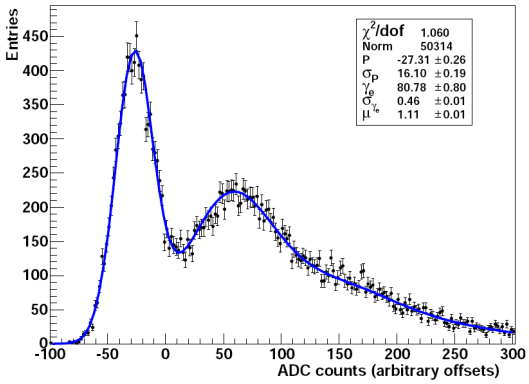

Figure 4.5: *Distribution of ADC values for a single pixel, illuminated by a dim light.*

which denotes the case of two p.e.

- **Estimating flat-fielding coefficients FF_i:** Flat-fielding is an additional procedure that guarantees a homogeneous response of the camera to a homogeneous source of light. The deviations from homogeneity occur due to different photocathode efficiencies and different optical efficiencies of individual pixels. These would otherwise not be corrected by the previous steps.

- **Pointing corrections:** This step corrects deviations from nominal pointing of the telescopes. These are caused by mechanical bending of the masts depending on the observation angle. This is corrected by a rather complicated procedure described in Braun (2007). The procedure comprises applying mechanical model, observing stars with known positions and observing projection of fixed LEDs on the camera plane from the mirror dish.

The calibration consists of other details that we omit here, including identification of defunct pixels and determination of night sky background.

The desired signal amplitude in one pixel can be then calculated as:

$$A_\mathrm{i} = \frac{ADC_\mathrm{i} - ADC_\mathrm{ped,i}}{G_\mathrm{i}} FF_\mathrm{i}, \tag{4.2}$$

where ADC_i is the value measured in one pixel i, $ADC_\mathrm{ped,i}$ is the pedestal value, FF_i flat-fielding coefficient and G_i gain.

After the calibration, data are stored in form of charge of the signal (in p.e.) per pixel per event. The data are checked to meet certain data quality criteria and can then analyzed.

4.5 Data quality

Data quality checks are an important part of the H.E.S.S. data flow. The main purpose is to identify possible problems during and after observations and also to reduce systematic

effects caused mainly by atmospheric and weather changes and further by a malfunctioning hardware. The suppression of systematic errors is crucial when striving for the best sensitivity and development of better data quality monitoring was therefore also a part of this work. The quality is monitored at several levels:

- *During observations:* Data are monitored directly by the shift crew in Namibia. The observed quantities are mainly the stability and absolute value of a trigger rate. The trigger rate is very sensitive to changes in the atmosphere and its stability is thus the most important data-quality criterium. Further, one monitors also a number of malfunctioning PMTs, weather conditions and also results of on-line analysis (Funk 2005b), which allows one to produce first preliminary results.

- *After each night:* After the end of each observation, *on-line data quality checks* are performed in order to identify hardware problems that could be repaired during the day. Work on these checks is part of this thesis and is discussed in more detail in 4.5.1.

- *After calibration:* After the calibration chain, data have to pass a given set of cuts on several hardware-related quantities. Only data passing these cuts are used for analysis.

4.5.1 On-line data quality monitoring

Each run is checked directly after it finished by a system of on-line checks. The run is calibrated using automatic preliminary calibration procedure using the most recently measured calibration coefficients. Afterwards, the run is processed using the standard analysis chain and various quality-related quantities are checked in order to identify malfunctions of individual subsystems of the telescope array. All checks are summarized in form of a web page, which is downloaded every morning to Europe (see Fig. 4.6).

4.5.2 Offline quality selection

After the data are transferred to Europe, they are calibrated using the standard calibration chain described in 4.4 and sorted based on their quality. The difference, as opposed to the on-line calibration, is that here, the various calibration coefficients are merged over an entire period to ensure full calibration of all pixels and remove problematic or erroneous calibration coefficients. The subsequent quality selection is based on a system of cuts on several indicators of malfunctioning hardware or bad atmospheric conditions. The criteria are summarized in the table 4.2.

These quality cuts were used in Aharonian et al. (2006a) for analyzing the Crab Nebula (a standard source in VHE astronomy). The resulting systematic error on determined flux was estimated to be $\sim$20%. Additionally, stricter cuts are applied when lightcurves and spectra have to be determined. The reason is that γ-detection efficiency and also the energy reconstruction rely on known atmospheric conditions. In case of too strong atmospheric fluctuations, the reconstructed flux and energies are correspondingly biased.

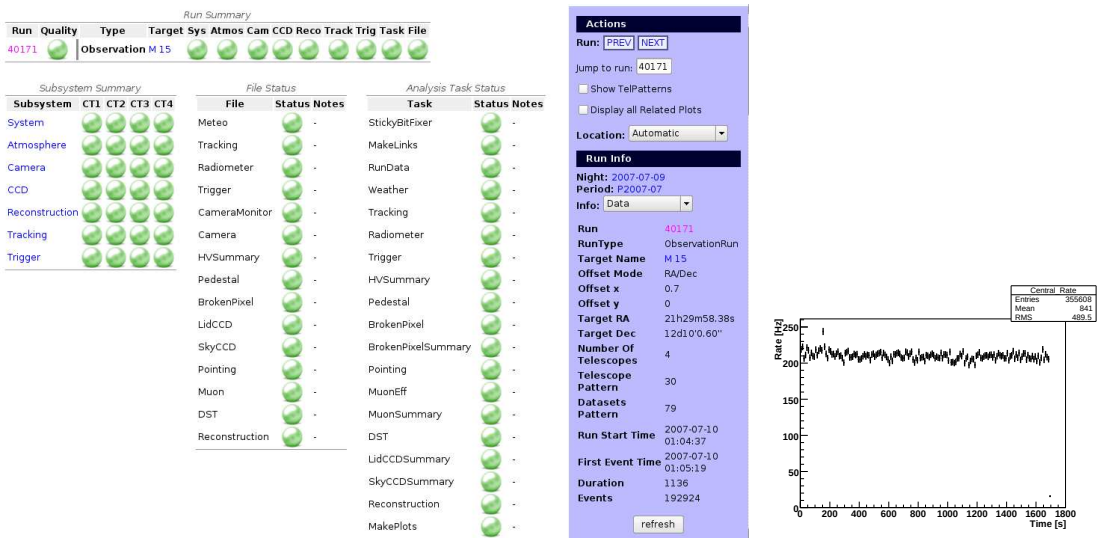

Figure 4.6: *Left: Web pages summarizing on-line data quality of a run, as processed by the automatic calibration procedure in Namibia. Right: Central trigger rate is the most important criterium for evaluating atmospheric conditions. It is a very sensitive indicator of unstable, bad weather and hazy atmosphere.*

Table 4.2: *Overview of the good data-quality selection criteria*

Quantity	Minimum value	Maximum value	Units	Affected subsystem
Run duration	10	-	min.	
RMS of the central trigger rate	0	10	Hz	Atmosphere, camera
Central trigger rate relative variation	-30	30	%	Atmosphere, camera
Number of broken pixels	0	120	pixels	Camera
Number of pixels manually turned off	0	50	pixels	Camera
Tracking deviation (alt/az)	0	10	arcsec.	Pointing
Tracking deviation (ra/dec)	0	1	arcmin.	Pointing
Fraction of dropped events	0	5	%	Camera
Participation fraction for one telescope	50	-	%	Camera

4.5.3 Observation summary

The summary of H.E.S.S. observations conducted since March 2004 is shown in Fig. 4.7. The dominant part of the observation time takes place during the dry season of Namibian winter. Short nights and rainy season complicate the observations during Namibian summer.

4.6 Analysis

In this work, the standard H.E.S.S. framework of analysis is used. This analysis chain was previously described in detail in e.g. Aharonian et al. (2006a); Funk (2005a); Berge (2002, 2006); Benbow (2005) and we thus restrain to giving only an overview of the basic analysis flow. Specific topics that are relevant for this work and were not previously published are addressed in sections 4.6.7 and in chapter 5.

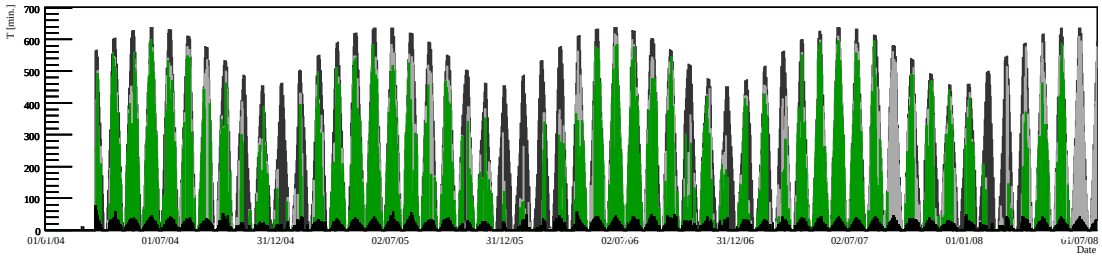

Figure 4.7: *A quantitative summary of H.E.S.S. observations starting from 21st March 2004 until 31st July 2008. The dark gray area corresponds to the total available darktime, light gray to the observation time including the transition time between runs (black color) and green area denotes good quality data passing the run selection cuts specified in 4.5.2. The seasonal trend is visible with the bad weather preventing observations during Namibian summer. Note that the transition time is estimated to be 100 s between two observation runs.*

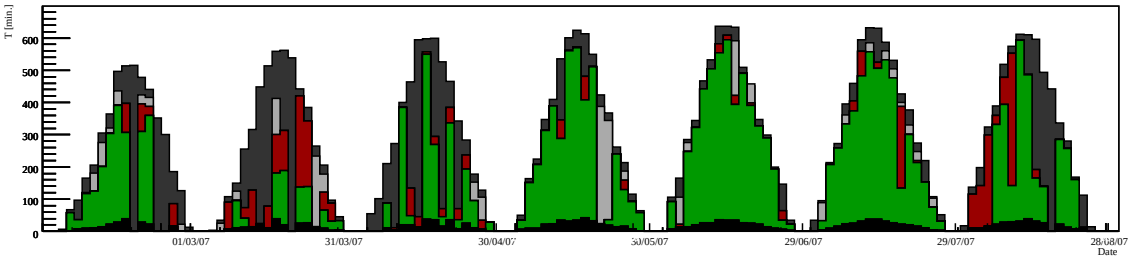

Figure 4.8: *A zoom into Fig. 4.7 showing only a part of the year 2007. Additionally, red shaded area denotes observation time of bad quality caused by bad weather conditions (haze, small clouds during observations, etc.). Light gray areas thus indicate time lost due to hardware problems, whereas red-shaded areas show time lost due to bad weather. The heights of the peaks are determined by the length of the night during given season, whereas the shapes of the peaks are determined by the phase of the moon.*

The analysis dataflow is shown in Fig. 4.4. The images in the camera plane are cleaned by a *tail-cut* procedure in order to get rid of a night-sky background (NSB) noise. The cleaned images are parametrized according to their shape and intensity (4.6.3). A set of predefined cuts is applied on the shower parameters in order to reduce the background (4.6.4). Selected images are used to reconstruct the primary direction (4.6.3) and the primary energy (4.6.5). Finally the remaining background is estimated using various background models (4.6.6). The background subtracted events are then used for calculating spectra, flux and for morphological studies.

4.6.1 Extracting images

A discriminating procedure is applied to the camera image to select only the pixels that belong to the shower image. This is performed by a *tail-cut* procedure, which keeps only pixels with more than 10 p.e. and, at the same time, neighboring pixels of more than 5 p.e — other pixels are cut away.

4.6.2 Image parametrization

The remaining image of a γ-ray induced shower can be approximately described by an ellipse and is commonly parametrized using *Hillas parameters* (Hillas 1985). The geometrical parametrization of a γ-shower image is illustrated in Fig. 4.9. The most important parameters for the H.E.S.S. analysis are:

- *Width (W)* — stands for the minor axis of the ellipse. A cut on a width-related parameter can be very efficient in background rejection because the γ-ray induced showers are significantly narrower than the hadronic showers.
- *Length (L)* — length of the major axis of the ellipse.
- *Centre of gravity (CoG)* — centre of gravity of the shower. It is calculated in the camera coordinates x and y as:

$$x_{\mathrm{cog}} = \frac{1}{A}\sum_{\mathrm{i}=1}^{N_{\mathrm{pix}}} a_{\mathrm{i}}\, x_{\mathrm{i}}, \quad \text{where } A = \sum_{\mathrm{i}=1}^{N_{\mathrm{pix}}} a_{\mathrm{i}}$$

$$y_{\mathrm{cog}} = \frac{1}{A}\sum_{\mathrm{i}=1}^{N_{\mathrm{pix}}} a_{\mathrm{i}}\, y_{\mathrm{i}},$$

  where a_{i} is amplitude of the pixel i and $(x_{\mathrm{i}}, y_{\mathrm{i}})$ are its coordinates in the camera plane.
- *Displacement (δ)* — the distance between the CoG and the reconstructed direction.
- *Amplitude (A)* — summed amplitude in all pixels in the image.

After the parametrization, the first preselection cuts are applied to reject events with less than 2 participating telescopes and with a total image amplitude lower than a specified value (depending on the set of cuts - typically in the range of 40 – 200 p.e.).

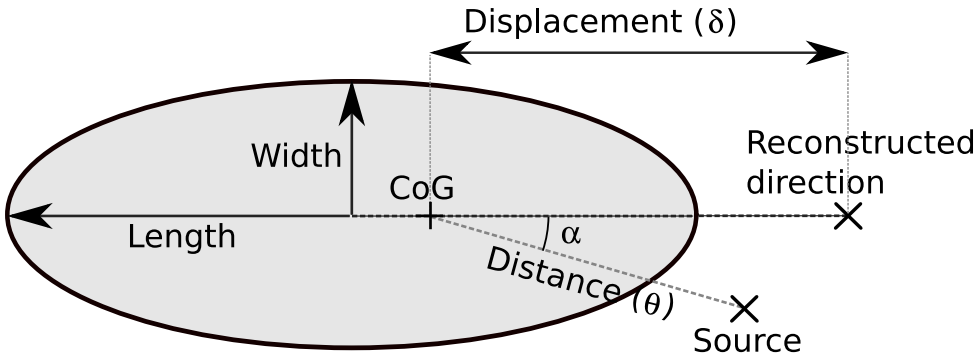

Figure 4.9: *Parametrization of the ellipse-like image of a γ-ray shower in a camera plane of an IACT. Because of the asymmetry in the intensity over the ellipse, the centre of gravity (CoG) is shifted with respect to the centre of the ellipse towards the shower direction.*

4.6.3 Shower reconstruction

In the next step, the geometric parameters of the shower image are used to reconstruct the direction of the shower and the *impact parameter* – the distance of the main shower core axis from a telescope. This parameter is very important for reconstructing the shower properties because of its strong influence on all the image parameters. Along with the image amplitude, it is used to reconstruct also the energy and additionally the *scaled shape parameters*.

Scaled shape parameters

These are entities derived from the width and the length that are later used by event selection cuts. They were introduced in order to allow one to apply one set of cuts under any observation conditions, i.e. the zenith angle θ_{Z} and target offset θ_{off}. The width and length of the observed EM shower depend on θ_{Z}, θ_{off} and on the impact parameter. These parameters are thus for each event scaled by the mean expected value for the given zenith and offset angle (calculated from simulations). As a result, a *mean reduced scaled width* are produced as:

$$MRSW = \frac{1}{N_{\mathrm{tel}}} \sum_{\mathrm{i}=1}^{N_{\mathrm{tel}}} \frac{W_{\mathrm{i}} - \langle W_{\mathrm{i}}(\theta_{\mathrm{Z}}, \theta_{\mathrm{off}}, A, IP)\rangle}{\sigma_{\mathrm{i}}(\theta_{\mathrm{Z}}, \theta_{\mathrm{off}}, A, IP)}, \tag{4.3}$$

where N_{tel} is the number of participating telescopes in the event, $\langle W_{\mathrm{i}}(\theta_{\mathrm{Z}}, \theta_{\mathrm{off}}, A, IP)\rangle$ is the mean width for the given θ_{Z}, θ_{off}, amplitude A and impact parameter (distance) IP obtained from simulations and σ_{i} is the appropriate RMS of the parameter distribution. Both of these values are stored in lookup tables, with one 2-dimensional lookup for each combination of $(\theta_{\mathrm{Z}}, \theta_{\mathrm{off}})$. In the very same way, also the *mean reduced scaled length* $MRSL$ is calculated. Note that the mean reduced scaled parameters are constructed in such way that the their value reflects the number of standard deviations, by which it differs from the expectation value for a given set of parameters; this number is averaged over the number of telescopes participating in the event.

4.6.4 Selection cuts

Several techniques exist for reducing the cosmic-ray dominated background remaining after the hardware trigger (see de Naurois (2006) for a review). In this work, a system of standard cuts on image parameters is used, as described in Aharonian et al. (2006a). Several sets of cuts were produced, each optimized for a different spectral type and γ-ray source strength. When searching for a signal from a candidate target, the set has to be defined *a priori* in order to avoid unnecessary statistical trial factors. The cuts are optimized for individual source classes by means of maximizing the telescope performance $S/\sqrt{T}$, where S is a significance of a signal. The following sets are used:

- *Standard cuts:* Optimized for a source with a flux at the level of ∼10 % of the Crab Nebula[2] and with a spectrum similar to the Crab Nebula, i.e. spectral index $\Gamma \sim 2.6$.

[2]The integral flux of the Crab Nebula as measured by Aharonian et al. (2006a) is $F_\gamma(> 1TeV) = (2.16 \pm 0.03) \times 10^{-11}\mathrm{cm}^{-2}\,\mathrm{s}^{-1}$

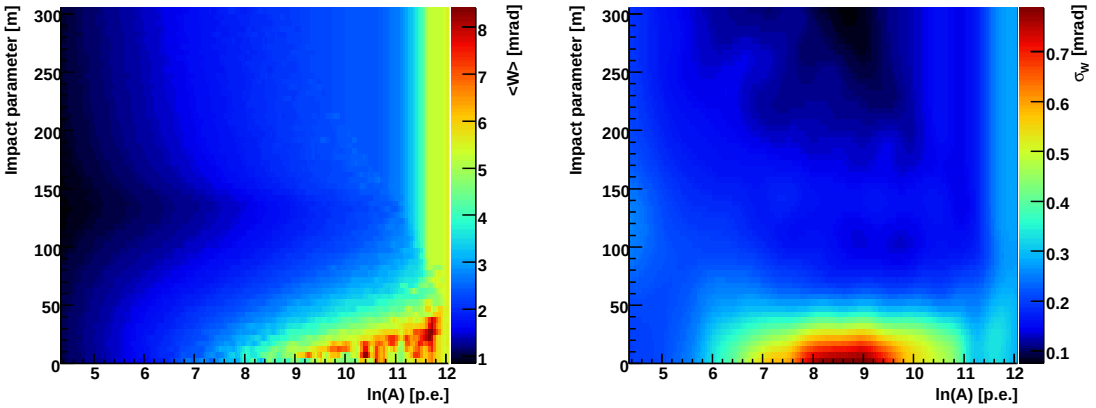

Figure 4.10: *An example of the image shape lookups. Shown are lookups of image mean width (left) and the RMS spread of the width (right) in the simulated sample of events for* $\theta_Z = 20°$ *and* $\theta_{off} = 0.5°$ *in case of standard cuts (with a cut on minimum image amplitude* $A_{min} = 80$*). The width (*W*) and its RMS (*σ_W*) are stored for each combination of* (θ_Z, θ_{off}) *in a form of 2-dimensional lookups as a function of the total image amplitude* A *and of the impact parameter. The lookups are smoothed and extrapolated in regions with low statistics.*

- *Hard cuts:* Optimized for a weak source exhibiting ∼1% flux of Crab Nebula and with a rather hard spectrum $\Gamma \sim 2.0$. Since most extragalactic sources in this work (apart from AGNs) are expected to be weak and hard, these cuts are used in the most cases. Their advantage at a cost of lower event statistics is a better angular resolution (discussed in Sec. 5.3) due to stricter cuts that reject badly defined shower images where direction reconstruction is complicated. A second advantage rests in lower systematic uncertainties due to the rejection of more background events. Their disadvantage is an increased energy threshold because of the stricter cut on the image amplitude.

- *Loose cuts:* Optimized for a strong source with an integral flux comparable to the Crab, but with a steeper spectrum of Γ ∼3.0. The steeper spectrum requires a lower energy threshold, which is achieved by lowering the cut on the image amplitude. This set of cuts is the loosest in the sense of rejecting the smallest number of events.

- *Spectrum cuts:* These additional cuts, not specified in Aharonian et al. (2006a), are optimized for weak sources with a soft spectrum of $\Gamma \sim 3.0$. They are thus usable for weak AGNs.

The cuts are specified in Tab. 4.3. The difference in sensitivity for the different sets of cuts is discussed in section 5.1.

4.6.5 Energy reconstruction

In order to estimate energy E_0 of a primary γ ray, IACTs use the atmosphere is a calorimeter. In the simple Heitler model, $E_0 \propto N_{max}$, where N_{max} is the number of particles in the maximum of the electromagnetic shower in the atmosphere. Therefore also the shower luminosity of the Čerenkov light $F_{\check{C}}$ is proportional to the energy E_0. The integrated

Table 4.3: *Event selection cuts optimized for different types of sources (see the main text).*

Cuts	$N^a_{\rm tel}$	$MRSL$ [mrad]	$MRSW$ [mrad]	$\theta^{2(b)}$ [deg.^{2}]	A^c [p.e.]	$D^d_{\rm loc}$ [m]
standard	2	$(-2.0, 2.0)$	(-2.0, 0.9)	<0.0125	>80	<0.525
hard	2	$(-2.0, 2.0)$	(-2.0, 0.7)	<0.01	>200	<0.525
loose	2	$(-2.0, 2.0)$	(-2.0, 1.2)	<0.04	>40	<0.525
spectrum	2	$(-2.0, 1.3)$	(-2.0, 0.9)	<0.02	>40	<0.525

[a]Number of telescopes participating in an event
[b]Angular distance of the event from the source position
[c]Total image amplitude in photoelectrons
[d]Distance of the image CoG from the centre of the field of view in the camera plane. Angular distance corresponding to 0.525 m is $\theta_{\rm D} = D_{\rm loc}/f = 2.0^\circ$.

image amplitude IA measured by an IACT thus depends in the first order only on E_0 and on the impact parameter (defined as the distance between a telescope and the shower core). The dependency on E_0 is to a good approximation linear, as can be seen in Fig. 4.12. The energy is therefore reconstructed using two-dimensional lookup histograms. For each telescope and selected zenith angles and offsets, a lookup was produced with energy as a function of image amplitude and impact parameter (see Fig. 4.11). The energy is interpolated between the closest values of zenith and offset angle.

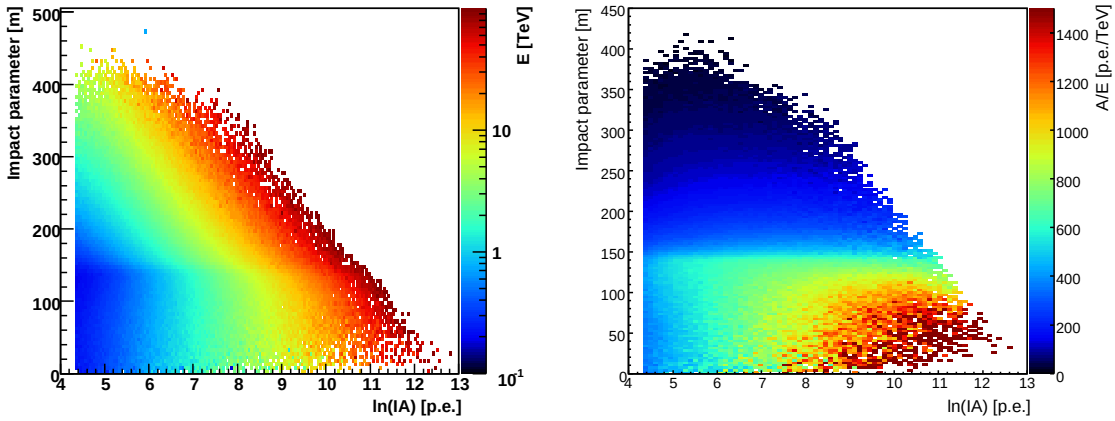

Figure 4.11: Left: *Two-dimensional lookup used for reconstructing energy of an event with a given zenith angle (20 deg. in this case), offset (0.5 deg. in this case), image amplitude (size in p.e.) and impact distance. The plot was produced using MC events passing standard cuts. True energy and impact distance and reconstructed image amplitude are plotted. Before using the lookup, it is smoothed and extrapolated (see Berge 2006).* **Right:** *A modified lookup for IA/E_0 is smoother than in the left panel.*

There are several remarkable characteristics of the energy reconstruction:

- The energy E_0 is approximately independent of the impact distance within the Čerenkov light pool (up to distances ∼150 m). This is caused by the fact that the intensity of Čerenkov light is approximately homogeneous in the Čerenkov light

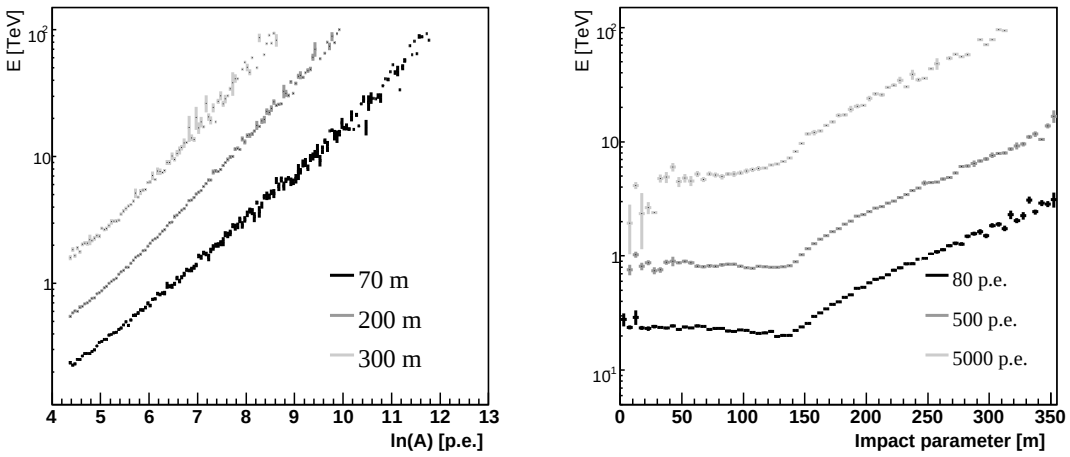

Figure 4.12: Left: *True energy as a function of image amplitude A for a fixed impact parameters of 70, 200 and 300 m. One can see that the energy is to a good approximation proportional to the image amplitude (standard cuts, θ_Z=20° and $\theta_{off} = 0.5°$.* **Right:** *Energy dependence of images of fixed amplitudes 80, 500 and 5000 p.e. The Čerenkov shoulder is obvious as a qualitative transition at the distance ∼150 m. It is possible to see that within the Čerenkov light pool, low-energy showers dominate, whereas beyond the shoulder only high-energy events trigger the array. The errors in both figures are errors of the mean value.*

pool and then falls off rapidly .

- Because of the linear dependency of the function $E_0(IA)$, it is reasonable to use a lookup for values IA/E_0. The lookup is then used only for correcting the non-linearities in the $E_0(IA)$ dependency and to resolve the impact distance dependency (see Fig. 4.11).

Estimating error of the energy reconstruction

Energy estimation is tested on simulated Monte Carlo events. For each event of a given (simulated) energy E_{true}, the energy E_{reco} is reconstructed using the energy lookups described above. The result is shown in Fig. 4.13. The top left figure illustrates that the energy reconstruction performs well over an energy range of approximately two decades (≈0.3–30 TeV, but strongly depending on the set of cuts and zenith angle). The regions around the energy threshold E_{th} and at the highest energies are problematic however. All shower images are subjected to fluctuations caused mainly by atmosphere and may lead to wrong shower reconstruction. The fluctuations follow approximately Gaussian distribution (see the both right panels of Fig. 4.13) and are thus symmetric for energies far from E_{th} and below the highest energies. In this energy range, the mean reconstructed energy $\langle E_{reco} \rangle$ equals to the true energy E_{true}. Around E_{th} only the events subjected to upward fluctuations of an image amplitude are selected, and hence a positive bias is created, that $\langle E_{reco} \rangle > E_{true}$. An inverse effect occurs at the highest energies, causing $\langle E_{reco} \rangle < E_{true}$. This is illustrated in the top right and bottom left panel in Fig. 4.13.

From the bottom right panel of the figure, one can see that the spread of the reconstructed energies above $E_{\rm safe}$ is at the order ≈10%. For larger zenith angles the energy reconstruction error is slightly higher. In (Aharonian et al. 2006a), it is estimated to be ≈15% for $\theta_{\rm Z} = 50°$.

Safe energy threshold

In order to avoid the high energy bias at the lowest energies, a *safe energy threshold* $E_{\rm safe}$ is introduced, which is later used for a spectrum determination. $E_{\rm safe}$ is defined in such way that the energy bias in the simulated sample is less than 10%. The safe energy threshold is shown in Fig. 4.13 and further in the text compared to the instrument energy threshold in Sec. 5.2.2.

4.6.6 Signal determination

After the applying the selection cuts mentioned above, the signal/background ratio is improved to ∼10/1 for *standard cuts* in case of a strong Crab-like γ-ray source. For weaker sources, this ratio is proportionally worse. The remaining background consists at energies >100 GeV predominantly of cosmic-ray hadronic showers. The γ-ray excess (i.e. the signal) is then determined as:

$$N_\gamma = N_{\rm ON} - \alpha N_{\rm OFF}, \tag{4.4}$$

where $\alpha = \frac{\rm Exp_{ON}}{\rm Exp_{OFF}}$ is a ratio of exposures at the ON and OFF regions and $N_{\rm off}$ is the estimate of the background remaining after the cuts. Exposure is in this case defined as the expected number of γ-ray events during a dead-time-corrected observation time T in a region Ω of the field-of-view:

$$\mathrm{Exp} = \int_\Omega \mathrm{d}S \int_0^T \mathrm{d}t \int_0^\infty \mathrm{d}E\, A_\gamma(r, \phi, E), \tag{4.5}$$

where $A_\gamma(r, \phi, E)$ is the acceptance of the system for a γ-ray like event with a reconstructed energy E at a given position (r, ϕ) of the field-of-view. By "γ-ray like" is meant any event (i.e. also cosmic-ray event) that passes the event-selection cuts and is thus a part of the post-selection background. Also note that the reconstructed reconstructed energy of such (e.g. hadronic) events can be substantially different from the true energy of the primary particle because of the lower photon yield of hadronic showers.

The acceptance is typically modeled *a priori*, based on a set of observation runs with no γ-ray source in the field-of-view. Since an accurate determination of the instrument acceptance is one of the crucial factors in analyzing weak sources, the topic is further discussed in section 4.6.7.

The statistical significance of the signal is then determined using a formula by Li & Ma (1983):

$$S = \sqrt{2}\left\{ N_{\rm on} \ln\left[\frac{(1+\alpha)N_{\rm on}}{\alpha(N_{\rm on}+N_{\rm off})}\right] + N_{\rm off} \ln\left[\frac{(1+\alpha)N_{\rm off}}{N_{\rm on}+N_{\rm off}}\right]\right\}^{1/2}. \tag{4.6}$$

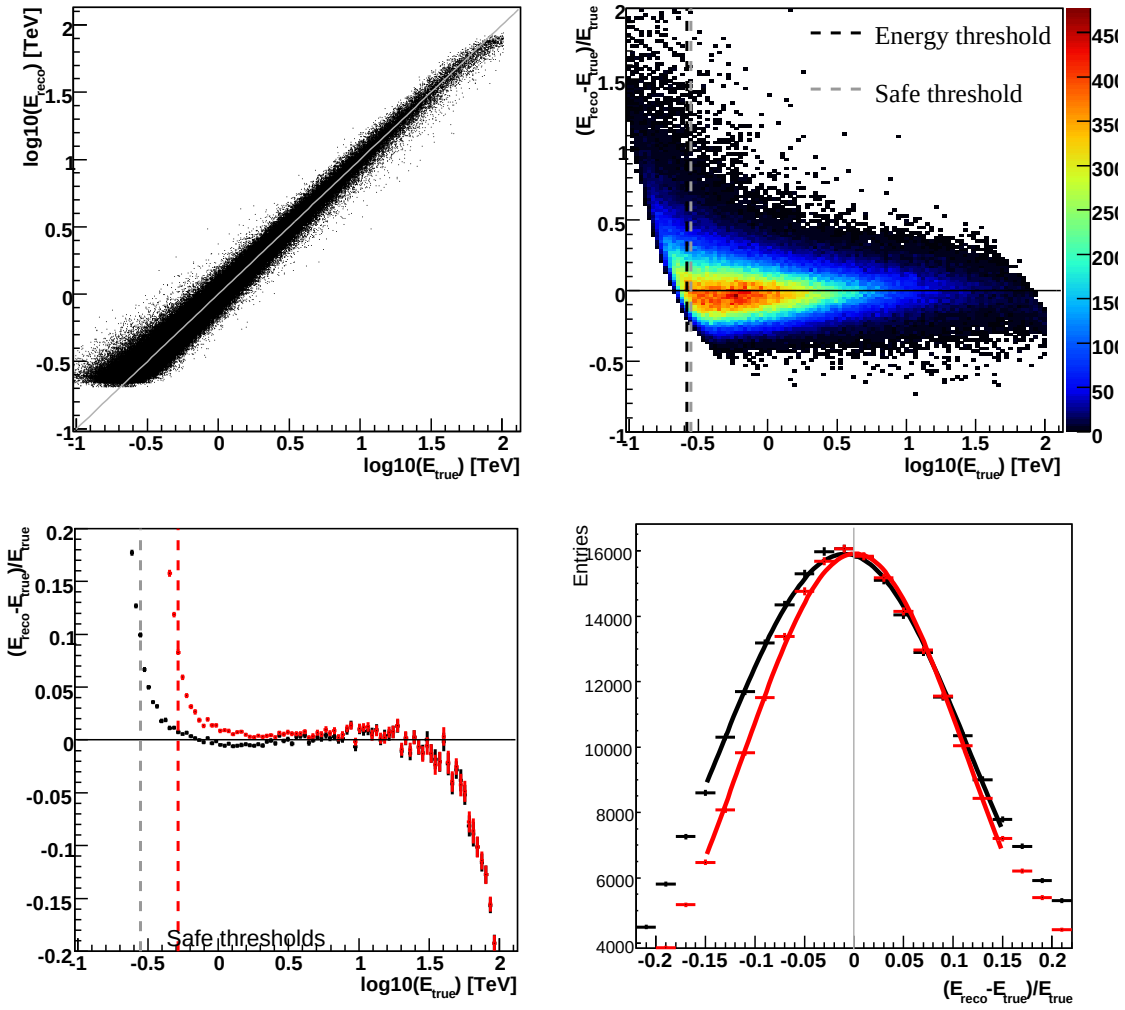

Figure 4.13: *Left top panel: A scatter plot showing reconstructed energy vs. true energy as simulated by a Monte Carlo (standard cuts, $\theta_Z = 20°$, $\theta_{off} = 0.5°$). Right top panel: A scatter plot that shows residuals $\Delta_E = (E_{reco} - E_{true})/E_{true}$ corresponding to the energy bias. It can be seen that the reconstructed energy at low energies exhibits a positive bias and at high energies a negative bias as expected(see the main text). Bottom left panel: The mean residuals as a function of a true energy for events post cuts. Bottom right panel: A distribution of the residuals Δ_E only for events within the safe energy range (i.e. where the mean bias is less than 10%). A Gaussian is fitted to the distribution. The fitted mean is $(-10.7 \pm 0.4) \times 10^{-4}$ (resp. $(-9.4 \pm 0.5) \times 10^{-3}$) for standard (resp. hard cuts) and the fitted RMS is $(12.9 \pm 0.2)\%$ ($(11.4 \pm 0.1)\%$)*

Contrary to the widely used relation $S = (N_{on} - \alpha N_{off})/\sqrt{N_{on} + \alpha^2 N_{off}}$, it can be also used for low statistics down to $N_{on}, N_{off} \gtrsim 10$ (Li & Ma 1983).

Background modeling

The remaining background N_{OFF} in equation 4.4 is modeled by several possible techniques. In the past (see e.g. Weekes et al. 1989), it was estimated using dedicated off-source runs

with and empty field of view that had to be taken under the same conditions as the on-source runs. This technique is commonly referred to as an *on-off background estimation*. The clear disadvantage is firstly a need for twice as much observation time, and secondly also increased systematic errors introduced by combining two different datasets.

Instruments with a large FOV, such as H.E.S.S. (5°), allow for the estimation of the background from the same FOV where the observed target is located. The observations are typically performed in a *wobble mode* with the source being at a specified offset θ_{off} (0.5–0.7°) from the centre of the FOV. The background is then estimated using one of the following methods (see Berge et al. (2007) for details):

- **Ring region method** - the background is estimated from a ring-shaped region around the assumed target position (see Fig. 4.14 for schematic illustration). This method is suitable for scanning FOV for serendipitous discoveries and producing skymaps. It is however not suitable for producing spectra, because the acceptance is strongly dependent on energy.

- **Reflected regions method** - the background is estimated from a series of circular regions, located at the same offset from the center of the FOV as the ON region. The advantage is that the method completely avoids using any acceptance models. Assuming that acceptance $A_\gamma(r, \phi)$ is radially symmetric, $A_\gamma(r)$ is then identical for all the ON and OFF control regions. α then depends solely on the number of OFF regions n: $\alpha = 1/n$. Hence there are no systematic errors arising from inaccurate acceptance modeling. An exception occurs, when runs with a different α are combined. Some method of wighted averaging of the α has to be then employed.

- **Template background model** - this method selects background events based on the properties of the shower images. Events with a high absolute value of $MRSW$ and $MRSL$ are used as a background.

- **Field-of-view background model** - the background normalization $Norm_{\mathrm{OFF}}$ is estimated from source-free regions of the field of view. The OFF signal at any point is then estimated using the model acceptance curves normalized to $Norm_{\mathrm{OFF}}$

In this work, the *ring region method* is used for producing skymaps and significance maps and the *reflected region method* is used to determined the γ-ray signal at a given position and for determining flux, spectra and upper limits.

4.6.7 Instrument acceptance

Camera acceptance represents a measure of how the telescope system is sensitive in different regions of the FOV. It is implicitly defined by equation (4.5). A precise knowledge of the acceptance is needed for background estimation (with the exception of the *reflected region method* - see section 4.6.6). It is critical especially at the outer regions of the FOV during very long exposures. It is important e.g. for the analysis of galaxy clusters with their very large extensions with diameters up to ∼3°. A biased acceptance model yields in such cases a systematic under- or overestimate of the background, leading to possible false signals. A careful control of the systematic effects influencing the acceptance is thus desirable.

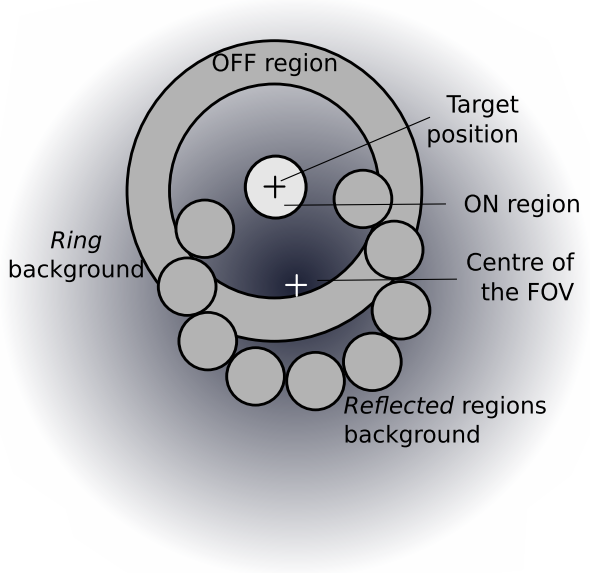

Figure 4.14: *A schematic illustration of a construction of the* ring *and* reflected *regions used for estimating the background. The system acceptance is schematically illustrated by the color gradient, falling off rapidly at the edges of the field-of-view (note that the gradient serves only for illustration and follows the true acceptance only approximately). One can see how the control regions of the* reflected *method are placed on a circle of a constant acceptance, contrary to the* ring *control region.*

The acceptance — as defined in eq. (4.5) — can generally depend on the zenith angle, energy, angular distance ψ from the pointing position and azimuth ϕ of the event. Zenith angle and energy dependence is investigated in 4.6.7. The azimuthal dependence can be neglected, as shown by e.g. Berge (2006). For one observation run of a given zenith angle and energy threshold, it is thus important to model precisely the functional dependence of acceptance on ψ. The function $A(\psi)$ describing this dependence is further called *radial acceptance*.

In this section, we first describe the production of model acceptance curves. Afterwards, we investigate the effect of aging of the system, possible azimuthal asymmetries, dependency on energy and multiplicity.

Modeling γ-ray acceptance of the system

Acceptance modeling comprises producing radial acceptance curves (see section 4.6.7) for individual observation runs and generating from these acceptance maps for a complete dataset. There are two principle approaches employed in modeling the acceptance: producing parameter dependent *lookups* and producing the acceptance curve *during the analysis*. Each method is suitable for a different type of dataset and will be discussed in the following.

Radial acceptance lookups

For each zenith angle band, a radial lookup $A(\psi)$ is produced. The lookups are produced using OFF-source observation data with no hint of a γ-ray signal. For each event passing the appropriate (standard, hard, ...) γ-ray cuts, the angular distance ψ from the obser-

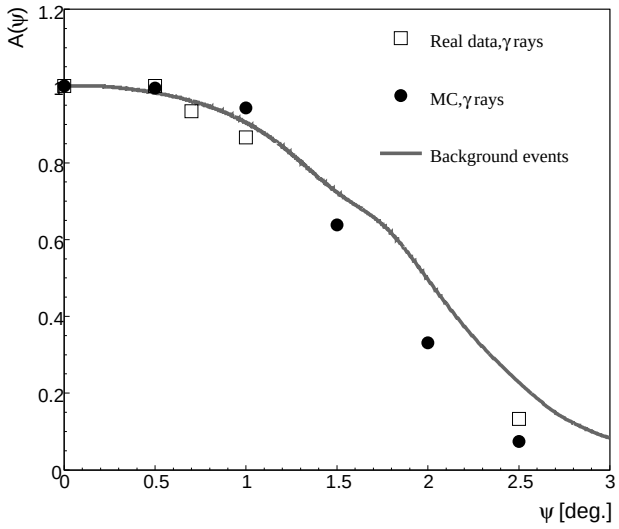

Figure 4.15: *Radial acceptance of the system for real data (Crab Nebula observations), Monte Carlo simulations and for background γ-like events post selection cuts. The background acceptance is determined using OFF-source runs with no contamination from γ-ray sources.*

vation position is determined and filled into a distribution $A_{\mathrm{B}}(\psi)$. The background in OFF-runs is assumed to be isotropic and therefore homogeneously distributed over the FOV. The resulting distribution thus corresponds to the acceptance of the system to a γ-like background.

Table 4.4: *Zenith angle bands used for producing the radial acceptance lookups*

θ_{ZA}	Events (post std. cuts)	Events (post hard. cuts)
0—20	2 235 640	290 113
20—30	1 742 820	262 208
30—40	1 681 290	261 019
40—45	554 220	87 394
45—55	708 033	115 625
55—90	236 957	39 307

For the production of the lookups, 926 OFF runs were used with the total livetime of 392.4 h. In order to optimize for the statistics, the acceptance curves are produced for zenith angle bands specified in the table 4.4. For each event, the zenith angle θ_{ZA} is determined and the ψ is then filled into a lookup for a zenith angle range containing θ_{ZA}.

γ-ray and background acceptance

The acceptance of the system to γ rays and γ-like background is generally different. The Fig. 4.15 shows that the background acceptance is flatter than the one of γ rays.

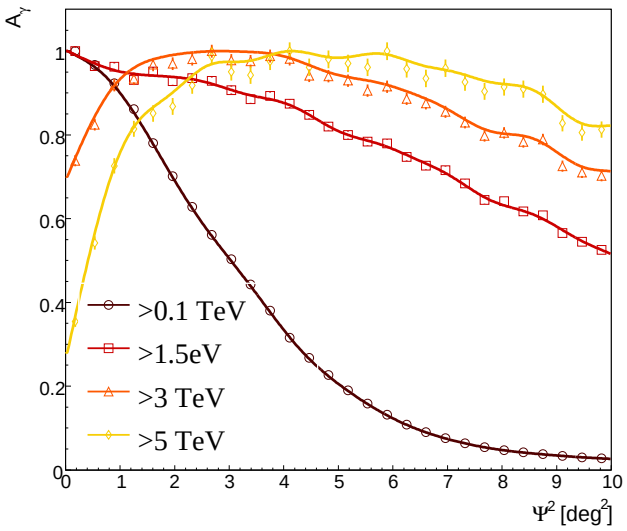

Figure 4.16: *Energy dependence of background radial acceptance curves for standard cuts and zenith angle 0-20°. One ca seen that the acceptance tends to be flatter and broader towards higher energies. At energies $\gtrsim 2$ TeV, the peak of the curve shifts from the center of the FOV.*

Energy dependence

The response of the instrument varies with the energy of an observed γ ray. The behavior is determined by the different image sizes and core distances. Showers of lower energies trigger the array typically at small impact distances. The images are, in the "nominal" coordinate system (system wide camera plane), closely concentrated around the projected cosmic-ray direction. Probability P that the core distance will be ψ degrees rapidly decreases with r. High energetic showers can trigger the system also at larger impact distances with core distance being typically higher. The probability of a shower core being further from the center of the FOV is thus higher and the $P(\psi)$ function is thus flatter. This behavior is shown in Fig. 4.16.

4.6.8 Spectrum determination

Once the number of on-source events N_{on} and background events N_{off} is determined and their energies are known, we can calculate the spectrum of an observed source. The spectrum determination in H.E.S.S. is well described in e.g. Berge (2006); Aharonian et al. (2006a). Only an overview is thus presented here.

A differential γ-ray spectrum is commonly defined as the number of particles per area, time and energy, i.e.:

$$F(E) = \frac{1}{A_{\mathrm{eff}}(E)} \frac{\mathrm{d}^2 N_\gamma(E)}{\mathrm{d}E\,\mathrm{d}t}, \tag{4.7}$$

where $N_\gamma(E)$ is a γ-ray excess at energy E and $A_{\mathrm{eff}}(E)$ is the effective area of the instrument, determined using Monte Carlo simulations[3]. The effective areas are further studied

[3]Effective area is here defined as a convolution of the instrument collection area and the efficiency of

in more detail in Sec. 5.2. The determination of the differential spectrum is however complicated by the non-ideal energy reconstruction. In principal, the measured differential γ-ray rate is a convolution of the source flux at the true energy $E_{\rm true}$ and of the probability $P(E_{\rm true}, E_{\rm reco})$ that an event of energy $E_{\rm true}$ is reconstructed with energy $E_{\rm reco}$. Thus:

$$\frac{\mathrm{d}N(E_{\rm reco})}{\mathrm{d}E_{\rm reco}} = \int_0^\infty P(E_{\rm true}, E_{\rm reco})\, A_{\rm eff}(E_{\rm true})\, F(E_{\rm true})\, \mathrm{d}E_{\rm true} \tag{4.8}$$

The inversion of the equation to obtain the $F(E_{\rm true})$ is complicated and the spectrum in this work is hence determined using effective areas as a function of the reconstructed energy $E_{\rm reco}$ as:

$$F(E_{\rm reco}) = \frac{1}{A_{\rm eff}(E_{\rm reco})} \frac{\mathrm{d}^2 N_\gamma(E_{\rm reco})}{\mathrm{d}E_{\rm reco}\, \mathrm{d}t}. \tag{4.9}$$

It was shown by e.g. Berge (2006) that this is a good approximation within the quoted systematic errors.

In practice, the spectrum is determined in a following way. Only events above the safe threshold $E_{\rm safe}$ are considered, which have energy bias of $< 10\%$ (see Sec. 4.6.5). The events with energy $E > E_{\rm safe}$ are sorted into energy bins of widths $\Delta E_{\rm i}$, where i denotes the i-th bin. For each energy $E_{\rm i}$ corresponding to the i-th energy bin and for each event, an appropriate effective area $A_{\rm eff}(E_{\rm i,reco})$ is determined as a function of a reconstructed energy (see also section 5.2). Both the ON and the OFF-events are then weighted by the correct effective areas, by the observation time T and by the bin width. This yields:

$$\frac{\mathrm{d}N(E_{\rm i})}{\mathrm{d}E} = \frac{1}{T \Delta E_{\rm i}} \left(\sum_{\rm j=1}^{N_{\rm ON}} \frac{1}{A_{\rm eff}(E_{\rm j})} - \alpha \sum_{\rm k=1}^{N_{\rm OFF}} \frac{1}{A_{\rm eff}(E_{\rm k})} \right), \tag{4.10}$$

which is the underlying spectrum of the source.

4.6.9 Upper limits calculation

In case of no significant signal, an upper limit can be determined. In this work, we adopt an approach used by previous H.E.S.S. works, such as Aharonian et al. (2005a); HESS Collaboration: F. Aharonian (2008). In this approach a primary γ-ray spectrum of a power-law type is assumed:

$$F(E) = I_0 \left(\frac{E}{E_0} \right)^{-\Gamma}, \tag{4.11}$$

where Γ is a fixed input parameter, estimated a priori. The task is now to determine the normalization I_0. To do this, we first examine the number $N_\gamma(> E_{\rm min}; I_0, T)$ of expected γ-ray photons above energy $E_{\rm min}$ detected by H.E.S.S. for a given normalization I_0 during an observation live-time T. This value can be estimated as:

$$N_\gamma^{exp}(> E_{\rm min}; I_0, T) = \int_{\rm E_{min}}^\infty \mathrm{d}E \int_0^T \mathrm{d}t\, F(E)\, A_{\rm eff}(E, t), \tag{4.12}$$

selection cuts.

where $A_{\rm eff}(E,t)$ is time-dependent, because the dataset typically includes several different zenith angles.

The number of expected γ rays is to be compared to an upper limit on the γ-ray excess count $N_\gamma^{UL}(>E_{\rm min},T)$, obtained in an observation of a duration T. The N_γ^{UL} is calculated at a given confidence level from the measured number of ON counts $N_{\rm ON}$, OFF counts $N_{\rm OFF}$ and α. This is performed using a method developed by Feldman & Cousins (1998), which assures a proper coverage of confidence intervals.

For a given upper limit on $N_\gamma^{UL}(>E_{\rm min};T)$, we can derive an upper limit on the normalization I_0 by comparing $N_\gamma^{UL}(>E_{\rm min};T)$ to the expected number of γ-rays for the normalization equal to unity, i.e.:

$$I_0^{UL} = \frac{N_\gamma^{UL}(>E_{\rm min};T)}{\int\limits_{\rm E_{min}}^{\infty} {\rm d}E \int\limits_0^T {\rm d}t \, \left(\frac{E}{1TeV}\right)^{-\Gamma} A_{\rm eff}(E,t)} \tag{4.13}$$

The upper limit on the integral flux above energy $E_{\rm min}$ can be then calculated as:

$$F_{\rm UL}(>E_{\rm min}) = I_0^{UL} \int\limits_{\rm E_{min}}^{\infty} \left(\frac{E}{1\ {\rm TeV}}\right)^{-\Gamma} {\rm d}E \tag{4.14}$$

Chapter 5

Sensitivity of the instrument

A substantial part of this work is dedicated to estimating observability of VHE γ rays with H.E.S.S. and to calculating upper limits in case of a non-detection. For these tasks, it is critical to understand the sensitivity of the instrument, which is discussed in this chapter.

The chapter introduces the general notion of sensitivity and the relevant sensitivity-related relations in section 5.1. It is shown how sensitivity depends on the angular resolution, the instrument effective area and on source extension. The production and properties of effective areas are further described in section 5.2, and are followed by a discussion of the H.E.S.S. angular resolution in section 5.3. In section 5.4, the H.E.S.S. sensitivity is shown for various selection cuts

5.1 Sensitivity

A sensitivity is defined as the minimum flux Φ required for a detection of a γ-ray signal N_γ at a given confidence level. Instead of the confidence level, a significance S is often used, expressed in units of standard deviations σ. The sensitivity thus corresponds to a minimum measured signal N_γ that can be resolved from a measured background N_B with a given significance $S = N_\gamma/\sigma_\mathrm{B}$, where σ_B is the standard deviation (RMS spread) of the background. In case that N_B follows Poisson statistics, the noise is estimated as $\sigma_\mathrm{B} = \sqrt{N_\mathrm{B}}$ and $S = N_\gamma/\sqrt{N_\mathrm{B}}$. The minimum signal $N_{\gamma,\mathrm{min}}$ necessary for a detection at a confidence level of S standard deviations is then $N_{\gamma,\mathrm{min}} = S\sqrt{B}$. In astroparticle physics, the required significance of the signal for claiming a detection is 5 σ. The reason for such a conservative requirement is twofold: due to the number of trials[1] and due to partly unknown systematic errors of the relatively young technique.

The background B for IACT arrays is dominated by hadronic cosmic rays and is to a good approximation isotropic over the field-of-view and constant in time (for constant observation conditions, i.e. a constant zenith angle and atmospheric conditions). It scales therefore linearly with the solid angle Ω, over which the signal is integrated and with the observation time T. For a circular integration region of radius θ, the background

[1] Every time in the history of VHE γ astronomy when a target is investigated for a signal, means a trial factor. With an increasing number of these trials, the probability rises that one source would reach e.g. 3σ value statistically by a chance. This probability is, however, negligible when the 5σ significance level is adopted.

$B \propto \pi\theta^2\, T\, F_\mathrm{B}\, \epsilon_\mathrm{B}\, A_\mathrm{col}$, where F_B is the incident background flux, ϵ_B is a detection efficiency of a background event and A_col is the collection area of the telescope system.

A VHE signal N_γ coming from a cosmic object of a flux F_γ and measured by the telescope system depends on the γ-ray detection efficiency ϵ_γ, observation time T and collection area A_col. From this, the significance of an observed signal can be expressed as:

$$S = \frac{N_\gamma}{\sqrt{N_\mathrm{B}}} = F_\gamma \epsilon_\gamma \sqrt{\frac{T\, A_\mathrm{col}}{F_\mathrm{B}\, \epsilon_\mathrm{B}\, \Omega}} \tag{5.1}$$

The sensitivity Φ, corresponding to a minimum flux F_γ detected at a significance level of $S = 5\sigma$ is then:

$$\Phi_{5\sigma} = \frac{1}{5} \frac{\sqrt{\epsilon_\mathrm{B}}}{\epsilon_\gamma} \sqrt{\frac{\Omega\, F_\mathrm{B}}{T\, A_\mathrm{col}}} \tag{5.2}$$

Note that instead of the collection area, the term *effective area* is often used, which also includes the selection efficiency of the events $A_\mathrm{eff} = \epsilon\, A_\mathrm{col}$.

From eq. 5.2, one can infer several ways of improving the sensitivity of a telescope system:

- Increasing the *quality factor* $Q = \epsilon_\gamma / \sqrt{\epsilon_\mathrm{B}}$, i.e. increase of the background rejection while keeping the γ-ray detection efficiency high enough. In H.E.S.S., this is achieved on two levels: hardware and software. In the hardware level, this is accomplished mainly using a central trigger, which dramatically reduces the dominant background of CR muons and also rejects the night-sky background (NSB) events (Funk et al. 2004). The software level increases the quality factor by incorporating the system of event selection cuts described in section 4.6.4.

- Reduction of the integration region Ω. This effectively means reducing the *angular resolution* θ_res. Note that the minimum detectable flux Φ is directly proportional to ${\theta_\mathrm{res}}^2$. The angular resolution of the H.E.S.S. instrument is described in this chapter in section 5.3.

- Increasing the *effective area* A_eff. The production and various characteristics of effective areas in case of the H.E.S.S. instrument is described in section 5.2.

- Increasing the *observation time* T. The maximum achievable time is however limited by two factors: Due to the limited amount of a usable time (∼1000 hours per year – see section 4.5.2), the feasible observation time on one target is $\lesssim$ 100 hours. When 100 hours are reached, an improvement by a factor of two in the sensitivity would require an enormous amount of total observation time (400 hours). The second factor limiting the observation time is related to systematic errors due to unresolved hardware and weather problems, which make very long observations of weak sources very challenging. The experience of a qualitatively similar experiment HEGRA shows that the maximum time reasonable for an analysis of one source is $\lesssim$ 200 hours — the approximate time necessary for HEGRA to claim evidence for a signal from Cassiopeia-A (Aharonian et al. 2000).

[2] Note that a higher value of the minimum detectable flux Φ means worse (lower) sensitivity.

5.1.1 Sensitivity in the case of extended sources

Let Φ_0 be the sensitivity of the instrument in case of a *point source*, which is a source with an angular radius $\theta_{\rm src}$ smaller than the instrument angular resolution $\theta_{\rm res}$. The measured radial angular distribution of the emission from a point source is referred to as a *point-spread-function* (PSF). For moderate source sizes, the minimum detectable flux increases by the ratio $\theta_{\rm src}^{\rm obs}/\theta_{\rm res}$, where $\theta_{\rm src}^{\rm obs}$ is an effective source size as measured by the instrument. The effective source size is equal to a convolution of the intrinsic angular distribution of the source emission and the instrument PSF. Assuming that both can be approximated by a Gaussian function, the effective observed source size is $\theta_{\rm src}^{\rm obs} = \sqrt{\theta_{\rm src}^2 + \theta_{\rm res}^2}$, and the extended-source sensitivity can be estimated as:

$$\Phi_{\rm ext} \approx \Phi_0 \frac{\sqrt{\theta_{\rm src}^2 + \theta_{\rm res}^2}}{\theta_{\rm res}} \tag{5.3}$$

The dependency is illustrated in Fig. 5.1 for a case of angular resolution $\theta_{\rm res} = 0.07°$and a point-source sensitivity $1 \times 10^{-13}{\rm cm}^{-2}\,{\rm s}^{-1}$.

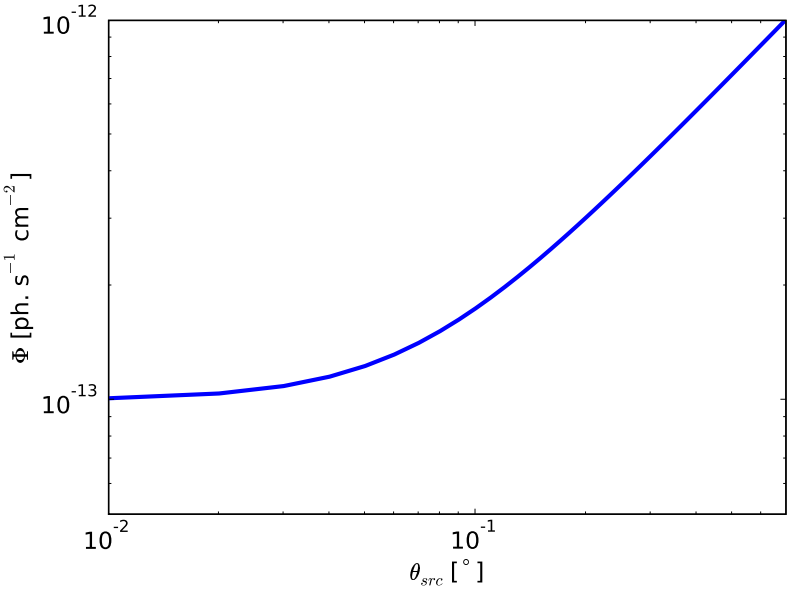

Figure 5.1: *Theoretical dependence of the instrument sensitivity (minimum detectable flux) on the source size $\theta_{\rm src}$. The plot assumes angular resolution $\theta_{\rm res} = 0.07°$ and a point-source sensitivity $1\times10^{-13} cm^{-2}\,s^{-1}$. Note that for source sizes $\gtrsim 0.6°$, the sensitivity is going to be limited additionally by systematic errors due to the necessity of using source-free runs for estimating the background.*

The figure shows that for $\theta_{\rm src} \sim \theta_{\rm res}$, the sensitivity is limited by the angular resolution $\theta_{\rm res}$. For $\theta_{\rm src} \gg \theta_{\rm res}$ the sensitivity scales linearly with the source size. Note that these considerations do not include systematic errors. These are in particular important for source extensions exceeding the wobble offset. In this case, the normally used reflected regions cannot be used for a background estimation and other background-modeling techniques have to be used, which are more prone to systematic errors.

In practice, instead of $\theta_{\rm res}$, a slightly extended integration region θ_0 is typically used for a point source analysis. Assuming that θ_0 was chosen to contain 80% of the point-source signal, then $\theta_0 \sim 1.3\,\theta_{\rm res}$. The qualitative conclusion of the previous paragraph remains, however, the same.

5.2 Effective area

Effective area $A_{\rm eff}$ is a measure of the area over which an instrument is sensitive to the incoming events. As shown in 5.1, the precise knowledge of this quantity is important for understanding the instrument sensitivity. It was shown above that the sensitivity scales with $\sqrt{A_{\rm eff}}$. Additionally, according to eq. (4.10,4.13), the spectrum and upper limits are proportional to $1/A_{\rm eff}$ and a possible bias in $A_{\rm eff}$ is thus directly reflected in the calculated spectrum. The determination of the effective area, its characteristics and possible systematic errors are described in more detail in the following.

5.2.1 Determining effective areas

The effective area is in general a function of energy E, observation zenith angle $\theta_{\rm Z}$, offset $\theta_{\rm off}$ of the target position from the center of the field-of-view, optical efficiency $\eta_{\rm o}$ and power-law index Γ of the incident γ-ray flux. The effective areas are thus determined individually for each combination of selection cuts, $\theta_{\rm Z}$, $\theta_{\rm off}$ and for two different optical efficiencies. In order to do that, Monte Carlo simulations of a γ-ray point source are used. The detector response is also simulated, which yields the probability of a detection of an event for any given system configuration, primary energy and direction. In general, the effective areas are then calculated as the area over which γ-ray events were generated in Monte-Carlo simulations weighted by a fraction of the simulated events that trigger the telescope system and pass the event-selection cuts.

Monte Carlo simulations

The *Monte Carlo (MC) simulations* for H.E.S.S. were performed using CORSIKA and `sim_telarray` codes. CORSIKA is a simulation package originally developed for the non-imaging wide-angle scintillator instrument HEGRA AIROBICC (see e.g. Martinez et al. 1995). The code is used for simulating the γ-ray induced electromagnetic showers in the atmosphere and for obtaining the photon yield on the Earth surface at a given height and for a given atmospheric profile. The second component of the MC simulations – `sim_telarray\`– is responsible for simulations of the detector response. It was originally developed for the H.E.S.S. array (as `sim_hessarray`), but was also used for planning the H.E.S.S. Phase II telescope and for simulating the upcoming CTA experiment (for a description of the code see Bernlöhr 2008c). The simulations were produced for two distinct optical efficiencies of the system, defined by the mirror and funnel reflectivities. The optical efficiency changes in time due to aging of the reflective surfaces. If not stated otherwise, the simulation set with a reduced optical efficiency is used.

Using the aforementioned code, a number of γ events from a point source of a given spectral index $\Gamma_{\rm MC}$ is simulated. The area used for simulations is a circle of radius 1000 m on the ground, i.e. the area $A_{\rm MC} = \pi \times 10^6$ m^2. The input spectrum, together with the

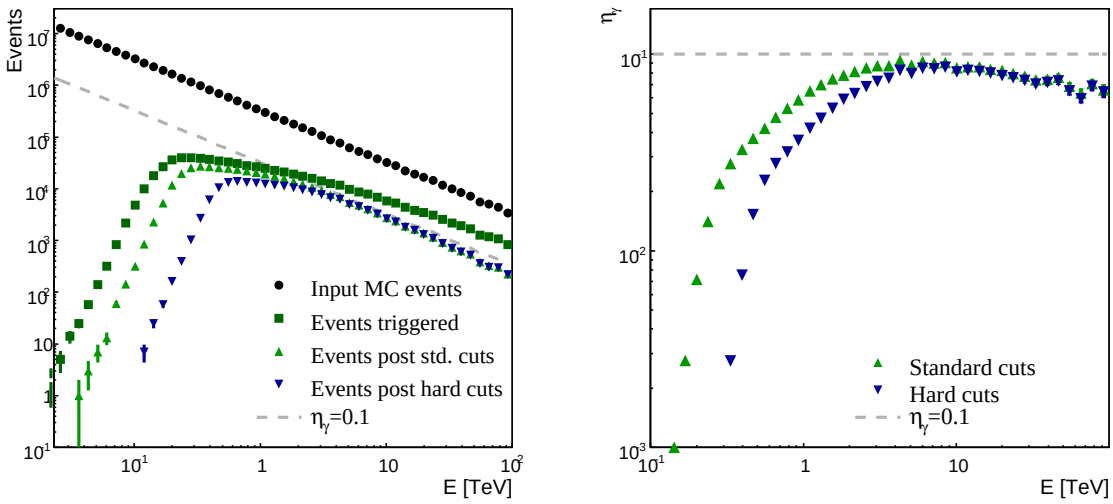

Figure 5.2: *Left: The simulated γ-ray spectrum (black circles) is compared to the events that trigger the system (green squares) and to the triggered events passing standard (green triangles) and hard cuts (blue triangles). 10% detection efficiency is depicted for illustration by a gray dashed line. Right: Total detection probability (efficiency) of an event to trigger the array and pass hard or standard cuts. One can see that the hard cuts reject more γ rays at lower energies as opposed to standard cuts. At higher energies both selection cuts have similar efficiency, close to 10%. Both figures are produced for 20° zenith angle and 0.5° offset.*

events that trigger the system and events that pass the selection cuts are shown in the left panel of Fig. 5.2. One can see that most γ rays are rejected at lower energies, mostly due to the trigger criterium. The standard cuts keep higher fraction of γ rays than hard cuts for energies below 3 TeV; beyond this energy both selection cuts have a similar γ-ray detection efficiency ϵ_γ, close to 10% (see the right panel of Fig. 5.2).

Calculation of effective areas

The effective area $A_{\rm eff}$ is calculated as $A_{\rm eff} = \frac{N_{\rm sel}}{N_{\rm MC}} A_{\rm MC}$, where $N_{\rm sel}$ is the number of events passing selection cuts and $N_{\rm MC}$ is the number of input MC-simulated events. The final effective areas as a function of a reconstructed as well as true energy are shown in Fig.5.3. One can see that the effective-area curves have a characteristic shape with a steep rise around the energy threshold and a plateau at higher energies. This plateau region remains almost constant up to the highest energies, where the plot is limited by finite statistics given by the power-law input spectrum. The exact energy ranges of these features depend on the selection cuts and on the zenith and offset angle.

In order to avoid artificial effects caused by a coarse binning in energy, the effective area histograms are fitted with an analytic function and only the fits are later used in practice. To achieve a higher stability of the fit, it is performed in a $\log(E)/\log(A_{\rm eff})$ representation. The histograms with a true energy (further referred to as true-energy histograms) are fitted by a sixth order polynomial function. The reconstructed-energy histograms are fitted using the same procedure, but using a seventh-order polynomial

complemented by an exponential function:

$$f(E) = \sum_{\mathrm{n}=0}^{7} a_{\mathrm{n}}\, E^n + a_8\, \mathrm{e}^{(b\,E)}, \tag{5.4}$$

where a_{i} and b are free parameters. In order to further improve the stability, various starting parameters are tried, and a check of a convergence of the fit is always performed. The upper bound of the fit range is limited by energy where at least two events in the simulations pass the selection cuts, in order to allow for an error calculation. The additional exponential term in the reconstructed energy histogram is necessary because of the different behavior of this dependency at the lowest energies (the steeper rise of this histogram can be seen in the Fig. 5.3). This is caused by the reconstructed energies being positively biased in an energy region near to the threshold (see also Fig. 4.13 in section 4.6.5).

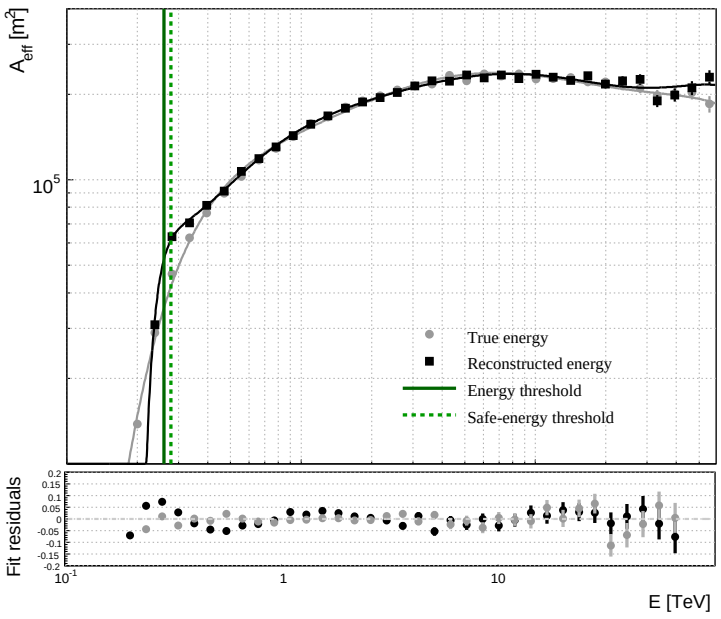

Figure 5.3: *Effective area as a function of true (black) and reconstructed (gray) energy. Also shown is a polynomial fit, which is in practice used instead of the coarsely binned effective area histogram. The spill-over effect due to overestimating energy can be seen in the case of the reconstructed energy plot (see the main text). The energy threshold is shown as a green solid line. Safe-energy threshold (dashed green line) shows the energy, above which the energy bias is less than 10%. Fit residuals for both effective area plots are shown in the bottom part of the figure.*

The figure shows that the difference between the reconstructed and true-energy histograms at the threshold region. This effect can be modeled by convolving the true-energy histogram with the energy-bias histogram. Figure 5.2.1 shows that this model well reproduces the observed "spill-over" behaviors. One can see that the distribution obtained by the convolution of the true-energy histogram is consistent with the reconstructed-energy histogram.

Zenith angle dependency

The effective areas depend strongly on the observation zenith angle and offset (Fig. 5.5). One can see a trend of increasing effective areas with higher zenith angles. This is caused by the larger light pool of more inclined γ-induced showers in case of larger zenith angles. Based on purely geometrical considerations, expected behavior far from the energy

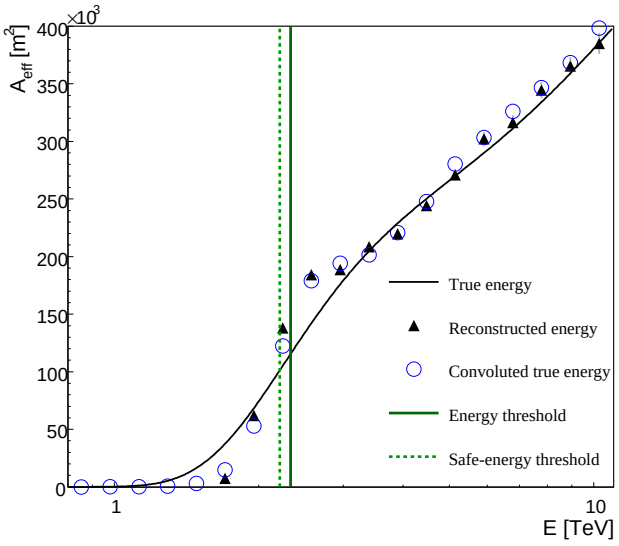

Figure 5.4: *The figure shows how the difference between the reconstructed- (black triangles) and true-energy (black line) effective area histograms can be modeled. The blue circles were produced by convoluting the corresponding energy bias (see histogram 4.13) with the true energy histogram. The general trend of the spill-over can be reconstructed. One can also see that the spill-over effect is strongest in the region around the energy threshold (in this case hard cuts, 55° zenith angle and 0.5° offset)*

threshold is:

$$A_{\text{eff}} \propto R_{\text{C}}^2 \frac{1}{\cos^2(\theta_{\text{Z}})}, \tag{5.5}$$

where R_{C} is the radius of the Čerenkov light pool on the ground. One finds that this behavior indeed holds for high enough energies (see Fig. 5.5). The dependency around the energy thresholds is more complicated as it is not governed solely by the geometry, but also by the sensitivity to the dim images of lower energies. The higher effective areas during large zenith angle observations increase event statistics at higher energies. This effect has been previously employed for extending spectra to larger energies (see e.g. Kosack & VERITAS Collaboration 2004). A second effect occurring at larger zenith angles is an increase of the energy threshold. This is caused by the larger path to be traversed by Čerenkov photons from the shower maximum, and correspondingly higher absorption, causing the images to be dimmer. Additionally, due to the larger size of the Čerenkov light pool on the ground, the observed density for an event of the same energy is lower in case of large zenith angles. Energy thresholds are discussed further in paragraph 5.2.2.

Interpolation

In practice, effective areas are stored only for the fixed combinations of zenith angles θ_{Z}, offset angles θ_{off}, for each set of cuts and for two azimuthal directions, corresponding to observations in the northern and southern directions. For an observation with arbitrary values of θ_{Z}, θ_{off}, θ_{azm}, four effective area lookups for the given selection cuts and azimuthal orientation (south or north) are obtained, corresponding to the closest θ_{Z} and θ_{off}. A resulting effective area value is calculated by an *interpolation* between these four values. The interpolation is linear between the offset values and between the zenith angles the $\cos(\theta_{\text{Z}})$ is interpolated. The result of the interpolation is illustrated in Fig. 5.5, where a dependency of the effective areas is plotted as a function of a zenith angle θ_{Z} .

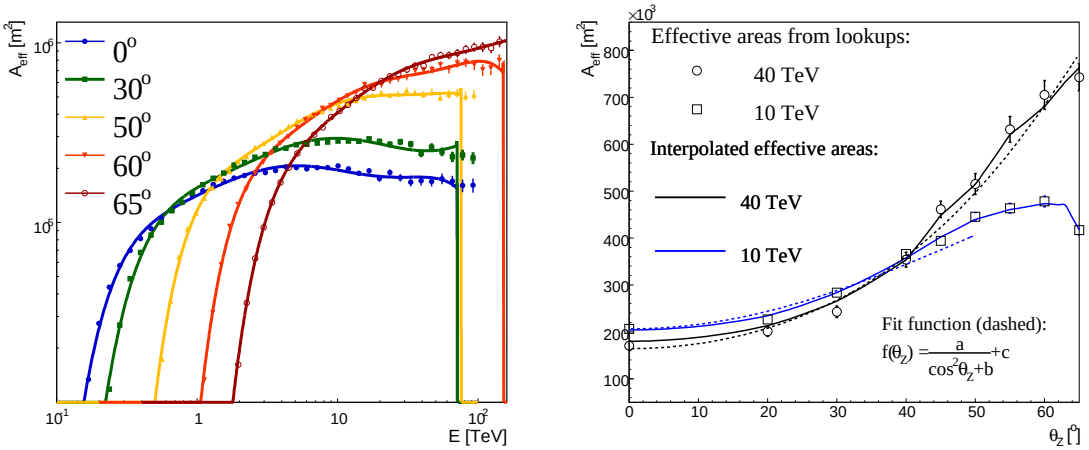

Figure 5.5: Left: *Effective areas as a function of a true energy for various simulation zenith angles for standard cuts and 0.5° offset. The effective areas generally increase with an increasing zenith angle and the energy threshold also increases. The fits extend to energies where at least two events pass the selection cuts.* **Right:** *An illustration of the zenith angle dependency of effective areas. Two cases are shown; 10 TeV (boxes, blue lines) and 40 TeV (circles, black lines). Plotted are the values from Monte Carlo simulations for fixed zenith angle θ_Z values (boxes and circles), along with the interpolated curves (see the main text) to illustrate the interpolation procedure. Additionally, the datapoints from simulations are fitted by a function describing the expected behavior far from energy threshold (see the main text). It can be seen, that in the case of 40 TeV, the fit function well describes the simulated data up to the highest energies. In the 10 TeV case (generally at lower energies), the effective areas don't follow this behavior because of their high energy threshold.*

5.2.2 Energy threshold

The energy threshold is defined as the energy where the post-analysis differential γ-ray rate reaches its maximum. The differential rate is calculated as a convolution of a given source spectrum and the appropriate effective area. It is plotted for several relevant cases in Fig. 5.6. It can be seen that the energy threshold is only rather weakly dependent on the source spectrum. The power-law index, however, changes significantly the overall γ-rate at a given energy. In the right plot of the figure 5.6, the zenith angle dependency of the energy thresholds is depicted. As mentioned before, the threshold rises steeply with an increasing zenith angle. This is an important fact to bear in mind when observations are planned.

In practice, a second energy threshold, the *safe-energy threshold*, is used during the analysis for deriving spectra and fluxes (see also section 4.6.5). It is used for deriving spectra and fluxes because it reflects the limitations of the analysis. The safe-energy threshold is defined by the energy above which the energy-reconstruction bias is less than 10%. The systematic error from energy reconstruction is thus limited by a fixed value. The safe-energy threshold however mostly coincides with the energy threshold as it is defined above (see e.g. Fig. 5.6).

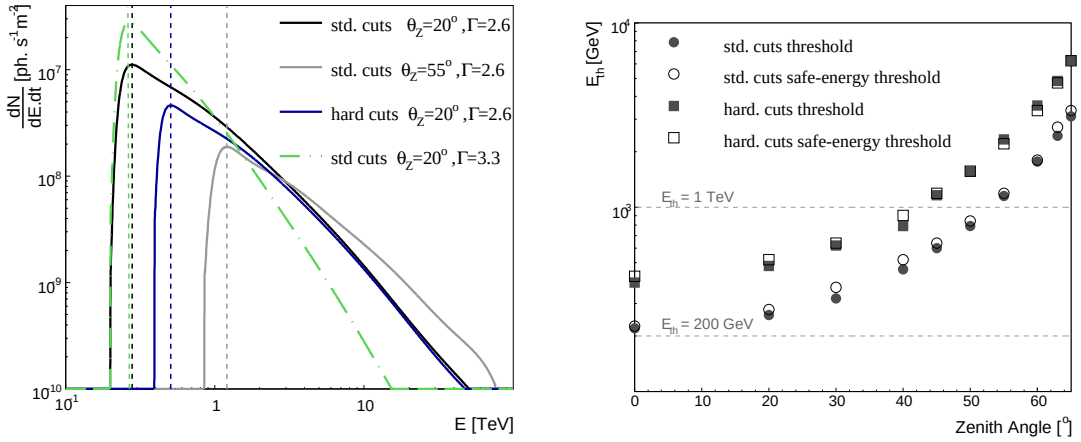

Figure 5.6: Left: *Post analysis differential γ-ray rates. Energy thresholds are shown as dashed lines. The curves are shown for standard and hard cuts, for zenith angles 20° and 55°, and for spectral indices $\Gamma = 2.6$ and for a softer spectrum $\Gamma = 3.3$. One can see that the spectral index doesn't affect the energy threshold, but significantly changes the shape of the differential-rate curve.* **Right:** *A zenith angle dependence of the energy and safe-energy threshold.*

5.2.3 Systematic errors

As mentioned above, the knowledge of the absolute scale of effective areas is crucial for determination of spectra and fluxes. In this section, the systematic errors of the effective area determination are discussed. These include mainly modeling of the atmospheric density profile and its temporal changes.

Atmospheric models

A precise determination of the atmospheric density profile is important for all ground-based experiments that use the atmosphere as a calorimeter. An imprecise density value is directly reflected in a biased effective area, and consequently in the calculated fluxes and estimated sensitivity. Several studies have been performed elaborating on the importance of atmospheric monitoring for IACTs (Bernlöhr 2000; Osborne et al. 2002).

The profile of the atmosphere depends on the location and on the season, as can be seen in Fig. 5.7. The figure shows that the photon yield for different locations can vary by as much as 60%. The seasonal variations translate into photon yield changes of 15–20% within a year.

To illustrate the effect of a different atmospheric profile on the analysis and estimate the systematic error of the atmospheric uncertainty, the effective areas were produced using two different profiles: *US maritime* and a *desert*-like profile. The maritime atmosphere assumes lower transparency and has a boundary layer at the sea-level. The desert atmosphere is clearer and has the boundary layer at 1800 m, i.e. adopted to the H.E.S.S. altitude. The effect of the two models on the simulated trigger rate was studied by Funk et al. (2004), where it was also compared to the real measurements (left panel in Fig. 5.8). In Fig. 5.8, one can see that the atmosphere conditions at the H.E.S.S. site lie in between of the two models. By comparing the effective areas corresponding to the two

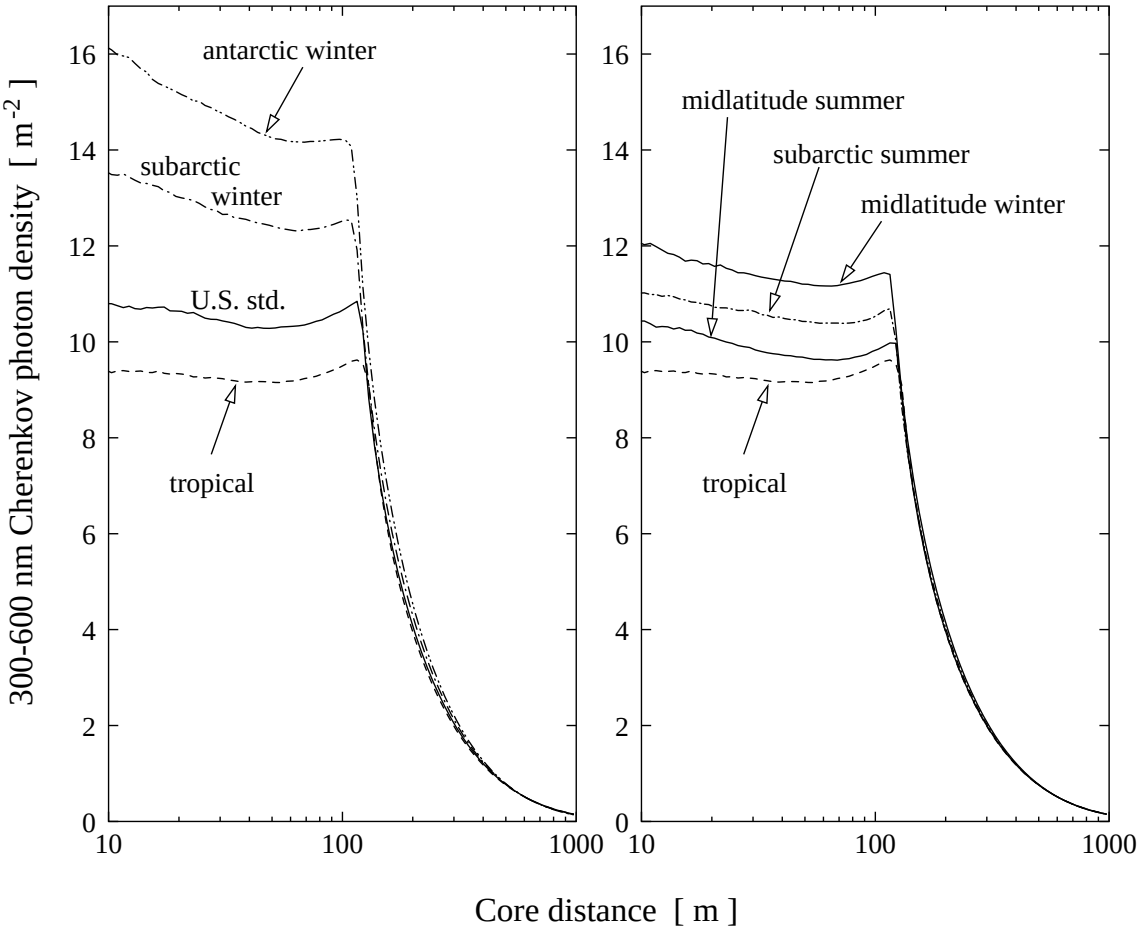

Figure 5.7: *Average radial distribution of Čerenkov photons in wavelength range 300–600 nm for vertical 100 GeV γ rays. The simulations were performed using CORSIKA code and assuming altitude of 2200 m above the sea level. Figure from Bernlöhr (2000)*

different profiles it is possible to estimate the systematic error on the differential flux that arises from the uncertainty in atmospheric modeling.

The residua $(A_{\rm eff}^M - A_{\rm eff})/A_{\rm eff}^M$, where $A_{\rm eff}^M$ are effective areas produced using the US maritime profiles and $A_{\rm eff}$ are the desert profiles, are plotted in the right panel in Fig. 5.8 for two zenith angles 20° and 50°. By fitting the residua by a constant function above the energy threshold of the desert effective areas, one finds that the desert effective areas are larger by $(5.6 \pm 0.9_{\rm stat})$ % in case of 20° zenith angle and by $(12.6 \pm 2.0_{\rm stat})$ % in case of a larger zenith angle of 50%. The desert atmosphere yields as expected higher values of $A_{\rm eff}$ because of its higher transparency. The systematic error from the atmospheric modeling alone is in the order 5–15% with a rising tendency towards higher zenith angles. This is expected because at higher zenith angles, the Čerenkov light has a longer path length and a bias in the density has hence a stronger effect.

Note that throughout this thesis, we use the simulations produced using the desert atmospheric profiles.

Another effect (as discussed above) is caused by temporal changes in the atmosphere.

This was studied by Aharonian et al. (2006a) for H.E.S.S. by measuring the flux of a steady γ-ray source (the Crab Nebula) over a longer time period . As a result, the systematic error on the integral flux was estimated to be $\sim$15% for a large-zenith-angle observations ($\sim$50°). By combining the effect of the possible bias in atmospheric models and the effect of temporal variations, one can estimate the systematic error on flux to be $\lesssim$20%.

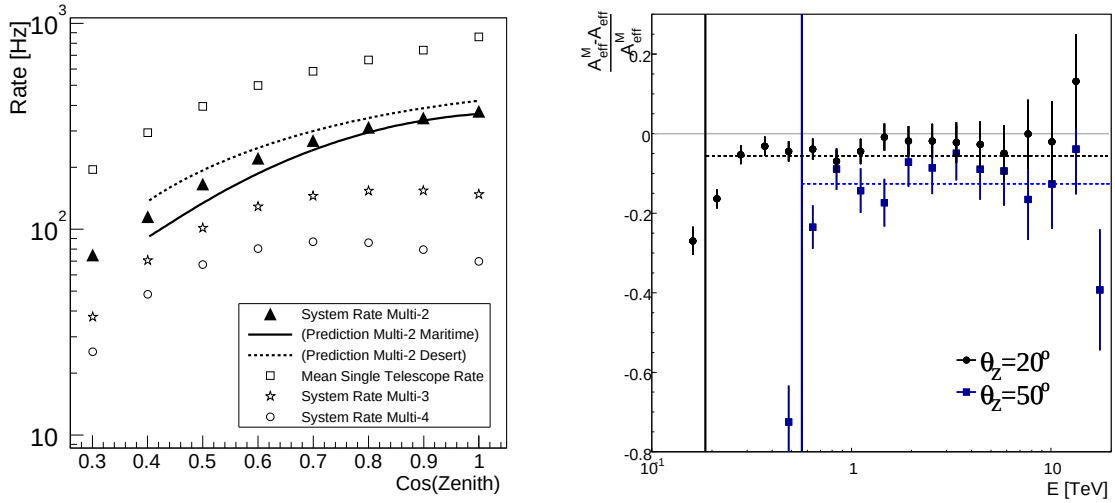

Figure 5.8: Left: *Comparison of simulated and measured trigger rates of the H.E.S.S. array with 1, 2, 3 and 4 telescopes. In case of the two-telescope system, the trigger rate was simulated for two atmospheric models: maritime and desert (see the main text). The measured trigger rate lies between the two models.* **Right:** *An effect of using two different atmospheric profiles is illustrated. The difference between effective areas produced using simulations with US maritime atmospheric profile ($A^M_{\rm eff}$) and the desert atmosphere in Namibia ($A_{\rm eff}$) is shown. The latter simulations are used elsewhere in the analysis in this work. Plotted are only residua, fitted by a constant function (dashed line) above the energy thresholds of the desert model(vertical solid lines). The fitted constant functions are $(-5.6 \pm 0.9_{\rm stat}) \times 10^{-2}$ for a zenith angle of 20° and $(-12.6 \pm 2.0_{\rm stat}) \times 10^{-2}$ for a zenith angle of 50°. In both cases, offset of 0.5° is used.*

The atmosphere is monitored on the H.E.S.S. site in Namibia by several instruments (Le Gallou & H. E. S. S. Collaboration 2003). The transmissivity of the atmosphere above the site is measured by a LIDAR – an instrument measuring the backscatter of laser pulses, capable recreating an optical density profile of the atmosphere. A cloud level affecting a trigger rate can be estimated using IR radiometers, pointing paraxially with the telescopes and measuring the infrared radiation of clouds. Additionally, the transmissivity of the low altitude levels of the atmosphere is monitored by observing a blue LED light positioned on a mountain Gamsberg. These instruments have been previously used for calibrating data in Brown & et al. (2005), but they are not a part of the standard calibration procedure, used in this work.

5.3 Angular resolution

It is shown in section 5.1 that a sensitivity of an IACT is directly proportional to the angular resolution in case of point sources and is thus of primary importance for the

analysis. The angular resolution $\theta_{\rm res}$ is typically defined as a 68% containment radius θ_{68} ($\sim$ RMS) of the point-spread-function (PSF). The spread of the PSF distribution is governed by the quality of direction reconstruction of primary γ-ray events. Because of its importance, the direction reconstruction in case of the H.E.S.S. instrument is here described and the angular resolution is shown in cases of different selection cuts and zenith angles.

5.3.1 Direction reconstruction

The problem of γ-ray direction reconstruction is greatly simplified using stereoscopic arrays of multiple IACTs, a technique pioneered by the HEGRA instrument (see e.g. Daum et al. 1997, for a review of the HEGRA performance). When more telescopes are available, a simple geometrical method can be used to reconstruct the primary direction, which significantly improves the angular resolution. The general approaches to stereoscopic direction reconstruction are described by Hofmann et al. (1999). The standard technique used in H.E.S.S.-related works is the Algorithm 1 from this work.

Algorithm 1

When a γ-ray induced atmospheric shower is observed by an array of IACTs separated by a given non-zero distance, each telescope "observes" the shower from a different angle. The projection of the shower onto the camera planes is therefore different for each telescope, resulting in images that point in different directions (see Fig. 5.3.1). These images are approximated by ellipses, with the major axis pointing in the angular direction of the primary γ-ray. In case of two telescopes, the primary direction is found as the intersection of the major axes of the images in a common coordinate system of the cameras. This is illustrated in Fig. 5.3.1.

Slightly more complicated is the case where more than two telescopes are triggered. Let N be the number of telescopes passing the trigger and preselection criteria[3]. The number of intersections is then $N(N-1)/2$. Each intersection point is then weighted and an average is built from the weighted intersection points. The weight $w_{\rm ij}$ of intersection between image i and j is calculated as:

$$w_{\rm ij} = |\sin(\phi_{\rm i} - \phi_{\rm j})| \left(\frac{1}{\frac{1}{A_{\rm i}} + \frac{1}{A_{\rm j}}} \right) \left(\frac{1}{\frac{W_{\rm i}}{L_{\rm i}} + \frac{W_{\rm j}}{L_{\rm j}}} \right), \tag{5.6}$$

where Φ describes the shower image orientation in the camera plane (see Fig. 5.3.1), L and W are lengths of its major and minor axis respectively, and A is the image amplitude in photoelectrons. The first term reflects the fact that a reconstruction by intersecting two images is most accurate when the two images are perpendicular. The second and third term are not part of the Algorithm 1 as described by Hofmann et al. (1999). The second term prefers brighter showers and the third term favors showers that are more prolonged along their major axis and have thus a better defined direction.

[3] As a reminder, preselection is a preliminary selection of images based on their geometric parameters, mainly on the shower amplitude.

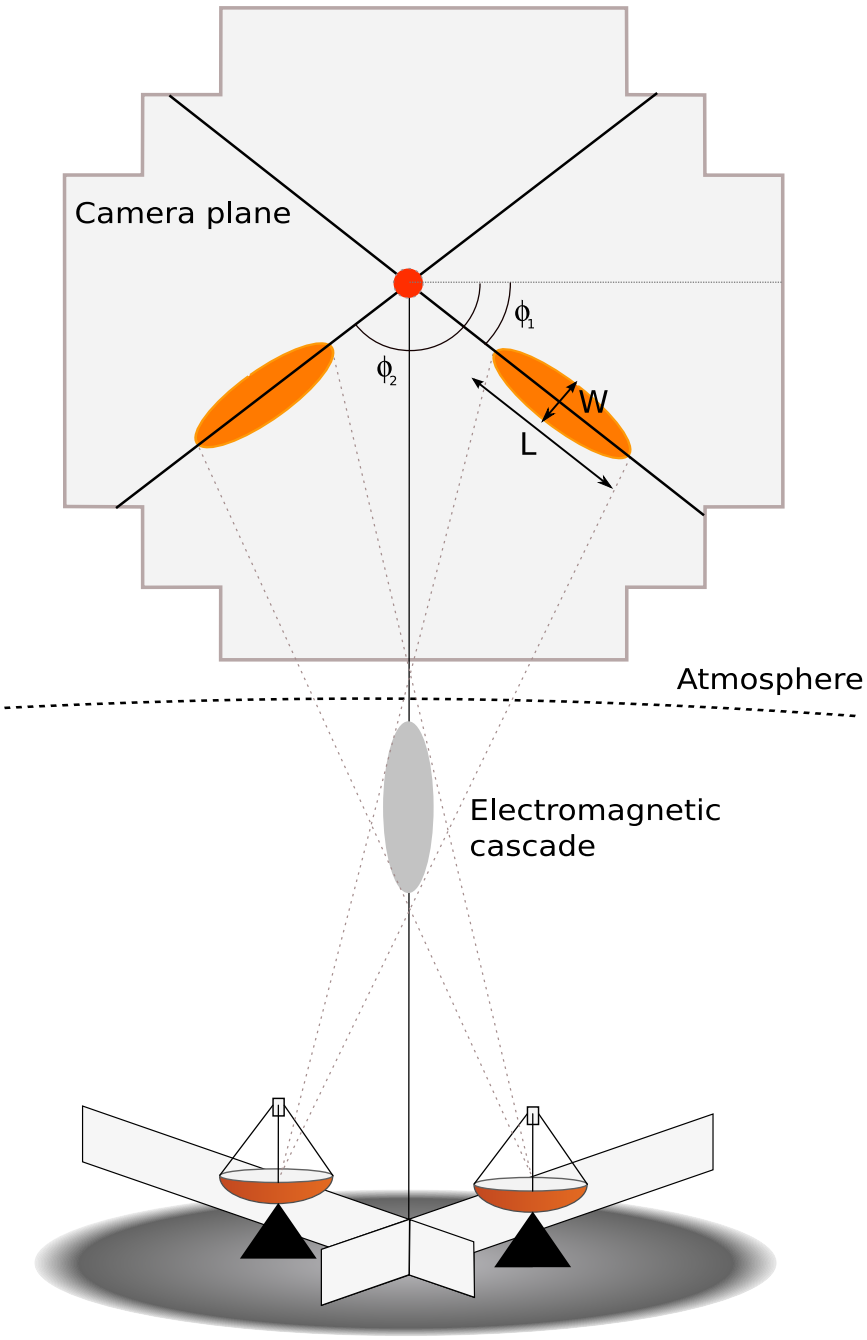

Figure 5.9: *Illustration of reconstructing the primary γ-ray direction. The primary direction is reconstructed by intersecting projections of the main axes of the shower images in individual telescopes. The case of more than two telescopes is discussed in the main text.*

Algorithm 3

This procedure represents an improved version of the "algorithm 1" described above. In addition to the latter technique, for each shower image, the following shower parameters

are reconstructed:

- The distance d of the image centre-of-gravity (CoG) to the primary direction.
- An error on the determination of the CoG
- An error on the determination of ϕ, i.e. the orientation of the shower main axis.

These parameters are reconstructed by means of lookup tables using the amplitude, width and length of the shower images. They are then combined to provide error ellipses on either side of the shower images, corresponding to the estimated γ-ray direction. When multiple images exist within one event, the ellipses are analytically combined to obtain the reconstructed direction and its error. The technique was originally described by Hofmann et al. (1999) as *algorithm 3*, hence the name. The improvement of the angular resolution is in particular significant at large-zenith-angle observations (see Berge 2006).

5.3.2 Angular resolution

As mentioned before (section 5.3), angular resolution is defined as the 68% containment radius of reconstructed γ-ray events from a point source. In this work, this is investigated by means of a *point-spread function (PSF)* – a function describing the radial profile of reconstructed directions of simulated γ-ray events from a point source. The angular resolution $\theta_{\rm res}$ can be then measured as a 68% containment radius of this function, i.e.:

$$\theta_{\rm res} \equiv \theta_{68}; \quad \int_0^{\theta_{68}} \theta^2 \, {\rm d}\theta = 0.68 \int_0^{\infty} \theta^2 \, {\rm d}\theta \tag{5.7}$$

The PSF of H.E.S.S. is illustrated in Fig. 5.10, along with real data from observations of the Crab Nebula. Plotted is the excess distribution of the Crab data as a function of the squared angular distance of a reconstructed event from a nominal target position. This involves firstly producing the distribution of on-source events, which are extracted from a region around the source. Secondly, the off-source events distribution is extracted from a region that is placed at a position constructed by reflecting the target position around the observation position (see section 4.6.6). Clearly, this method can be only used for observations in a wobble mode. The PSF can be described by a double Gaussian, the second one being wider and corresponds mainly to the badly reconstructed events.

The figure also shows that the PSF of hard cuts is typically narrower than for standard cuts. This can be understood by the fact that the direction of higher-energy events can be better reconstructed, and because hard cuts reject more background events.

Zenith angle dependence

The angular resolution depends strongly on the zenith angle. With increasing zenith angle, it tends to get worse, a fact illustrated in the right panel of Fig. 5.10. One can see that the angular resolution remains rather constant until $\theta_{\rm Z} \approx 50^\circ$and then steeply rises, becoming twice the value at zenith at $\sim 60^\circ$.

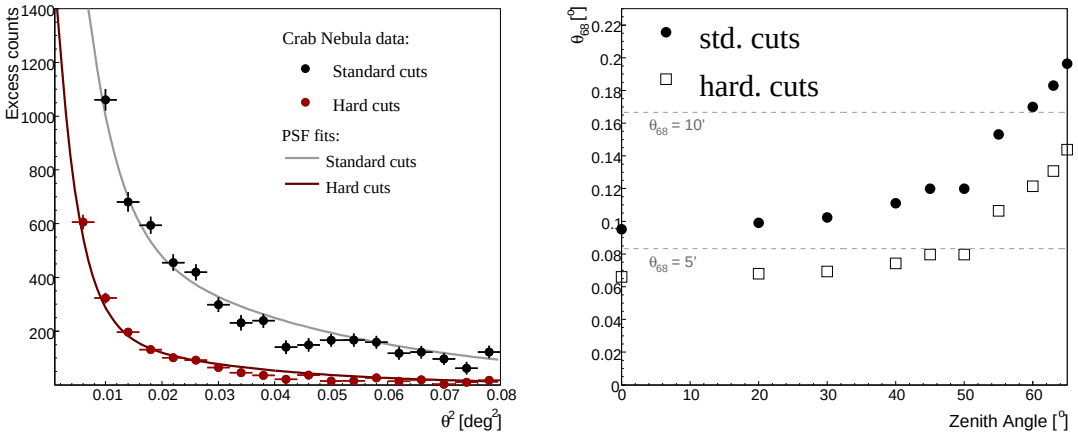

Figure 5.10: Left: *Angular distribution of γ-ray events extracted from Crab Nebula observations (points) and a point-spread function fit (solid lines) of a double Gaussian. Shown is a case of standard and hard cuts. Due to the northern position of the Crab Nebula, the corresponding zenith angle is $\sim 60°$.* **Right:** *Zenith angle dependence of the angular resolution. Also shown is that hard cuts perform in this sense better than standard cuts. The angular resolution was calculated assuming a power-law spectrum with spectral index $\Gamma = 2.6$ and using 0.5° offset Monte-Carlo simulations.*

Telescope multiplicity

Here, we address the question of how the angular resolution depends on the number of telescopes participating in an event. In a simple model, assuming independent shower images of similar parameters, the reconstructed direction will follow a Gaussian distribution with the mean centered on the true direction (if no bias is present). The spread of the Gaussian is $\sqrt{(N)}$, where N is the number of images (telescopes) used for the reconstruction. The spread of the mean reconstructed position is thus expected to scale as $1/\sqrt{N}$ with the number of telescopes (multiplicity).

The dependency is shown in Fig. 5.11 and tabulated in Tab. 5.1. The angular resolution is substantially improved between two and four-telescope multiplicity. The right panel of the figure also illustrates that the dependency follows, to a good approximation, the expected behavior described above. The remaining residuals to the fit are caused by the fact that 4-telescope events are more probably triggered by higher energy events, where the angular resolution is better (see the following paragraph). When constraining the dataset to only events between 1 and 2 TeV, the expected behavior is almost exact (see inset of the right panel in Fig. 5.11). A similar result is achieved by Hofmann et al. (1999).

Energy dependence

A direction of a high-energy γ-ray event is significantly better defined than for low energy events. This can be seen in the figure 5.12. The angular resolution thus improves at higher energies. See figure 5.12 for the dependency. The behavior is stronger for in case of standard cuts. A possible reason is that the tighter MSCW cut of hard cuts assures a better direction reconstruction already at lower energies.

Table 5.1: *Angular resolution for standard and hard cuts for different number of telescopes participating in the direction reconstruction. The angular resolution is determined using 20° zenith angle and 0.5° offset Monte Carlo simulations of a power law source with* $\Gamma = 2.0$.

Selection cuts	All events	2 telescopes	3 telescopes	4 telescopes
Standard	0.095°	0.126°	0.097°	0.058°
Hard	0.065°	0.084°	0.068°	0.042°

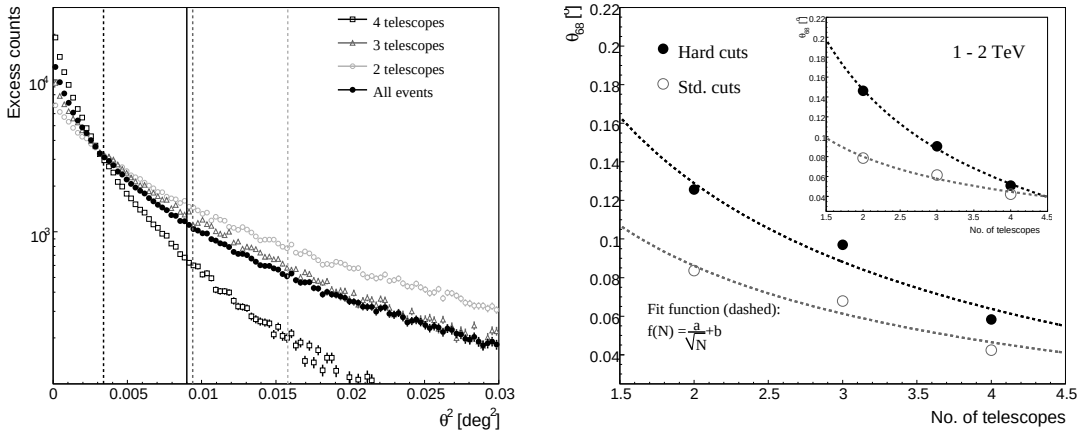

Figure 5.11: Left: *Point-spread function for 2, 3 and 4 telescopes participating in the shower direction reconstruction (open symbols). Also plotted is the PSF in the case that no restriction is made on the number of telescopes (solid circles). The points represent number of counts at the given angular distance* θ *from the simulated target position. Vertical lines represent the corresponding angular resolution (68% containment radius).* **Right:** *Angular resolution as a function of a number of telescopes (see also Tab. 5.1). The points are well fitted by the expected behavior of* $a/\sqrt{\theta} + b$. *The inset shows the same for a subsample of events with energies 1–2 TeV. All figures are made for case of* $\theta_Z = 20°$ *and offset of 0.5°.*

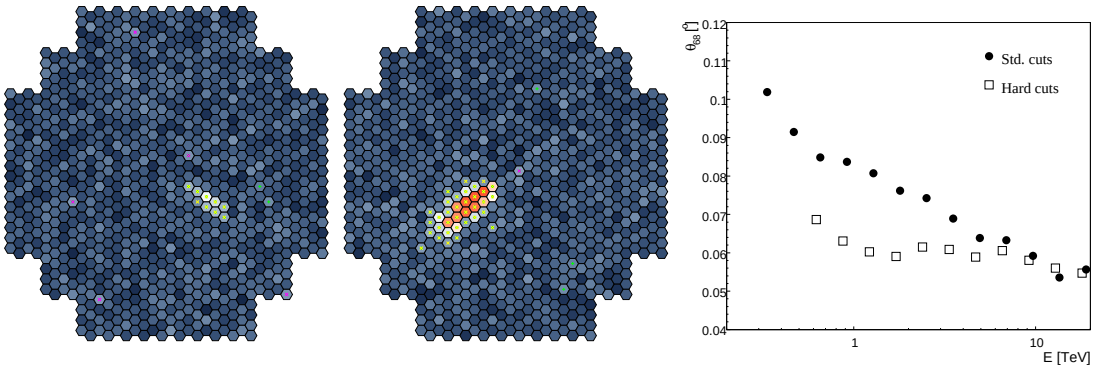

Figure 5.12: *Comparison of Monte-Carlo simulated* γ*-ray event of primary energy 100 GeV (left) and 1 TeV (middle), observed by the H.E.S.S. telescope. The scale depicts amplitude in each pixel. Events of higher energy are clearer, with the main shower image axis better defined.* **Right:** *Energy dependence of the angular resolution for hard and standard cuts at 20° zenith angle and 0.5° offset.*

5.4 Sensitivity estimate

The sensitivity of the instrument can be calculated using a background rate extracted from real data. The assumed γ-ray signal is iteratively decreased until a 5σ significance level according to Li & Ma (1983) is reached. In order to derive a sensitivity above a certain energy, it is necessary to know the reconstructed energy distribution of the on-source and off-source events. The ON and OFF signal and the significance is then calculated only for events above the given energy. The H.E.S.S. sensitivity was published by e.g. Aharonian et al. (2006a) and is also shown by Bernlöhr (2008b). The results are shown in Fig. 5.13.

The figure shows well that hard cuts are suitable for weak sources and rather long observations, whereas the loose cuts are appropriate for very strong signals, comparable with the flux of the Crab Nebula.

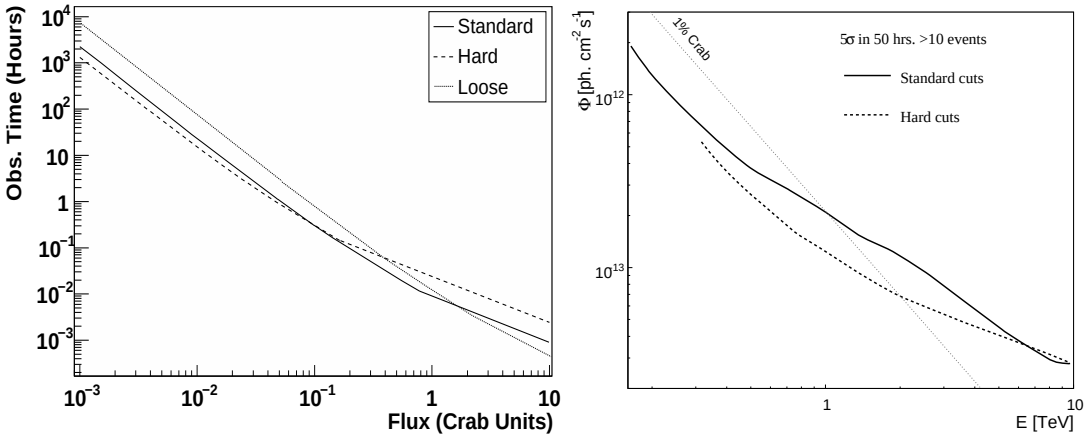

Figure 5.13: Left: *A dependence of time required for a detection of a Crab-like source at a 5σ significance level on the γ-ray flux. A minimum of 10 events is required in case of very short observations. This requirement causes the break in the otherwise smooth curve. The sensitivity is shown for three different selection cuts. Figure from Aharonian et al. (2006a).* **Right:** *A sensitivity expressed as the minimum integral flux necessary for a 5σ detection above a given energy for 50 hours of observations. Again, a minimum of 10 events is required.*

Chapter 6

Results

In this chapter, the results of H.E.S.S. observations of selected VHE γ-emitting candidate extragalactic objects are presented. The target selection is described, along with theoretical estimates in chapter 2. The focus here is placed on galaxy clusters that are currently of a prime interest in the group of *extended extragalactic objects* within the H.E.S.S. collaboration. Results of H.E.S.S. observations of starburst galaxies and of one ULIRG are presented. Additionally, a discovery of one object of an already established TeV-emitting class – BL Lac AGNs – is presented.

All the targets are first shortly described, introducing their general characteristics that could be relevant for their non-thermal properties. Afterwards, for each object the VHE observations are summarized and the results are presented, together with an interpretation of the results.

All presented results are obtained using the standard H.E.S.S. analysis chain as described in chapters 4 and 5 and in Aharonian et al. (2006a). Upper limits are in all cases calculated using Feldman & Cousins (1998) method of estimating confidence levels. The confidence level is 99.9% if not stated otherwise.

6.1 Galaxy clusters

Galaxy clusters are prime candidates for non-AGN VHE-emitting extragalactic objects, because they are likely to contain large populations of non-thermal particles (demonstrated in section 3.1.3). Here, we present the results of H.E.S.S. observations of a relaxed cluster, Abell 496, and a massive hot cluster, Abell 85. No significant signal is found from these objects. Nevertheless, the upper limits allow one to derive theoretically very challenging upper limits on the non-thermal energy content in these clusters. Results of observations of other galaxy clusters (Coma, Abell 754, Centaurus and Hydra A) are also presented. These targets are discussed in less detail than the former two because of either unfavorable observation position (e.g. the northern hemisphere location of the Coma cluster) or because they were not ranked as better candidates than Abell 496 and Abell 85 (see section 3.1.6 for the target selection of the galaxy clusters).

6.1.1 Abell 496

Abell 496 (Fig. 6.1), located at $\alpha_{\mathrm{J2000}} = 04^{\mathrm{h}}33^{\mathrm{m}}37.1^{\mathrm{s}}$, $\delta_{\mathrm{J2000}} = -13°14'46''$ (Abell et al. 1989), is a prime candidate for H.E.S.S., selected on the basis of the largest L_{X}/R ratio, where L_{X} is X-ray luminosity and R is the apparent angular radius. Abell 496 is a relatively nearby (z = 0.033) compact relaxed cluster of a richness class I (Abell 1958); meaning that in the original work of Abell (1958), there were 50–79 clusters recognized with optical flux within 2 mag. from the brightest galaxy in the cluster. The cluster features a *cooling core* (Heckman 1981; Fabian et al. 1981) at its center (see section 3.1.1 for a review of cooling cores). The total mass is estimated to be $\sim 3 \times 10^{14}$ $M_{\odot}$ (Markevitch et al. 1999). It is found to be a very regular and symmetrical cluster (Durret et al. 2000), with no signs of an on-going merger activity. It is thus considered to be an archetype for a *relaxed galaxy cluster* (Durret et al. 2000). In the adopted cosmological model (see Appendix A), the redshift of Abell 496 corresponds to a distance of 134 Mpc, thus 1° in angular distance relates to 2.35 Mpc at the target.

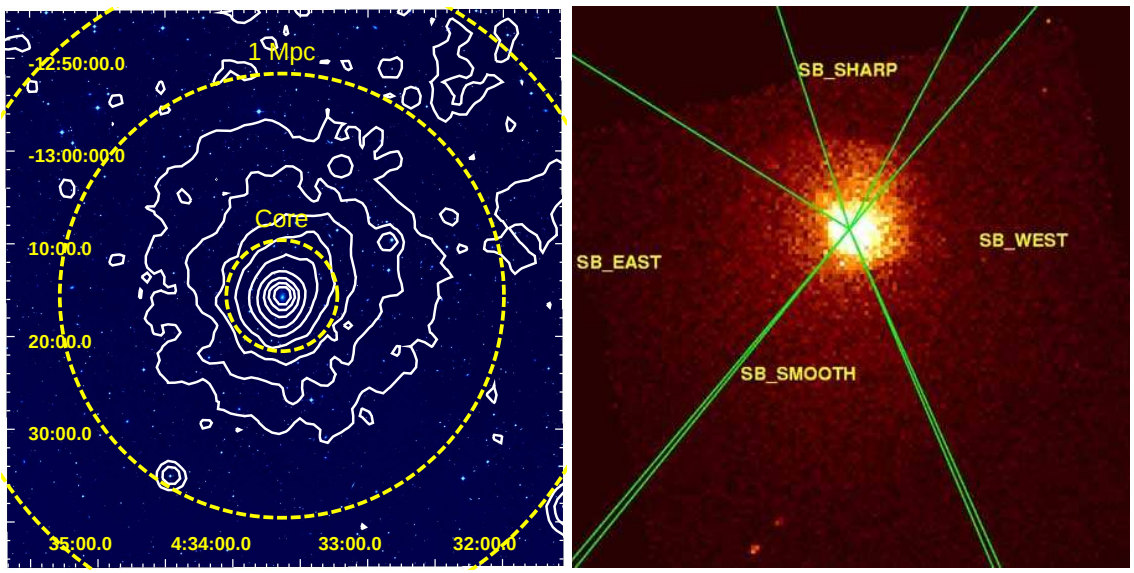

Figure 6.1: Left: *Optical image of Abell 496 from the STScI Digitized Sky Survey (HST Phase 2). Shown is a region of 1°×1°, coordinates are in Ra/Dec J2000. Overlaid in white are contours of ROSAT PSPC. Yellow dashed circles show the integration regions (in the order smallest to largest) of the core, 1 Mpc and extended analysis.* **Right:** *Chandra X-ray exposure-corrected image in the energy range 0.3–10 keV (one pixel corresponding to 4″. One can see a sharp discontinuity in the X-ray surface brightness towards north. This* cold front*, as discussed in the main text, is a debatable feature as far as the origin is concerned. There is no pressure discontinuity as would be expected from a merger-induced shock front (figure from Dupke & White 2003).*

The object has been well studied in X-rays by Chandra (Dupke & White 2003, 2002), XMM (Tamura et al. 2001) and *RXTE* (Valinia et al. 2000). A metallicity gradient with an increase towards the central cD galaxy[1] was established. The source of metal enrichment in the intracluster medium was extensively investigated in this cluster, confirming that it

[1]The term "cD galaxy" galaxy denotes particularly luminous D galaxies that are typically located in the centres of rich clusters. D galaxy is, according to the Morgan's classification, a rotationally symmetric galaxy without any pronounced spiral or elliptical structure and with a more diffuse appearance.

is from the matter expelled by supernova explosions, predominantly by the type SN II. No hint of a non-thermal X-ray emission was found using the *RXTE* instrument (Valinia et al. 2000).

Abell 496 is also one of the most suitable objects for directly constraining the cosmological matter density parameter $\Omega_{0,\mathrm{m}}$. For such a relaxed cluster, the fraction $\Omega_{\mathrm{B}}/\Omega_{0,\mathrm{m}}$ of baryonic to total matter density can be assumed to be representative of the whole Universe. This ratio can be directly measured by comparing measurements of the total cluster mass (using velocity dispersion measurements, X-ray observations and gravitational lensing) and the baryonic mass measured by means of the X-ray luminosity. Further, by comparing the relative light element abundances to the predictions of primordial nucleosynthesis, one can constrain the total matter density $\Omega_{0,\mathrm{m}}$ (White et al. 1993). Abell 496 is a very luminous and relaxed cluster, and thus suitable for this study. The results of these measurements in case of Abell 496 were used to place a constraint of $\Omega_{0,\mathrm{m}} < 0.3$ (Markevitch et al. 1999). These limits are consistent, though not competitive with the recent findings from CMB measurements.

Despite being relaxed, the cluster shows evidence for activity in the central region. It is a typical example of a cluster harbouring *cold front* substructures (Dupke & White 2003), sharp discontinuities in the X-ray surface brightness that are inconsistent with the appearance of shock fronts (see the right panel of Fig. 6.1). Contrary to the shock fronts, the gas pressure remains constant across the cold front. The origin of this puzzling feature of some clusters is not yet fully understood, however it could be caused by several mechanisms, including an accretion of a group of galaxies, or by a dynamic activity of the central galaxy. The latter seems to be the case of Abell 496 (Dupke & White 2003).

VHE observations

The object was observed by the H.E.S.S. instrument during moonless night time in the period from October to December 2005 and in October 2006. The observations were performed in a *wobble mode*[2] with the target being typically at 0.7° offset from the center of the field of view. The average zenith angle of the observations was 28° resulting into post-analysis energy threshold of 570 GeV (for *hard cuts*).

The analysis was performed using the standard H.E.S.S. analysis chain with hard cuts. These are selected a priori because of the low expected flux and a rather hard expected spectrum. All upper limits are derived assuming a power-law gamma-ray spectrum with spectral index $\Gamma = 2.1$. This value is based upon the expectations of Völk et al. (1996). In order to check the dependency of the results on the assumed index, the upper limits for $\Gamma = 2.3$ are also given. The difference in upper limits determined using the two indices is, however, less than 10%.

Results

Since the size of the VHE gamma-ray emitting region is unknown, four different analyses are used, integrating the signal over three sizes (θ) of circular on-source regions at the

[2] Wobble mode refers to an observation mode with the target being offset from the centre of the field-of-view (see section 4.6.6)

position of Abell 496, referred to as the *core*, *extended*, *very extended* and *1 Mpc* regions. Apart from the very extended one, they are depicted in the left panel of Fig. 6.1.

- *Core analysis* — used to search for a signal coming from the X-ray core region of the cluster. The core size of the β-model (Cavaliere & Fusco-Femiano 1976) was measured by Markevitch et al. (1999) as 178 kpc, corresponding to 0.08°. This size is about equal to the size of a point source as imaged by the H.E.S.S. instrument (see Sec. 5.3). The signal is therefore integrated over a larger area with radius $\theta_1 = 0.1°$, optimized for a search of point-like sources (Aharonian et al. 2006a).

  No significant emission is found from the central region above the hard cuts threshold energy of 570 GeV. In order to search for other point sources away from the center of Abell 496 a map was created with significances of point-like TeV gamma-ray signals on a grid around the center of the cluster (Fig. 6.2). The significance distribution over the FOV is consistent with background fluctuations (right panel of Fig. 6.2). The upper limit on the integral flux from the core region is derived to be $F_\gamma(> 570 \text{ GeV}) < 4.8 \times 10^{-13}$ ph. s^{-1} cm^{-2}, assuming $\Gamma = 2.1$ and $F_\gamma(> 570 \text{ GeV}) < 5.2 \times 10^{-13}$ ph. s^{-1} cm^{-2} for $\Gamma = 2.3$ at the 99.9% confidence level, corresponding to 0.9% and 1% of the integral Crab Nebula flux as measured by Aharonian et al. (2006a) for the two spectral indices respectively. The integral upper limit is also shown in Fig. 6.3.

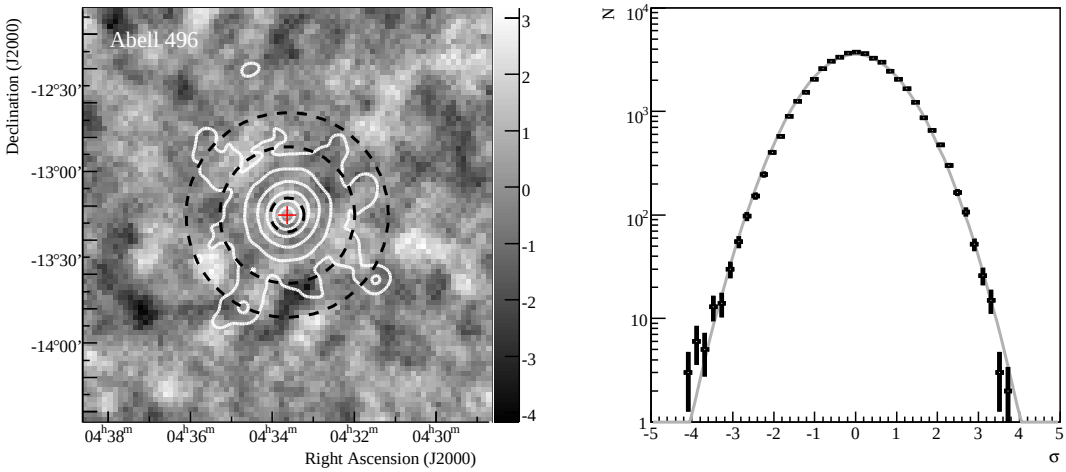

Figure 6.2: Left: *Correlated significance map of the region around Abell 496 obtained using the core (point-source) analysis. The correlation radius is 0.1°. Black dashed circles depict the on-source regions used for the core, 1 Mpc and extended analysis respectively (from the smallest to the largest). The red cross denotes the nominal centre of Abell 496. Also shown are white contours from hard-band ROSAT PSPC observations (Durret et al. 2000), smoothed by the H.E.S.S. angular resolution.* **Right:** *A distribution of significances in bins of the map on the left panel. The distribution is fitted by a Gaussian (gray line) with RMS of 1 centered on 0, leaving the normalization as a free parameter. The consistency of the distribution with the Gaussian fit indicates, that there is no significant signal apart from background fluctuations.*

- *Extended source analysis* — performed on the whole region of the X-ray overdensity, using $\theta_2 = 0.6°$ as measured by Reiprich & Böhringer (2002). No signal is found

above the energy of 570 GeV. A 99.9% upper limit on the integral flux is determined $F_\gamma(> 570\text{GeV}) < 2.4 \times 10^{-12}$ph. s^{-1} cm^{-2}, which corresponds to 4.6% Crab. Figure 6.3 compares this result with the core analysis. Assuming photon index of $\Gamma = 2.3$ the upper limit is $F_\gamma(> 570\text{ GeV}) < 2.6 \times 10^{-12}$ph. s^{-1} cm^{-2} (5.0% Crab).

- *Very extended analysis* — aimed at investigating possible emission from the accretion shocks. A very large on-source region of radius $\theta_3 = 1.5°$ is used, corresponding to 3.5 Mpc. The data set is reduced to 9.8 live hours, because not every on-source run had a corresponding good-quality off-source run that could be used for the background estimation. Again, no significant signal is found. A 99.9% upper limit is determined to be $F_\gamma(> 570\text{ GeV}) < 5.8 \times 10^{-12}$ph. s^{-1} cm^{-2} (10.9% Crab flux) for $\Gamma = 2.1$ and $F_\gamma(> 570\text{ GeV}) < 6.2 \times 10^{-12}$ph. s^{-1} cm^{-2} (11.7% Crab flux) for $\Gamma = 2.3$.

- *1 Mpc analysis* — uses integrating radius $\theta_4 = 0.4°$ that corresponds to a radius of 1 Mpc from the center of Abell 496. The radius of 1 Mpc is not physically motivated, but other physical quantities are well measured within this radius. Hence these results are later used for modeling in section 6.1.3. The resulting upper limits were $F_\gamma(> 1\text{TeV}) < 7.2 \times 10^{-13}$ph. s^{-1} cm^{-2} for $\Gamma = 2.1$ and $F_\gamma(> 1\text{TeV}) < 7.5 \times 10^{-13}$ph. s^{-1} cm^{-2} for $\Gamma = 2.3$ with this spatial extension.

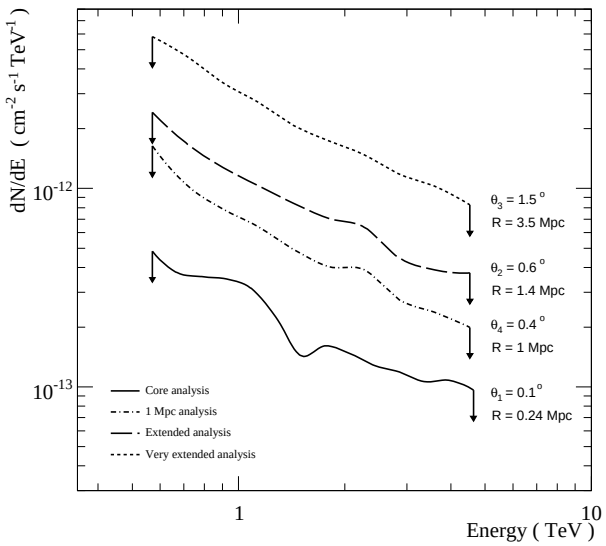

Figure 6.3: *The H.E.S.S. integral upper limits for Abell 496 assuming four different sizes of the emission region. The curves are obtained by comparing the gamma-ray excess above a given reconstructed energy to the number of events expected for the observation parameters and an assumed spectrum of the incoming gamma-rays. The result for core analysis exhibits fluctuations caused by low number of excess events. All curves were produced assuming a power law with a spectral index of* $\Gamma = 2.1$.

All results are summarized in table 6.1 and are partly published in Domainko et al. (2007). An independent calibration and analysis method combining a semi-analytical shower model and the Hillas analysis (de Naurois 2003) was used as a cross-check, yielding consistent results.

Although no significant signal was detected, the result can be used for constraining the non-thermal energy content of the cluster. This is discussed, together with Abell 85 in section 6.1.3.

Table 6.1: *Summary of the results from VHE observations of Abell 496 for various integration radii $\theta_{\rm R}$ and assumed spectral indices Γ.*

Abell 496

$\theta_{\rm R}$ [°]	R^a [Mpc]	Assumed Γ	$F_\gamma^{\rm UL}(> E_{\rm th})^b$ [% Crab flux]
0.1	0.2	2.1	0.9
0.1	0.2	2.3	1.0
0.4	1	2.1	3.2
0.4	1	2.3	3.3
0.6	1.4	2.1	4.6
0.6	1.4	2.3	5.0
1.5	3.5	2.1	10.9
1.5	3.5	2.3	11.7

[a] Radius corresponding to $\theta_{\rm R}$ using the distance of 134 Mpc.
[b] Integral flux above energy threshold, tabulated as a fraction (in percent) of the integral VHE γ-ray flux of the Crab Nebula as measured by Aharonian et al. (2006a).

6.1.2 Abell 85

The second target, Abell 85, is a massive galaxy cluster with a complex morphology at a redshift of 0.055, and located at $\alpha_{J2000} = 0^h41^m37.8^s$, $\delta_{J2000} = -9°20'6''$ (Abell et al. 1989). The object is well studied in both X-ray (with ROSAT by Pislar et al. (1997); Lima Neto et al. (1997), BeppoSAX by Lima Neto et al. (2001), Chandra (Kempner et al. 2002) XMM (Durret et al. 2005)) and optical wavelengths (Slezak et al. 1998). In the adopted cosmological model, the redshift of Abell 85 corresponds to a distance of 220 Mpc and 1° corresponds to 3.86 Mpc at the distance of the target.

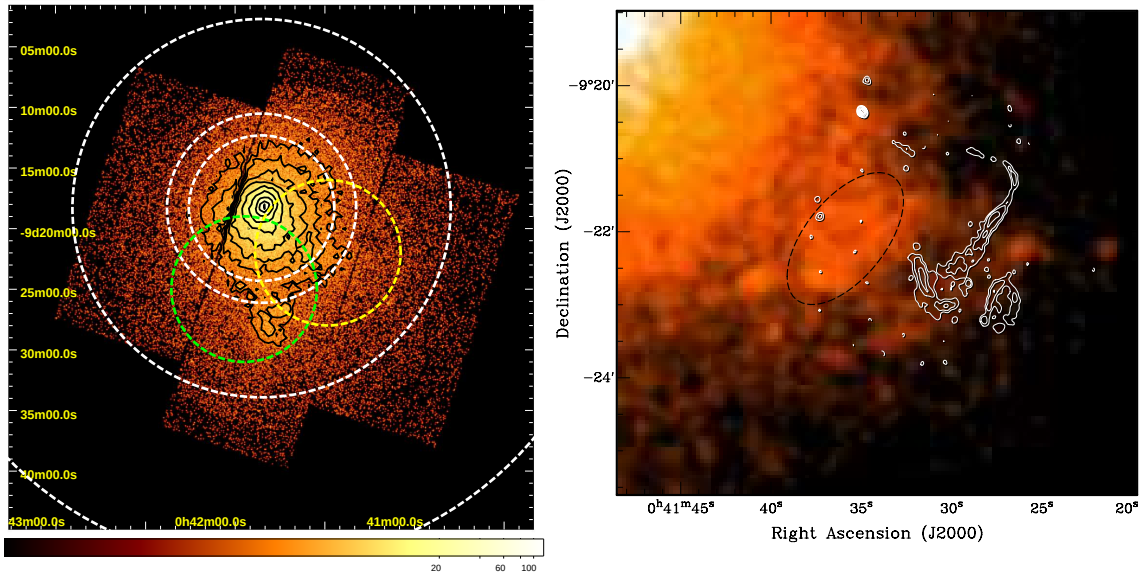

Figure 6.4: **Left:** *Illustration of the main structures of Abell 85 and of the integration radii of the various analysis. The background image corresponds to XMM-MOS1 raw counts, black contours represent smoothed version of the same image. The scale is logarithmic and coordinates are RA/Dec J2000. The southern subcluster is clearly seen, which might be hitting the main cluster (see the main text). Also distinguishable is the subcluster in the SW region (see detail in the right panel). White dashed circles correspond to the analyses of the main cluster; from the smallest to the largest they depict the core analysis $\theta_1 = 0.1°$, 95% X-ray containment analysis $\theta_2 = 0.13°$, 1 Mpc analysis $\theta_4 = 0.26°$and the extended analysis $\theta_3 = 0.49°$. Yellow circle limits the integration region used for investigating the radio relic in the SW of the main cluster and green circle the analysis focused on the merger of the southern subcluster onto the main one.* **Right:** *XMM MOS1+MOS2 X-ray image with the 21 cm radio isocontours from Slee et al. (2001). The white radio contours show the very steep spectrum radio relic. It is located at the outer edge of the southwest X-ray excess emission, which is approximately limited by the black dashed ellipse. The projected distance of the relic from the cluster center is ∼400 kpc (figure from Durret et al. 2005)*

The cluster shows an extensive merger activity, and is currently undergoing a merger with one massive subcluster from the south and with another less massive one from the southwest (Kempner et al. 2002). By measuring the temperatures of the subclusters, it was shown that they indeed belong to the main cluster and that they are not fore- or background objects (Markevitch et al. 1998; Durret et al. 2005). In the case of independent clusters, the two subclusters would have much lower temperature than the main cluster due to the lower mass, which is not observed (see the temperature map in the left panel of Fig. 6.5). Further, it was shown to contain an X-ray filament with a large extension of

∼4 Mpc (Durret et al. 2005).

An existence of a radio structure, consistent with a radio relic has been shown by Bagchi et al. (1998) and studied in detail by Slee et al. (2001). It is located near the position of an X-ray excess[3] emission (see the right panel in Fig. 6.4) and was found to have a very steep spectrum and a high degree of polarization (35%). The relic has a filamentary structure, and its size is ∼2' along the major axis.

In addition, Abell 85 features a cooling core (see section 3.1.1) at its center which is quite uncommon for merging clusters, where the core is typically disrupted by the on-going merger. Presumably the merging sub-clusters have not yet reached the central region of the cluster and have therefore not affected the existing cooling core (Kempner et al. 2002).

Corrected test position

The traditional reference position comes from the original work of Abell et al. (1989). The quoted position is however not consistent with following observations by e.g. ROSAT, where the centre of the emission is at $\alpha_{\rm J2000} = 0^{\rm h}41^{\rm m}51.2^{\rm s}$, $\delta_{\rm J2000} = -9°18'19''$, being ∼4' away from the reference position. Since the X-ray emission is most important while searching for non-thermal processes, we use the position determined by ROSAT (Reiprich & Böhringer 2002) . See Fig. 6.5 for an overview of the archival optical and X-ray data.

VHE observations

Abell 85 was observed in October 2006, November 2006 and in August 2007. The observations were performed in wobble mode with the target being at 0.7° offset from the center of the field of view. In total 32.5 hours of live time on Abell 85 meet the standard data quality selection criteria and are used for the analysis. The average zenith angle of the observations 18° resulting in a post-analysis energy threshold of 460 GeV for *hard cuts* from Aharonian et al. (2006a).

Results

Similar to the case of Abell 496, several integration radii (θ) were probed to search for a signal from the main cluster of Abell 85. Additionally, the SW region including the radio relic was investigated and also the region where the southern subcluster is believed to be colliding with the main cluster. The integration regions (apart from the largest one) are illustrated in Fig. 6.4.

- *Core analysis* — The size of the core region is 226 kpc (Mohr et al. 1999), corresponding to ∼ 3'. The core analysis thus again uses $\theta_1 = 0.1°$, the radius optimized for a search of point-like sources. As a result no significant signal is found and an upper limit on the integral flux is derived $F_\gamma(> 460{\rm GeV}) < 3.9 \times 10^{-13}$ph. s^{-1} cm^{-2} (0.5% Crab flux) for $\Gamma = 2.1$ and $F_\gamma(> 460{\rm GeV}) < 4.1 \times 10^{-13}$ph. s^{-1} cm^{-2} (0.6% Crab flux) for $\Gamma = 2.3$.

[3]The excess here denotes a deviation from the symmetrical (double)beta-profile of the X-ray surface brightness, expected from a relaxed cluster (see section 3.1.1.

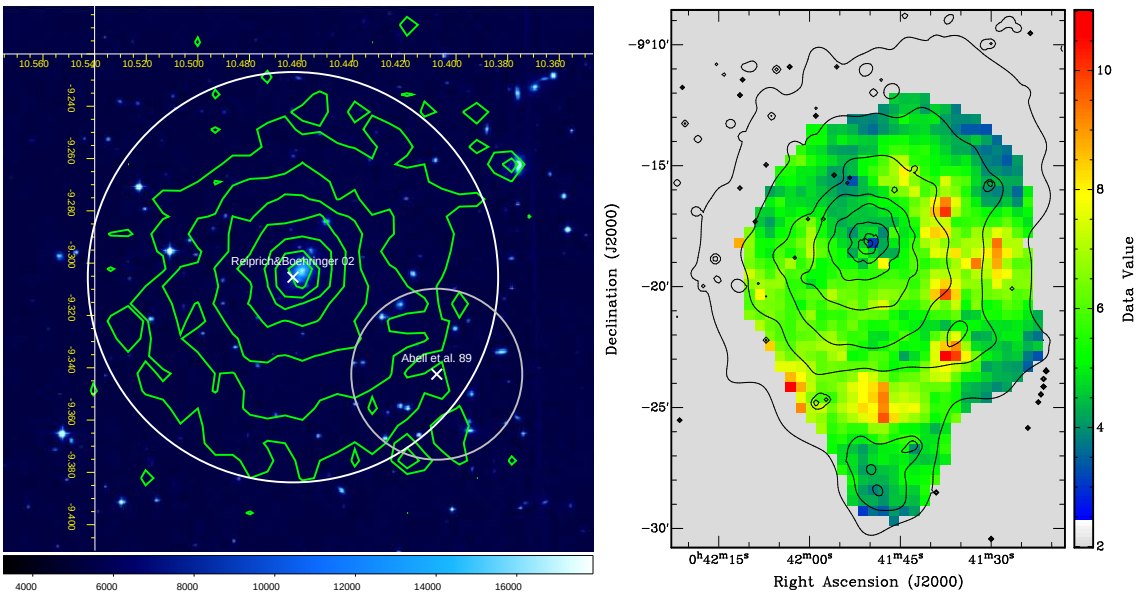

Figure 6.5: Left: *Optical image of the central region of Abell 85 cluster (DSS UK Schmidt), illustrating the corrected test position. Overlaid are green contours of ROSAT-HRI instrument. Two white crosses correspond to the original reference position (Abell et al. 1989) with a gray circle denoting the quoted error (150″) and the position quoted by Reiprich & Böhringer (2002). The white circle shows the radius of the* point source *integration region of 0.1°.* **Right:** *A temperature map of Abell 85 obtained by XMM observations (figure from Durret et al. 2005). The collision region between the main cluster and the southern subcluster has a significantly higher temperature.*

A significance map of the region around the center of the cluster was produced (Fig. 6.6). Also in this case the significance distribution is consistent with background fluctuations.

- *95% X-ray containment analysis* — Probes region of 95% X-ray containment, which according to Perkins et al. (2006) is 510 kpc (based on parameters from Mohr et al. (1999), corresponding to an angular cut of $\theta_2 = 0.13°$. No signal is found either and the upper limit on integral flux is calculated to be $F_\gamma(> 460\text{GeV}) < 3.4 \times 10^{-13}$ph. s^{-1} cm^{-2} (0.5% Crab flux) for $\Gamma = 2.1$ and $F_\gamma(> 460\text{GeV}) < 3.6 \times 10^{-13}$ph. s^{-1} cm^{-2} (0.5% Crab flux) for $\Gamma = 2.3$.

- *Extended analysis* probes the region of X-ray overdensity, i.e. $\theta_2 = 0.49°$ as measured by Reiprich & Böhringer (2002). The integral upper limit in this case is $F_\gamma(> 460\text{GeV}) < 1.5 \times 10^{-12}$ph. s^{-1} cm^{-2} (2.0% Crab flux) for $\Gamma = 2.1$ and $F_\gamma(> 460\text{GeV}) < 1.6 \times 10^{-12}$ph. s^{-1} cm^{-2} (2.2% Crab flux) for $\Gamma = 2.3$.

- *Very extended analysis* uses an on-source region of radius $\theta_3 = 0.91°$ corresponding to 3.5 Mpc. The data set is reduced to 8.6 live hours due to a lack of appropriate off-source data. No significant signal is found. A 99.9% upper limit is determined to be $F_\gamma(> 460\text{ GeV}) < 9.9 \times 10^{-12}$ph. s^{-1} cm^{-2} (13.6% Crab flux) for $\Gamma = 2.1$ and $F_\gamma(> 460\text{ GeV}) < 1.1 \times 10^{-11}$ph. s^{-1} cm^{-2} (15.1% Crab flux) for $\Gamma = 2.3$.

- *1 Mpc analysis* — Probes the 1 Mpc region, corresponding to $\theta_4 = 0.26°$. Again no signal is found and upper limits are derived: $F_\gamma(> 1\text{TeV}) < 3.2 \times 10^{-13}$ph. s^{-1} cm^{-2}

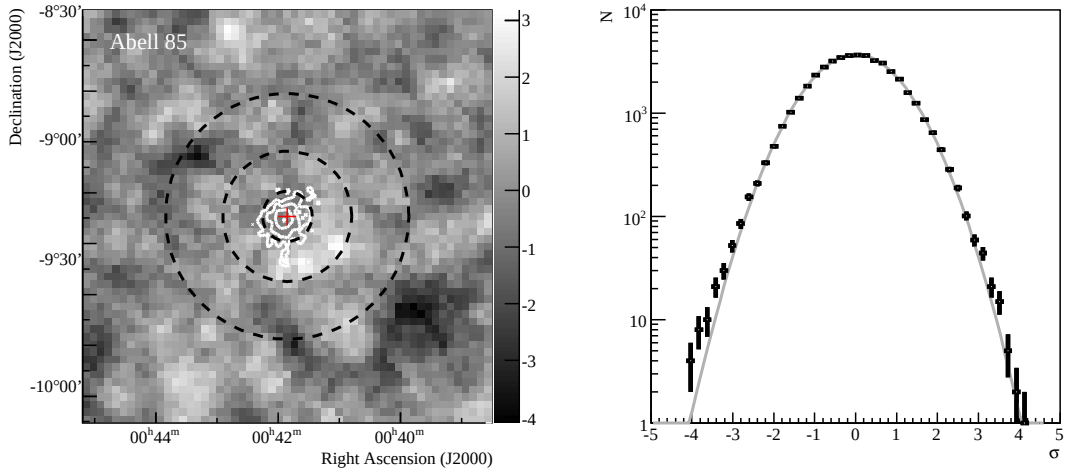

Figure 6.6: Left: *Correlated significance map of the region around Abell 85 obtained using the* point source analysis. *The correlation radius is 0.1°. Black dashed circles depict the on-source regions used for the core and 95% containment analysis. The red cross denotes the nominal centre of Abell 85 (from Böhringer et al. 2004). Also shown are white contours from hard-band ROSAT PSPC observations (Pislar et al. 1997).* **Right:** *A distribution of significances in bins of the significance map. The distribution is fitted by a Gaussian (gray line) with RMS of 1 centered on 0, leaving the normalization as a free parameter. The distribution is consistent with background fluctuations.*

(1.4% Crab flux) for $\Gamma = 2.1$ and $F_\gamma(> 1\text{TeV}) < 3.3 \times 10^{-13}$ph. s^{-1} cm^{-2} (1.4% Crab flux) for $\Gamma = 2.3$.

Additionally two other regions were investigated, not centered on the main cluster:

- *Radio relic analysis* — Focused on the radio relic in the SW of the main cluster. It is centered on coordinates $\alpha_{\text{J2000}} = 0^{\text{h}}41^{\text{m}}29^{\text{s}}$, $\delta_{\text{J2000}} = -9°22'0''$ and an angular cut of 0.1° is used.

- *South merger analysis* — Probes the southern region where the subcluster is believed to be hitting the main cluster. The analysis is centered on coordinates $\alpha_{\text{J2000}} = 0^{\text{h}}41^{\text{m}}57^{\text{s}}$, $\delta_{\text{J2000}} = -9°25'0''$ and uses a point-source angular cut of 0.1°.

Also in case of these two regions, no signal was found and the upper limits were calculated to be $F_\gamma(> 0.46\text{TeV}) < 3.6 \times 10^{-13}\text{cm}^{-2}\,\text{s}^{-1}$ (0.5% Crab flux) for the relic region and $F_\gamma(> 0.46\text{TeV}) < 4.1 \times 10^{-13}$ (0.6% Crab flux) for the south merger region.

The upper limits on the integral fluxes are plotted in Fig. 6.7 and are summarized in Table 6.2.

An independent calibration and analysis method combining a semi-analytical shower model and the Hillas analysis (de Naurois 2003) was used as a cross-check, yielding consistent results.

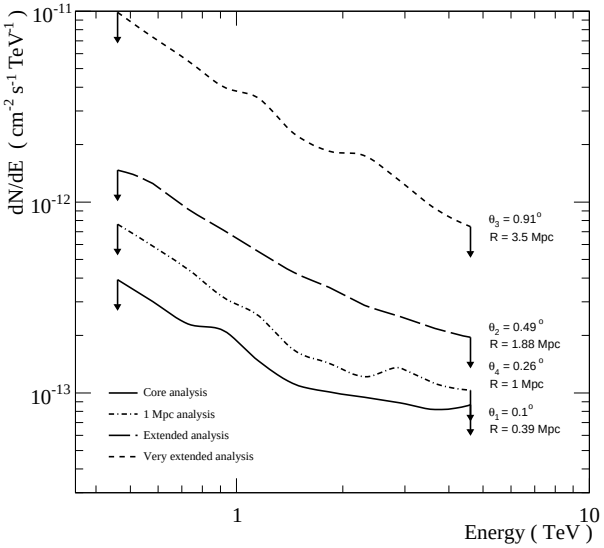

Figure 6.7: *The H.E.S.S. 99.9% upper limits on the integral flux assuming different sizes of the emission region. The curves are obtained in the same way as in Fig. 6.3. All curves were produced assuming a power law with a spectral index of* $\Gamma = 2.1$. *The upper limit for* $\theta_2 = 0.13$ *is not shown for the sake of readability. It lies however very close to the curve of* point source analysis. *Note that the upper limit for the very extended analysis was produced with a reduced dataset.*

Table 6.2: *Summary of the results from VHE observations of Abell 85 for various integration radii* $\theta_{\rm R}$ *and assumed spectral indices* Γ.

Abell 85

$\theta_{\rm R}$ [°]	R^a [Mpc]	Assumed Γ	$F_\gamma^{\rm UL}(> E_{\rm th})^b$ [% Crab flux]
0.10	0.4	2.1	0.5
0.10	0.4	2.3	0.6
0.13	0.5	2.1	0.5
0.13	0.5	2.3	0.5
0.26	1.0	2.1	1.1
0.26	1.0	2.3	1.1
0.49	1.9	2.1	2.0
0.49	1.9	2.3	2.2
0.91	3.5	2.1	13.6
0.91	3.5	2.3	15.1

[a] Radius corresponding to $\theta_{\rm R}$ using the distance of 220 Mpc.
[b] Integral flux above energy threshold, tabulated as a fraction (in percent) of the integral VHE γ-ray flux of the Crab Nebula as measured by Aharonian et al. (2006a).

6.1.3 Constraining the non-thermal energy content in galaxy clusters

In this section, the VHE upper limits are used to experimentally constrain the non-thermal component of the observed galaxy clusters Abell 496 and Abell 85. An upper limit on the ratio $E_{\rm nonth}/E_{\rm th}$ is calculated, where $E_{\rm th}$ is the total thermal energy and $E_{\rm nonth}$ the total non-thermal energy of the corresponding cluster.

In order to estimate $E_{\rm nonth}/E_{\rm th}$, we adopt the same approach as the one used for estimating the integral γ-ray flux in the section 3.1.5. This approach estimates the integral γ-ray flux $F_\gamma(> 1$ TeV) above 1 TeV from the π^0 decay for a given gas density $n(R)$ and cosmic-ray energy density profile $\epsilon_{\rm CR}(R)$and a given power-law spectral index Γ of primary protons. The non-detection of F_γ allows one to impose an upper limit on the total cosmic-ray energy density $E_{\rm nonth} = \int\limits_{\rm V} \epsilon_{\rm CR}(R){\rm d}V$. The upper limits were calculated assuming three different CR energy density profiles — constant, following the gas density (including cooling cores) and following the gas density excluding the cooling cores (for more information see section 3.1.5). The results are calculated using the VHE upper limits for the 1 Mpc region and for a 95% X-ray containment region. The necessary total thermal energy of both clusters was estimated earlier in section 3.1.3 as $E_{\rm th} \approx 4.3 \times 10^{62}$ erg (Abell 496) and $E_{\rm th} \approx 2.4 \times 10^{63}$ erg (Abell 85). The resulting upper limits of the ratio $E^{UL}_{\rm nonth}/E_{\rm th}$ are summarized in the table 6.3.

Table 6.3: *Upper limits on the ratio of energy in the non-thermal component with respect to the thermal energy of the ICM ($E_{\rm nonth}/E_{\rm th}$) for different spatial distributions of the CRs in the cluster and for different spectral indices Γ of both primary protons and secondary γ rays. All numbers are given for a radius of 1 Mpc with the exception of the numbers for the 95% containment radius (see main text). Particles of the non-thermal component have much larger energies (> 1 GeV) than can be obtained thermally and are responsible for the gamma-ray production, whereas the thermal component can be observed in X-rays. A value of $E_{\rm nonth}/E_{\rm th} > 1$ means that the energy of the non-thermal component exceeds the energy of the thermal component. This configuration is unrealistic since it would require that shocks are more efficient in accelerating particles than in heating up the shocked medium. Therefore, the presented observations can not constrain any models for such a case.*

Γ	spatial distribution of CRs	$E^{\rm UL}_{\rm nonth}/E_{\rm th}$ (Abell 496)	$E^{\rm UL}_{\rm nonth}/E_{\rm th}$ (Abell 85)
2.1	constant	1.12	0.15
	β model	0.51	0.08
	CC included	0.40	0.06
2.3	constant	5.66	0.75
	β model	2.56	0.40
	CC included	2.03	0.30
2.1	CC included 95% containment radius	0.40	0.03

Note that some models of other authors who concentrate on the external production mechanisms predict a ratio of CR energy to gas thermal energy of up to $\sim 50\%$ (Miniati et al. 2001; Ryu et al. 2003). Hence the upper limits constrain models which favor a similarly large ratio of non-thermal to thermal energy. Limits obtained for Abell 85 are especially interesting. These limits are for a hard spectrum, well within the prediction of the simple model developed in Sec. 3.1.3 and exclude an unduely large component of hadronic CRs ($E_{\rm nonth}/E_{\rm th} > 0.15$). The non-detection of Abell 85 may even disfavor very centrally concentrated distributions of CRs in galaxy clusters, since in this case an upper

limit of $E_{\mathrm{nonth}}/E_{\mathrm{th}} < 0.03$ can be derived which is smaller than moderate model estimates (see Sec. 3.1.3). However it is important to mention that for a steeper spectrum of the CR protons, the limit on the energetics of the non-thermal component would be larger than these optimistic model predictions.

For stronger constraints on the component of non-thermal particles in galaxy clusters, longer exposures of the observations are required. In this context it should be noted that the sensitivity of H.E.S.S. scales with the square of the observation time and therefore, in order to reach a twice as sensitive limit on the energetic in cosmic rays as presented here, it is necessary to perform a four times longer observation.

6.1.4 Other galaxy clusters

Here, the results of four additionally observed galaxy clusters are presented that were not studied in a greater detail: the Coma cluster, Abell 754, the Centaurus cluster and Hydra A. In the following, they are shortly discussed, together with the VHE observations by H.E.S.S.. No hint of a signal is found from these targets and upper limits were derived on the integral γ-ray flux. The results of the observations are summarized in Tab. 6.4.

Coma cluster

Coma cluster (ACO 1656) is one of the most massive ($M \sim 10^{15}\ M_{\odot}$) and nearest ($z = 0.023$) galaxy clusters. Being exceptionally rich, symmetric and near, it is considered to be an archetypal galaxy cluster and is for this reason very well studied. In longer wavelengths, a radio halo was discovered in the centre (Feretti & Giovannini 1998), confirming the existence of a non-thermal activity. The discovery of a non-thermal hard X-ray excess, published in works of both BeppoSAX (Fusco-Femiano et al. 1999, 2004) and RXTE (Rephaeli et al. 1999; Rephaeli 2001; Rephaeli & Gruber 2002) instruments, is still disputed Ajello et al. (2008).

The cluster was observed by H.E.S.S. in April and May 2006 for a total of 11.1 hrs. The total livetime passing data-quality selection amounts to 8.2 hrs. (out of this, 0.9 hrs. of lower-efficiency 3-telescope data). No significant signal is found. The results, together with other clusters, are summarized in the Tab. 6.4. Some of the results were published in Domainko et al. (2007).

Abell 754

Abell 754 has high X-ray luminosity and total mass ($\sim 1.8 \times 10^{15}\ M_{\odot}$) comparable to the Coma cluster, but it is approximately twice as distant (z = 0.053). It is a prototypical merger cluster with a complicated internal structure (Markevitch et al. 2003). X-ray observations confirm a violent merger activity (Henry & Briel 1995) and was found to be significantly non-isothermal (Henriksen & Markevitch 1996). It is a typical example of a galaxy cluster far from equilibrium (contrary e.g. to the very relaxed and symmetrical Abell 496). Numerical simulations of the merger activity suggest that the merger could be a recent one (Roettiger et al. 1998, ~ 0.5 Gyr according to). Radio emission was detected (Fusco-Femiano et al. 2003), proving an existence of non-thermal particles. Non-thermal X-ray emission was also claimed from this object (Fusco-Femiano et al. 2003), seem to

Figure 6.8: *A deep-field view of the rich galaxy cluster using the Coma Canada-France-Hawaii Telescope. A BVR trichromic image of a region $0.72^\circ \times 0.82^\circ$ is shown. North is up and East is left (Figure from Adami et al. 2006)*

be however ruled out by recent findings of the *Swift-BAT* instrument (Ajello et al. 2008). All of this activity suggest an existence of strong large-scale shocks, which is bound to accelerate cosmic rays.

The target was observed by the H.E.S.S. array in January, February and April 2008 for 11.2 hrs. Out of this, 10.5 hrs. pass quality selection criteria, which after a dead-time correction amounts to 9.6 hrs. of livetime (out of this, 0.4 hours are 3-telescope data).

Centaurus cluster

Centaurus cluster (Abell 3526) is at z=0.01 the nearest hot cluster (with T> 3 keV). It is characterized by an extraordinarily high metallicity, which according to Fabian et al. (2005) exceeds 2.5 times the solar value. The high abundance of heavy elements is a sign of an increased SN activity that implies acceleration of CRs in the SNRs and termination shocks of the galactic winds driven by supernovae. The central part is relatively relaxed, but the cluster shows signs of previous merger activity (Allen & Fabian 1994).

The object was observed by the H.E.S.S. array in February 2007 for 4.6 hours. After the run selection and dead-time correction, the livetime used is 3.8 hours (out of which 0.3 hours are with a 3-telescope array).

Hydra A

Hydra A (3C 218) is a typical example of a close (z=0.055) cluster of galaxies showing a cluster-scale AGN outburst (Nulsen et al. 2005). This phenomenon involves a powerful AGN that is a source of collimated bidirectional outflows that can be observed in radio energies (see e.g. Owen et al. 2000). The outbursts are responsible for creating large-scale cavities around the central AGN. At the interface with the ambient medium, a shock is formed that is observed in X-ray energies Nulsen et al. (2005). By a simple modeling of the outflow, Nulsen et al. (2005) find that the necessary driving energy is $\sim 10^{61}$ ergs. In the case of Hydra A, it seems likely that the cavities are supported by a cosmic-ray pressure (Hinton et al. 2007), which in turn means a very high energy content of non-thermal particles. In the work of Hinton et al. (2007), it is argued that the cosmic rays are of a hadronic origin and could be detectable by the current generation of IACTs.

The observations were performed in March and April 2007 for 11.1 hours. Of this, 5.0 hours of good dead-time corrected data was used for the analysis (0.4 hours of 3-telescope data).

6.1.5 Summary of H.E.S.S. results aimed at galaxy clusters

The results of the galaxy clusters mentioned above are summarized in Tab. 6.4. No significant signal is found. The table shows significances of observed γ-ray excesses, together with upper limits on the integral flux above the energy thresholds. All upper limits are calculated at 99.9% confidence level and assuming a power-law γ-ray spectrum with spectral index $\Gamma = 2.1$.

6.1.6 Conclusion of VHE observations of clusters of galaxies

As a conclusion, galaxy clusters remain undetected in VHE γ-rays, but H.E.S.S. observations allowed us to draw physically interesting conclusions regarding the non-thermal particles in galaxy clusters. In case of Abell 496 and Abell 85, the results were used to constrain the non-thermal energy content in the clusters. These results, constraining the non-thermal to thermal energy content to 8% in the case of the favored parameters of Abell 85, are already very challenging for theoretical models — some of which predict this ratio to be $\sim$50% (Miniati et al. 2001; Ryu et al. 2003). Taking this, and also the estimated fluxes (see section 3.1.5) that are comparable with the upper limits, into consideration, gives an optimistic outlook into the future with hope for a detection in either a very long H.E.S.S. exposure or with the planned CTA or AGIS projects.

Table 6.4: *A summary of observations of galaxy clusters with the H.E.S.S. experiment in the VHE energy band. Tabulated are integral flux upper limits at a 99.9% confidence level (according to Feldman & Cousins 1998), assuming a spectral index* $\Gamma = 2.1$.

Galaxy cluster	$T_{\rm live}$ [h]	$\langle ZA \rangle^a$ [°]	Offset [°]	$E_{\rm thresh}$ [GeV]	θ^b [°]	Excess	S [σ]	$F_\gamma^{UL}(> E_{\rm thresh})$ [10^{-13}cm^{-2} s^{-1}]	Crab^c [%]
Abell 496	14.6	27.8	0.7	570	0.10	5.9	0.8	4.8	0.9
					0.42	24.6	0.6	7.2	3.2
					0.60	29.0	0.5	24.0	4.6
Abell 85	32.5	17.6	0.7	460	0.10	-8.5	-0.7	3.9	0.5
					0.49	-32	-0.4	15.0	2.0
Abell 85 relic					0.1	13.5	1.1	4.1	0.6
Abell 85 south					0.1	-6.9	-0.6	3.6	0.5
Coma	8.2	53.8	0.7	2250	0.10	-5.1	-1.0	2.3	3.8
cluster					0.20	-8.9	-0.8	2.4	3.9
					0.40	-10.5	-0.4	5.7	9.3
Abell 754	9.6	16.2	0.7	460	0.10	5.4	0.8	5.5	0.8
					0.60	-53.0	-1.0	36.6	5.0
Centaurus	3.8	19.9	0.7	480	0.10	-5.6	-1.4	15.7	2.3
cluster					0.40	-22.5	-1.1	29.6	4.3
Hydra A	5.0	12.5	0.7	440	0.10	-7.5	-1.6	10.5	1.3
					0.41	1.5	0.1	31.5	4.1

[a] Mean zenith angle of the observations
[b] Radius of the on-source region used for extracting the signal
[c] Fraction of the integral flux of the Crab Nebula above the energy $E_{\rm thresh}$, as measured by Aharonian et al. (2006a).

6.2 Starburst galaxies

Starburst galaxies are galaxies characterized by a very enhanced star-formation activity in the central region. In section 3.2, it was shown that the high density of hadronic cosmic rays in these objects, along with high density of a target material, could lead to VHE γ-ray fluxes detectable by e.g. H.E.S.S.. A starburst galaxy NGC 253 was identified to be the best candidate for such emission that can be observed from the southern hemisphere (a similar object in the northern hemisphere is M 82). In this section, the results of H.E.S.S. observations of starburst galaxies NGC 253 and M 83 are summarized. The focus is placed on NGC 253, which is the best candidate for H.E.S.S.. First, the object characteristics are reviewed, followed by the VHE observations and results.

6.2.1 NGC 253

NGC 253 is a typical example of a starburst galaxy (Rieke et al. 1980). Located at $\sim$2.5 Mpc (the uncertainty is discussed further in text), it is one of the nearest starburst objects. The continuum spectrum of the galaxy is dominated by the FIR energy band around 100 μm, which is typical for regions with a high dust content.

Distance of NGC 253

The distance of the object is a crucial quantity for estimating the non-thermal properties in a quantitative way. There have been several publications presenting various distance estimates that substantially differ from the traditional value 2.5 Mpc. Rekola et al. (2005) reviews four different distance estimation methods. Globular cluster luminosity function analysis yields an estimate of 3.6 ± 0.7 Mpc, and Davidge et al. (1991) use AGB stars to obtain a maximum value of 2.5 Mpc. The tip of the red giant branch is used in Karachentsev et al. (2003) to get a value $D = 3.9 \pm 0.4$ Mpc, while Rekola et al. (2005) use the luminosity function of 14 planetary nebulae in NGC 253 to calculate the distance $3.34^{+0.26}_{-0.38}$ Mpc. After excluding AGB stars method because of its considerable error, a weighted average of the remaining most reliable measurements is calculated, yielding $D = 3.52 \pm 0.18$ Mpc (Rekola et al. 2005). Most of the parameters were derived for a distance of 2.5 or 2.6 Mpc, because these values are typically assumed in the cited works. If not, it is explicitly stated in the text.

High SN rate

Supernovae are believed to be the main driving force of cosmic-ray acceleration in starburst galaxies. The knowledge of SN rate is thus crucial for estimating all non-thermal processes. In order to estimate the SN rate in the central region we rely on IR observations. The FIR luminosity is assumed to be directly proportional to the SN rate. In the work of Van Buren & Greenhouse (1994), it is shown[4] that the supernova rate $r_{\rm SN}$ can be directly estimated from observations using a relation $r_{\rm SN} \approx 2 \times 10^{-12} L_{\rm FIR,\odot} {\rm yr}^{-1}$.

[4]The calculation is based on a modeling of radio emission from supernova blast waves expanding into the ejecta of their precursor stars. For details see Van Buren & Greenhouse (1994).

IR observations

NGC 253 exhibits a strong IR luminosity and is thus well studied in this energy band. The morphology of the IR emission using IRAS and ISOPHOT instruments was addressed by Melo et al. (2002), who also measured the total IR luminosity to be $L_{\rm IR} = (41.1 \pm 1.6) \times 10^9 L_\odot$. The high spatial resolution of ISOPHOT allowed them to measure the emission from the central $1'$ region, which reaches one half of the total emission, with $L_{\rm IR}^{\rm central} = (20.9 \pm 1.5) \times 10^9 L_\odot$. The central arcmin region itself thus accounts for the same $L_{\rm IR}$ as our own Galaxy (Dudley & Wynn-Williams 1999).

The FIR luminosity obtained by Telesco & Harper (1980) is $L_{\rm FIR} = 2.8 \times 10^{10} L_\odot$, yielding ∼0.06 SN/yr. Other results of SN rate for NGC 253 range between 0.1 and 0.3 $\rm yr^{-1}$ (Rieke et al. 1988). The total star formation rate (SFR) is estimated to be 5 $M_\odot$, with 70% coming from the nuclear starburst (Melo et al. 2002) - (assuming D=3.4 Mpc).

Galactic wind

The galaxy harbours a galactic wind (McCarthy et al. 1987; Zirakashvili & Völk 2006), driven mainly by the hot gas. The galactic wind creates a cavity of hot gas, which expands into the cool ambient medium. At the interface of the two environments, a strong shock is created (McCarthy et al. 1987).

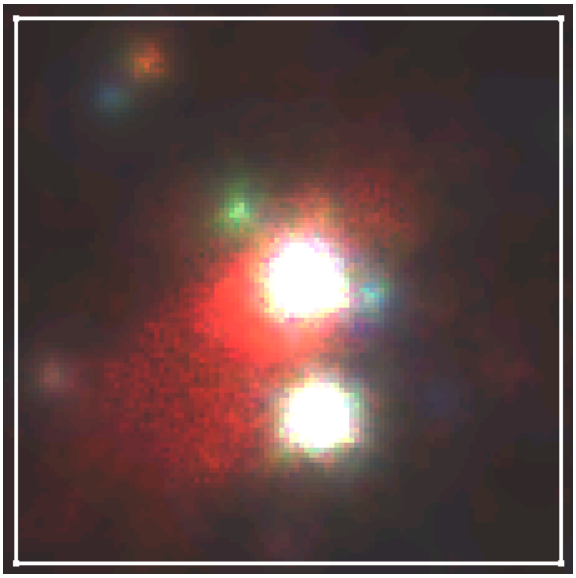

Figure 6.9: *A color coded three-band X-ray image from the XMM-EPIC instrument, showing the central 2'×2' region. The energy bands used were 0.3–2.0 keV (red), 2.0–4.0 keV (green) and 4.0–10.0 keV (blue). The galactic wind can be clearly seen (the red diffuse region), together with several point sources (figure from Barnard et al. 2008).*

In order to estimate *CR convective losses* through the wind, it is necessary to know the wind speed $V_{\rm wind}$. Zirakashvili & Völk (2006) provide an improved estimate of the speed, which is used for calculations in this work. They derive an analytical model for the outflow from the disk and use it to fit radio observations (Mohan et al. 2005). As a result, they estimate $V_{\rm wind} = 900^{+1100}_{-400}$ km $\rm s^{-1}$.

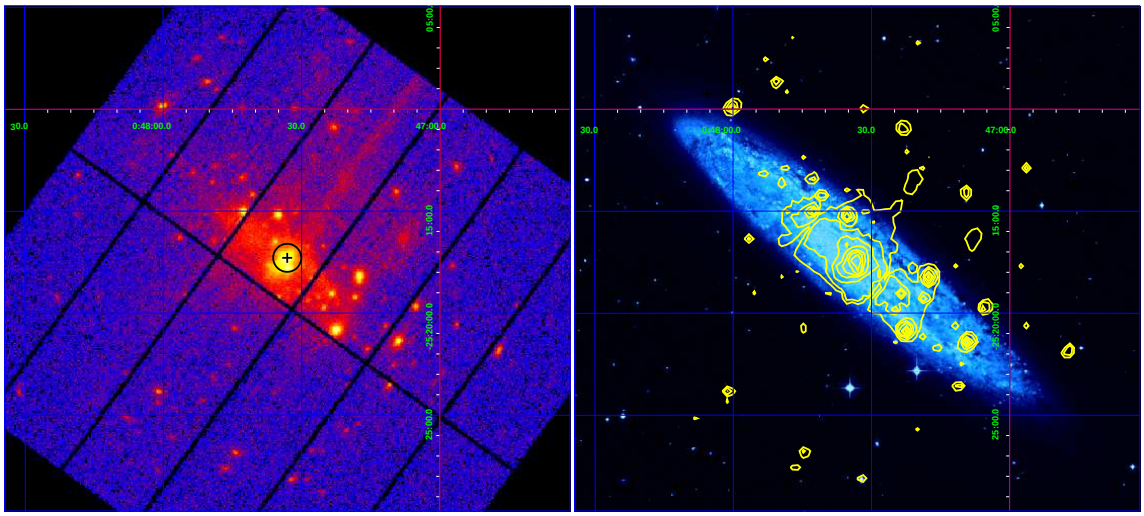

Figure 6.10: Left: *X-ray image of NGC 253 from XMM EPIC instrument. The black cross denotes the nominal position of the central starburst region. The black circle shows central 13.8', corresponding to ∼10 kpc assuming distance of 2.5 Mpc.* **Right:** *Optical image of the whole galaxy NGC 253 from the Digital Sky Survey (UK Schmidt 4680 Å). Overlaid in yellow are X-ray contours from XMM EPIC.*

Central starburst region

The central starburst region is responsible for most of the non-thermal activity in the galaxy. The relevant parameters of the nuclear region are summarized in Table 6.2.1.

Table 6.5: *Parameters of the starburst region of NGC 253 assuming distance 2.5 – 2.6 Mpc*

Parameter	Abbr. in text	Value	Reference
Distance	D	2.5 Mpc	(a)
Mass	M	$4 \times 10^7 - 3 \times 10^8\ M_\odot$	(b)
Supernova rate	$\nu_{\rm SN}$	0.03 - 0.08 $\rm yr^{-1}$	(c)(d)
Radius	R[5]	150 pc	(e)
Height	H	60 pc	(e)
Magnetic field	B	$<270\ \mu$G	(e)
Wind speed	$\rm V_{wind}$	900 km $\rm s^{-1}$	(f)

(a) Puche & Carignan (1988), (b) Mauersberger et al. (1996), (c) Engelbracht et al. (1998), (d) Van Buren & Greenhouse (1994), (e) Weaver et al. (2002), (f) Zirakashvili & Völk (2006)

NGC 253 has already been previously observed at TeV energies by HEGRA and CANGAROO. The HEGRA Collaboration observed the target for 32.5 hours and derived a 99% upper limit of $F_\gamma(> 5.2\,\rm TeV) < 1.3 \times 10^{-13} \rm cm^{-2}\,s^{-1}$(Götting 2005). The CANGAROO-II experiment initially claimed a detection (Itoh et al. 2002) of a steep spectrum (spectral index $\Gamma = 3.85$) source (Itoh et al. 2003) with integral flux above 400 GeV of $\approx 1.4 \times 10^{-11}$ $\rm cm^{-2}$ $\rm s^{-1}$ (∼16% Crab flux). The result was contradicted by results of a more sensitive

H.E.S.S. instrument that derived a 99% upper limit on the integral flux of 1.9×10^{-12} photons cm^{-2} s^{-1}, assuming a spectral index $\Gamma = 3.85$ (Aharonian et al. 2005a). The results of CANGAROO were corrected in a subsequent work of the CANGAROO-III experiment (Itoh et al. 2007), where an upper limit of 5.8% Crab flux at 0.58 TeV was found. Results of the H.E.S.S. observations with a reduced dataset were also published in Nedbal (2007).

VHE observations and analysis

The observations of the target with the full H.E.S.S. array of 4 telescopes were performed in August to November 2005 (29.3 hours) and in October to November 2007 (55.4 hours) for a total of 84.7 hours. Of this time, 36.8 hours of live good-quality data are used for the following analysis. The quality of the remaining data was mostly deteriorated due to a dusty atmosphere in 2007. The observations were performed in a *wobble mode* (mean observations offset 0.6°) and using a small zenith angle, with the mean of 12°. This corresponds to a post-analysis energy threshold of $E_{\rm th} = 440$ GeV (using hard cuts).

The object was analyzed using the standard analysis procedure described in chapter 4.2. The extension of the source is expected to be point-like for the H.E.S.S.instrument. The signal is assumed to come mostly from the central starburst region of size ∼100 pc, which corresponds to ∼8″. The second possibility mentioned was the potential CR flux from the superwind termination shocks that can be located at a distance of several kpc from the nucleus, corresponding to ≈2'. Both of these regions are well below the H.E.S.S. angular resolution of ∼0.1°and represent thus *point sources*. Hard cuts (see section 4.6.4) were used for the analysis due to the expected low flux and hard spectrum. In order to reduce the PSF, the Algorithm 3 (see section 5.3.1) was used for the direction reconstruction of events.

Results

As a result, 35 excess γ-ray photons were detected above the threshold energy of 440 GeV, corresponding to a signal significance of 2.8 σ. No significant signal is thus found from the position of NGC 253. A signal of $\sim 3\sigma$ is generally in TeV astronomy not accepted as significant, can be however considered as a hint of a signal.

The 2.4°×2.4° map of the γ-ray excess around the target position is shown in the left panel of Fig. 6.11. The right panel of the figure shows an enlarged version of this excess map, together with X-ray contours from XMM-EPIC. The latter figure shows that the ∼3-σ hint of a signal coincides directly with the reference position of NGC 253 and with the X-ray emission.

A significance map of the region around the target is shown in the top panel of Fig. 6.12, along with the distribution of significances in the same region. The middle row of the figure depicts the rise of the accumulated significance (left) and excess (right) in time. Although not strictly behaving as expected from a real signal, a rising tendency can be observed.

The angular displacement θ of the ON and OFF events from the nominal target position is depicted in Fig. 6.12. The hint of a signal is visible within the integrating region defined by $\theta = 0.1$.

With the low significance of the hint of a signal, it is not possible to derive a reliable

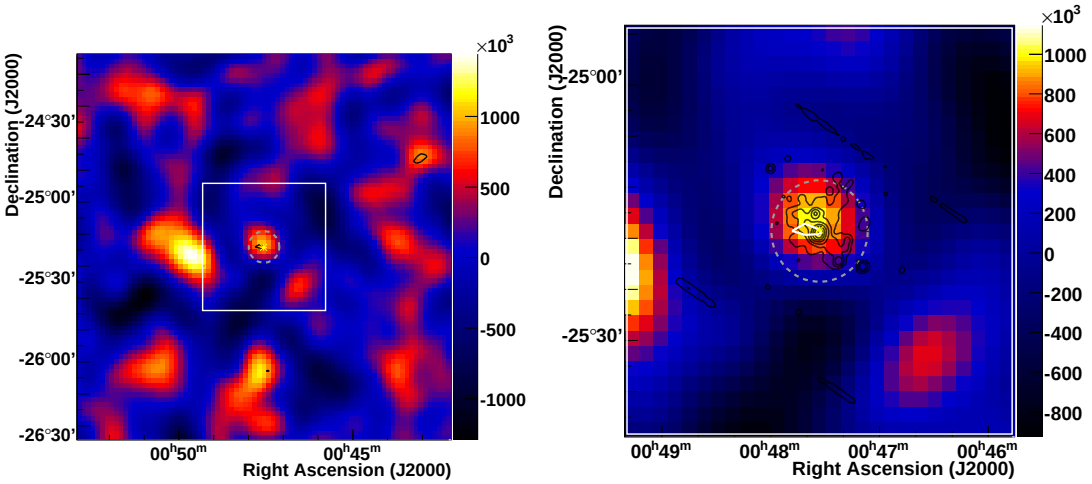

Figure 6.11: Left: *The figure shows an oversampled gamma-ray excess in a* $2.4°\times2.4°$ *region around NGC 253. The black contours correspond to a 3-*σ *significance level. Grey dashed circle shows the 0.1° integration region, used for extracting the signal. The white box illustrates the region shown in the right panel. The spot with an increased excess to the east from NGC 253 is not significant (see the black 3*σ *contours).* **Right:** *Linearly scaled plot from the left panel. A region of* $0.8°\times0.8°$ *is shown. Additionally, the contours represent XMM-EPIC MOS X-ray smoothed counts in the 0.2–12 keV energy band (Pietsch et al. 2001). The 3-*σ *VHE contours are shown in white.*

spectrum. Nevertheless, by analysis of the energetic distribution of the excess, it is possible to gain a spectral information about how hard the excess is relatively to the background. The Fig. 6.13 shows that the differential excess per energy bin rises to a maximum at 1 TeV and decreases at larger energies. Also the significance of the signal peaks for a signal integrated in energy range 1–∞ TeV. The significance approaches 4.6σ for these energies, which is close to a detection (without considering statistical trial factors). This result is very promising for further observations.

Flux upper limits

Using the results, upper limits are derived, constraining the VHE γ-ray flux. The 99.9% upper limit on the integral flux above the threshold energy $E_{\mathrm{thresh}} = 440$ GeV was calculated to be $F_\gamma(> 440\ \mathrm{GeV}) < 6.3 \times 10^{-13}$ (0.8% of the Crab flux) and above 1 TeV as $F_\gamma(> 1\ \mathrm{TeV}) < 3.7 \times 10^{-13}$ (1.6% of the Crab flux). Both results were calculated assuming a power-law photon index $\Gamma = 2.1$. Note that the upper limit is increased due to the $\sim 3\sigma$ excess that is highest around 1 TeV (see the discussion further). In order to evaluate the effect of this positive excess, an additional upper limit was calculated assuming a zero excess. This corresponds to the sensitivity of the instrument for this dataset and was calculated to be $F_{\mathrm{sens}}(> 440\ \mathrm{GeV}) = 2.8 \times 10^{-13}$ (0.35% of the Crab flux). In order to investigate the energy dependency, the integral flux upper limits and the sensitivity curve are plotted as a function of the minimum energy in Fig. 6.14.

If the signal is real, the estimated flux level is $F(> 440\ \mathrm{GeV}) < (2.9 \pm 0.9) \times 10^{-13}$ (0.4% of the Crab flux) and $F(> 1\ \mathrm{TeV}) < (1.9 \pm 0.4) \times 10^{-13}$ (0.8% of the Crab flux)

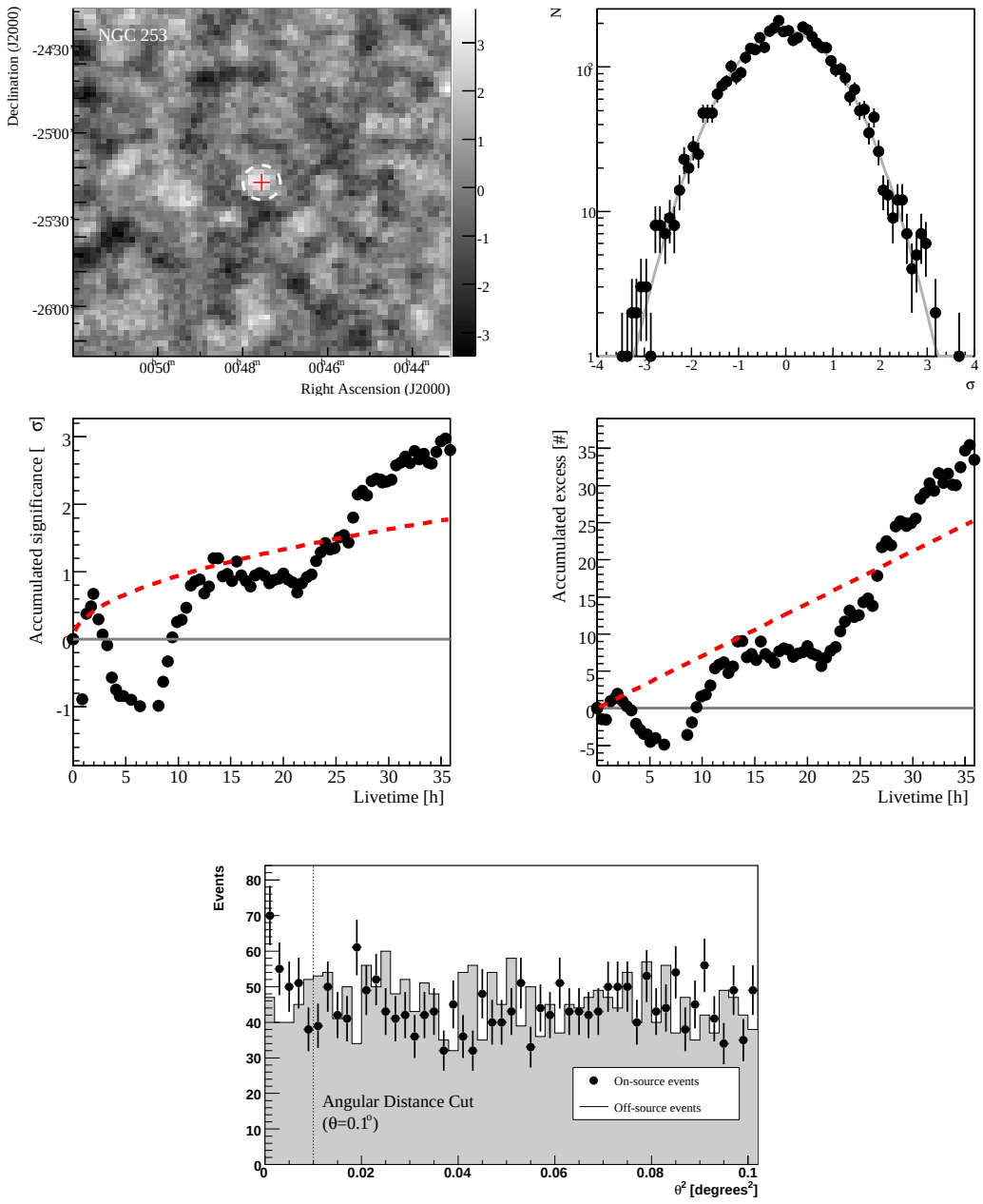

Figure 6.12: *Results of observations of NGC 253. Top left: A significance map showing a* $1.8°\times1.8°$ *region around NGC 253. White dashed circle represents the point-source integration radius (0.1°) and the red cross the nominal position of NGC 253. Top right: The distribution of significances in the region shown in the left panel is shown. It is fitted by a Gaussian with a fixed RMS of 1 and a fixed mean of 0 (*$\chi^2/NDF = 74.7/66$*). Middle left: Accumulated significance as a function of time, fitted by the expected signal rise of a form* $f(t) = a\sqrt{t}$*. each point represent one observation run of duration <28 min. Middle right: Accumulated excess, fitted by a linear function* $f(t) = b\,t$*. Bottom: Distribution of ON and OFF events as a function of the square angular distance from the nominal position of NGC 253. A flat distribution of ON events consistent with the level of OFF events is expected in case of no signal.*

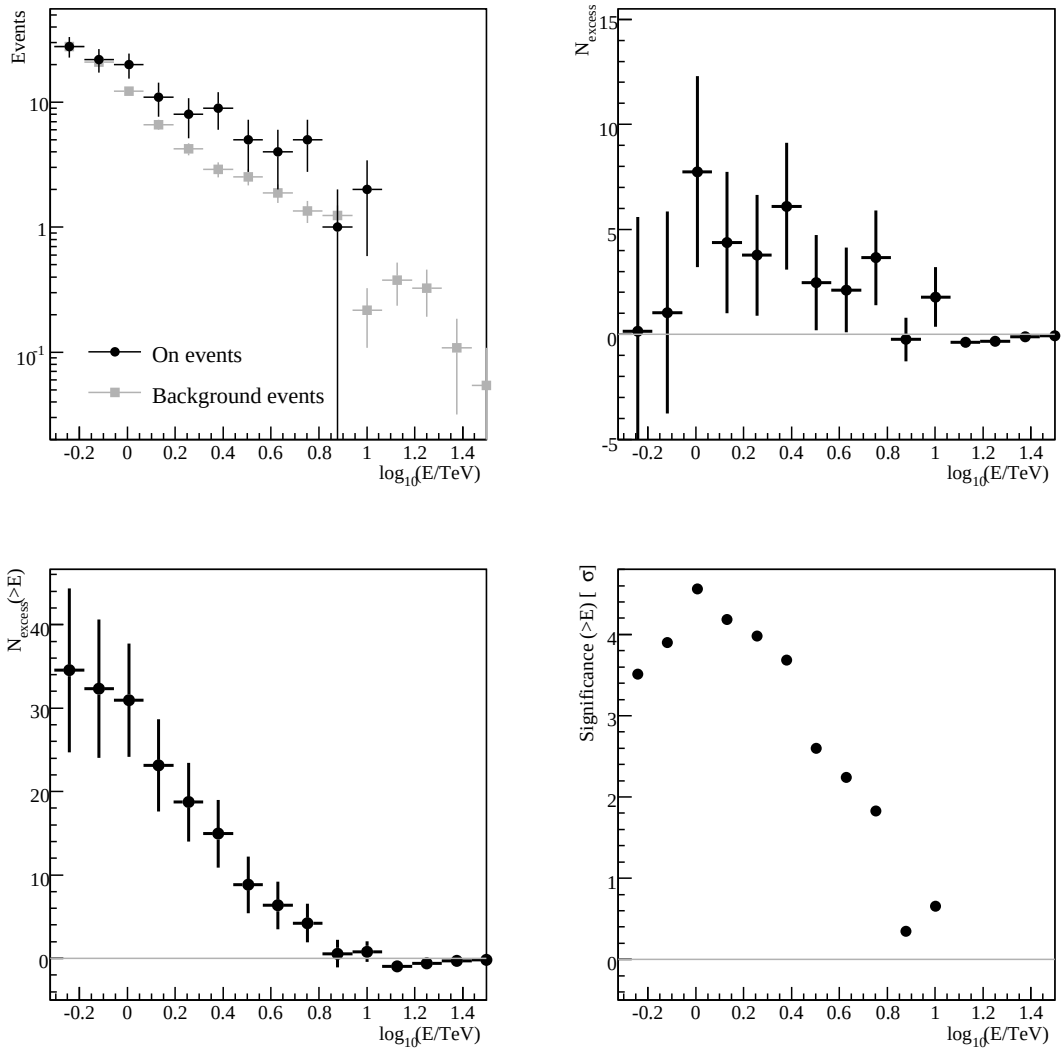

Figure 6.13: *Top left: Energy distribution of the on-source (red) and background (blue) events. Background events were extracted from the reflected control regions and normalized to the same acceptance as the on-source events. Top right: Number excess per energy bin. The horizontal error bars denote the bin size. The figure shows that the excess is positive over the whole energy range and peaking around 1 TeV. Bottom left: Integrated excess above energy E. Bottom right: Significance of the excess above energy E. The significance peaks again around 1 TeV.*

assuming the spectral index $\Gamma = 2.1$.

Discussion

Based on the current observations, no detection can be claimed, and additional data are necessary to decide whether the VHE signal is real. Given the observed $S_0 = 2.8\ \sigma$ excess in T_0 =36.8 hours, further observation time T, necessary for a 5-σ detection assuming a

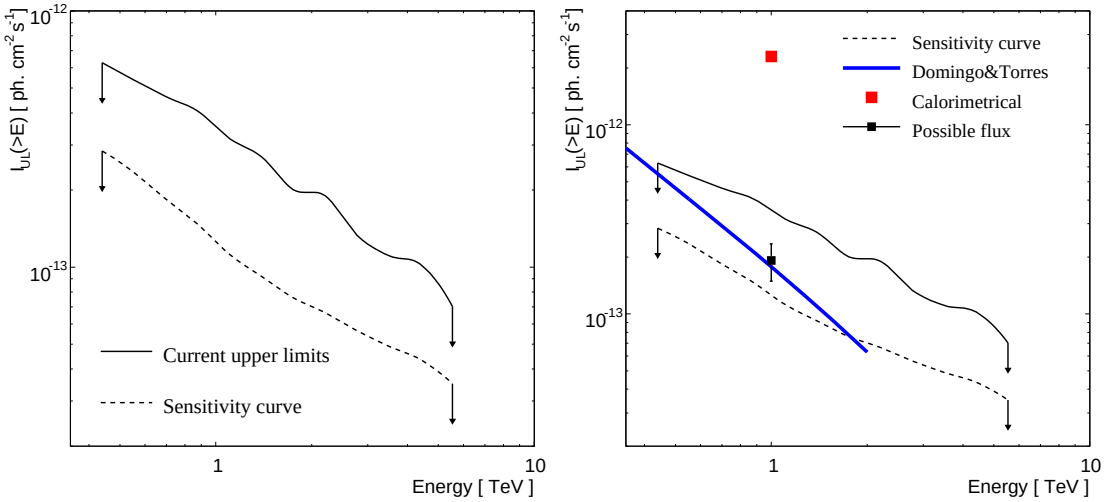

Figure 6.14: *Left: Integral flux upper limits as a function of the minimum energy (solid line). Dashed line represent the upper limit corresponding to a zero excess (see text). Right: The upper limits are compared to the estimate of Domingo-Santamaría & Torres (2005) for their preferred starburst parameters and to the calorimetrical estimate of equation (3.11). This estimate assumes that all CR proton energy is lost in inelastic pp collisions. The calorimetrical estimate is thus ruled out by the upper limits. Also shown is a point corresponding to a flux estimate, if the observed excess should be real. The point is thus no claim of a detection.*

rise of significance according to the relation $\propto \sqrt{t}$, would be:

$$T = T_0 \left[\left(\frac{5}{S_0} \right)^2 - 1 \right] \approx 80 \text{ hrs.} \tag{6.1}$$

This represents a substantial amount of observation time, compared to the total available time per year (∼1000 hrs. of observations). It is however still feasible due to the low competition of other candidate sources in the R.A. band of NGC 253.

The derived upper limits are compared to the estimate by Domingo-Santamaría & Torres (2005) in Fig. 6.14 and to the calorimetrical estimate of eq. (3.11) presented in the section 3.2.3. The following conclusions can be drawn from this comparison:

1. The upper limit at 1 TeV is by a factor of more than 6 lower than the calorimetrical estimate. The uncertainty of this estimate is dominated by the unknown efficiency η of the conversion of SN kinetic energy into CR energy[6]. The uncertainty is however unlikely to be as large as a factor 6 (e.g. Zirakashvili & Völk (2006) derives $\eta \sim 0.15$ as opposed to the value 0.1 used for the modeling here). The results thus allow one to draw a conclusion that the cosmic-rays in the starburst region don't behave calorimetrically and the escape due to convection and diffusion is significant.

2. The upper limits are above the estimates of Domingo-Santamaría & Torres (2005). Here, it has to be noted again, that the upper limits are derived using data with a ∼

[6] Note that the uncertain distance D doesn't play any role for this estimate, because it is only proportional to the observed IR flux.

3σ signal. If the signal should be proven to be real, the flux level corresponding to this excess is also shown in the figure. It is surprisingly consistent with the estimates of Domingo-Santamaría & Torres (2005). Note that the zero-excess sensitivity curve for this dataset is considerably below the prediction. Further observations are therefore desirable that would allow to either derive either a stronger upper limit that could constrain the model, or detect the possible signal.

6.2.2 M 83

M 83 (NGC 5236) is a close bright spiral galaxy, located at a distance of ∼4.5 Mpc (Thim et al. 2003). It is viewed at a nearly face-on angle $i = 24°$ (de Vaucouleurs et al. 1991) and shows a high metallicity (∼twice solar according to Bresolin & Kennicutt 2002). A semicircular starburst region lies $3'' - 8''$ from the photometric peak of the galaxy.

VHE Observations and results

Observations of M 83 with the H.E.S.S. array were performed in July 2006 for 12.0 hours. Out of this, 9.2 hours pass the data-quality selection, corresponding to a dead-time corrected 8.2 hours of data used for analysis. The mean observation zenith angle was 24°, which after hard cuts translates into an energy threshold of ∼560 GeV.

Heard cuts and a point-source integration region were used in the analysis. As a result, no hint of a signal was found. The measured integrated γ-ray excess is 0.5 events, corresponding to 0.06 standard deviations. The significance map is shown in Fig. 6.15. Using the result, an upper limit on the integral flux was derived $F_\gamma^{UL}(> 560 \text{ GeV}) = 6.7 \times 10^{-13}\text{cm}^{-2}\,\text{s}^{-1}$(1.2% flux of the Crab Nebula above the same threshold).

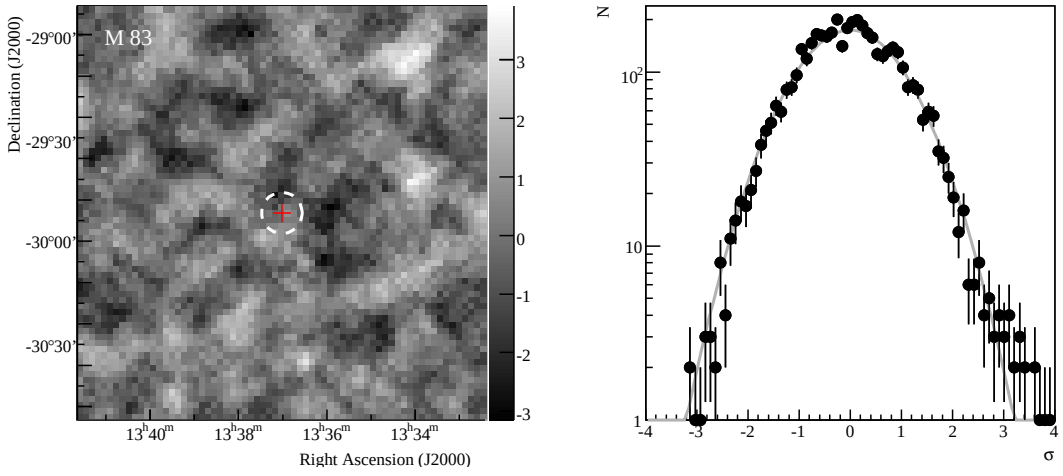

Figure 6.15: Left: *A significance map showing a region of 2°×2° around the nominal position of M 83 (red cross). The map was produced using a ring background method and using a point-source integration region with radius* 0.1°. *No significant signal is found in the field-of-view.* **Right:** *A significance distribution in the region shown in the left panel. The gray line shows a Gaussian fit with a mean of 0 and RMS of 1. The* $\chi^2/NDF = 92.5/70$.

6.3 The ultraluminous infrared galaxy Arp 220

Ultraluminous infrared galaxies are galaxies with total IR luminosity higher than 10^{12} $L_{\odot}$. In section 3.3, it is shown that these objects could also be sources of VHE γ-ray flux. The ULIRGs are in this work represented only by Arp 220. All other ULIRGs are significantly more distant and their observations are thus not as promising as in the case of Arp 220. The galaxy is first described, then the results are presented.

6.3.1 Arp 220

Arp 220 (IC 4553) is the closest (z=0.018 corresponding to 77 Mpc) ULIRG with a wealth of multi-wavelength observational data, often described as a prototype of a ULIRG (Sanders et al. 1988). It was recognized as strongly interacting system already by Arp (1966) and Nilson (1973). The object is formed by two distinct nuclei, both experiencing a strong star formation, triggered by an on-going merger of them. The two nuclei are distinguished in radio (Rodríguez-Rico et al. 2005) as well as in IR energies (Soifer et al. 1999). According to the radio results, they are only 0.97″ apart (projected distance 365 pc). Their relatively undisturbed geometry however requires them to be more separated; they are thus believed to be one behind the other (Baan 2007). The geometry of the system can be seen in Fig. 6.3.1

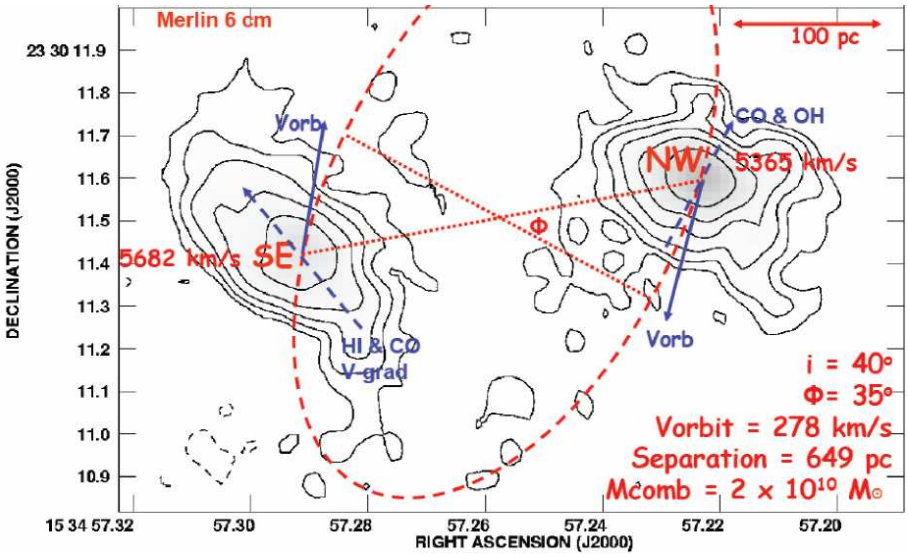

Figure 6.16: *A model of the orbital dynamics in the Arp 220 system superimposed over the 6 cm radio data by an interferometer network of radio telescopes MERLIN (Baan 2007). The two starburst nuclei can be seen, orbiting at an orbital velocity* $V_{\rm orb} = 278$ km s^{-1}. *The north-western nucleus is assumed to be located in front of the south-eastern one. The inclination and direction of motion of the objects is indicated (figure from Baan 2007).*

The system is exceptional for its starburst activity. VLBI 18 cm radio observations reveal a supernova rate of (4 ± 2) yr^{-1}. CO and HCN line observations confirm very high densities of molecular gas and high star formation in the nuclear region. All of these characteristics support an existence of non-thermal cosmic-ray population, which could

produce VHE γ rays, mainly via the π^0-decay channel.

Estimates of the VHE γ-ray flux were presented by Torres (2004) and Torres & Domingo-Santamaría (2005), suggesting that it could be detectable by the current generation of IACTs. Arp 220 was observed by the MAGIC telescope with a negative result (Albert et al. 2007a) and 3-σ upper limits of 10^{-14} ph cm^{-2} s^{-1} GeV^{-1} in energy range 200-400 GeV, i.e. slightly above the estimate of Torres & Domingo-Santamaría (2005).

VHE observations

Observations of this target were performed in April – June 2005 with a total observation time of 15.2 hours. The observation time usable for analysis is 14.7 hours, corresponding to 14.1 hours of live-time. Due to the northern position of the target, the observations were carried out under a high zenith angle of 49°, which leads to an increased energy threshold of ∼1430 GeV (hard cuts).

For the analysis, point-source hard cuts were used. No significant signal was found also in this case. The γ-ray excess was -3 events, corresponding to a signal significance of -0.4σ. Upper limits were derived to be $F_\gamma^{UL}(> 1.43 \text{ TeV}) = 2.5 \times 10^{-13}\text{cm}^{-2}\,\text{s}^{-1}$. It is possible that the potential VHE spectrum could be suffering energy cut-off due to pair-production processes at the source, characteristic by a high photon density. For this reason, also *standard* and *soft* cuts were used (see section 4.6.4 for a definition) that are characterized by a lower energy threshold (720 GeV and 520 GeV respectively) and looser cuts. No signal was found also in this case. The results are summarized in table 6.6.

Table 6.6: *Significance of the VHE excess from Arp 220 using various selection cuts. No hint of a signal is observed.*

Selection cuts	E_{thresh} [TeV]	On	Off[a]	N_{excess}	S [σ]
Hard cuts	1.43	42	722	-2.8	-0.4
Standard cuts	0.72	530	7328	5.2	0.2
Soft cuts	0.52	2015	20197	29.1	0.6

[a]Off-events, extracted from the reflected control regions as defined in the section 4.6.6

The upper limits are plotted in Fig. 6.17 and compared with the theoretical predictions of Torres & Domingo-Santamaría (2005). As a conclusion, the presented upper limits are comparable to the latter estimates. At the energy threshold, the upper limits are already below the estimates by a factor ~ 1.5. Given the theoretical uncertainties of the prediction, it is however not yet possible to place any strong constraints on the model.

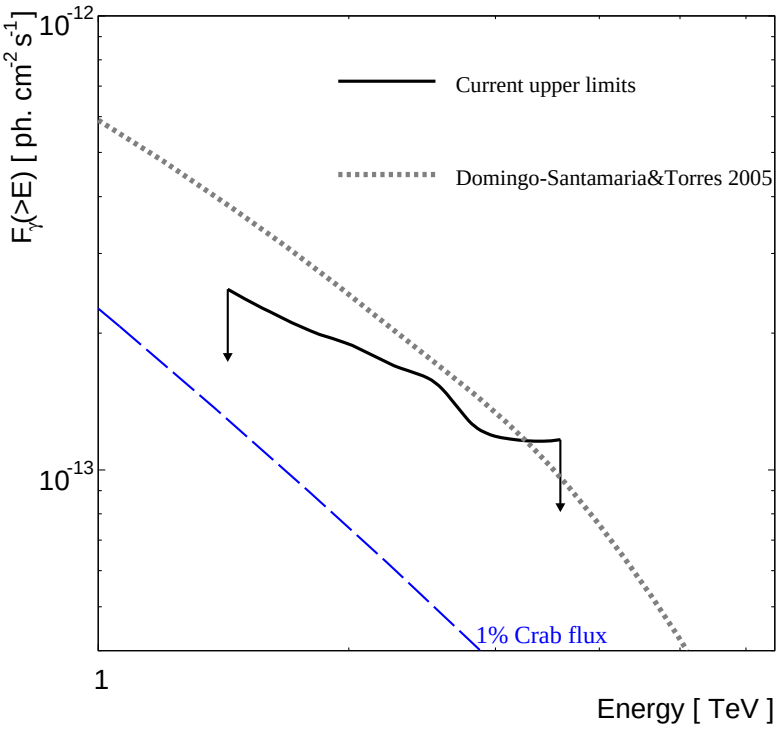

Figure 6.17: *Upper limits on the integral flux of the ULIRG Arp 220. The results are compared to the theoretical predictions of Torres & Domingo-Santamaría (2005) and to the 1% integral flux according to Aharonian et al. (2006a).*

6.4 The Active Galactic Nucleus RGB J0152+017

Active galactic nuclei (AGNs) were described in section 3.4. These objects distinguish themselves from the previous ones, because they represent an already established class of VHE γ-ray emitters. Although AGNs were not the main topic of the thesis, a discovery of one AGN (RGB J0152+017) was accomplished during the work, yielding interesting results. A discovery of RGB J0152+017 — an AGN of an HBL BL Lac type — is thus presented in this section, demonstrating an example of a positive result obtained using the analysis technique described in chapters 4 and 5, and used to derive the previously described results.

6.4.1 Discovery of RGB J0152+017

RGB J0152+017 is an AGN from the Rosat-Green Bank catalogue that combines bright radio and X-ray active galactic nuclei. It was first detected as a radio source (Becker et al. 1991) by the NRAO Green Bank Telescope and in the Parkes-MIT-NRAO surveys (Griffith et al. 1995). Later it was identified as a BL Lac object by Laurent-Muehleisen et al. (1998) and located at a redshift of $z = 0.080$. It was claimed as an intermediate-frequency-peaked BL Lac (IBL - see B for details on distinguishing HBL — IBL — LBL) object by Laurent-Muehleisen et al. (1999).

A first X-ray detection was reported by Brinkmann et al. (1997). The host galaxy is an elliptical galaxy with optical luminosity $M_{\mathrm{R}} = -24.0$ according to Nilsson et al. (2003). Until the H.E.S.S. observations, there was no detailed study or multiwavelength observations performed on this object. The results presented here were announced shortly after the observations (Nedbal et al. 2007) and later published by Aharonian et al. (2008b).

VHE observations

RGB J0152+017 was observed by the H.E.S.S. array from October 30$^{\mathrm{th}}$ to November 14$^{\mathrm{th}}$ 2007. The observations were performed in *wobble* mode with the object located at 0.7°offset from the centre of the field-of-view. A total of 44 runs were taken, yielding 19.5 h of observation time. After applying selection cuts to the data (see 4.5.2) to reject periods affected by poor weather conditions and hardware problems, the total live-time used for analysis amounts to 14.7 h. Out of this, there were 10.2 h with all four telescopes and 4.5 h of three-telescope data. The mean altitude of the observations is 60.1°. [7]

For rejecting cosmic ray background, the *standard* cuts (see Sec. 4.6.4) were employed, if not stated otherwise. The background was estimated using *reflected regions*)(see section 4.6.6).

Results

A signal of 173 γ-ray events is found from the direction of RGB J0152+017. The statistical significance of the signal is 6.6 σ according to Li & Ma (1983). The preliminary detection was reported by Nedbal et al. (2007). A two-dimensional Gaussian fit of the excess yields

[7] The object was re-observed in December 2007, but these data were not used for the results presented in this work since they are subject of an on-going analysis.

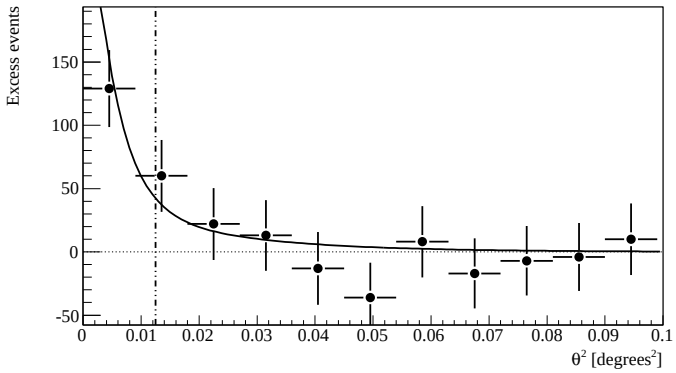

Figure 6.18: *Angular distribution of excess events from RGB J0152+017. The dot-dashed line shows the angular distance cut used for extracting the signal. The excess distribution is consistent with the H.E.S.S. point spread function as derived from Monte Carlo simulations (solid line).*

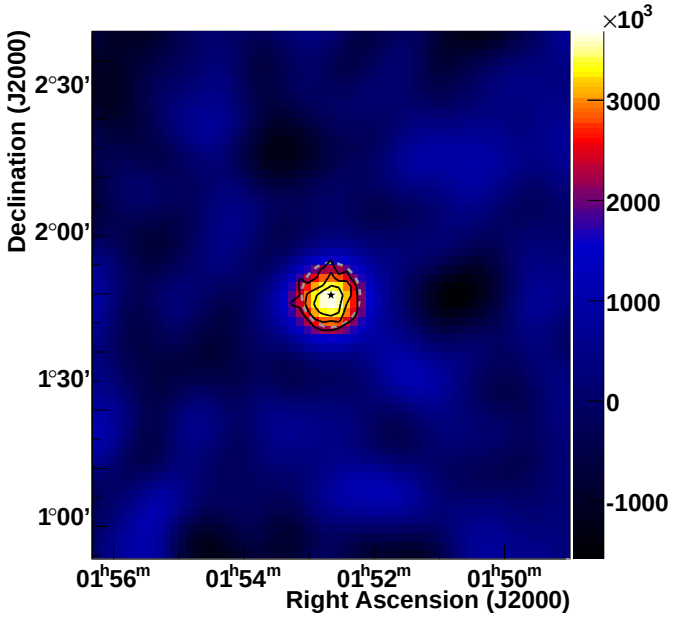

Figure 6.19: *Map showing γ-ray excess from RGB J0152+017 smoothed by the PSF of the instrument. The star denotes the nominal position of RGB J0152+017 and the gray dashed circle shows the integration radius. The black contours show 3, 4 and 5-σ H.E.S.S. significance contours. Only 4-telescope data were used for producing the map.*

a position $\alpha_{\mathrm{J2000}} = 1^{\mathrm{h}}52^{\mathrm{m}}33^{\mathrm{s}}5 \pm 5^{\mathrm{s}}3_{\mathrm{stat}} \pm 1^{\mathrm{s}}3_{\mathrm{syst}}$, $\delta_{\mathrm{J2000}} = 1°46'40''3 \pm 107''_{\mathrm{stat}} \pm 20''_{\mathrm{syst}}$. The measured position is compatible with the nominal position of RGB J0152+017 ($\alpha_{\mathrm{J2000}} = 1^{\mathrm{h}}52^{\mathrm{m}}39^{\mathrm{s}}78$, $\delta_{\mathrm{J2000}} = 1°47'18''70$) at the 1σ level. Given this spatial coincidence, we identify the source of γ-rays with RGB J0152+017. The angular distribution of events coming from RGB J0152+017, shown in the left panel of Fig. 6.18, is compatible with the expectation from the Monte Carlo simulations of a point source.

Spectrum

Figure 6.20 shows the time-averaged differential spectrum. The spectrum was derived using *standard cuts* with an energy threshold of 300 GeV. Another set of cuts, the *spectrum cuts* described in Aharonian et al. (2006b), were used to lower the energy threshold and improve the photon statistics (factor ∼2 increase above the *standard cuts*). Both give consistent results (see right panel in Fig. 6.20 and caption). Because of the better statistics and energy range, we use the spectrum derived using *spectrum cuts* in the following. Between the threshold of 240 GeV and 3.8 TeV, this differential spectrum is described well (χ^2/d.o.f.=2.16/4) by a power law $\mathrm{d}N/\mathrm{d}E = \Phi_0(E/1\mathrm{TeV})^{-\Gamma}$ with a photon index $\Gamma = 2.95 \pm 0.36_{\mathrm{stat}} \pm 0.20_{\mathrm{syst}}$ and normalization at 1 TeV of $\Phi(1\mathrm{TeV}) = (5.7 \pm 1.6_{\mathrm{stat}} \pm 1.1_{\mathrm{syst}}) \times 10^{-13}$ cm^{-2} s^{-1} TeV^{-1}. The 99% confidence level upper limits for the highest three bins shown in Fig. 6.20 were calculated using Feldman & Cousins (1998).

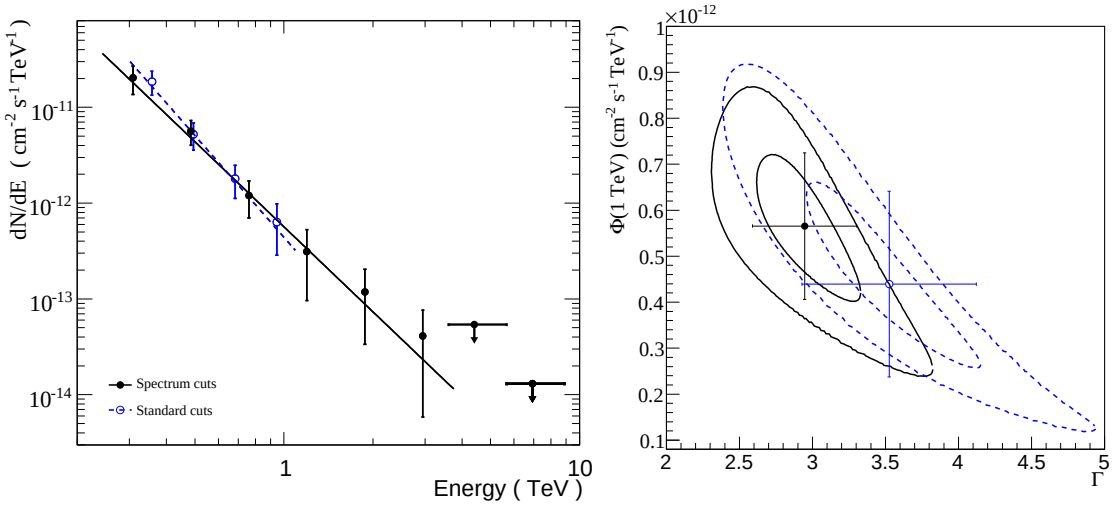

Figure 6.20: Left: *Differential spectrum of RGB J0152+017. The spectrum obtained using* spectrum cuts *(black closed circles) is compared with the one obtained by the* standard cuts *(blue open circles). The black line shows the best fit by a power-law function of the former. The three points with the highest photon energy represent upper limits at 99% confidence level, calculated using Feldman & Cousins (1998). All error bars are only statistical. The fit parameters of a power-law fit are* $\Gamma = 2.95 \pm 0.36_{\mathrm{stat}} \pm 0.20_{\mathrm{syst}}$ *and* $\Phi(1\mathrm{TeV}) = (5.7 \pm 1.6_{\mathrm{stat}} \pm 1.1_{\mathrm{syst}}) \times 10^{-13}$ *cm^{-2} s^{-1} TeV^{-1} for the* spectrum cuts, *and* $\Gamma = 3.53 \pm 0.60_{\mathrm{stat}} \pm 0.2_{\mathrm{syst}}$ *and* $\Phi(1\mathrm{TeV}) = (4.4 \pm 2.0) \times 10^{-13}$ *cm^{-2} s^{-1} TeV^{-1} for the* standard cuts. **Right:** *1 and 2σ confidence levels of the fit parameters.*

Flux and lightcurve

The integral flux above 300 GeV is $F_\gamma(> 300\ \mathrm{GeV}) = (2.70 \pm 0.51_{\mathrm{stat}} \pm 0.54_{\mathrm{syst}}) \times 10^{-12}\mathrm{cm}^{-2}\,\mathrm{s}^{-1}$, which corresponds to ∼2% of the flux of the Crab nebula above the same threshold as determined by Aharonian et al. (2006a). Figure 6.21 shows the nightly evolution of the γ-ray flux above 300 GeV. There is no significant variability between nights in the lightcurve. The χ^2/d.o.f. of the fit to a constant is 17.2/12, corresponding to a χ^2 probability of 14%.

All results were checked with independent analysis procedures and calibration chains giving consistent results.

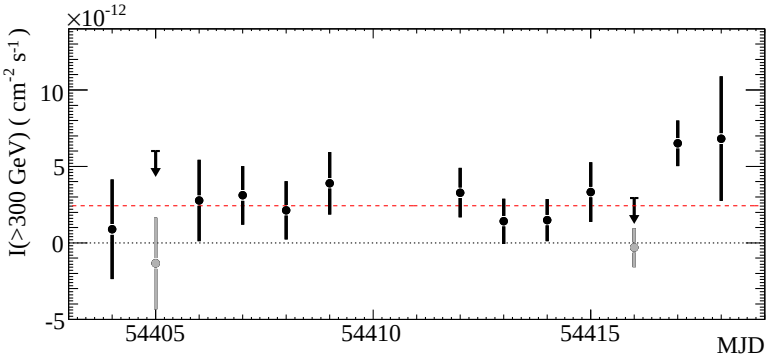

Figure 6.21: *Mean nightly integral flux from RGB J0152+017 above 300 GeV. Only the statistical errors are shown. Upper limits at 99% confidence level are calculated when no signal is found (gray points). The dashed line shows a fit of a constant to the data points with* χ^2/d.o.f. *of* 17.2/12. *The fit was performed using all nights.*

X-ray data from *Swift* and *RXTE*

Target of opportunity (ToO) observations of RGB J0152+017 were performed with *Swift* and *RXTE* on November 13, 14, and 15, 2007 triggered by the H.E.S.S. discovery. The *Swift*/XRT (Burrows et al. 2005) data (5.44 ks) were taken in photon-counting mode. The spectra were extracted with `xselect v2.4` from a circular region with a radius of 20 pixels (0.8′1) around the position of RGB J0152+017, which contains 90% of the PSF at 1.5 keV. An appropriate background was extracted from a region next to the source with four times this area. The auxiliary response files were created with the script `xrtmkarf v0.5.6` and the response matrices were taken from the *Swift* package of the calibration database `caldb v3.4.1`. Due to the low count rate of 0.3 cts/s, any pileup effect on the spectrum is negligible. We find no significant variability during any of the pointings or between the three subsequent days; hence, individual spectra were combined to achieve better photon statistics. The spectral analysis was performed using the tool `Xspec v11.3.2`. A broken power law ($\Gamma_1 = 1.93 \pm 0.20, \Gamma_2 = 2.82 \pm 0.13, E_{\rm break} = 1.29 \pm 0.12$ keV) with a Galactic absorption of $2.72 \times 10^{20}\,{\rm cm}^{-2}$ (LAB Survey, Kalberla et al. 2005) is a good description (χ^2/d.o.f. = 24/26), and the resulting unabsorbed flux is $F_{0.5-2\,{\rm keV}} \sim 5.1 \times 10^{-12}\,{\rm erg\,cm^{-2}\,s^{-1}}$ and $F_{2-10\,{\rm keV}} \sim 2.7 \times 10^{-12}\,{\rm erg\,cm^{-2}\,s^{-1}}$.

Simultaneous observations at higher X-ray photon energies were obtained with the *RXTE*/PCA (Jahoda et al. 1996). Only data of PCU2 and the top layer were taken to obtain the best signal-to-noise ratio. After filtering out the influence of the South Atlantic Anomaly, tracking offsets, and the electron contamination, an exposure of 3.2 ks remains. Given the low count rate of 0.7 cts/s, the "faint background model" provided by the *RXTE* Guest Observer Facility was used to generate the background spectrum with the script `pcabackest v3.1`. The response matrices were created with `pcarsp v10.1`. Again no significant variations were found between the three observations, and individual spectra were combined to achieve better photon statistics. The PCA spectrum can be described by an absorbed single power law with photon index $\Gamma = 2.72 \pm 0.08$ (χ^2/d.o.f. = 20/16) between 2 and 10 keV, using the same Galactic absorption as for *Swift* data. The resulting flux $F_{2-10\,{\rm keV}} \sim 6.8 \times 10^{-12}\,{\rm erg\,cm^{-2}\,s^{-1}}$ exceeds the one obtained *simultaneously* with *Swift* by a factor of 2.5. We attribute this mostly to contamination by the nearby galaxy

cluster Abell 267 (44.6′ offset from RGB J0152+017 but still in the field of view of the non-imaging PCA).

A detailed decomposition is beyond the scope of this paper, so we exclude *RXTE* data from broadband modeling. The *RXTE* data-set confirms the absence of variability during November 2007, also in the energy range up to 10 keV. For the SED modeling, the average spectrum is treated as an upper limit.

Optical data from *ATOM*

Optical observations were taken using the ATOM telescope (Hauser et al. 2004) at the H.E.S.S site from November 10, 2007. The R-band image of the object is seen in Fig. 6.22. No significant variability was detected during the nights between November 10 and November 20; R-band fluxes binned nightly show an RMS of 0.02 mag.

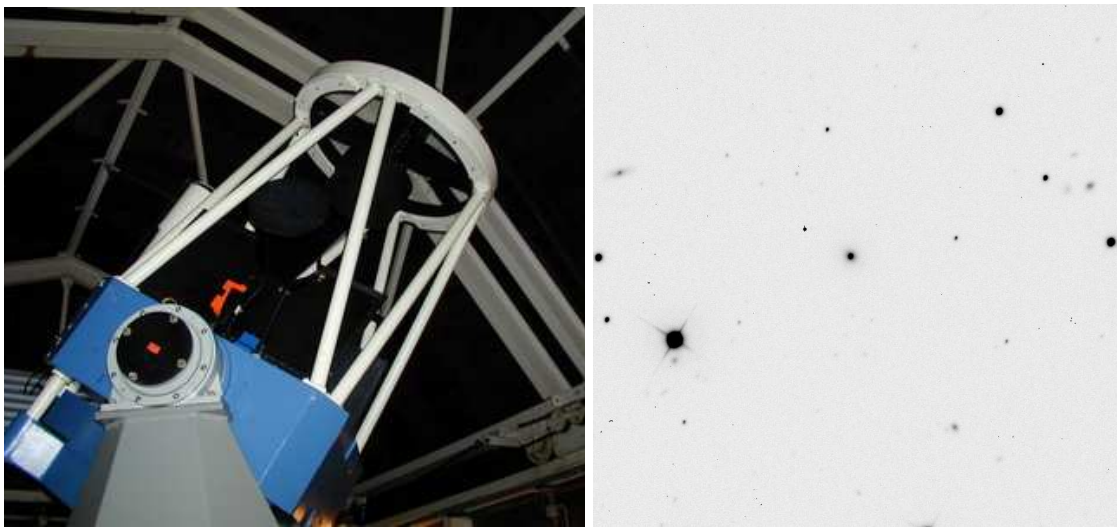

Figure 6.22: **Left:** *ATOM (Atmospheric Telescope for Optical Monitoring, located at the H.E.S.S. site in Namibia.* **Right:** *R-band (640 nm) optical exposure of RGB J0152+017 (the diffuse object in the center). The field-of-view is approx. 7′x7′ (Image by Hauser (2008)).*

Absolute flux values were found using differential photometry against stars calibrated by K. Nilsson (priv. comm.). We measured a total flux of $m_{\mathrm{R}} = 15.25 \pm 0.01$ mag (host galaxy + core) in an aperture of 4″ radius. The host galaxy was subtracted with galaxy parameters given in Nilsson et al. (2003), and aperture correction given in Eq. (4) of Young (1976) was applied. The core flux in the R-band (640 nm) was found to be 0.62 ± 0.08 mJy. This value was not corrected for Galactic extinction.

Radio data from *Nançay Radio Telescope*

The Nançay Radio Telescope (NRT) is a meridian transit telescope with a main spherical mirror of 300 m × 35 m (Theureau et al. 2007). The low-frequency receiver, covering the band 1.8–3.5 GHz was used, with the NRT standard filterbank backend.

The NRT observations were obtained in two contiguous bands of 12.5 MHz bandwidth, centered at 2679 and 2691 MHz (average frequency: 2685 MHz). Two linear polarisa-

tion receivers were used during the 22 60-second drift scan observations on the source on November 12 and 14, 2007. The data have been processed with the standard NRT software packages NAPS and SIR. All bands and polarisations have been averaged, giving an RMS noise of 2.2 mJy. The source 3C 295 was observed for calibration, on November 11, 13, and 15, 2007.

Taking into account a flux density for this source of 12.30 ± 0.06 Jy using the spectral fit published by Ott et al. (1994), we derived a flux density of 56 ± 6 mJy at 2685 MHz for RGB J0152+017. No significant variability was found in the radio data.

Spectral energy distribution

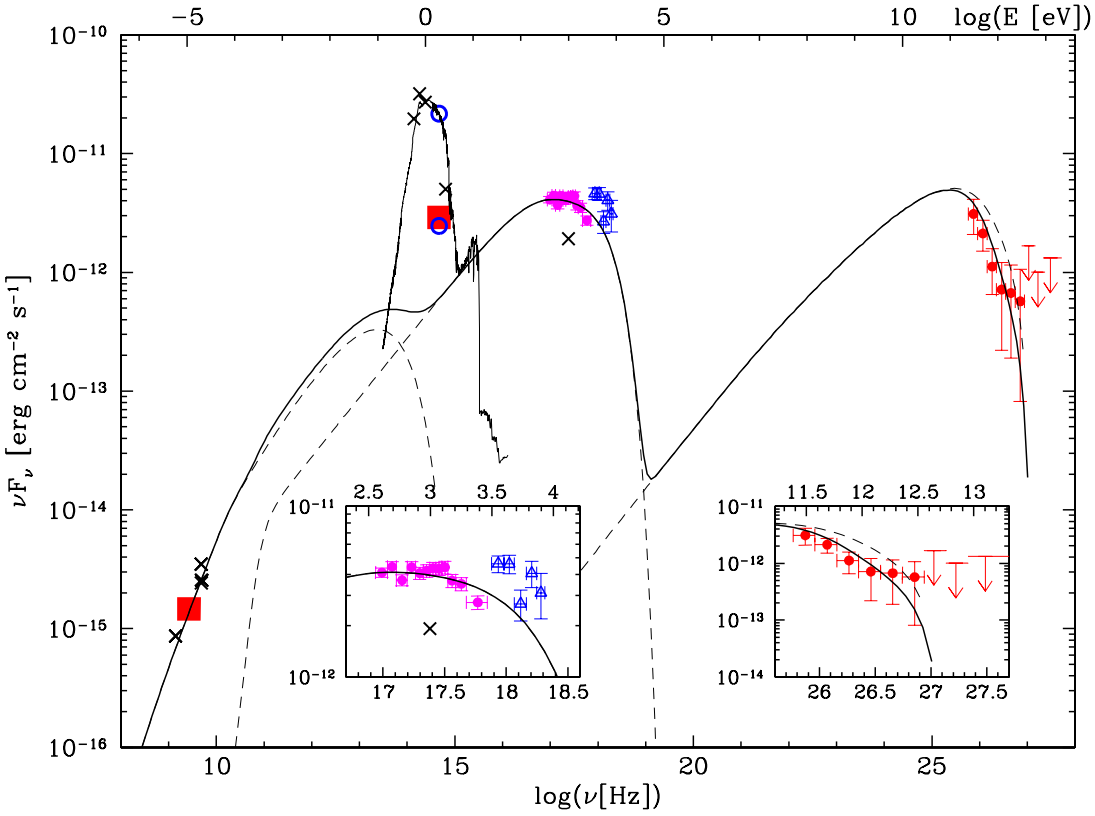

Figure 6.23: *The spectral energy distribution of RGB J0152+017. Shown are the H.E.S.S. spectrum (red filled circles and upper limits), and contemporaneous RXTE (blue open triangles), Swift/XRT (corrected for Galactic absorption, magenta filled circles), optical host galaxy-subtracted (ATOM) and radio (Nançay) observations (large red filled squares). The black crosses are archival data. The blue open points in the optical R-band correspond to the total and the core fluxes from Nilsson et al. (2003). A blob-in-jet synchrotron self-Compton model (see text) applied to RGB J0152+017 is also shown, describing the soft X-ray and VHE parts of the SED, with a simple synchrotron model shown at low frequencies to describe the extended part of the jet. The contribution of the dominating host galaxy is shown in the optical band. The dashed line above the solid line at VHE shows the source spectrum after correcting for EBL absorption. The left- and right-hand side inlays detail portions of the observed X-ray and VHE spectrum, respectively.*

Figure 6.23 shows the SED of RGB J0152+017 with the data from Nançay, ATOM,

Swift/XRT, *RXTE*/PCA, and H.E.S.S. Even though some data are not strictly simultaneous, no significant variability is found in the X-ray and optical bands throughout the periods covered; hence, a common modeling of the contemporaneous X-ray and VHE data appears justified.

The optical part of the SED is mainly due to the host galaxy, which is detected and resolved in optical wavelengths (Nilsson et al. 2003). A template of the spectrum of such an elliptic galaxy is shown in the SED, as inferred from the code PEGASE (Fioc & Rocca-Volmerange 1997). The host-galaxy-subtracted data point from the ATOM telescope might include several additional contributions—from an accretion disk, an extended jet (see below), or a central stellar population—so that it is considered as an upper limit in the following SSC model. A model including the optical ATOM data with possible additional contributions is beyond the scope of this paper.

The modeling of the SED was performed in cooperation with Jean-Philippe Lenain. A non-thermal leptonic SSC model (Katarzyński et al. 2001) is applied to account for the contemporaneous observations by *Swift* in X-rays and by H.E.S.S. in the VHE band. The radio data are assumed to originate in an extended region, described by a separate synchrotron model for the extended jet (Katarzyński et al. 2001) to explain the low-frequency part of the SED (as in, e.g., Aharonian et al. 2005b, 2008a).

It should be emphasized that the aim of applying this model in this work is not to present a definitive interpretation for this source, but rather to show that a standard SSC model is able to account for the VHE and *Swift* X-ray observations.

For the SSC model, the system is described as a small homogeneous spherical, emitting region (blob) of radius R within the jet, filled with a tangled magnetic field B and propagating with a Doppler factor $\delta = [\Gamma\,(1 - \beta\cos\theta)]^{-1}$. Here Γ is the bulk Lorentz factor of the emitting plasma blob, $\beta = v/c$, and θ is the angle of the velocity vector, with respect to the line-of-sight. The electron energy distribution (EED) is described by a broken power law, with indices n_1 and n_2, between Lorentz factors $\gamma_{\rm min}$ and $\gamma_{\rm max}$, with a break at $\gamma_{\rm break}$ and density normalization K.

The model also accounts for the absorption by the extragalactic background light (EBL) with the parameters given in Primack et al. (2005). RGB J0152+017 is too nearby ($z = 0.08$) to add to the constraints on the EBL that were found by H.E.S.S. measurements of other blazars (Aharonian et al. 2006d). In all the models, we assume $H_0 = 70\,{\rm km\,s^{-1}\,Mpc^{-1}}$, giving a luminosity distance of $d_{\rm L} = 1.078 \times 10^{27}$ cm for RGB J0152+017.

The EED can be described by $K = 3.1 \times 10^4\,{\rm cm^{-3}}$, $\gamma_{\rm min} = 1$, and $\gamma_{\rm max} = 4 \times 10^5$. The break energy is assumed at $\gamma_{\rm break} = 7.0 \times 10^4$ and is consistent with the *Swift*/XRT spectrum, while providing good agreement with the H.E.S.S. data. We assume the canonical index $n_1 = 2.0$ for the low-energy part of the EED, in accordance with standard Fermi-type acceleration mechanisms. The value $n_2 = 3.0$ for the high-energy part of the EED is constrained by the high-energy part of the X-ray spectrum. A good solution is found with the emitting region characterized by $\delta = 25$, $R = 1.5 \times 10^{15}\,{\rm cm}$, and $B = 0.10\,{\rm G}$.

For the extended jet, the data are described well by $R_{\rm jet} = 10^{16}\,{\rm cm}$, $\delta_{\rm jet} = 7$, $K_{\rm jet} = 70\,{\rm cm^{-3}}$, $B_{\rm jet} = 0.05\,{\rm G}$, and $\gamma_{\rm break,\,jet} = 10^4$ at the base of the jet, and $L_{\rm jet} = 50\,{\rm pc}$ (all the parameters are detailed in Katarzyński et al. 2001).

Assuming additional contributions in the optical band, the multi-wavelength SED can thus be explained with a standard shock-acceleration process. The parameters derived from

the model are similar to previous results for this type of source (see, e.g., Ghisellini et al. 2002).

Confirmation of the HBL nature

From the current Nançay radio data and the *Swift* X-ray data, we obtain a broad-band spectral index $\alpha_{\rm rx} \sim 0.56$ between the radio and the X-ray domains. The obtained SED, the corresponding location of the synchrotron peak, and the flux and shape of the *Swift* spectrum lead us to conclude that RGB J0152+017 can clearly be classified as an *HBL object* at the time of H.E.S.S. observations.

Summary of the AGN section

In this work, discovery of a BL Lac AGN RGB J0152+017 in VHE γ rays is presented. A spectral energy distribution (SED) including radio, optical, X-ray and VHE γ-ray data is for the first time derived. The X-ray and VHE observations can be well fitted by a simple SSC model. In order to account for the radio emission, one one needs to extend the SSC model by an external population of radio-emitting electrons. The optical emission from the jet exceeds the modeled one, which could be caused by a complications with disentangling the signal from the jet from the other regions of the galaxy. As a robust result, the object was confirmed as an HBL BL Lac by identifying the peak of the synchrotron emission.

Chapter 7

Expectations for the Cherenkov Telescope Array

7.1 CTA

Cherenkov Telescope Array (CTA) is a planned project of the next generation of IACT arrays. It is aimed to be an order of magnitude more sensitive than the current generation, represented by H.E.S.S., MAGIC, VERITAS and CANGAROO III experiments, and also to have an unprecedented spectral coverage, angular and temporal resolution. The experiment would substantially improve our knowledge of the high-energetic processes connected to VHE γ-ray production in the Universe.

Currently, an on-going design study is being performed and several candidate designs were proposed (see e.g. Bernlöhr 2008b):

- *Low energy* — Smaller number (in the order of 10) of telescopes with a large mirror area ($\sim$600 m^2) aimed at reaching very low energies ($\sim$20 GeV). An example array, studied by Bernlöhr (2008b), is an array consisting of 9 telescopes at 2000 m altitude.
- *High sensitivity* — More ($\sim$40) H.E.S.S.-type I telescopes with a mid-size mirror dish ($\sim$100 m^2), being more or less a quantitatively improved version of the H.E.S.S. experiment. An example array would consist of 41 telescopes of a type similar to the H.E.S.S. Phase I telescopes.
- *Broad energy range* — An array combining both mid-size and large-area telescopes could combine advantages of both techniques to extend the energy range and improve sensitivity. The array of this type, studied in the cited work, consists of 4 large telescopes and 85 smaller ones.
- *High energy* — Larger number ($\sim$40) of small telescopes ($\sim$40 m^2) with an increased spacing that would aim for large collection area, important for increasing the event statistics at higher energies.

The preliminary expectations of a sensitivity based on Monte Carlo simulations of the first three designs mentioned above are plotted in Fig.7.1 and compared to the sensitivity of the current-generation IACT arrays. One can see that the experiment could reach a

sensitivity equivalent to $\sim 1/10^3$ of the flux level from the Crab Nebula, the strongest steady VHE-emitting source, and to $\sim 1/10^4$ of the strongest flux levels observed in flares from BL Lac AGNs (Aharonian et al. 2007). This superior sensitivity and a high dynamic range would allow one to discover new classes of VHE emitters (e.g. the ones discussed in chapter 3), to perform temporal variability studies over a larger dynamic range of fluxes and to study the currently known VHE-emitting classes with an unprecedented precision with a reduced bias (due to the significantly higher event statistics). The improved sensitivity is the key aspect that should help in establishing the new extragalactic classes of VHE emitters.

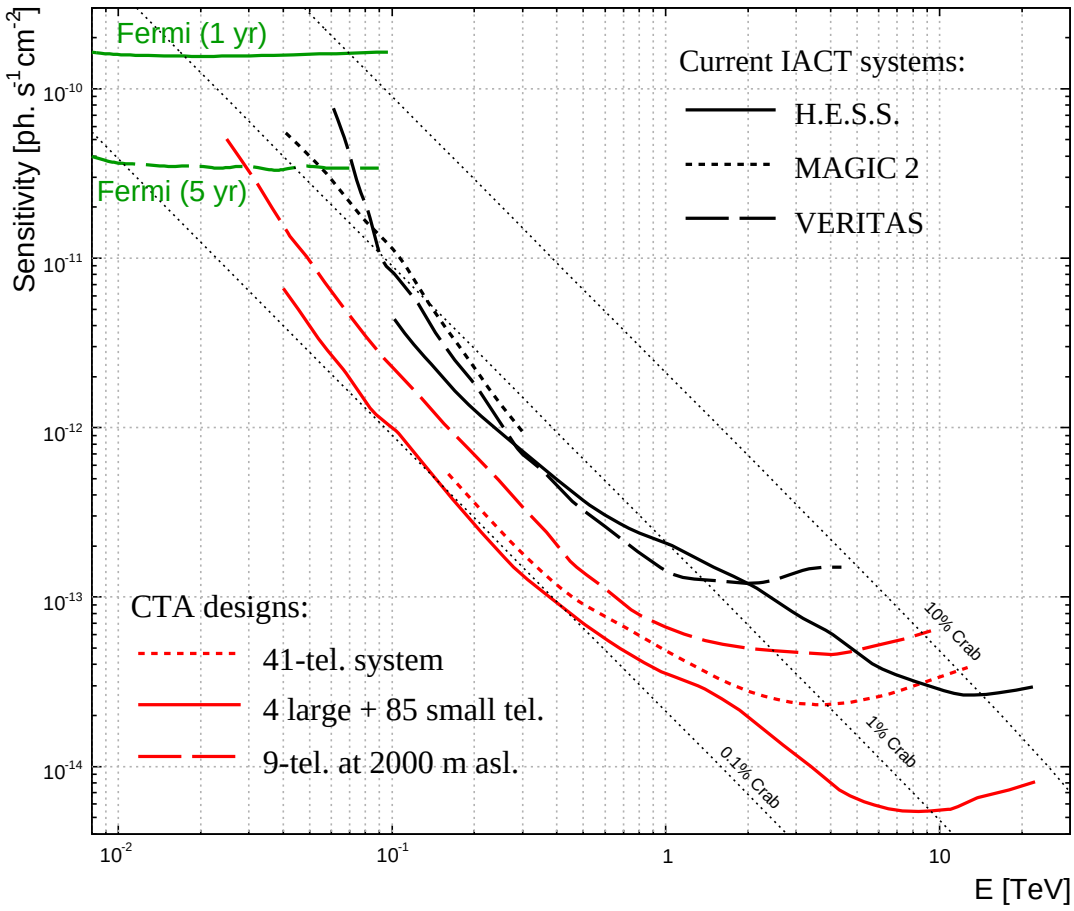

Figure 7.1: *Simulated performance of several potential designs of the CTA experiment. Shown are simulated integral flux sensitivities for a 5-σ detection in 50 hours with a minimum of 10 events (the black curves), and are compared to the ones of the current generation of IACT arrays: H.E.S.S., MAGIC and VERITAS (red curves), and to the expected performance of the Fermi space mission. The figure is based on data from Bernlöhr (2008b). One can see that the CTA might already reach the miliCrab sensitivity in the energy range ∼0.1–1 TeV. Also, it is possible to see the overlap in spectral coverage with the Fermi experiment, which will be of a high importance for multi-wavelength studies of acceleration of cosmic rays and subsequent γ-ray production.*

The expected angular resolution[1] is $\theta_{\rm res} = 0.03^\circ$ 10 TeV, $\theta_{\rm res} = 0.05^\circ$ at 1 TeV, and $\theta_{\rm res} = 0.12^\circ$ at 0.1 TeV (Bernlöhr 2008a).

7.2 Expectations for galaxy clusters and starburst regions

In this section, the advantages of the CTA experiments for observing galaxy clusters and starburst regions are discussed. The CTA sensitivity is also compared to the expected VHE fluxes to obtain an illustration of detectability of the sources.

7.2.1 Galaxy clusters

The results presented in chapter 6 demonstrate that the VHE fluxes of galaxy clusters are too weak to be detected within ∼40 hours with the current IACTs. The crucial aspect important for detecting them is thus an improvement of sensitivity. In chapter 3, it is, however, shown that the expected flux level from these objects could already be accessible for the current IACT assuming e.g. spectral index of primary particles of $\Gamma = 2.1$. By improving the sensitivity by an order of magnitude, it will be possible to test more conservative assumptions of $\Gamma = 2.3$ and a homogeneous distribution of cosmic rays within the clusters.

A second important parameter for observations of galaxy clusters is a large field of view. As shown in section 3.1, the source of VHE emission could be as extended as several Mpc, translating to ∼1°, depending on the distance of the cluster.

The lower energy threshold will extend the photon horizon and allow observations of more distant objects. This is, however, not so important for observing galaxy clusters, because there are no significantly more massive and X-ray luminous clusters than e.g. the Coma cluster (z=0.023) beyond the pair-production photon horizon for γ rays in the 1 TeV region (where the current telescopes are most sensitive), which is around $z \sim 0.1$. The decrease in energy threshold could be an advantage only in case that the VHE spectrum from galaxy cluster is rather steeper, which could be the case for VHE γ rays of a leptonic origin.

The expected integral flux at 1 TeV, estimated in section 3.1.5, is compared with the simulated sensitivity of the CTA experiment in the left panel of Fig. 7.2. One can see that CTA is going to be able to probe also very conservative assumptions of the primary CR spectrum and CR energy density.

7.2.2 Starburst regions

Similar to the case of galaxy clusters, a detection of starburst regions, such as NGC 253 or Arp 220, requires the improved sensitivity of CTA. It was shown in section 6.2.1 that there might be a hint of a signal already present in the results of the H.E.S.S. observations. In such case, the CTA would be bound to detect this object, as well as a number of similar ones.

An estimate of Domingo-Santamaría & Torres (2005) for the VHE emission from NGC 253 and of Torres & Domingo-Santamaría (2005) for Arp 220 is compared with the

[1] Note that these are preliminary estimates, subjected to possible changes

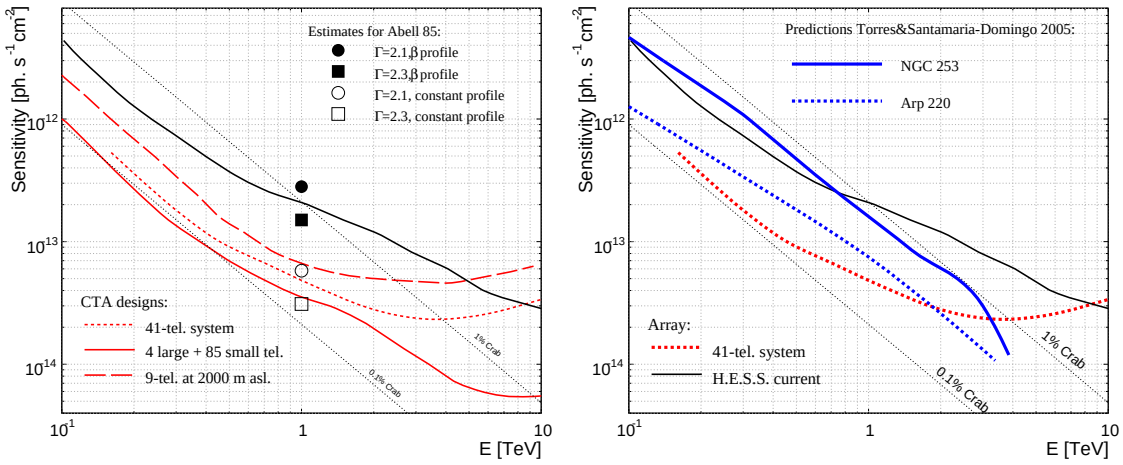

(a) Galaxy clusters (b) Starburst regions

Figure 7.2: Left: *Expected integral flux at 1 TeV from Abell 85, compared to the simulated CTA sensitivity according to Bernlöhr (2008b). The solid symbols refer to expectations based on the assumption that the cosmic-ray energy density follows the gas-density profile (β profile), the open symbols assume a flat profile of the energy density. The square (circular) symbols in a similar way correspond to an assumption of the proton primary spectrum of* $\Gamma = 2.1$ *(*$\Gamma = 2.3$*).* **Right:** *Sensitivity of the 41-telescope configuration of CTA is compared with the predictions of Domingo-Santamaría & Torres (2005) for the starburst galaxy NGC 253 and Torres & Domingo-Santamaría (2005) for the ULIRG Arp 220*

expected CTA sensitivity in the right panel of Fig. 7.2. One can see that NGC 253 should be observed by CTA. The case of Arp 220 is not so strong and might not be accessible to some of the planned configurations. Additionally, the northern location of Arp 220 disfavors its observations from the southern hemisphere, where no similar object is found.

Chapter 8

Summary & Conclusions

This work presented results of a search for a VHE γ-ray emission from non-AGN extragalactic objects using the H.E.S.S. experiment. Up to now, there has been no experimental evidence for such a signal from these objects, and its discovery is thus of a prime importance, because it would provide us with a new type of a cosmic laboratory for studying the highest energetic processes in the Universe. Unfortunately, no significant signal was found in this work, but the results seem to be very promising for a future project with an enhanced sensitivity.

In order to select the suitable candidate objects for such a study, a basic *theoretical overview* of cosmic-ray acceleration and VHE γ-ray production was presented. The particle acceleration via the first order Fermi acceleration in shocks was discussed, which is currently the most widely acknowledged CR acceleration mechanism. Further, an overview of the CR energy losses was given, which is in particular important for estimating the confinement time of the particles in extragalactic objects. Also summarized were VHE γ-ray production mechanisms, since their knowledge is necessary for estimating the γ flux.

The physical background of CR particle acceleration and γ-ray production, presented in chapter 2, was then used to select the classes of objects and individual targets suitable for observations with the H.E.S.S. instrument; these include *galaxy clusters*, *starburst galaxies* and *ultraluminous infrared galaxies*. Additionally, *AGNs* were discussed, but these form a specific group of objects, which have already been established as VHE emitters by Punch et al. (1992). All of these objects show an evidence of a non-thermal activity and are capable of accelerating CR particles to VHE or UHE energies, possibly up to 10^{20} eV.

The primary class investigated by this work are *galaxy clusters*. A detection of γ rays from these largest gravitationally bound objects in the Universe would allow one to study the production of cosmic rays over a timescale comparable with the age of the Universe, establishing thus an important link between astroparticle physics and cosmology. It was shown that CR protons are confined within the volume of a cluster for times exceeding the Hubble time. The clusters thus act as storehouses of hadronic cosmic rays up to energies $\sim 10^{15}$ eV, which are capable of producing VHE γ rays that could be observed by IACT arrays, such as H.E.S.S.. The processes leading to particle acceleration in the clusters were qualitatively and quantitatively summarized in chapter 3. It was shown that the energy content in CR protons can be $\sim 10^{62}$ eV for selected clusters Abell 85 and Abell 496. The γ-ray flux was approximately estimated for them and it was shown that it could be in principle observable by H.E.S.S. assuming a hard spectrum of primary CR protons and

their energy density profile to follow the gas density profile.

The analysis and results of observations of galaxy clusters Abell 85, Abell 496 and of Coma cluster, Abell 754, Centaurus cluster and of Hydra A were presented in chapter 6. Unfortunately, no hint of a signal was found from neither of these, even when using extended integration radii for the signal extraction. The results of the first two targets were, however, used to derive upper limits on the non-thermal energy content of CR protons in the clusters. In case of Abell 85, the calculated limit on the ratio $E_{\mathrm{CRp,nonth}}/E_{\mathrm{thermal}}$ for a hard spectrum and ICM-like CR energy density profile is 8%. This value is very challenging for some theoretical models (e.g. Miniati et al. 2001; Ryu et al. 2003) that estimate this ratio to be up to 50%. In the chapter 7, it was shown that also the more conservative assumptions[1] can be probed using the planned CTA telescope array.

The second class of objects investigated in this work are *starburst galaxies* and their more distant and more extreme form of *ultraluminous infrared galaxies (ULIRGs)*. These are objects with a very enhanced star-formation rate in their centres. Consequently, they are bound to harbour proportionally more supernova remnants than a Milky-Way-type galaxy, which are capable of creating a significant population of energetic CR protons. The high density of material in these regions provides targets for the protons, which can through a p-p interaction and a subsequent π^0-decay produce γ rays. Using simple arguments, it was shown that such objects can produce a VHE emission detectable by H.E.S.S.. This is supported also by works of e.g. Domingo-Santamaría & Torres (2005) and Torres & Domingo-Santamaría (2005). Starburst galaxies NGC 253 and M 83 and an ULIRG Arp 220 were investigated in this work. No significant signal was found from these objects using data from H.E.S.S. observations. In case of NGC 253, a hint of a signal at a $\sim 3\sigma$ level was, however, found. If the signal is real, its flux would well match the one predicted by Domingo-Santamaría & Torres (2005) and the spectrum would be rather hard, as expected. Further data are necessary in order to either confirm or refuse the signal.

In addition to the study of non-AGN sources, a discovery of one BL Lac AGN, RGB J0152+017, in VHE γ-ray band was presented in this work. Although not the main topic of this work, it illustrates a positive result of the analysis used in the previously mentioned studies. A quasi-simultaneous spectral energy distribution of this target was derived for the first time, extending from radio energies, over optical and X-ray energies up to VHE γ rays. The identification of the synchrotron peak in the X-ray energy band allowed one to identify the BL Lac as a high-frequency peaked one (HBL).

In order to demonstrate the robustness of the experimental and analysis technique used in this work, it is described in chapter 4. An overview of the IACT technique is given, along with a description of the H.E.S.S. experiment and the analysis methods. A special emphasis was placed on different aspects of the instrument performance in chapter 5, since its knowledge is important for calculating upper limits and estimating observability of the studied objects.

In summary, although no new class of non-AGN extragalactic source of VHE γ radiation has been presented, the results are very promising for the future generation of IACT telescopes, represented by e.g. CTA telescope array. This will achieve an unprecedented sensitivity, which should be sufficient to guarantee establishing starburst galaxies and possibly also galaxy clusters as VHE emitters (see chapter 7).

[1] E.g. a softer spectrum of the primary protons and a flatter profile of the CR energy density

Appendix A

Scaling quantities for a different H_0

The estimates of the Hubble constant $H_0 = h\ 100$ km/(s Mpc) changed in the last several years significantly. The older traditionally assumed value of $h = 0.5$ has been corrected to the current value of $\sim$0.7. That is the value used throughout this work. Many cited articles used, however, the older values to derive quantities cited in this work. They have to be therefore rescaled for the proper cosmology in order to be consistent. A summary of scalings used in this work is given in the table A.1.

Table A.1: *Scaling of quantities relevant to this work to a different cosmology specified by h*

Quantity	Abbreviation	Scaling factor
Total mass	M	h^{-1}
Core radius	$R_{\rm core}$	h^{-1}
Central electron number density	$n_{\rm e0}$	$h^{1/2}$
X-ray luminosity	$L_{\rm X}$	h^{-2}
Gass mass	$m_{\rm g}$	$h^{-5/2}$

Appendix B

Classification of BL Lac objects — HBL vs. LBL

Blazars are commonly distinguished as high-frequency-peaked BL Lacs (HBLs) and low-frequency-peaked BL Lacs (LBLs). This classification Padovani & Giommi (1995) is of a high interest for the TeV astronomers since HBLs are more likely to emit VHE γ rays than LBLs. A general qualitative criterium to distinguish these two types is whether the synchrotron peak of the spectrum is located in the X-ray energy range (HBL) or around the radio wave band (LBL case). Since the classification of one AGN is also part of the results of this thesis (see 6.4.1) we will specify the criteria more precisely.

In order to define a quantitative criterium to distinguish the latter types a *spectral index* α_{rx} has to be introduced:

$$\alpha_{\mathrm{rx}} = -\frac{\log(L_{5\mathrm{GHz}}/L_{1\mathrm{keV}})}{\log(\nu_{5\mathrm{GHz}}/\nu_{1\mathrm{keV}})}, \tag{B.1}$$

where L is a monochromatic flux at the given frequency (energy). The spectral index α_{rx} thus gives a measure for comparing energy output in the radio and X-ray band. The lower the value of the index, the steeper is the rise of the spectral energy distribution between the two frequencies.

- **HBL Blazars** have $\alpha_{\mathrm{rx}} < 0.7$. The synchrotron peak of the spectrum is located in the X-ray energy band.

- **LBL Blazars** are characterised by $\alpha_{\mathrm{rx}} > 0.8$ and a synchrotron peak in the radio energy band.

- **IBL Blazars** represent an intermediate type of the latter two. The spectral index is $\alpha_{\mathrm{rx}} \in (0.7, 0.8)$ and synchrotron peak falls into the optical region, whereby the steep fall of the peak is located in the soft X-ray band. Hard X-ray band are already produced by the inverse Compton process.

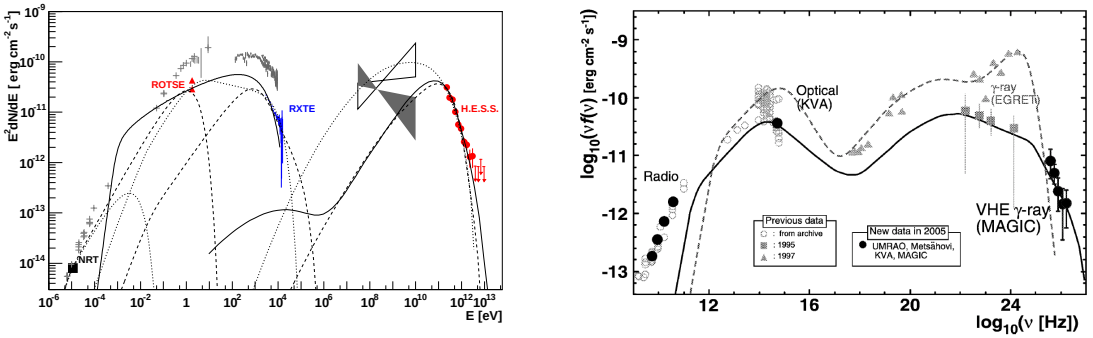

Figure B.1: *An example of a high-frequency-peaked BL Lac (***left***) PKS 2155-304 (Aharonian et al. 2005b) and of a low-frequency-peaked BL Lac (***right***) BL Lacertae (Albert et al. 2007b).*

List of Abbreviations

ADC Analogue to digital converter

AGN Active galactic nucleus

CoG Centre of gravity

CR Cosmic rays

DAQ Data acquistion

EAS Extensive air shower

EBL Extragalactic background light

FIR Far-IR

FOV Field of view

GRB γ-ray burst

H.E.S.S. High Energy Stereoscopic System

IACT Imaging atmospheric Čerenkov telescope

IGMF Intergalactic magnet fiels

IR Infrared

NSB Night-sky background

p.e. Photoelectron

PMT Photomultiplier tube

PSF Point-spread-function

RM Rotation measure

SB Starburst

SED Spectral energy distribution

SFR Star formation rate

SN Supernova

SNR Supernova remnant

UHECR Ultra-high-energy cosmic ray

ULIRG Ilutraluminous IR galaxy

VHE Very-high energy

Bibliography

Abbasi, R. U., Abu-Zayyad, T., Amman, J. F., et al. 2005, Astroparticle Physics, 23, 157 1

Abell, G. O. 1958, ApJS, 3, 211 6.1.1

Abell, G. O., Corwin, Jr., H. G., & Olowin, R. P. 1989, ApJS, 70, 1 6.1.1, 6.1.2, 6.1.2, 6.5

Abraham, J., Abreu, P., Aglietta, M., et al. 2007, Science, 318, 938 1

Abraham, J., Aglietta, M., Aguirre, I. C., et al. 2004, Nuclear Instruments and Methods in Physics Research A, 523, 50 1

Adami, C., Picat, J. P., Savine, C., et al. 2006, A&A, 451, 1159 6.8

Aharonian, F. 2004, Very High Energy Cosmic Gamma Radiation, A Crucial Window on the Extreme Universe (World Scientific Publishing Co. Pte. Ltd., 2004) 3.4.2

Aharonian, F., Akhperjanian, A. G., Aye, K.-M., et al. 2004a, Astroparticle Physics, 22, 109 4.4

Aharonian, F., Akhperjanian, A. G., Barres de Almeida, U., et al. 2008a, A&A, 477, 481 6.4.1

Aharonian, F., Akhperjanian, A. G., Barres de Almeida, U., et al. 2008b, A&A, 481, L103 6.4.1

Aharonian, F., Akhperjanian, A. G., Bazer-Bachi, A. R., et al. 2007, ApJ, 664, L71 7.1

Aharonian, F., Akhperjanian, A. G., Bazer-Bachi, A. R., et al. 2006a, A&A, 457, 899 4.5.2, 4.6, 4.6.4, 2, 4.6.5, 4.6.8, 5.2.3, 5.4, 5.13, 6, 6.1.1, 6.1, 6.1.2, 6.2, 6.4, 6.17, 6.4.1

Aharonian, F., Akhperjanian, A. G., Bazer-Bachi, A. R., et al. 2006b, A&A, 448, L19 6.4.1

Aharonian, F., Akhperjanian, A. G., Bazer-Bachi, A. R., et al. 2006c, A&A, 449, 223 1

Aharonian, F., Akhperjanian, A. G., Bazer-Bachi, A. R., et al. 2006d, Nature, 440, 1018 2.4.3, 6.4.1

Aharonian, F., Akhperjanian, A. G., Bazer-Bachi, A. R., et al. 2005a, A&A, 442, 177 3.2.3, 3.2.3, 4.6.9, 6.2.1

Aharonian, F., Akhperjanian, A. G., Bazer-Bachi, A. R., et al. 2005b, A&A, 442, 895 6.4.1, B.1

Aharonian, F., Akhperjanian, A. G., Bazer-Bachi, A. R., & et al. 2006e, Science, 314, 1424 3.4

Aharonian, F. A. 2002, MNRAS, 332, 215 3.1.3, 3.1.3

Aharonian, F. A., Akhperjanian, A. G., Aye, K.-M., et al. 2004b, Nature, 432, 75 1

Aharonian, F. A. & Atoyan, A. M. 1981, Ap&SS, 79, 321 2.4.2

Aharonian, F. A. & Atoyan, A. M. 1996, A&A, 309, 917 2.4.1

Aharonian, F. A., Krawczynski, H., Puehlhofer, G., Rowell, G. P., & HEGRA Collaboration. 2000, in Bulletin of the American Astronomical Society, Vol. 32, Bulletin of the American Astronomical Society, 1239–+ 5.1

Ajello, M., Rebusco, P., Cappelluti, N., et al. 2008, ArXiv e-prints, 809 3.1.3, 3.2, 6.1.4, 6.1.4

Albert, J., Aliu, E., Anderhub, H., et al. 2008, Science, 320, 1752 2.4, 3.4

Albert, J., Aliu, E., Anderhub, H., et al. 2007a, ApJ, 658, 245 6.3.1

Albert, J., Aliu, E., Anderhub, H., et al. 2007b, ApJ, 666, L17 3.4.1, B.1

Allen, S. W. & Fabian, A. C. 1994, MNRAS, 269, 409 6.1.4

Anchordoqui, L. A., Romero, G. E., & Combi, J. A. 1999, Phys. Rev. D, 60, 103001 1, 3.2.2

Antoni, T., Apel, W. D., Badea, F., et al. 2003, Nuclear Instruments and Methods in Physics Research A, 513, 490 1

Arp, H. 1966, ApJS, 14, 1 6.3.1

Atoyan, A. M. & Völk, H. J. 2000, ApJ, 535, 45 3.1.3

Axford, W. I., Leer, E., & Skadron, G. 1977, in International Cosmic Ray Conference, Vol. 11, International Cosmic Ray Conference, 132–+ 2.1.1

Baan, W. A. 2007, in IAU Symposium, Vol. 242, IAU Symposium, 437–445 6.3.1, 6.16

Bagchi, J., Durret, F., Neto, G. B. L., & Paul, S. 2006, Science, 314, 791 3.1.3, 3.2

Bagchi, J., Pislar, V., & Lima Neto, G. B. 1998, MNRAS, 296, L23+ 6.1.2

Barnard, R., Shaw Greening, L., & Kolb, U. 2008, in ESAC faculty workshop on x-rays from nearby galaxies : Proceedings of ESAC faculty workshop on x-rays from nearby galaxies, European Space Agency, ESAC, Madrid (Spain), ed. S. Carpano, M. Ehle, & W. Pietsch, 69–72 6.9

Becker, R. H., White, R. L., & Edwards, A. L. 1991, ApJS, 75, 1 6.4.1

Bell, A. R. 1978, MNRAS, 182, 443 2.1.1

Benbow, W. e. a. 2005, in Conference Proceedings "Towards a Network of Atmospheric Cherenkov Detectors VII", Palaiseau, France, 163–172 4.6

Berge, D. 2002, Master's thesis, Humboldt-Universität zu Berlin, http://www-eep.physik.hu-berlin.de/hess/public/diplom_david_berge.pdf 4.6

Berge, D. 2006, PhD thesis, Ruprecht-Karls Universität, Heidelberg 4.2, 4.6, 4.11, 4.6.7, 4.6.8, 4.6.8, 5.3.1

Berge, D., Funk, S., & Hinton, J. 2007, A&A, 466, 1219 4.6.6

Bergman, D. R. & Belz, J. W. 2007, Journal of Physics G Nuclear Physics, 34, 359 5

Bernlöhr, K. 2000, Astroparticle Physics, 12, 255 5.2.3, 5.7

Bernlöhr, K. 2008a, private communication 7.1

Bernlöhr, K. 2008b, in Gamma 08 Conference, Gamma 08 Conference, in preparation 5.4, 7.1, 7.1, 7.2

Bernlöhr, K. 2008c, ArXiv e-prints, 808 4.2, 5.2.1

Bernlöhr, K., Carrol, O., Cornils, R., et al. 2003, Astroparticle Physics, 20, 111 4.1

Bird, D. J., Corbato, S. C., Dai, H. Y., et al. 1995, ApJ, 441, 144 1

Blandford, R. D. & Konigl, A. 1979, ApJ, 232, 34 3.4.2

Blandford, R. D. & Ostriker, J. P. 1978, ApJ, 221, L29 2.1.1

Böhringer, H., Schuecker, P., Guzzo, L., et al. 2004, A&A, 425, 367 3.1.6, 6.6

Bolz, O. 2004, PhD thesis, Ruprecht-Karls Universität, Heidelberg 4.2

Bowyer, S., Korpela, E. J., Lampton, M., & Jones, T. W. 2004, ApJ, 605, 168 3.1.3

Braun, I. 2007, PhD thesis, Ruprecht-Karls Universität, Heidelberg 4.4

Bresolin, F. & Kennicutt, Jr., R. C. 2002, ApJ, 572, 838 6.2.2

Briel, U. G., Henry, J. P., & Boehringer, H. 1992, A&A, 259, L31 3.1.1

Brinkmann, W., Siebert, J., Feigelson, E. D., et al. 1997, A&A, 323, 739 6.4.1

Brown, A. M. & et al. 2005, in International Cosmic Ray Conference, Vol. 4, International Cosmic Ray Conference, 411–+ 5.2.3

Burrows, D. N., Hill, J. E., Nousek, J. A., et al. 2005, Space Science Reviews, 120, 165 6.4.1

Byram, E. T., Chubb, T. A., & Friedman, H. 1966, Science, 152, 66 3.1.1

Cavaliere, A. & Fusco-Femiano, R. 1976, A&A, 49, 137 3.1.1, 6.1.1

Cavaliere, A., Gursky, H., & Tucker, W. 1971, Nature, 231, 437 3.1.1

Chevalier, R. A. & Clegg, A. W. 1985, Nature, 317, 44 3.2.1

Chiba, N., Hashimoto, K., Hayashida, N., et al. 1992, Nuclear Instruments and Methods in Physics Research A, 311, 338 1

Churazov, E., Forman, W., Jones, C., & Böhringer, H. 2003, ApJ, 590, 225 3.1.1

Clarke, T. E., Kronberg, P. P., & Böhringer, H. 2001, ApJ, 547, L111 3.1.2, 3.1.2

Colafrancesco, S. & Blasi, P. 1998, Astroparticle Physics, 9, 227 3.1.3

Coppi, P. S. & Blandford, R. D. 1990, MNRAS, 245, 453 2.4.2

Corbató, S. C., Dai, H. Y., Elbert, J. W., et al. 1992, Nuclear Physics B Proceedings Supplements, 28, 36 1

Costamante, L. & Ghisellini, G. 2002, A&A, 384, 56 3.4.2, 3.10

Cox, P. & Mezger, P. G. 1989, A&A Rev., 1, 49 3.2.1

Daum, A., Hermann, G., Hess, M., et al. 1997, Astroparticle Physics, 8, 1 5.3.1

Davidge, T. J., Le Fevre, O., & Clark, C. C. 1991, ApJ, 370, 559 6.2.1

Davies, J. M. & Cotton, E. S. 1957, J. Solar Energy Sci. and Eng., 1, 16 4.2

De Grandi, S., Ettori, S., Longhetti, M., & Molendi, S. 2004, A&A, 419, 7 3.1.3

de Naurois, M. 2006, ArXiv Astrophysics e-prints 4.6.4

de Naurois, M. e. a. 2003, in International Cosmic Ray Conference, Vol. 5, International Cosmic Ray Conference, 2907–+ 6.1.1, 6.1.2

de Vaucouleurs, G., de Vaucouleurs, A., Corwin, Jr., H. G., et al. 1991, Third Reference Catalogue of Bright Galaxies (Volume 1-3, XII, 2069 pp. 7 figs.. Springer-Verlag Berlin Heidelberg New York) 6.2.2

Dermer, C. D. 2007, ArXiv e-prints, 711 1

Dermer, C. D., Schlickeiser, R., & Mastichiadis, A. 1992, A&A, 256, L27 3.4.2

Domainko, W., Benbow, W., Hinton, J. A., et al. 2007, ArXiv e-prints, 708 6.1.1, 6.1.4

Domainko, W., Gitti, M., Schindler, S., & Kapferer, W. 2004, A&A, 425, L21 3.1.3

Domingo-Santamaría, E. & Torres, D. F. 2005, A&A, 444, 403 3.2.2, 3.2.3, 6.14, 6.2.1, 2, 7.2.2, 7.2, 8

Dorfi, E. A. 1991, A&A, 251, 597 3.1.3, 3.1.3

Dorfi, E. A. & Voelk, H. J. 1996, A&A, 307, 715 3.1.3, 3.1.3

Drury, L. O., Aharonian, F. A., & Völk, H. J. 1994, A&A, 287, 959 2.4.1, 2.4.1

Dudley, C. C. & Wynn-Williams, C. G. 1999, MNRAS, 304, 549 6.2.1

Dunn, R. J. H. & Fabian, A. C. 2006, MNRAS, 373, 959 3.1.3

Dunn, R. J. H., Fabian, A. C., & Taylor, G. B. 2005, MNRAS, 364, 1343 3.1.3

Dupke, R. & White, III, R. E. 2002, in Astronomical Society of the Pacific Conference Series, Vol. 262, The High Energy Universe at Sharp Focus: Chandra Science, ed. E. M. Schlegel & S. D. Vrtilek, 377–+ 6.1.1

Dupke, R. & White, III, R. E. 2003, ApJ, 583, L13 6.1, 6.1.1

Durret, F., Adami, C., Gerbal, D., & Pislar, V. 2000, A&A, 356, 815 3.1.1, 3.1, 6.1.1

Durret, F., Lima Neto, G. B., & Forman, W. 2005, A&A, 432, 809 6.1.2, 6.4, 6.1.2, 6.5

Ebeling, H., Edge, A. C., Bohringer, H., et al. 1998, MNRAS, 301, 881 3.1.1

Engelbracht, C. W., Rieke, M. J., Rieke, G. H., Kelly, D. M., & Achtermann, J. M. 1998, ApJ, 505, 639 6, 6.5

Ensslin, T. A., Biermann, P. L., Kronberg, P. P., & Wu, X.-P. 1997, ApJ, 477, 560 3.1.3, 3.1.3

Fabian, A. C. 1994, ARA&A, 32, 277 3.1.1

Fabian, A. C., Celotti, A., Blundell, K. M., Kassim, N. E., & Perley, R. A. 2002, MNRAS, 331, 369 3.1.3

Fabian, A. C., Nulsen, P. E. J., Stewart, G. C., et al. 1981, MNRAS, 196, 35P 6.1.1

Fabian, A. C., Sanders, J. S., Taylor, G. B., & Allen, S. W. 2005, MNRAS, 360, L20 6.1.4

Feldman, G. J. & Cousins, R. D. 1998, Phys. Rev. D, 57, 3873 4.6.9, 6, 6.4, 6.4.1, 6.20

Felten, J. E., Gould, R. J., Stein, W. A., & Woolf, N. J. 1966, ApJ, 146, 955 3.1.1

Feretti, L. & Giovannini, G. 1998, in Untangling Coma Berenices: A New Vision of an Old Cluster, ed. A. Mazure, F. Casoli, F. Durret, & D. Gerbal, 123–+ 6.1.4

Fermi, E. 1949, Physical Review, 75, 1169 2.1.1

Fioc, M. & Rocca-Volmerange, B. 1997, A&A, 326, 950 6.4.1

Fossati, G., Buckley, J. H., Bond, I. H., et al. 2008, ApJ, 677, 906 3.9

Fritz, G., Davidsen, A., Meekins, J. F., & Friedman, H. 1971, ApJ, 164, L81+ 3.1.1

Funk, S. 2005a, PhD thesis, Ruprecht-Karls Universität, Heidelberg 4.6

Funk, S. 2005b, Master's thesis, Humboldt-Universität zu Berlin, http://www-eep.physik.hu-berlin.de/hess/public/diplom_sebastian_funk.pdf 4.3, 4.5

Funk, S., Hermann, G., Hinton, J., et al. 2004, Astroparticle Physics, 22, 285 4.2, 5.1, 5.2.3

Fusco-Femiano, R., dal Fiume, D., Feretti, L., et al. 1999, ApJ, 513, L21 3.1.3, 6.1.4

Fusco-Femiano, R., Landi, R., & Orlandini, M. 2007, ApJ, 654, L9 3.1.3

Fusco-Femiano, R., Orlandini, M., Brunetti, G., et al. 2004, ApJ, 602, L73 6.1.4

Fusco-Femiano, R., Orlandini, M., De Grandi, S., et al. 2003, A&A, 398, 441 6.1.4

Gabici, S. & Blasi, P. 2003, Astroparticle Physics, 19, 679 3.1.6

Gabici, S. & Blasi, P. 2004, Astroparticle Physics, 20, 579 3.1.6

Gao, Y. & Solomon, P. M. 2004, ApJ, 606, 271 3.6, 3.3.1

Ghisellini, G., Celotti, A., & Costamante, L. 2002, A&A, 386, 833 6.4.1

Ghisellini, G. & Madau, P. 1996, MNRAS, 280, 67 3.4.2

Giovannini, G., Feretti, L., Venturi, T., Kim, K.-T., & Kronberg, P. P. 1993, ApJ, 406, 399 3.1.3

Gitti, M., Brunetti, G., & Setti, G. 2002, in Astronomical Society of the Pacific Conference Series, Vol. 268, Tracing Cosmic Evolution with Galaxy Clusters, ed. S. Borgani, M. Mezzetti, & R. Valdarnini, 373–+ 3.3

González Delgado, R. M., Muñoz Marín, V. M., Pérez, E., Schmitt, H. R., & Cid Fernandes, R. 2008, Ap&SS, 121 3.2

Götting, N. 2005, PhD thesis, Universität Hamburg 6.2.1

Greisen, K. 1966, Physical Review Letters, 16, 748 1, 2.4.1

Griffith, M. R., Wright, A. E., Burke, B. F., & Ekers, R. D. 1995, ApJS, 97, 347 6.4.1

Gursky, H., Solinger, A., Kellogg, E. M., et al. 1972, ApJ, 173, L99+ 3.1.1

Hauser, M. 2008, private communication 6.22

Hauser, M., Möllenhoff, C., Pühlhofer, G., et al. 2004, Astronomische Nachrichten, 325, 659 6.4.1

Hauser, M. G. & Dwek, E. 2001, ARA&A, 39, 249 2.4.3

Hayashida, N., Honda, K., Honda, M., et al. 1994, Physical Review Letters, 73, 3491 1

Heckman, T. M. 1981, ApJ, 250, L59 6.1.1

Heckman, T. M., Armus, L., & Miley, G. K. 1990, ApJS, 74, 833 3.2.1

Heitler, W. 1960, The quantum theory of radiation (Oxford, Clarendon) 2.4.3

Henriksen, M. J. & Markevitch, M. L. 1996, ApJ, 466, L79+ 6.1.4

Henry, J. P. & Briel, U. G. 1995, ApJ, 443, L9 6.1.4

HESS Collaboration: F. Aharonian. 2008, ArXiv e-prints 4.6.9

Hillas, A. M. 1984, ARA&A, 22, 425 2.3

Hillas, A. M. 1985, in International Cosmic Ray Conference, Vol. 3, International Cosmic Ray Conference, ed. F. C. Jones, 445–448 4.1, 4.6.2

Hillas, A. M. 1996, Space Science Reviews, 75, 17 4.1

Hinton, J. 2008, ArXiv e-prints, 803 4

Hinton, J. A. 2004, New Astronomy Review, 48, 331 4.2

Hinton, J. A., Domainko, W., & Pope, E. C. D. 2007, MNRAS, 382, 466 3.1.3, 3.1.3, 3.1.5, 3.1.6, 6.1.4

Hofmann, W., Jung, I., Konopelko, A., et al. 1999, Astroparticle Physics, 12, 135 5.3.1, 5.3.1, 5.3.1, 5.3.2

Hörandel, J. R. 2003, Astroparticle Physics, 19, 193 1.1

Hörandel, J. R. 2008, Advances in Space Research, 41, 442 1.1

Itoh, C., Enomoto, R., Yanagita, S., et al. 2002, A&A, 396, L1 6.2.1

Itoh, C., Enomoto, R., Yanagita, S., et al. 2007, A&A, 462, 67 6.2.1

Itoh, C., Enomoto, R., Yanagita, S., et al. 2003, A&A, 402, 443 6.2.1

Ivanov, A. A., Knurenko, S. P., & Sleptsov, I. Y. 2003, Nuclear Physics B Proceedings Supplements, 122, 226 1

Jahoda, K., Swank, J. H., Giles, A. B., et al. 1996, in Presented at the Society of Photo-Optical Instrumentation Engineers (SPIE) Conference, Vol. 2808, Proc. SPIE Vol. 2808, p. 59-70, EUV, X-Ray, and Gamma-Ray Instrumentation for Astronomy VII, Oswald H. Siegmund; Mark A. Gummin; Eds., ed. O. H. Siegmund & M. A. Gummin, 59–70 6.4.1

Kalberla, P. M. W., Burton, W. B., Hartmann, D., et al. 2005, A&A, 440, 775 6.4.1

Kamae, T., Karlsson, N., Mizuno, T., Abe, T., & Koi, T. 2006, ApJ, 647, 692 2.4.1

Kang, H., Jones, T. W., & Gieseler, U. D. J. 2002, ApJ, 579, 337 3.1.3

Kang, H., Ryu, D., & Jones, T. W. 1996, ApJ, 456, 422 1

Kappes, A., Hinton, J., Stegmann, C., & Aharonian, F. A. 2007, ApJ, 656, 870 2.4.1

Karachentsev, I. D., Grebel, E. K., Sharina, M. E., et al. 2003, A&A, 404, 93 6.2.1

Katarzyński, K., Sol, H., & Kus, A. 2001, A&A, 367, 809 6.4.1

Kelner, S. R., Aharonian, F. A., & Bugayov, V. V. 2006, Phys. Rev. D, 74, 034018 2.2.1, 2.4.1

Kempner, J. C., Sarazin, C. L., & Ricker, P. M. 2002, ApJ, 579, 236 6.1.2, 6.1.2

Keshet, U., Waxman, E., & Loeb, A. 2004, New Astronomy Review, 48, 1119 3.1.3

King, I. 1962, AJ, 67, 471 3.1.1

Kosack, K. & VERITAS Collaboration. 2004, in Bulletin of the American Astronomical Society, Vol. 36, Bulletin of the American Astronomical Society, 927–+ 5.2.1

Kronberg, P. P. 2001, in American Institute of Physics Conference Series, Vol. 558, American Institute of Physics Conference Series, ed. F. A. Aharonian & H. J. Völk, 451–+ 3.1.2

Krymskii, G. F. 1977, Soviet Physics Doklady, 22, 327 2.1.1

Lagage, P. O. & Cesarsky, C. J. 1983, A&A, 125, 249 2.1.1

Lahav, O., Fabian, A. C., Edge, A. C., & Putney, A. 1989, MNRAS, 238, 881 3.1.1

Laurent-Muehleisen, S. A., Kollgaard, R. I., Ciardullo, R., et al. 1998, ApJS, 118, 127 6.4.1

Laurent-Muehleisen, S. A., Kollgaard, R. I., Feigelson, E. D., Brinkmann, W., & Siebert, J. 1999, ApJ, 525, 127 3.10, 6.4.1

Le Gallou, R. & H. E. S. S. Collaboration. 2003, in International Cosmic Ray Conference, Vol. 5, International Cosmic Ray Conference, 2879–+ 5.2.3

Lehnert, M. D. & Heckman, T. M. 1996, ApJ, 472, 546 3.2.1

Levenson, N. A., Weaver, K. A., & Heckman, T. M. 2001, ApJ, 550, 230 3.2

Levinson, A. 2000, Physical Review Letters, 85, 912 2.4.1

Li, T.-P. & Ma, Y.-Q. 1983, ApJ, 272, 317 4.6.6, 4.6.6, 5.4, 6.4.1

Lieu, R., Mittaz, J. P. D., Bowyer, S., et al. 1996, Science, 274, 1335 3.1.3

Lima Neto, G. B., Pislar, V., & Bagchi, J. 2001, A&A, 368, 440 6.1.2

Lima Neto, G. B., Pislar, V., Durret, F., Gerbal, D., & Slezak, E. 1997, A&A, 327, 81 6.1.2

Loeb, A. & Waxman, E. 2000, Nature, 405, 156 3.1.3

Longair, M. S. 1992, High energy astrophysics. Vol.1: Particles, photons and their detection (High Energy Astrophysics, by Malcolm S. Longair, pp. 436. ISBN 0521387736. Cambridge, UK: Cambridge University Press, March 1992.) 2.4.2

Longair, M. S. 1994, High energy astrophysics. Vol.2: Stars, the galaxy and the interstellar medium (Cambridge: Cambridge University Press, —c1994, 2nd ed.) 2.1.1, 2.1.1, 2.1.1, 2.2

Mac Low, M.-M. 2002, Ap&SS, 281, 429 3.3.1

Markevitch, M., Forman, W. R., Sarazin, C. L., & Vikhlinin, A. 1998, ApJ, 503, 77 6.1.2

Markevitch, M., Mazzotta, P., Vikhlinin, A., et al. 2003, ApJ, 586, L19 6.1.4

Markevitch, M., Vikhlinin, A., Forman, W. R., & Sarazin, C. L. 1999, ApJ, 527, 545 3.1.1, 3.1, 3.1.3, 6.1.1, 6.1.1, 6.1.1

Marscher, A. P. & Gear, W. K. 1985, ApJ, 298, 114 3.4.2

Martinez, S., Arqueros, F., Fonseca, V., et al. 1995, Nuclear Instruments and Methods in Physics Research A, 357, 567 5.2.1

Matsushita, K., Belsole, E., Finoguenov, A., & Böhringer, H. 2002, A&A, 386, 77 3.1.1

Mauersberger, R., Henkel, C., Wielebinski, R., Wiklind, T., & Reuter, H.-P. 1996, A&A, 305, 421 6.5

McCarthy, P. J., van Breugel, W., & Heckman, T. 1987, AJ, 93, 264 6.2.1

McHardy, I. M., Lawrence, A., Pye, J. P., & Pounds, K. A. 1981, MNRAS, 197, 893 3.1.1

McNamara, B. R., Wise, M. W., Nulsen, P. E. J., et al. 2001, ApJ, 562, L149 3.1.3

Meekins, J. F., Gilbert, F., Chubb, T. A., Friedman, H., & Henry, R. C. 1971, Nature, 231, 107 3.1.1

Melo, V. P., Pérez García, A. M., Acosta-Pulido, J. A., Muñoz-Tuñón, C., & Rodríguez Espinosa, J. M. 2002, ApJ, 574, 709 3.2.1, 6.2.1

Miniati, F. 2003, MNRAS, 342, 1009 3.1.3

Miniati, F., Ryu, D., Kang, H., & Jones, T. W. 2001, ApJ, 559, 59 6.1.3, 6.1.6, 8

Mitchell, R. J., Culhane, J. L., Davison, P. J. N., & Ives, J. C. 1976, MNRAS, 175, 29P 3.1.1

Mohan, N. R., Goss, W. M., & Anantharamaiah, K. R. 2005, A&A, 432, 1 3.2.1, 6.2.1

Mohr, J. J., Mathiesen, B., & Evrard, A. E. 1999, ApJ, 517, 627 3.1.1, 3.1.1, 6.1.2, 6.1.2

Moskalenko, I. V., Stawarz, L., Porter, T. A., & Cheung, C. C. 2008, ArXiv e-prints, 805 1

Nedbal, D., Benbow, W., Costamante, L., et al. 2007, The Astronomer's Telegram, 1295, 1 6.4.1, 6.4.1

Nedbal, D. e. a. f. t. H. C. 2007, in International Cosmic Ray Conference, in preparation, International Cosmic Ray Conference 6.2.1

Nilson, P. 1973, Uppsala general catalogue of galaxies (Acta Universitatis Upsaliensis. Nova Acta Regiae Societatis Scientiarum Upsaliensis - Uppsala Astronomiska Observatoriums Annaler, Uppsala: Astronomiska Observatorium, 1973) 6.3.1

Nilsson, K., Pursimo, T., Heidt, J., et al. 2003, A&A, 400, 95 6.4.1, 6.4.1, 6.23, 6.4.1

Nulsen, P. E. J., McNamara, B. R., Wise, M. W., & David, L. P. 2005, ApJ, 628, 629 6.1.4

Oegerle, W. R. & Hill, J. M. 2001, AJ, 122, 2858 3.1.1

Osborne, J. L., Aye, M., Chadwick, P. M., et al. 2002, Bulletin of the Astronomical Society of India, 30, 51 5.2.3

Ott, M., Witzel, A., Quirrenbach, A., et al. 1994, A&A, 284, 331 6.4.1

Owen, F. N., Eilek, J. A., & Kassim, N. E. 2000, ApJ, 543, 611 6.1.4

Padovani, P. & Giommi, P. 1995, ApJ, 444, 567 B

Parker, E. N. 1966, ApJ, 145, 811 1

Perkins, J. S., Badran, H. M., Blaylock, G., et al. 2006, ApJ, 644, 148 3.1.1, 1, 3.1.5, 6.1.2

Peterson, J. R. & Fabian, A. C. 2006, Phys. Rep., 427, 1 3.1.1, 3.1.6

Pfrommer, C. & Enßlin, T. A. 2004, A&A, 413, 17 3.1.3

Pfrommer, C., Enßlin, T. A., & Springel, V. 2008, MNRAS, 385, 1211 3.1.3, 3.1.5, 3.4, 3.1.5, 3.5

Pietsch, W., Roberts, T. P., Sako, M., et al. 2001, A&A, 365, L174 6.11

Pislar, V., Durret, F., Gerbal, D., Lima Neto, G. B., & Slezak, E. 1997, A&A, 322, 53 6.1.2, 6.6

Porter, N. A. & Weekes, T. C. 1977, SAO Special Report, 381 4

Primack, J. R., Bullock, J. S., & Somerville, R. S. 2005, in American Institute of Physics Conference Series, Vol. 745, High Energy Gamma-Ray Astronomy, ed. F. A. Aharonian, H. J. Völk, & D. Horns, 23–33 6.4.1

Puche, D. & Carignan, C. 1988, AJ, 95, 1025 6.5

Punch, M., Akerlof, C. W., Cawley, M. F., et al. 1992, Nature, 358, 477 3.4, 8

Reiprich, T. H. & Böhringer, H. 2002, ApJ, 567, 716 3.1.6, 6.1.1, 6.1.2, 6.5, 6.1.2

Rekola, R., Richer, M. G., McCall, M. L., et al. 2005, MNRAS, 361, 330 6.2.1

Renzini, A. 2004, in Clusters of Galaxies: Probes of Cosmological Structure and Galaxy Evolution, ed. J. S. Mulchaey, A. Dressler, & A. Oemler, 260–+ 3.1.1, 3.1.3

Renzini, A., Ciotti, L., D'Ercole, A., & Pellegrini, S. 1993, ApJ, 419, 52 3.1.3

Rephaeli, Y. 2001, in American Institute of Physics Conference Series, Vol. 558, American Institute of Physics Conference Series, ed. F. A. Aharonian & H. J. Völk, 427–+ 6.1.4

Rephaeli, Y. & Gruber, D. 2002, ApJ, 579, 587 6.1.4

Rephaeli, Y., Gruber, D., & Blanco, P. 1999, ApJ, 511, L21 3.1.3, 6.1.4

Rice, W., Lonsdale, C. J., Soifer, B. T., et al. 1988, ApJS, 68, 91 3.2.1

Rieke, G. H., Lebofsky, M. J., Thompson, R. I., Low, F. J., & Tokunaga, A. T. 1980, ApJ, 238, 24 3.2, 6.2.1

Rieke, G. H., Lebofsky, M. J., & Walker, C. E. 1988, ApJ, 325, 679 3.2.2, 6.2.1

Rodríguez-Rico, C. A., Goss, W. M., Viallefond, F., et al. 2005, ApJ, 633, 198 6.3.1

Roettiger, K., Stone, J. M., & Mushotzky, R. F. 1998, ApJ, 493, 62 6.1.4

Rossetti, M. & Molendi, S. 2007, ArXiv Astrophysics e-prints 3.1.3

Ruderman, M. A. & Spiegel, E. A. 1971, ApJ, 165, 1 3.1.1

Ryu, D., Kang, H., Hallman, E., & Jones, T. W. 2003, ApJ, 593, 599 3.1.3, 6.1.3, 6.1.6, 8

Sanders, D. B. & Mirabel, I. F. 1996, ARA&A, 34, 749 3.3

Sanders, D. B., Soifer, B. T., Elias, J. H., et al. 1988, ApJ, 325, 74 6.3.1

Sarazin, C. L. 1986, Reviews of Modern Physics, 58, 1 3.1.1, 3.1.1

Sarazin, C. L. 1988, X-ray emission from clusters of galaxies (Cambridge Astrophysics Series, Cambridge: Cambridge University Press, 1988) 3.1.1

Scoville, N. Z., Sargent, A. I., Sanders, D. B., & Soifer, B. T. 1991, ApJ, 366, L5 3.3

Siebenmorgen, R. & Krügel, E. 2007, A&A, 461, 445 3.6

Sikora, M., Begelman, M. C., & Rees, M. J. 1994, ApJ, 421, 153 3.4.2

Slee, O. B., Roy, A. L., Murgia, M., Andernach, H., & Ehle, M. 2001, AJ, 122, 1172 6.4, 6.1.2

Slezak, E., Durret, F., Guibert, J., & Lobo, C. 1998, A&AS, 128, 67 6.1.2

Smialkowski, A., Giller, M., & Michalak, W. 2002, Journal of Physics G Nuclear Physics, 28, 1359 3.3

Sofia, S. 1973, ApJ, 179, L25+ 3.1.1

Soifer, B. T., Neugebauer, G., Matthews, K., et al. 1999, ApJ, 513, 207 6.3.1

Stecker, F. W., de Jager, O. C., & Salamon, M. H. 1992, ApJ, 390, L49 2.4.3

Struble, M. F. & Rood, H. J. 1999, ApJS, 125, 35 3.1.1

Tamura, T., Bleeker, J. A. M., Kaastra, J. S., Ferrigno, C., & Molendi, S. 2001, A&A, 379, 107 6.1.1

Tamura, T., Kaastra, J. S., den Herder, J. W. A., Bleeker, J. A. M., & Peterson, J. R. 2004, A&A, 420, 135 3.1.3

Telesco, C. M. & Harper, D. A. 1980, ApJ, 235, 392 6.2.1

Tennent, R. M. 1967, Proceedings of the Physical Society, 92, 622 1

Theureau, G., Hanski, M. O., Coudreau, N., Hallet, N., & Martin, J.-M. 2007, A&A, 465, 71 6.4.1

Thim, F., Tammann, G. A., Saha, A., et al. 2003, ApJ, 590, 256 6.2.2

Thornton, K., Gaudlitz, M., Janka, H.-T., & Steinmetz, M. 1998, ApJ, 500, 95 3.1.3

Torres, D. F. 2004, ApJ, 617, 966 3.3.1, 6.3.1

Torres, D. F. & Anchordoqui, L. A. 2004, Reports of Progress in Physics, 67, 1663 1, 3.3

Torres, D. F. & Domingo-Santamaría, E. 2005, Modern Physics Letters A, 20, 2827 3.3.1, 3.7, 6.3.1, 6.3.1, 6.17, 7.2.2, 7.2, 8

Torres, D. F., Reimer, O., Domingo-Santamaría, E., & Digel, S. W. 2004, ApJ, 607, L99 3.3.1

Urry, C. M. & Padovani, P. 1995, Publ. Astron. Soc. Pac., 107, 803 3.4, 3.8, 3.4.1

Čerenkov, P. A. 1937, Physical Review, 52, 378 4.1

Valinia, A., Arnaud, K., Loewenstein, M., Mushotzky, R. F., & Kelley, R. 2000, ApJ, 541, 550 6.1.1

Van Buren, D. & Greenhouse, M. A. 1994, ApJ, 431, 640 3.2.1, 5, 6.2.1, 4, 6.5

van Eldik, C., B. O., I., B., et al. 2007, in International Cosmic Ray conference, Merida, ICRC proceedings, in preparation 4.1

Völk, H. J., Aharonian, F. A., & Breitschwerdt, D. 1996, Space Science Reviews, 75, 279 3.1.3, 3.1.3, 3.1.3, 3.1.5, 3.2.2, 6.1.1

Wagner, R. 2008, `http://www.mpp.mpg.de/~rwagner/sources/index.html` 1.2

Weaver, K. A., Heckman, T. M., Strickland, D. K., & Dahlem, M. 2002, ApJ, 576, L19 3.2, 3.2.3, 6.5

Weekes, T. C., Cawley, M. F., Fegan, D. J., et al. 1989, ApJ, 342, 379 4, 4.1, 4.6.6

White, S. D. M., Navarro, J. F., Evrard, A. E., & Frenk, C. S. 1993, Nature, 366, 429 6.1.1

Young, P. J. 1976, AJ, 81, 807 6.4.1

Zaritsky, D., Gonzalez, A. H., & Zabludoff, A. I. 2004, ApJ, 613, L93 3.1.3

Zatsepin, G. T. & Kuz'min, V. A. 1966, Soviet Journal of Experimental and Theoretical Physics Letters, 4, 78 1, 2.4.1

Zirakashvili, V. N. & Völk, H. J. 2006, ApJ, 636, 140 3.2.1, 3.2.3, 6.2.1, 6.2.1, 6.5, 1

Acknowledgements

I would like to express my thanks to all the many people that helped me on the long way towards finishing this work. It has been a truly excellent experience to work in the MPIK group of prof. Hofmann among such enthusiastic and motivating colleagues and friends. I thank prof. Werner Hofmann for giving me the opportunity to work in MPIK, Heidelberg on the H.E.S.S. experiment and for his support during the work.

I also want to express my gratitude to the whole "old guard," namely Jim Hinton, Conor Masterson, Wystan Benbow, David Berge, Stefan Funk and Bruno Khelifi, who helped me at the beginnings and showed me how interesting the work in the field can be. Jim and Conor I thank for the great climbing and their friendship also "out of the office." To Wystan belongs also a particular thank for the great steaks and the nice shift in Namibia.

Further, I thank to the group of my PhD student colleagues, Rolf Bühler, Stefan Hoppe, Isabel Braun, Svenja Carrigan, Kathrin Egberts, Dominik Hauser, Stefan Ohm and Daniil Nekrassov for the motivating discussions and for the great working atmosphere. A special thank belongs to Rolf and Stefan for their friendship, the climbing and the encouragement in the work.

Last but not least from the HD group, a thank goes to the current post-doctorands Karl Kosack, Wilfried Domainko, Christopher van Eldik, Matthieu Renaud, Andre-Claude Clapson and Andreas Förster. To Karl especially, for his careful reading of the thesis, and to Willie for the encouraging collaboration on the topic of galaxy clusters.

I would also like to thank the people who helped me on my two shifts in Namibia, especially when having the responsibility of a shift expert. Here, I thank espicially Eben, Maveipi and Toni for their help in solving numerous problems, even in the middle of the night. Matthias Füßling also deserves a big thank for being the best DAQ expert on a shift and for his friendly and tireless help with problems occuring almost every night.

Rád bych také poděkoval prof. Ladislavu Robovi za jeho přátelskou pomoc a za uvedení do zajímavé problematiky kosmického záření. Prof. Hořejšímu děkuji za podporu mojí práce ze strany Ústavu částicové a jaderné fyziky.

Velmi významnou zásluhu na dokončení této práce má hlavně moje rodina, které tímto děkuji, a to obzvláště mým rodičům za jejich neustálou a nezištnou podporu, kterou jim doufám jednou budu moci opětovat.

Největší dík patří mojí nádherné Janičce za to, že to tady se mnou tak dlouho vydržela, celou dobu mě podporovala a za to, že mi dala takovou krásnou dcerušku Klárku. Děkuju za oporu, kterou mi obě děvčata byla během posledních měsíců psaní této práce.